

**UNIVERSITÀ
DEGLI STUDI
DI GENOVA**

**Fast control of light through
acousto-optics**

Ph.D. Thesis submitted by:
Alessandro ZUNINO

Supervisors:
Prof. Martí DUOCASTELLA
Prof. Alberto DIASPRO

Ph.D. Course in *Physics and Nanosciences* – XXXIV cycle

Contents

1	Introduction	4
1.1	Structured Light	5
1.2	Technologies for structuring the light	6
1.2.1	Diffractive Optical Elements	7
1.2.2	Deformable Mirrors	7
1.2.3	Digital Micromirror Devices	8
1.2.4	Liquid Crystal Spatial Light Modulators	8
1.2.5	Electro-optic devices	8
1.2.6	Acousto-Optic devices	9
1.3	Aim and organization of the thesis	9
2	Acousto-optic Effect and Devices	12
2.1	The acousto-optic effect	12
2.1.1	Diffraction regimes	14
2.1.1.1	Raman-Nath regime	14
2.1.1.2	Bragg regime	15
2.1.2	Anisotropic Diffraction	16
2.2	Acousto-optic devices	18
2.2.1	Bragg Cells	18
2.2.1.1	AO deflectors	19
2.2.1.2	AO modulators	20
2.2.1.3	AO tunable filters	21
2.2.2	Raman-Nath Cells	21
2.2.2.1	TAG lens	23
2.2.2.2	AOF device	23
3	AOF Device: Theoretical Model	27
3.1	Design and realization of the device	28
3.2	Mechanical model	29
3.2.1	Resonant solution	30
3.2.1.1	Transient behavior	30
3.2.1.2	Steady-state solution	30
3.2.2	Traveling solution	33

3.2.3	From density to refractive index	34
3.3	Optical model	34
3.3.1	Fresnel Diffraction	35
3.3.2	Fraunhofer Diffraction	37
3.3.3	Parallelization of non-conventional beams	38
3.4	Conclusion	38
4	AOF Device: Characterization and Applications	42
4.1	Dynamic generation of structured light	43
4.1.1	Acousto-Optofluidic device implementation	44
4.1.2	Stability and performance of the AOF device	44
4.1.3	Speed and tunability	46
4.1.4	Role of the work parameters	48
4.2	Laser Direct Writing with the AOF device	51
4.2.1	Material processing setup	51
4.2.2	Multi-focus processing of materials	51
4.2.3	Parallelized tailored writing	53
4.2.4	Sample preparation and characterization	55
4.2.5	Considerations over the damage threshold	55
4.3	Conclusion	55
5	Multiplane Encoded Light-Sheet Microscopy	61
5.1	Working principle of MELM	64
5.2	MELM implementation	67
5.2.1	Microscope setup	70
5.2.2	Acousto-optic light sculpting	70
5.2.3	TAG Lens calibration	70
5.3	Feasibility of MELM	71
5.3.1	Simulations	71
5.3.2	Experimental results	73
5.3.2.1	SPED measurements	74
5.3.2.2	Imaging of biological samples	74
5.3.3	Sample preparation	76
5.4	Image analysis	77
5.5	Conclusion	78
6	Conclusion	83
A	Elements of Geometrical Optics	85
A.1	Rays and ray transfer matrices	85
A.2	Scanning lens	86
A.3	Image formation	86
A.3.1	Single lens system	86

A.3.2	Two lenses system	86
B	Elements of Fourier Optics	88
B.1	Diffraction	88
B.1.1	Fresnel diffraction	89
B.1.2	Fraunhofer diffraction	90
B.2	Fourier transforming property of the lenses	90
B.3	Image Formation	91
B.4	Impulse response of an imaging system	92
B.5	Coherence of light	93
B.6	Incoherent imaging	94
B.7	Lateral and axial resolution	95
C	Principles of Acousto-Optics	96
C.1	Electromagnetic wave equation in a sound field	96
C.2	Raman-Nath equations and their solutions	98
C.2.1	Traveling wave	99
C.2.1.1	Solutions of the Raman-Nath equation	101
C.2.1.2	Bragg regime	103
C.2.1.3	Raman-Nath regime	104
C.2.1.4	About the meaning of the parameter Q	105
C.2.2	Standing wave	105
C.2.2.1	Bragg Regime	107
C.2.2.2	Raman-Nath Regime	107
D	Wave Equation in Liquids	109
D.1	Conservation of mass	109
D.2	Conservation of momentum	110
D.3	Equation of state	112
D.4	Linearization of variables	112
D.5	The damped wave equation	114
E	Solution of the Acoustic Wave Equation	115
E.1	Actuators in phase	115
E.1.1	Boundary conditions	115
E.1.1.1	Homogeneous solution	117
E.1.1.2	Complete solution	119
E.2	Actuators in phase opposition	121
E.2.1	Boundary conditions	121
E.2.2	Complete solution	122
E.3	Reflecting plate	123
E.3.1	Boundary conditions	123
E.3.2	Complete solution	124

E.4	Traveling wave	125
E.4.1	Boundary conditions	125
E.4.2	Complete solution	125
F	Derivation of the Diffraction Patterns	127
F.1	Acousto-optic interaction regime	127
F.2	Transmittance function	127
F.3	Gaussian beam	129
F.4	Fraunhofer diffraction	130
F.5	Fresnel diffraction	132
G	The Tunable Acoustic Gradient Lens	136
G.1	Cylindrical acoustic wave equation	136
G.2	TAG lens focal length	138
G.2.1	Working distance of the detection system	139
G.3	Time-averaged Point Spread Function	139
G.3.1	Effect on the MTF	140
H	Noise Reduction Through Parallelization	142
H.1	Noise types	142
H.1.1	Random noise	142
H.1.2	Photon Noise	143
H.1.3	Background	144
H.2	Encoding matrices	145
H.2.1	Sequential Scan	145
H.2.2	Black Light Sheet	145
H.2.3	Hadamard Encoding	146
I	Image Analysis	149
I.1	Fourier Ring Correlation	149
I.2	Image deconvolution	150
I.2.1	Wiener Filter	151
I.2.2	Richardson-Lucy	152

List of acronyms and symbols

Acronyms

AO	Acousto-Optics
AOD	Acousto-Optic Deflector
AOF	Acousto-Opto-Fluidic
AOM	Acousto-Optic Modulator
AOTF	Acousto-Optic Tunable Filter
AM	Amplitude Modulation
CMOS	Complementary Metal–Oxide–Semiconductor
CW	Continuous Wave
DM	Deformable Mirror
DMD	Digital Micromirror Device
DOE	Diffractive Optical Element
DoF	Depth of Field
EDoF	Extended Depth of Field
EOD	Electro-Optic Deflector
EOM	Electro-Optic Modulator
FM	Frequency Modulation
FoV	Field of View
FRC	Fourier Ring Correlation
LDW	Laser Direct Writing
LSFM	Light-Sheet Fluorescence Microscopy
MELM	Multiplane Encoded Light-sheet Microscopy
NA	Numerical Aperture
PSF	Point Spread Function
sCMOS	scientific Complementary Metal–Oxide–Semiconductor
SLM	Spatial Light Modulator
SNR	Signal-to-Noise Ratio
SPED	SPHERICAL-aberration-assisted Extended Depth-of-field
TAG	Tunable Acoustic Gradient
1D	One-Dimensional
2D	Two-Dimensional
3D	Three-Dimensional

Symbols

c	Speed of light
c_s	Speed of sound
ν	Kinematic viscosity
ρ	Volumetric mass density
λ	Optical wavelength
Λ	Acoustic wavelength
k	Optical wave number
K	Acoustic wave number
ω	Optical angular frequency
Ω	Acoustic angular frequency
n	Refractive index
J_q	Bessel function of first kind of order q
η	Diffraction efficiency
V_{pp}	Peak-to-Peak Voltage
Π	Rectangular function
h	Point Spread Function
\mathcal{H}	Optical Transfer Function
\mathcal{F}	Fourier Transform

Abstract

The capability to structure the light in space or time is key in many important scientific and industrial fields, such as telecommunications, imaging, and manufacturing. So far, the technological advancements have been pushed by a variety of different beam-shaping tools, which typically provide either a high degree of customization or high-speed, but not both. This trade-off hinders the throughput of many photonic-based technologies. To address this issue, we developed multiple strategies to control the light at high-speed exploiting the acousto-optic effect. This latter is a well-known phenomenon that consists of the diffraction of light by ultrasonic waves. Notably, the spatio-temporal properties of the diffracted photons are directly related to those of the acoustic wave, which can be easily controlled with an electronic driver. Additionally, ultrasonic frequencies range from MHz to GHz, enabling high-speed generation of tailored light. Those exceptional features led us to the design and implementation of a new instrument called the acousto-opto-fluidic device. It is an acoustic resonant cavity immersed in a fluid, capable of generating ultrasonic standing waves that can diffract a laser beam in multiple beamlets. Thus, the device parallelizes the output of a laser source. However, the beamlets can be easily recombined to create interference fringes. In this case, the device works as a structured light generator. Importantly, the structure of the light patterns can be tuned using the driving parameters, and it is possible to switch between different patterns in less than a microsecond. In this thesis, we present a complete theoretical model of the acousto-opto-fluidic device and full experimental characterization of its optical performance. Additionally, we provide proof-of-principle experiments to demonstrate how our novel device can be successfully integrated into a laser-direct-writing station to increase its throughput greatly. The last important contribution of this thesis is the design and development of an all-acousto-optic light-sheet microscope. Indeed, light-sheet fluorescence microscopy enables gentle volumetric imaging of large samples, but it is limited in speed by the movement of bulky components required to produce a z-stack. We used a tunable acoustic gradient lens – namely a resonant varifocal lens – to perform a fast axial scan of the sample, which enables the acquisition of images of different samples with no mechanical movements. However, this approach degrades the signal-to-noise ratio of the images. To compensate, we designed a strategy to illuminate simultaneously multiple planes at choice, using a couple of acousto-optic deflectors. The parallelized excitation enables the acquisition of multiple planes in a single frame, thus requiring a decoding process. The retrieval of the individual images is performed via a simple algorithm, which returns a decoded z-stack with an enhanced signal-to-noise ratio. Therefore, our novel imaging technique enables fast volumetric imaging without sacrificing the quality of the images. In conclusion, the work presented in this thesis paves the way for the fast and tailored generation of tailored light, opening new roads for high-throughput material processing and microscopy.

1

Introduction

Light is a tool at the core of a wide range of fields, such as imaging, manufacturing, and telecommunications. Thus, the ability to tailor its features opens the door for many possibilities of technological advancement. Light structuring – or beam shaping – is a very general concept that refers to the customization of the spatial, temporal, or polarization properties of light [1]. So far, the impact of structured light has led to transformational breakthroughs in several areas. Just to mention a few examples, beam shaping has been at the centerpiece of optical super resolution methods capable to break the diffraction limit and achieve nanometric spatial resolution. Among them, the microscopy technique called Stimulated Emission Depletion (STED) can be achieved through point-scanning with a donut-shaped laser beam [2] and – thanks to its astounding capabilities – it has been awarded a Nobel prize in 2014. Structured light enables other very important microscopy techniques. A famous example is called Structured Illumination Microscopy (SIM), which exploits periodic illumination patterns to double the resolution of wide-field fluorescence microscopes [3, 4]. Spatial patterning of light can also enable imaging using a single element detector, which can be advantageous with respect to a camera thanks to their sensitivity of non-visible wavelengths and high temporal resolution. If the light is structured in detection the technique is known as ghost imaging [5, 6], while if the patterning is on the illumination we talk about single-pixel imaging [7]. More recently, the fine-tuning of quantum states of photons enabled Raman microscopy to achieve an unprecedented signal-to-noise ratio [8]. Quantum correlations have also been exploited to perform interaction-free imaging [9] and holographic imaging with incoherent light [10].

As anticipated, light structuring plays a key role in many fields other than imaging. Laser manufacturing, either additive or subtractive, can benefit from non-conventional laser beams. Flat top beams provide a constant flux of energy [11], enabling homogeneous irradiation. Bessel beams, thanks to their self-healing and non-diffracting properties, guarantee an elongated depth-of-focus even in presence of obstacles [12, 13]. Other beam profiles, such as annular or vortex

beams, provide unique features to the processed material [14].

The number of applications where shaped light proves advantageous is steadily growing. However, the most advanced technologies currently available to control the light either lack tunability or speed. Therefore, structuring the light is still a challenging task and a heavy burden for the large-scale implementation of these methods. In the next sections, a brief overview of the current light-structuring process and the most important devices apt for this purpose are presented.

1.1 Structured Light

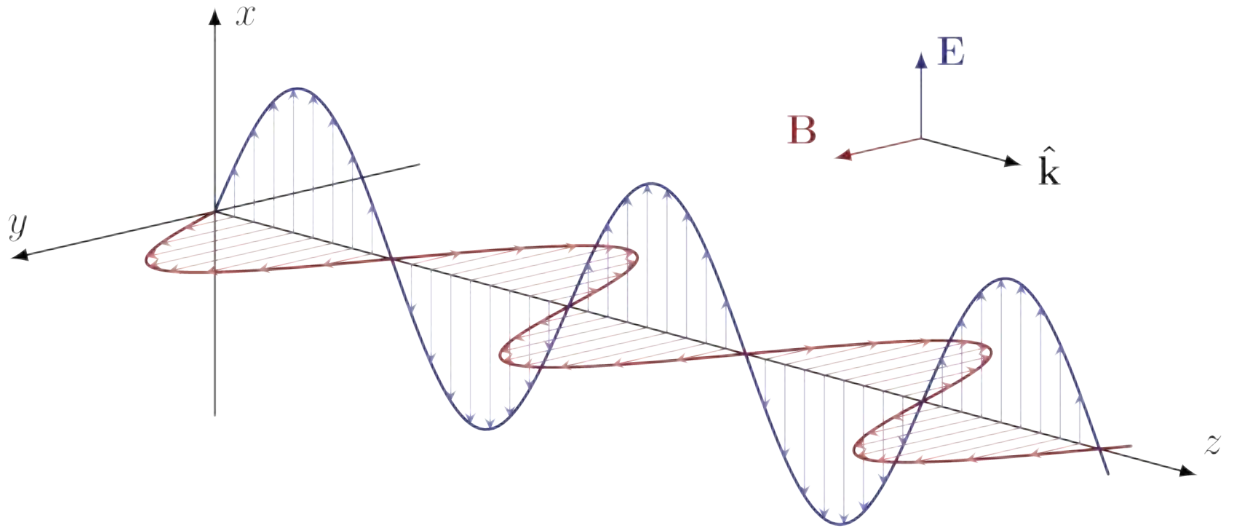


Figure 1.1: Depiction of an electromagnetic linearly polarized plane wave. The electric field \mathbf{E} is drawn in red and the magnetic field \mathbf{B} is drawn in blue.

To understand the fundamentals of light shaping, we must consider the wave nature of light. Classically, light is described by the Maxwell equations [15]. In a non-conducting medium, these are

$$\begin{aligned} \nabla \cdot \mathbf{E} &= 0 & \nabla \times \mathbf{E} &= -\frac{\partial \mathbf{B}}{\partial t} \\ \nabla \cdot \mathbf{B} &= 0 & \nabla \times \mathbf{B} &= \mu\epsilon \frac{\partial \mathbf{E}}{\partial t} \end{aligned} \quad (1.1)$$

Where \mathbf{E} and \mathbf{B} are, respectively, the electric and magnetic field, μ is the magnetic permeability, and ϵ is the dielectric permittivity of the medium. Combining these equations, it is possible to obtain the following vector wave equations describing the propagation of light

$$\nabla^2 \mathbf{E} = \frac{n^2}{c^2} \frac{\partial^2 \mathbf{E}}{\partial t^2} \quad \nabla^2 \mathbf{B} = \frac{n^2}{c^2} \frac{\partial^2 \mathbf{B}}{\partial t^2} \quad (1.2)$$

where $c = (\mu\epsilon)^{-\frac{1}{2}}$ is the speed of light in vacuum and n is the refractive index of the medium. The simplest solution is the plane wave, depicted in Figure 1.1. It is composed by the two following orthogonal fields oscillating at the angular frequency ω :

$$\mathbf{E} = \mathbf{E}_0 \exp(i\mathbf{k} \cdot \mathbf{x} - i\omega t) \quad \mathbf{B} = \mathbf{B}_0 \exp(i\mathbf{k} \cdot \mathbf{x} - i\omega t) \quad (1.3)$$

Here the fields are written for convenience as phasors, whose real parts represent the physical fields. Light travels along the direction of the wave vector \mathbf{k} , orthogonal to both fields. \mathbf{E}_0 is the 2-dimensional complex amplitude of the electric field and $\mathbf{B}_0 = \frac{n}{c} \hat{\mathbf{k}} \times \mathbf{E}_0$ is the 2-dimensional complex amplitude of the magnetic field. The average intensity – namely the energy per unit area per unit time – transported by the electromagnetic wave is described by the Poynting vector

$$\mathbf{S} = \frac{\mathbf{E} \times \mathbf{B}^*}{2\mu} = \sqrt{\frac{\epsilon}{\mu}} \frac{|\mathbf{E}_0|^2}{2} \hat{\mathbf{k}} \quad (1.4)$$

Interestingly, the intensity can be written proportional to the square modulus of the electric field. Moreover, the majority of light-matter interactions are due to the response of electrons of a medium to the oscillating electric field. Therefore, it is usually convenient to consider only this latter to describe the light.

Thanks to equation 1.3, we can easily describe the process of tailoring the light as the act of modulating the amplitude and the phase of the electric field. Amplitude modulation is performed through absorption or partial reflection. The amplitude of the field passing through a medium with thickness L and absorption coefficient α is

$$\mathbf{E}(x, y) = \mathbf{E}_0 \exp\left(-\int_0^L \alpha(x, y, z) dz\right) \quad (1.5)$$

Phase modulation is performed by retarding the wave. The phase retard accumulated by a field passing through a medium with thickness L and refractive index n is

$$\Phi(x, y) = \int_0^L n(x, y, z) dz \quad (1.6)$$

Importantly, the electric field is a 2-dimensional vector, with each element describing a polarization state. Therefore, through anisotropic media, it is possible to modulate the two polarization directions separately. In order to define the result as structured light, the modulation processes need to have a dependency (a *structure*) either on space or on time. In general, the finer is the control on those dimensions and the wider is the range of complex patterns that is possible to achieve. Thus, the ideal tool to generate structured light should be able to modulate the amplitude or phase of light with high spatial and temporal resolution.

1.2 Technologies for structuring the light

In this section, we present the main state-of-the-art technologies used to structure the light, summarized in Figure 1.2. In particular, we place particular attention to highlighting the advantages

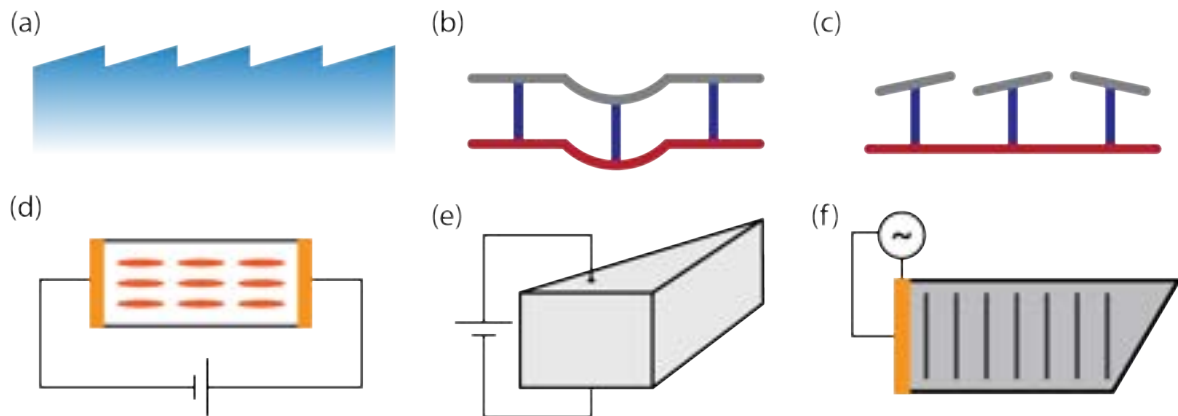


Figure 1.2: A sketch of the most important devices used for structuring the light. (a) A diffractive optical element, (b) a deformable mirror, (c) a digital micromirror device, (d) a liquid crystal cell, the constitutive element of a spatial light modulator, (e) an electro-optic deflector, (f) an acousto-optic device.

and disadvantages of each device.

1.2.1 Diffractive Optical Elements

A Diffractive Optical Element (DOE) is an engineered diffraction grating [16]. It consists of a micro-structured material, whose pattern is designed to shape either the amplitude or the phase of an incident beam. They can work either in reflection or transmission. Thanks to diffraction, the shape of the beam is modified accordingly to the microstructure of the DOE. The result can be almost arbitrary, being limited only by the precision of the manufacturing process. However, such devices are fixed elements incapable of providing any degree of tunability. Thus, any particular beam shape requires a different DOE.

1.2.2 Deformable Mirrors

A Deformable Mirror (DM) [17] is typically made by a continuous reflective surface which shape can be modified with an array of actuators. Each one is independent and can deform locally the mirror up to around $100\ \mu\text{m}$. Thus, the reflected beam is shaped accordingly to the form imposed on the mirror. This device enables a high degree of flexibility, but its beam shaping capabilities are severely hindered by some practical limitations. In particular, the number of actuators is typically limited to a few hundred and they are separated by a pitch of as large as $1\ \text{mm}$. Such coarse disposition of the active elements does not permit sophisticated structuring of the light. Moreover, the deformation speed of this device is usually limited to $1\text{--}2\ \text{kHz}$.

1.2.3 Digital Micromirror Devices

A Digital Micromirror Device (DMD) [18] is conceptually similar to a DM. Indeed, it is composed of an array of micro-actuators controlling the orientation of a micro-mirror. Therefore, the surface of a DMD is pixelated. This device contains a large number of pixels, typically millions, and the pixel pitch can be as small as 5 μm . However, each micro-mirror can be in only two states, thus enabling solely a digital modulation of light. The two states, *on* and *off*, are achieved by tilting the micro-mirror at two opposite angles – usually $\pm 12^\circ$. Both the pixelation and the binary modulation limit the beam-shaping capabilities of this device. This latter could be compensated with pulse width modulation, which enables gray values on average. Unfortunately this approach limits the speed of the devices. Indeed, the refresh rate is usually in the order of 10 kHz [19].

1.2.4 Liquid Crystal Spatial Light Modulators

A Liquid Crystal Spatial Light Modulator (LC-SLM, or simply SLM) is an advanced tool that exploits the optical properties of liquid crystals – usually nematic or ferroelectric – to perform light shaping [20, 21]. The molecules composing such liquid crystals are elongated and exhibit a highly birefringent behavior. Indeed, the refractive index is higher on the long axis and smaller on the short axis. Such molecules are also sensitive to electric fields as they tend to align their long axis parallel to the field lines. Thus, a liquid crystal cell acts as an electrically tunable optical retarder. An SLM is an array of liquid crystal cells, being a pixelated phase or amplitude modulator. Indeed, if a linear polarizer is placed at the output of each cell, it acts as an intensity modulator. Otherwise, it acts as a phase modulator. These devices can contain millions of pixels, with a pitch around 5 μm , enabling the highest level of tunability for beam shaping. Nonetheless, such devices are extremely sensitive to polarization and wavelength. However, their biggest drawback lies in the speed. Indeed, the frame rate of a typical SLM is of the order of 100 Hz.

1.2.5 Electro-optic devices

Electro-optic (EO) devices leverage the Pockels effect to change the optical properties of a material [22]. If a voltage is applied to a non-centrosymmetric crystal, it exhibits a change of refraction index proportional to the electric field. Thus, an Electro-Optic Modulator (EOM) controls electrically the amount of retardance applied to the light. Notably, if an EOM is integrated in a Mach-Zender interferometer, the phase modulation can be transformed into an amplitude modulation. The Pockels effect can also be used to design an Electro-Optic Deflector (EOD). This latter consists in a wedged crystal, which fully refracts the incident beam exploiting the electronically-controllable transmission angle [23]. These devices are amongst the fastest available, with a rise time as low as a few tens of ns. However, they lack in degrees of freedom for the spatial control of light, limiting their use to almost exclusively high-speed scanners or modulators. Additionally, they typically require additional instrumentation to provide extremely high driving voltages, up to thousands of volts.

1.2.6 Acousto-Optic devices

Acousto-optic (AO) devices [24] are tools that exploit pressure waves to modify the refractive index of a medium – typically a birefringent crystal – in order to generate a phase grating. The properties of this grating, and thus of the diffracted light, can be tuned with the driving signal. Traditional devices work in the Bragg regime and are sensitive to polarization and wavelength. A single instrument usually produce diffraction along a single axis, thus more devices in cascade are needed to provide a spatial control over all the spatial dimensions. Notably, the sound frequencies used are in the range from MHz to GHz, placing them among the fastest devices available for light modulation.

1.3 Aim and organization of the thesis

Current devices for light shaping present a tradeoff between speed and flexibility. Among them, the devices based on the acousto-optic effect enable high-speed control of light and provide many degrees of freedom, suggesting that the road for fast and tunable structuring of light should exploit this phenomenon.

The goal of this thesis is to demonstrate how acousto-optics can be leveraged to build effective beam-shaping solutions in demanding fields such as material processing and fluorescence microscopy. More in detail, this thesis is composed by the following chapters:

1. In the current chapter, I discussed the concept of structured light, described the most advanced tool used to tailor the light, and argued the need for faster and more flexible techniques.
2. In this chapter, I discuss the physics that lies behind the acousto-optic effect and I explain the working principle of the most important acousto-optic devices.
3. In this chapter, I introduce a novel instrument – named acousto-opto-fluidic device – with a full theoretical description. The result is a complete and predictive model realized with analytical and computational methods.
4. In this chapter, I provide a complete experimental characterization of the acousto-opto-fluidic device and its capabilities. I present experimental evidence of the implementation of the AOF device in a direct-writing workstation for high-speed and high-throughput material processing and I show how the AOF device can be used in synergy with other beam-shaping tools, in order to further extend its beam shaping capabilities.
5. In this chapter, I describe how acousto-optic deflectors can be used to produce tailored illumination patterns. This approach, combined with the depth-of-field extension enabled with an acoustic varifocal lens, extends the capabilities of light-sheet microscopes. The discussed technique, called multiplane encoded light-sheet microscopy, enables fast volumetric imaging at high signal-to-noise ratios.

6. In the last chapter, I conclude the thesis with a summary of the results and discussing the new paths paved by the research work presented herein.

Additionally, a vast number of appendices is available at the end. In those supplementary chapters I discuss in greater detail most of the concepts mentioned in the thesis.

References

- [1] Halina Rubinsztein-Dunlop, Andrew Forbes, M V Berry, M R Dennis, David L Andrews, Masud Mansuripur, Cornelia Denz, Christina Alpmann, Peter Banzer, Thomas Bauer, Ebrahim Karimi, Lorenzo Marrucci, Miles Padgett, Monika Ritsch-Marte, Natalia M Litchinitser, Nicholas P Bigelow, C Rosales-Guzmán, A Belmonte, J P Torres, Tyler W Neely, Mark Baker, Reuven Gordon, Alexander B Stilgoe, Jacqueline Romero, Andrew G White, Robert Fickler, Alan E Willner, Guodong Xie, Benjamin McMorran, and Andrew M Weiner. Roadmap on structured light. *Journal of Optics*, 19(1):013001, jan 2017.
- [2] Stefan W. Hell and Jan Wichmann. Breaking the diffraction resolution limit by stimulated emission: stimulated-emission-depletion fluorescence microscopy. *Optics Letters*, 19(11):780, 1994.
- [3] M. G. L. Gustafsson. Surpassing the lateral resolution limit by a factor of two using structured illumination microscopy. *Journal of Microscopy*, 198(2):82–87, may 2000.
- [4] Mats G.L. Gustafsson, Lin Shao, Peter M. Carlton, C. J. Rachel Wang, Inna N. Golubovskaya, W. Zacheus Cande, David A. Agard, and John W. Sedat. Three-dimensional resolution doubling in wide-field fluorescence microscopy by structured illumination. *Biophysical Journal*, 94(12):4957–4970, 2008.
- [5] Jeffrey H. Shapiro. Computational ghost imaging. *Physical Review A*, 78(6):061802, dec 2008.
- [6] Jeffrey H. Shapiro and Robert W. Boyd. The physics of ghost imaging. *Quantum Information Processing*, 11(4):949–993, aug 2012.
- [7] Graham M. Gibson, Steven D. Johnson, and Miles J. Padgett. Single-pixel imaging 12 years on: a review. *Optics Express*, 28(19):28190, 2020.
- [8] Catxere A Casacio, Lars S Madsen, Alex Terrasson, Muhammad Waleed, Kai Barnscheidt, Boris Hage, Michael A Taylor, and Warwick P Bowen. Quantum-enhanced nonlinear microscopy. *Nature*, 594(7862):201–206, jun 2021.
- [9] Gabriela Barreto Lemos, Victoria Borish, Garrett D. Cole, Sven Ramelow, Radek Lapkiewicz, and Anton Zeilinger. Quantum imaging with undetected photons. *Nature*, 512(7515):409–412, 2014.

- [10] Hugo Defienne, Bienvenu Ndagano, Ashley Lyons, and Daniele Faccio. Polarization entanglement-enabled quantum holography. *Nature Physics*, 17(5):591–597, 2021.
- [11] John A. Hoffnagle and C. Michael Jefferson. Design and performance of a refractive optical system that converts a Gaussian to a flattop beam. *Applied Optics*, 39(30):5488, 2000.
- [12] Michael Mazilu, D. James Stevenson, Frank Gunn-Moore, and Kishan Dholakia. Light beats the spread: “non-diffracting” beams. *Laser & Photonics Reviews*, 4(4):529–547, jun 2010.
- [13] Svetlana Nikolaevna Khonina, Nikolay Lvovich Kazanskiy, Sergey Vladimirovich Karpeev, and Muhammad Ali Butt. Bessel beam: Significance and applications —A progressive review. *Micromachines*, 11(11), 2020.
- [14] Marti Duocastella and Craig B Arnold. Bessel and annular beams for materials processing. *Laser & Photonics Reviews*, 6(5):607–621, 2012.
- [15] J. D. Jackson. *Classical Electrodynamics*. Wiley-VCH Verlag GmbH & Co. KGaA, Weinheim, Germany, apr 2003.
- [16] Shlomit Katz, Natan Kaplan, and Israel Grossinger. Using Diffractive Optical Elements. *Laser Technik Journal*, 15(4):29–32, oct 2018.
- [17] Thomas Bifano. MEMS deformable mirrors. *Nature Photonics*, 5(1):21–23, jan 2011.
- [18] Yu-Xuan Ren, Rong-De Lu, and Lei Gong. Tailoring light with a digital micromirror device. *Annalen der Physik*, 527(7-8):447–470, aug 2015.
- [19] Ahmed B. Ayoub and Demetri Psaltis. High speed, complex wavefront shaping using the digital micro-mirror device. *Scientific Reports*, 11(1):18837, dec 2021.
- [20] Zichen Zhang, Zheng You, and Daping Chu. Fundamentals of phase-only liquid crystal on silicon (LCOS) devices. *Light: Science & Applications*, 3(10):e213–e213, oct 2014.
- [21] John Goodman. *Introduction To Fourier Optics*. W.H. Freeman, 4th edition, 2017.
- [22] Ivan P. Kaminov. *An Introduction to Electrooptic Devices*. Elsevier, 1974.
- [23] G. R.B.E. Römer and P. Bechtold. Electro-optic and acousto-optic laser beam scanners. *Physics Procedia*, 56(C):29–39, 2014.
- [24] Adrianus Korpel. Acousto-Optics—A Review of Fundamentals. *Proceedings of the IEEE*, 69(1):48–53, 1981.

2

Acousto-optic Effect and Devices

In this chapter we discuss the physics of the acousto-optic effect, namely a non-linear interaction between the photons of light and the phonons of sound, mediated by a material. In the second part of the chapter we will explore the most important acousto-optic devices and their working principles. Note that a mathematically rigorous derivation of equations and concepts presented in this chapter is available in appendix C.

2.1 The acousto-optic effect

The acousto-optic (AO) effect consists of the diffraction of light by ultrasonic waves [1–5]. All kinds of materials – solids, liquids, or gases – can sustain the acousto-optic effect, even if in different substances the efficiency of the diffraction can significantly vary. This phenomenon, also known as the elasto-optic effect, is originated from the interaction of an electromagnetic wave with a sound wave. Indeed, the sound creates regions of compression and rarefaction of the propagating medium, changing the local values of the refractive index. This causes the light beam to suffer from a phase transformation – as described in chapter 1 – and the overall effect is that the light is split in multiple beams (see Figure 2.1). In Acousto-Optic devices, the sound wave is generated by one or many piezoelectric transducers bonded to the facet of a solid material, typically a crystal. In this case, the maximal mechanically induced variation of refractive index is

$$\Delta n \propto \left(\frac{n_0^6 p^2}{\rho c_s^3} \right)^{1/2} = \sqrt{M_2} \quad (2.1)$$

Where n_0 is the static refractive index, p is the elasto-optic coefficient, ρ is the density and c_s is the speed of sound of the material. The quantity M_2 is called the figure of merit and it is used to quantify the magnitude of the acousto-optic effect. As it is possible to see, solids with high

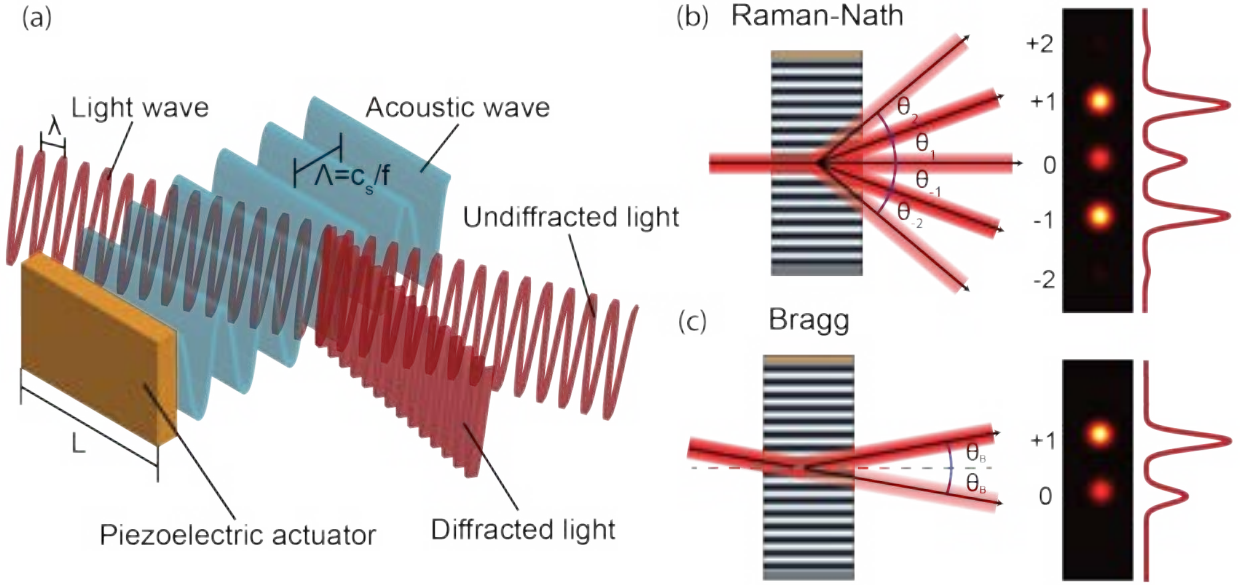


Figure 2.1: The acousto-optic effect. (a) Interaction of light with an ultrasound wave: A piezoelectric actuator generates an acoustic wave that periodically modulates the refractive index of a medium. A light wave upon traversing the vibrating region is diffracted into one or multiple beams, depending on the operating regime. (b) In the Raman-Nath regime, the diffraction pattern consists of multiple beams separated by angles θ_m . The resulting light pattern is symmetrical around the undiffracted beam ($m = 0$). (c) In the Bragg regime, only a single beam is diffracted at the incidence angle.

refractive index and low density and speed of sound show a more intense interaction [6, 7]. As anticipated, Acousto-optic interaction can also take place in fluids. Acousto-optofluidic devices are built filling a piezoelectric cavity with a liquid and sealing the edges with optically transparent windows. In liquid materials, the maximal variation of the refractive index is

$$\Delta n \propto \frac{c_s^2 n_0^4 + n_0^2 - 2}{\tau n_0} \quad (2.2)$$

where τ is the kinematic viscosity of the fluid. Once again, materials with a high refractive index show a stronger acousto-optic interaction, but in this case substances with high speed of sound and low viscosity should be preferred [8–10]. For either solids or fluids, the maximal variation of the refractive index increases with the pressure-induced inside the material that ultimately depends on the voltage applied to the piezoelectric actuator.

The exact attributes of acousto-optic interaction - such as the number, intensity, and angle of diffracted beams - depend heavily on many variables. Klein and Cook [11] identified a parameter, defined as

$$Q = \frac{K^2 L}{kn_0} \quad (2.3)$$

that summarizes the role of the most important physical quantities. L is the length of the

mechanical transducer, $k = \frac{2\pi}{\lambda}$ is the wave number of light, and $K = \frac{2\pi}{\Lambda}$ is the wave number of sound. The parameter Q is a quantification of the effective thickness of the vibrating medium [12]. It can be used to identify two limit regimes, as shown in Figure 2.2. Even though no sharp transition exists between them, when $Q \ll 1$ the sound wave acts as a thin phase grating and diffraction is said to occur in the Raman-Nath regime. When $Q \gg 1$, the modulated medium acts as a thick phase grating and diffract occurs in the Bragg regime. The characteristics of the two regimes are explained next.

2.1.1 Diffraction regimes

For simplicity and without loss of generality, we consider now the case of an acoustic wave traveling along a single direction. If the acoustic medium is in between an piezoelectric actuator and an acoustic absorber, the generated acoustic wave is a traveling one. The corresponding refractive index profile assumes the form

$$n(x, t) = n_0 + \Delta n \sin(Kx - \Omega t) \quad (2.4)$$

where $\Omega = 2\pi f$ is the acoustic angular frequency and Δn is maximum variation of refractive index. Instead, when the acoustic medium is in between two actuators or one actuator and an acoustic reflector, a resonant cavity is formed. Provided the sound frequency matches the resonances of the cavity, a standing wave is established, whose refractive index profile is

$$n(x, t) = n_0 + \Delta n \sin(Kx) \sin(\Omega t) \quad (2.5)$$

Traveling waves are prevailing in most AO devices, particularly in those operating at the Bragg regime. Their main advantage is the possibility of usage over a continuous range of acoustic frequencies. Standing waves are more commonly used with devices working in the Raman-Nath regime. Because the cavity needs to be maintained in resonant conditions, it may be susceptible to temperature fluctuations. Thus, feedback systems are helpful to maintain the diffraction pattern at the resonant condition. Note, however, that once the steady-state is reached, standing waves offer high-speed modulation of the diffracted intensity – only limited by the driving frequency. Resonance also allows for minimal driving power of the ultrasound actuators [13].

2.1.1.1 Raman-Nath regime

When $Q \ll 1$, which typically occurs at low acoustic frequencies ($f < 10$ MHz), the diffraction pattern consists of many beamlets symmetrically distributed with respect to the 0th order. Every beamlet is deflected at a different angle $\theta_m = mK/n_0k$, and is frequency shifted by $m\Omega$ (see Figure 2.1b) – where m is the index order. In more detail, the diffraction efficiency of the m^{th} order, defined as the ratio of the intensity of that diffracted beamlet to the intensity of the incident beam, is

$$\eta_m = J_m^2(kL\Delta n) \quad (2.6)$$

where J_m is the Bessel function of the first kind. The diffraction efficiency is limited in the Raman-Nath regime. Indeed, the maximal efficiency of the first order is 33.86%, while higher orders reach lower values.

In the case of a standing wave, the diffraction efficiency depends on time as follows

$$\eta_m(t) = J_m^2[kL\Delta n \sin(\Omega t)] \quad (2.7)$$

Interestingly, the oscillation frequency is the same as the acoustic wave, enabling fast modulation of the diffracted intensity. Moreover, the time dependency implies a larger spectrum. Diffracted orders are frequency shifted of integer multiples of Ω .

In the Raman-Nath regime, it is possible to describe the acousto-optic device as a thin phase grating. This means that it simply shifts the phase of the incident beam by $\Delta\phi = kL\Delta n(x, t)$. This is a powerful description of the interaction process, that enables the calculation of the diffraction pattern with any arbitrary shape of the acoustic wave [14, 15].

2.1.1.2 Bragg regime

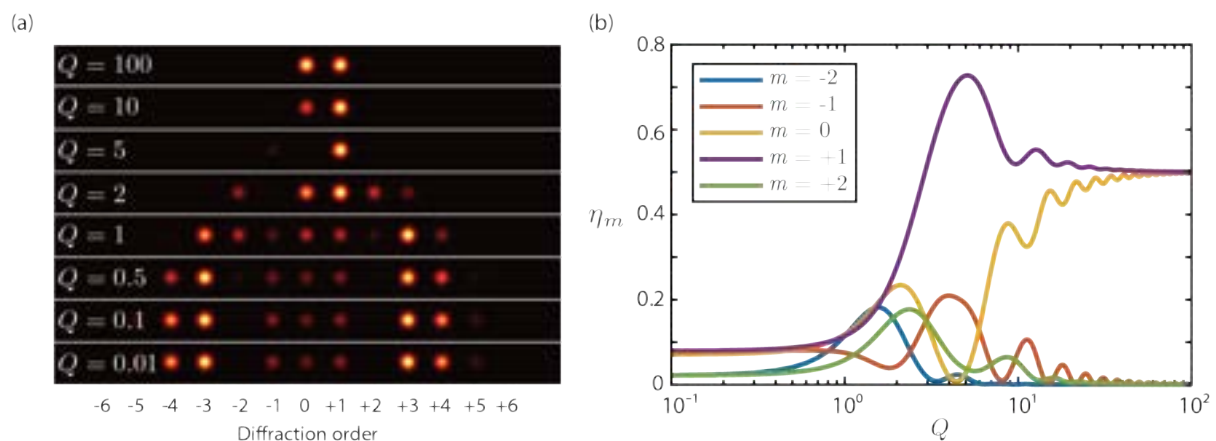


Figure 2.2: Smooth transition from Raman-Nath to Bragg regime as a function of the Klein-Cook parameter Q . The simulations are run at the Bragg angle and at $kL\Delta n = 3\pi/2$. (a) Diffraction pattern. (b) Diffraction efficiencies of the orders from -2 to $+2$. Higher orders are not shown for clarity.

Bragg diffraction occurs if $Q \gg 1$, that typically means at acoustic frequencies $f > 10$ MHz. In this case, only a single order is diffracted (see Figure 2.1c). In order for the process to take place, the angle of the incident beam needs to satisfy the following relation

$$\sin \theta_B = \mp \frac{K}{2n_0k} \quad (2.8)$$

where θ_B is known as the Bragg angle. This requirement can be written equivalently as a phase-matching condition

$$\mathbf{k}_i - \mathbf{k}_d = \mathbf{K} \quad (2.9)$$

where \mathbf{k}_i and \mathbf{k}_d are respectively the wave vector of the incident and diffracted beam and \mathbf{K} is the sound wave vector (see Figure 2.3a). In other words, Bragg diffraction requires the conservation of momentum.

The diffraction efficiencies of the undiffracted beam and the first order at the exit of the vibrating medium are

$$\eta_0 = \cos^2(kL\Delta n/2) \quad (2.10)$$

$$\eta_1 = \sin^2(kL\Delta n/2) \quad (2.11)$$

It is interesting to notice that when $kL\Delta n = (2j + 1)\pi$ (where j is an integer), the diffraction intensities become $\eta_1 = 1$ and $\eta_0 = 0$. This is the case in which the diffraction efficiency reaches the theoretical maximum, namely 100% of the energy of the incident light is transferred to the diffracted beam [16]. An interesting feature of Bragg diffraction is that the direction of the 1st order is deflected by the Bragg angle. Thus, incident and diffraction angle are the same – similarly to Bragg's law for crystals. Moreover, the frequency of the diffracted order is down or upshifted by Ω , depending on the sign of the incident angle.

In the case of a standing wave, the diffraction efficiencies are time-modulated

$$\eta_0(t) = \cos^2[kL\Delta n \sin(\Omega t)/2] \quad (2.12)$$

$$\eta_1(t) = \sin^2[kL\Delta n \sin(\Omega t)/2] \quad (2.13)$$

The time-dependency implies the presence of multiple harmonics in its spectrum. Indeed, both the 0th and 1st diffraction orders are frequency shifted of integer multiples of Ω .

2.1.2 Anisotropic Diffraction

So far, we have discussed acoustic diffraction in isotropic materials. We have implicitly assumed that the polarization state of the incident beam is the same as the diffracted beam. However, in birefringent materials, another type of diffraction is possible, with some peculiar attributes. In an anisotropic crystal the refractive index and the photo-elastic coefficient are not scalar quantities, but tensors. This implies that their values depend on the orientation of the crystal and the polarization of light. In the simplest case of a uniaxial crystal, two axes are different from the third one: the ordinary axes have refractive index n_o and the extraordinary axis has refractive index n_e . With this crystals it is possible to have anisotropic Bragg diffraction: the incident beam has a polarization state parallel to the extraordinary axis and the diffracted beam has a polarization state parallel to the ordinary axis. Then, the diffracted and incident angles are defined by the following relations

$$\sin \theta_i = \frac{\lambda}{2n_e c_s} \left[f + \frac{c_s^2}{f\lambda^2} (n_e^2 - n_o^2) \right] \quad (2.14)$$

$$\sin \theta_d = \frac{\lambda}{2n_o c_s} \left[f - \frac{c_s^2}{f\lambda^2} (n_e^2 - n_o^2) \right] \quad (2.15)$$

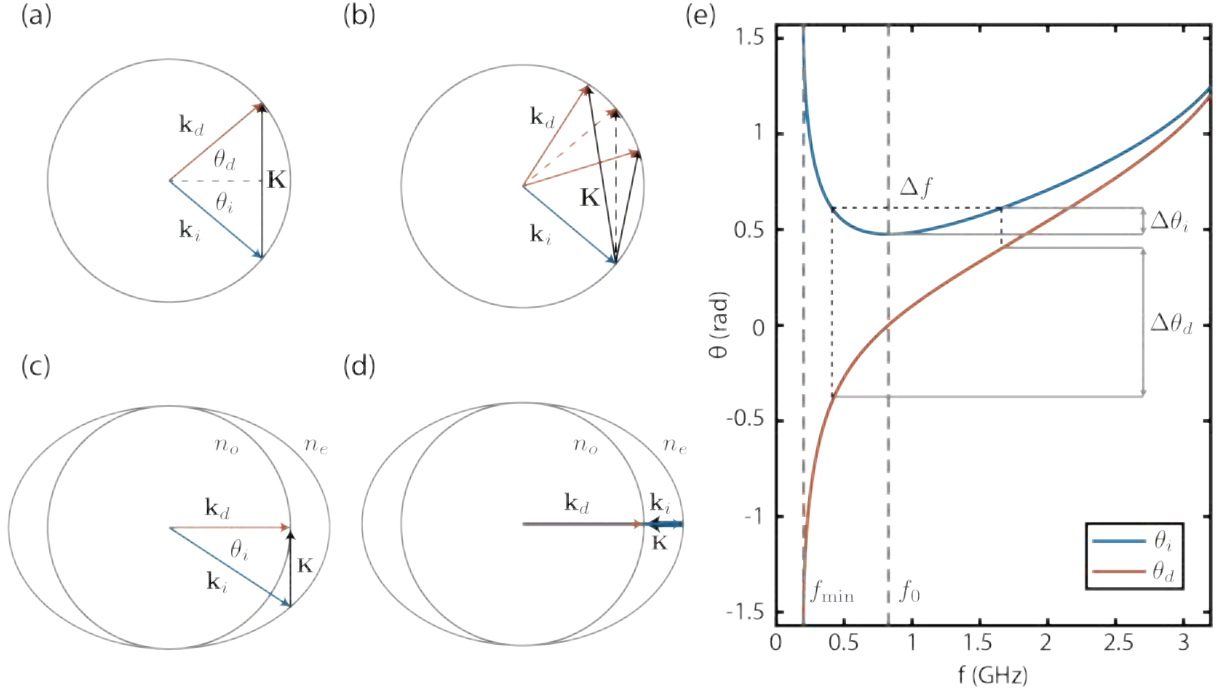


Figure 2.3: Representation of the Bragg diffraction using wave vector diagrams. (a) Isotropic diffraction; in this case $\theta_d = -\theta_i$. (b) Isotropic diffraction with a sound wave with a large angular spectrum. A larger variability of K allows a larger range of k_d that satisfy the phase matching condition, thus obtaining a larger angular band for the diffracted beam. (c) Anisotropic diffraction at the tangential limit; in this case $\theta_d = 0$. (d) Anisotropic diffraction at the collinear limit; in this case the incident and diffracted beams are parallel. (e) Plot of the angles of the incident and diffracted beams as a function of the acoustic frequencies, in the case of anisotropic diffraction. The collinear limit occurs at frequency f_{\min} , while the tangential limit occurs at frequency f_0 .

Interestingly, in the case of anisotropic diffraction, the incident and diffraction angles are not the same [17, 18], as shown in Figure 2.3e. In this scenario, two limits of particular interest can be identified. The *tangential* limit is reached at the acoustic frequency $f_0 = \frac{c_s}{\lambda} \sqrt{|n_e^2 - n_o^2|}$ and the resulting diffraction angle θ_d is zero, as shown in Figure 2.3c. Note that around the frequency f_0 a small change in the incident angle $\Delta\theta_i$ corresponds to a larger change in the diffraction angle $\Delta\theta_d$. In other words, any driving frequency close to f_0 fulfills the Bragg condition, enabling a large range of diffraction angles with approximately constant diffraction efficiency. This phenomenon is exploited to design deflectors with a wide frequency band. The *collinear* limit, depicted in Figure 2.3d, occurs at the acoustic frequency is $f_{\min} = (n_e - n_o) \frac{c_s}{\lambda}$. In this limit, the angles θ_d and θ_i are both equal to $\pi/2$, implying that the two beams exit parallel, while the acoustic wave is anti-parallel. Many acousto-optic tunable filters are designed to exploit a collinear interaction. Importantly the frequency f_{\min} is also the minimum acoustic frequency usable for anisotropic acoustic diffraction is possible. However, in an anisotropic crystal, is still possible to fulfill the phase-matching condition with both beams with the same polarization state. In this case, isotropic diffraction can occur for any acoustic frequency. Notably, Raman-Nath diffraction can only be

isotropic.

2.2 Acousto-optic devices

The need for optimizing light control has spurred the development of an entire family of AO devices. They all operate under the same principle and also feature the same key elements, including an acousto-optic medium transparent to light, an ultrasound source (usually a piezoelectric transducer), and the control electronics. The latter enables adjusting the frequency and amplitude of the driving signal, and consequently, the ultrasound waves and the diffraction regime. Because all AO devices achieve light control without the inertia of moving mechanical components, they have typical response times well below milliseconds. Despite these similarities, each AO device has distinct characteristics suitable for performing a specific task, as briefly summarized in Figure 2.3. In the next sections, we detail the main features of the most important AO devices.

2.2.1 Bragg Cells

Acousto-optic devices working in the Bragg regime are called Bragg cells. Those devices exist in different implementations, designed for different purposes, but they all share some common characteristics. They typically consist of a piezoelectric actuator bonded to a facet of a crystal. Since the vast majority of the Bragg cells work with traveling waves, the opposite facet of the crystal is bonded to an acoustic absorber that prevents reflection. In this regime a light beam hitting the device at the Bragg angle is split into two beams, separated by an angle. This latter is controlled with the driving frequency, while the intensity of the two beams depends on the voltage applied to the piezoelectric transducer. Even if – theoretically - it is possible to create Bragg cells using liquid materials, their acousto-optic efficiency decreases with frequency, and liquids cannot be anisotropic. Therefore, all the commercially available devices use solid materials as the vibrating medium. The most common ones are Tellurium Dioxide (TeO_2), α -quartz, Fused Silica, and Germanium. The choice between one or another material depends on cost and availability as well as the inherent properties of the medium, such as refractive index, birefringence, acoustic attenuation, and transparency [6]. Among the many, Tellurium Dioxide became one of the material of choice – especially for deflectors – thanks to its birefringence ($n_o = 2.25$ and $n_e = 2.411$ at $\lambda = 633$ nm) and high transparency in the visible range. Additionally, it allows the propagation of shear waves with a speed of sound as low as 650 m/s. The material of choice for the piezoelectric actuator is Lithium Niobate (LiNbO_3), being able to handle high powers, having low dissipation, and having an acoustic impedance similar to the acousto-optic medium. Both of its faces are bonded to a metallic electrode, usually made of gold. However, the exact material and design choices are made depending on the particular application. Based on the purpose they serve, we can distinguish three main implementations of Bragg cells, called Deflectors, Modulators, and Tunable Filters. Further details are presented next.

2.2.1.1 AO deflectors

An Acousto-Optic Deflector (AOD) is designed to work as a single-axis scanner of the 1st diffraction order [19]. Interestingly, since the deflected beam is also frequency shifted by the acoustic frequency, it is possible to use deflectors as well as variable frequency shifters [20]. The highest diffraction efficiency is obtained at the Bragg angle which is a function of the acoustic frequency. Therefore, by changing the driving frequency it is possible to tune the direction of the deflected beam. However, if the incident angle is fixed, that typically causes a phase-mismatch and a consequent loss of intensity of the diffracted beam. Hence, in order to scan over a wide angular range, it is very important for these devices to maintain the diffraction efficiency as high as possible over a broad range of frequencies. This latter is known as the band Δf and it is one of the main parameters for an AOD. The second parameter is the resolution. The number of resolvable spots is calculated as the ratio of the angular scanning range $\Delta\theta_d$ to the divergence angle $\Delta\Phi$ of the light beam at the exit of the AOD. From the equation of the isotropic Bragg angle, we have that $\Delta\theta_d = \frac{\lambda\Delta f}{n_0 c_s}$. The divergence angle $\Delta\Phi$ for a Gaussian beam is approximately $\Delta\Phi \sim \frac{\lambda}{n_0 w}$, where w is the size of the beam. Therefore, the number of resolvable spots is

$$N = \tau\Delta f \quad (2.16)$$

where $\tau = w/c_s$ is the time needed for the acoustic wave to pass through the light beam and it is generally known as access time. This latter defines the time needed to switch between different angular positions and it is usually in the order of microseconds. Hence, materials with a slow speed of sound c_s can be used to build devices with high resolution. Practical devices implement solutions to enlarge the range of possible working frequencies Δf , while maintaining fixed the incident angle. The simplest one is to reduce the length L of the piezoelectric transducer: a shorter actuator increases the diffraction angle of the acoustic wave. Indeed, a larger angular band of the acoustic wave relax the phase-matching condition, as depicted in Figure 2.3b, practically widening the band of the device. However, the length L can be reduced only down to a certain size, therefore other solutions are needed if an even broader band is required. Another option is to use phased array transducers: a sequence of piezoelectric actuators is bonded in series on top of the crystal and they are driven with a fixed phase-shift. This approach enables the control of the direction of the acoustic wave, which can be tuned to compensate for the change of driving frequency and restore the Bragg condition [21]. This is an effective solution but requires complex manufacturing and proper design. Another successful solution is to use a birefringent crystal, such as TeO₂. Designing a device to work at the tangential limit, it is possible to achieve a large range of diffraction angles with a minimal variation of the incident angle [17]. In this way, it is possible to maintain a high diffraction frequency over a wide frequency interval (see Figures 2.3d and 2.3e). All the above solutions can be found combined sometimes in high-performance devices with a broad frequency band and consequently a wide scanning range. The broad-band feature of AODs makes possible to drive them with a multifrequency signal. Each harmonic component of the wave diffracts the incident beam at the corresponding Bragg angle. Using this strategy, it is possible to create an array of independently controlled beams [22], enabling highly tunable beam shaping. However, Acousto-Optic devices are not linear systems, thus crosstalk and intermodulation may occur [23]. While electronic crosstalk could be in principle eliminated

using a controller with excellent linearity, acousto-optic intermodulation is unavoidable, and it consists in the appearance of spurious diffraction orders. These latter have a lower intensity with respect to the pure diffraction orders, hence they can be neglected if the AOD is operated at low driving amplitudes. However, their presence should always be taken into account while driving deflectors with signals having multiple frequency components. Interestingly, it is possible to optically conjugate two orthogonal AODs in order to create a 2-axes scanner. With this approach, a high-performance AOD system can resolve thousands of different spots over angular ranges of the order of 50 mrad^2 . Combined with the high speed, deflectors have become an invaluable tool for laser scanning and beam shaping [24]. Additionally, if driven with a chirped signal, an AOD acts as a cylindrical lens [25]. Therefore, two orthogonal AODs can be used to design a complete 3D scanner [26].

2.2.1.2 AO modulators

An acousto-optic modulator (AOM) is typically operated through a driving signal with fixed frequency and time-varying amplitude. Thus, the intensity of the diffracted beams is modulated in time. The main parameters of an AOM are contrast, throughput, and speed. The contrast is defined as the ratio of the intensity of the full-on state to the off state, while the throughput is the ratio between the experimental diffraction efficiency to the theoretical one. It is possible to work with the 0th order and block the 1st one or do the opposite: both configurations have advantages and disadvantages. The most common way to use an AOM is to exploit the 1st diffraction order as the modulated beam. This approach enables the highest possible static contrast ratio (the off state is easily provided by shutting down the driver), but due to the natural divergence of the optical beam, not all the light is diffracted. This effect typically reduces the throughput efficiency to around 70%. Moreover, the 1st order is frequency shifted by the acoustic frequency. Alternatively, it is possible to use the 0th order. This approach grants the maximal throughput efficiency since all the undiffracted light is parallel to the 0th order, but the contrast ratio is limited. Indeed, in the off state, there is typically some residual light. The modulation speed is of extreme importance and the main limiting factors are the rise and fall time. Both of them are proportional to the access time. More in detail - for a Gaussian Beam - the rise time is

$$\tau_R = 0.64 w/c_s \quad (2.17)$$

where w is the size of the light beam and c_s is the speed of sound. Since the last is fixed by the choice of the material, it is useful to decrease the dimension of the incident beam. The most efficient way to do it is by focusing the beam inside the modulator. If the beam waist is narrow enough, in the fastest modulators it is possible to achieve a rise time as low as a few nanoseconds. Unfortunately, the narrower is the waist, the larger is the divergence angle. As a consequence, if this angle is wider than the divergence angle of the acoustic wave, degradation of the 1st order occurs. The two main side effects are the broadening of the diffracted spot and a worsening of the throughput efficiency. Therefore, a trade-off exists between speed and beam quality. Thanks to the high speed and tunability of AOMs, they are a key tool for fast optical switching.

2.2.1.3 AO tunable filters

An acousto-optic tunable filter (AOTF) is a narrow-band wavelength selector [27]. An AOTF diffracts a polychromatic light beam in a monochromatic 1st order and a 0th order containing the rest of the spectrum. The device is a tunable band-pass filter since the driving frequency can select the diffracted wavelength. The most important features of an AOTF are the resolution and the wavelength scan rate. The first one is determined by the bandwidth that can be smaller than 1 nm. However, the band normally contains undesired sidelobes that would cause different colors to not be filtered out. In order to avoid this issue, commercial AOTFs adopt apodization technologies – such as acoustic beam shaping – that suppress this effect. The scan rate is the inverse of the time needed to pass from one filtered wavelength to a different one. Once again, the limiting factor for the scan rate is the access time which can be as low as a few microseconds. All the AOTFs exploit anisotropic Bragg diffraction and they can be divided into two typologies: collinear and non-collinear filters. Collinear AOTFs are designed to work close to the acoustic frequency f_{min} , where the incident and diffracted beams are parallel (see Figure 2.3d-e). In this region, the angular sensitivity is maximal, therefore any color that does not fulfill almost exactly the phase-matching condition is not diffracted and the device acts as a narrow-band filter. Conversely, the diffracted beam contains only the phase-matched wavelength. Moreover, the 1st order does not change the direction of propagation but rotates the polarization by 90°. Simply placing a polarizer or a polarizing beam splitter, it is possible to separate the filtered beam from the original one that maintains the original polarization state. However, the collinear architecture restricts the usage of non-centrosymmetric crystals exclusively, which are unfortunately characterized by a relatively small figure of merit [6]. Therefore, non-collinear AOTFs have been developed and are now more common – especially for imaging applications [28, 29]. Additionally, they require less optical components both in input and output. The filtered and unfiltered beams are no longer parallel, therefore they can be separated without the need of a polarizer.

The central wavelength λ_c of the filters can be tuned by changing the acoustic driving frequency f as follows

$$\lambda_c = \frac{c_s \Delta n_B}{f} \quad (2.18)$$

where Δn_B is the birefringence of the crystal. Thanks to their tunability, high-speed, and narrow-band AOTFs have become a precious tool to separate wavelengths. Indeed, they are typically implemented in the beam-combining unit of laser-scanning systems to control intensity and wavelength of multiple laser lines. They can also be used as fast tunable beam splitters for multi-color imaging [30, 31].

2.2.2 Raman-Nath Cells

Raman-Nath (RM) cells are the acousto-optic devices working in the Raman-Nath regime. A RM device typically consists of a sealed chamber filled with an appropriate liquid – the acousto-optic medium – with two optically transparent windows at the edges. The chamber contains one or more piezoelectric transducers, in order to create a resonant cavity. The distance between the

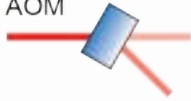



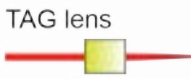
Device	Regime	Function	Main features	Cautionary remarks
 AOM	Bragg	Optical attenuator	Contrast Rise time: 5 - 500 ns	Speed/efficiency trade-off
 AOD	Bragg	Angular scanner	Angular range: 1 - 50 mrad Resolution: 5 - 500 spots	Speed/resolution trade-off
 AOTF	Bragg	Wavelength selector	Bandwidth: 0.1-50 nm Tuning time: 1 - 10 μ s	Efficiency up to 90%
 AOF device	Raman-Nath	Pattern generator	Tunability Speed: 0.1-10 MHz	Diffracted beams are not independent
 TAG lens	Raman-Nath	Varifocal lens	Optical power: 0 - 10 m^{-1} Speed: 0.01 - 1 MHz	Sinusoidal scanning

Figure 2.4: Types of Acousto-Optic devices. Top to bottom: Acousto-Optic Modulator (AOM), Acousto-Optic Deflector (AOD), Acousto-Optic Tunable Filter (AOTF), Acousto-Opto-Fluidic (AOF) device, and Tunable Acoustic Gradient (TAG) lens.

actuators and the speed of sound define the resonant frequencies at which the devices work. An RM device drove to resonance establishes a standing wave in the cavity. This latter can diffract an incident light beam with a size larger than the acoustic wavelength in many orders, symmetrically spaced around the optical axis. Instead, if the light beam size is smaller than the acoustic wavelength, the device acts as a lens whose symmetry is the same as the device – for example a spherical or cylindrical lens. The optical properties of the diffraction pattern can be tuned using the driving amplitude and frequency, as with the Bragg cells. However, the standing wave nature of the refractive index modulation grants an additional degree of freedom, namely the phase of the wave. Because the diffraction efficiency of the different orders is a function of time (see Equation 2.7), it is possible to synchronize a pulsed light source with the driving frequency. In this way, the diffraction pattern can be tuned at the same speed as the acoustic frequency, down to sub-microsecond time scales. In the Raman-Nath regime, the acoustic frequencies are significantly smaller with respect to the Bragg regime. Since the variation of refractive index Δn in fluids is inversely proportional to the frequency, liquids are good acousto-optic materials for RM cells. In general, any transparent liquid with low viscosity and high refractive index can be used to build a Raman-Nath cell and the two most common ones are de-ionized water and silicone oil. The last is particularly suited for this purpose, having a vapor pressure of less than 700 Pa and a refractive index of 1.403. Note that low vapor pressure is key to avoid the formation of cavitation bubbles, that would otherwise scatter the light passing through the device. Considering the

symmetry of the resonant cavity, we can distinguish cylindrical and rectangular RM cells, known as TAG lenses and AOF devices, respectively.

2.2.2.1 TAG lens

A Tunable Acoustic Gradient (TAG) lens is an AO device operating as a fast varifocal lens. It is typically used in microscopy to extend the Depth-of-Field (DoF) of high numerical aperture (NA) objective lenses, and as a fast axial scanner for high-speed volumetric imaging [32–35]. A TAG lens has a cylindrical geometry, unique within the family of AO devices. It consists of a piezoelectric tube filled with a liquid. When driven on resonance, an ultrasound standing wave is formed, which can be described with a Bessel function [10]. Typically, a TAG lens requires the illumination beam clearly underfilling its aperture, in order to remain smaller than the central lobe of the Bessel function. In this mode, a TAG lens acts as a parabolic gradient-index (GRIN) lens, with the optical power sinusoidally varying over time. The normal frequency range of a TAG lens is between 50 kHz and 1 MHz. The effective NA of a TAG lens is low – as the aperture is limited by the central lobe of the Bessel function. Thus, for imaging applications, TAG lenses are always used in combination with high NA objectives. By placing the TAG lens in a conjugate plane of the back focal plane of an objective lens, magnification effects can be avoided, and the lens enables fast z-focus scanning [36]. Such continuous z-focusing at microsecond time scales is faster than the integration time of many optical detectors. In this case, the collection of multiple focal planes leads to a virtually extended DOF. Notably, if synchronized stroboscopic illumination or fast detectors with appropriate electronics are used, information from multiple axial positions can be acquired. When illuminated with a beam larger than the central lobe of the Bessel function, the TAG lens acts as an axicon with a user-selectable cone angle [37]. In this case, a pseudo-Bessel beam is formed.

2.2.2.2 AOF device

The Acousto-optofluidic device (AOF) functions as an electronic beam shaper to generate tunable optical patterns. It consists of a water-filled chamber containing two pairs of piezoelectric plates. Each pair is orthogonal to each other and forms an acoustic resonant cavity. When driven on resonance, it produces an ultrasound standing wave that diffracts an incoming beam into an array of beamlets. Thus, the direct construction of two-dimensional beam arrays is possible when both cavities are operative [9]. Interestingly, by adding a focusing lens between the device and the objective lens, the beamlets interfere, generating three-dimensional patterns in the focal plane of the objective [8]. Working in the Raman-Nath regime, AOFs offer a wide acceptance angle for the incident light, which eases alignment procedures and facilitates integration in microscopy systems. The main features of AOFs are their high tunability and speed. By controlling the frequency and amplitude of the driving signal, the properties of the diffraction pattern, such as the number, spacing, and intensity of the diffraction orders, can be selected with the only constraint that the diffracted beams are not independent of each other. Also, the use of standing waves offers an extra control parameter. Employing synchronized pulsed illumination, the temporal phase difference between light pulses and the ultrasound wave enables to select a diffraction pattern

faster than the acoustic access time. Given typical operation frequencies in the 0.5 - 5 MHz, AOFs can operate at a timescale below 1 μ s. This is the only non-commercial device presented here and its design and development is the core of the research work described in the two following chapters.

References

- [1] C. V. Raman and N. S. Nagendra Nathe. The diffraction of light by high frequency sound waves: Part I. *Proceedings of the Indian Academy of Sciences - Section A*, 2(4):406–412, oct 1935.
- [2] C V Raman and N S Nagendra Nath. The diffraction of light by high frequency sound waves: Part II. *Proceedings of the Indian Academy of Sciences - Section A*, 3(4):406–412, 1936.
- [3] C. V. Raman and N. S. Nagendra Nath. The diffraction of light by high frequency sound waves: Part III. *Proceedings of the Indian Academy of Sciences - Section A*, 3(1):75–84, jan 1936.
- [4] C. V. Raman and N. S. Nagendra Nath. The diffraction of light by high frequency sound waves: Part IV. *Proceedings of the Indian Academy of Sciences - Section A*, 3(2):119–125, feb 1936.
- [5] C. V. Raman and N. S. Nagendra Nath. The diffraction of light by high frequency sound waves: Part V. *Proceedings of the Indian Academy of Sciences - Section A*, 3(5):459–465, may 1936.
- [6] Akis P. Goutzoulis. *Design and Fabrication of Acousto-Optic Devices*. CRC Press, New York, may 2021.
- [7] T. Smith and A. Korpel. Measurement of light-sound interaction efficiencies in solids. *IEEE Journal of Quantum Electronics*, 1(6):283–284, sep 1965.
- [8] S. Surdo and M. Duocastella. Fast Acoustic Light Sculpting for On-demand Maskless Lithography. *Advanced Science*, 2019.
- [9] Alessandro Zunino, Salvatore Surdo, and Martí Duocastella. Dynamic Multifocus Laser Writing with Acousto-Optofluidics. *Advanced Materials Technologies*, 4(12):1–7, 2019.
- [10] Euan McLeod and Craig B. Arnold. Mechanics and refractive power optimization of tunable acoustic gradient lenses. *Journal of Applied Physics*, 102(3):1–9, 2007.
- [11] W. R. Klein and Bill D. Cook. Unified Approach to Ultrasonic Light Diffraction. *IEEE Transactions on Sonics and Ultrasonics*, 14(3):123–134, 1967.
- [12] Adrian Korpel. *Acousto-Optics*. MARCEL DEKKER, INC, New York, second edition, 1997.

- [13] Martí Duocastella, Salvatore Surdo, Alessandro Zunino, Alberto Diaspro, and Peter Saggau. Acousto-optic systems for advanced microscopy. *Journal of Physics: Photonics*, 3(1):012004, nov 2020.
- [14] John Goodman. *Introduction To Fourier Optics*. W.H. Freeman, 4th edition, 2017.
- [15] Ireneusz Grulkowski, Dawid Jankowski, and Piotr Kwiek. Acousto-optic interaction of a Gaussian laser beam with an ultrasonic wave of cylindrical symmetry. *Applied Optics*, 46(23):5870–5876, aug 2007.
- [16] P. Phariseau. On the diffraction of light by progressive supersonic waves. *Proceedings of the Indian Academy of Sciences - Section A*, 44(4):165–170, 1956.
- [17] R. W. Dixon. Acoustic Diffraction of Light in Anisotropic Media. *IEEE Journal of Quantum Electronics*, 3(2):85–93, 1967.
- [18] I. C. Chang. 1. Acoustooptic Devices and Applications. *IEEE Transactions on Sonics and Ultrasonics*, 23(1):2–21, 1976.
- [19] James D. Lechleiter, Da Ting Lin, and Use Sieneart. Multi-photon laser scanning microscopy using an acoustic optical deflector. *Biophysical Journal*, 83(4):2292–2299, 2002.
- [20] Eric D. Diebold, Brandon W. Buckley, Daniel R. Gossett, and Bahram Jalali. Digitally synthesized beat frequency multiplexing for sub-millisecond fluorescence microscopy. *Nature Photonics*, 7(10):806–810, 2013.
- [21] Joumane Aboujeib, André Pérennou, Véronique Quintard, and Jean Le Bihan. Planar phased-array transducers associated with specific electronic command for acousto-optic deflectors. *Journal of Optics A: Pure and Applied Optics*, 9(5):463–469, may 2007.
- [22] Dimitris Trypogeorgos, Tiffany Harte, Alexis Bonnin, and Christopher Foot. Precise shaping of laser light by an acousto-optic deflector. *Optics Express*, 21(21):8619–8625, 2013.
- [23] David L. Hecht. Multifrequency Acoustooptic Diffraction. *IEEE Transactions on Sonics and Ultrasonics*, 24(1):7–18, 1977.
- [24] Dorian Treptow, Raúl Bola, Estela Martín-Badosa, and Mario Montes-Usategui. Artifact-free holographic light shaping through moving acousto-optic holograms. *Scientific Reports*, 11(1):1–13, 2021.
- [25] Gaddum Duemani Reddy and Peter Saggau. Fast three-dimensional laser scanning scheme using acousto-optic deflectors. *Journal of Biomedical Optics*, 10(6):064038, 2005.
- [26] SeungYeon Kang, Martí Duocastella, and Craig B. Arnold. Variable optical elements for fast focus control. *Nature Photonics*, 14(9):533–542, sep 2020.
- [27] S. E. Harris and R. W. Wallace. Acousto-Optic Tunable Filter. *Journal of the Optical Society of America*, 59(6):744, jun 1969.

- [28] T. Yano and A. Watanabe. Acoustooptic TeO₂ tunable filter using far-off-axis anisotropic Bragg diffraction. *Applied Optics*, 15(9):2250, 1976.
- [29] I.C. Chang. Analysis of the noncollinear acousto-optic filter. *Electronics Letters*, 11(25-26):617, 1975.
- [30] Dennis R. Suhre. Spatial resolution of imaging noncollinear acousto-optic tunable filters. *Optical Engineering*, 31(10):2118, 1992.
- [31] Elliot S. Wachman, Wen Hua Niu, and Daniel L. Farkas. AOTF microscope for imaging with increased speed and spectral versatility. *Biophysical Journal*, 73(3):1215–1222, 1997.
- [32] Alexandre Mermillod-Blondin, Euan Mcleod, and Craig B. Arnold. High-speed varifocal imaging with a tunable acoustic gradient index of refraction lens. *Optics Letters*, 33(18):2146, sep 2008.
- [33] Nicolas Olivier, Alexandre Mermillod-Blondin, Craig B Arnold, and Emmanuel Beaurepaire. Two-photon microscopy with simultaneous standard and extended depth of field using a tunable acoustic gradient-index lens. *Optics Letters*, 34(11):1684, jun 2009.
- [34] Martí Duocastella, Bo Sun, and Craig B. Arnold. Simultaneous imaging of multiple focal planes for three-dimensional microscopy using ultra-high-speed adaptive optics. *Journal of Biomedical Optics*, 17(5):050505, 2012.
- [35] Simonluca Piazza, Paolo Bianchini, Colin Sheppard, Alberto Diaspro, and Martí Duocastella. Enhanced volumetric imaging in 2-photon microscopy via acoustic lens beam shaping. *Journal of Biophotonics*, 11(2):e201700050, feb 2018.
- [36] Manuel Martinez-Corral, Po-Yuan Yuan Hsieh, Ana Doblaz, Emilio Sanchez-Ortiga, Genaro Saavedra, and Yi-Pai Pai Huang. Fast Axial-Scanning Widefield Microscopy with Constant Magnification and Resolution. *IEEE/OSA Journal of Display Technology*, 11(11):913–920, nov 2015.
- [37] Euan McLeod and Craig B Arnold. Optical analysis of time-averaged multiscale Bessel beams generated by a tunable acoustic gradient index of refraction lens. *Appl Opt*, 47(20):3609–3618, 2008.

3

AOF Device: Theoretical Model

Laser-scanning systems are widely used for imaging and manufacturing purposes because of their capability to guide light to specific sample locations. The precise control of beam position enables to perform material modification [1] or excite fluorescence [2] at precise points, typically scanning the sample on a pixel-by-pixel approach. However, the point-scanning nature of these systems constrains their speed and thus their throughput. A shift of the paradigm is needed to overcome this limitation. Indeed, higher throughput can be reached by irradiating large regions with structured light or simultaneously shining multiple beams on the sample, thus parallelizing the process.

As discussed in chapter 1, currently available light-sculpting devices either lack flexibility or speed. In this chapter, we present a novel acousto-optofluidic (AOF) device, shown in Figure 3.1a, which is capable of performing beam sculpting at high-speed [3, 4]. The idea behind this device is to exploit standing acoustic waves – established in a resonant cavity – that modulates the light both in space and in time. A laser beam is split into multiple beamlets with properties – such as number and intensity – tunable in less than a microsecond. Those beamlets can be used independently, achieving beam parallelization, or can be easily combined, obtaining customizable interference patterns. Moreover, the AOF device is compatible with virtually any other beam-shaping tool. Thus, its flexibility can be further extended if used in synergy with other devices. With an unprecedented combination of speed and tunability, the AOF device paves the way for high-speed tailored light.

In the first part of this chapter, we introduce the AOF device by describing its design and implementation. In the second part, we provide a complete theoretical model of the formation of the acoustic wave inside the cavity. In the third and last part, we use the Raman-Nath theory [5] to develop a complete optical model to predict the structure of the diffraction patterns. The physics behind the AOF device is described in greater detail in appendices D, E, and F.

3.1 Design and realization of the device

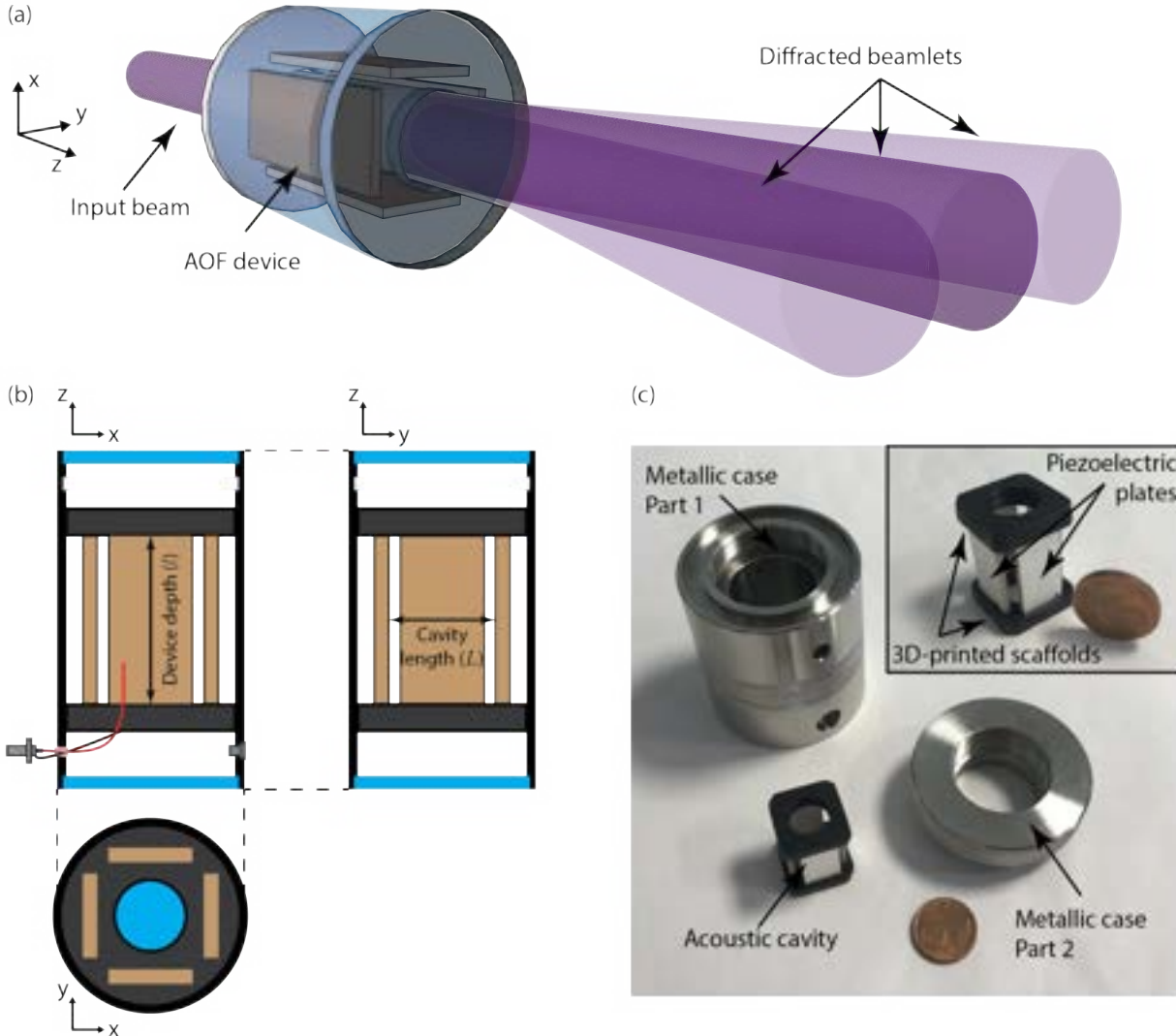


Figure 3.1: (a) Sketch of the AOF device diffracting light. (b) Orthogonal views of the AOF device with all its components. (c) Photograph of a disassembled AOF device. The coin is placed as a reference for the size.

As schematically shown in 3.1b, the AOF device is essentially an acoustic cavity composed of four piezoelectric plates arranged with a rectangular symmetry: we paired the plates so each element in a group would face each other, while the groups were orthogonal. To hold the plates in the required positions – namely to form two rectangular cavities – we used two 3D-printed plastic scaffolds with a doughnut shape that featured four sockets, one for each piezoelectric plate. In the current implementation, we used deionized water as the acoustic propagation medium. This choice has numerous conveniences: water is cheap, safe, readily available, and, being an isotropic and homogeneous material, is not sensitive to light polarization. Once assembled, we placed the

acoustic cavity inside a hollow aluminum cylinder (3.1c) consisting of two independent parts that can be screwed together. This enables easy access to the core components for maintenance or customization. Both sides of each piezoelectric plate are soldered to a single wire, such that each actuator can be driven individually. The electric wires reach the connectors located outside the cavity, passing through holes on the metallic case. We sealed the holes using epoxy resin to avoid possible leakages. Finally, we used two optically transparent circular windows to close the cylinder, each glued to one of the cylinder bases. An inlet port, which can be closed with a screw and an o-ring, allows replacing or refilling the cylinder with the liquid. Notably, air bubbles can be present in the cavity, compromising its functionality. Therefore, we excavated an annular pit onto the inner surface of the cylinder, acting as a bubble-trap [6, 7].

3.2 Mechanical model

The acousto-optic interaction in the AOF device depends dramatically on the properties of sound. Thus, it is important to model the generation and propagation of acoustic waves in response to the mechanical stimuli produced by the piezoelectric actuators. Once the acoustic wave is known, it can be easily related to a refractive index variation. Thus, a full mechanical model enables to predict the beam-shaping capabilities of the AOF device. To this end, we use the Navier-Stokes equations [8]. These laws govern the motion of sound waves in a viscous liquid, as inside the AOF device. Typically, acoustic phenomena perturb only slightly the fluid density and velocity. In this case, the Navier-Stokes equations can be simplified, leading to the acoustic damped wave equation

$$\frac{\partial^2 \rho}{\partial t^2} - c_s^2 \nabla^2 \rho - \nu \nabla^2 \frac{\partial \rho}{\partial t} = 0 \quad (3.1)$$

Here ρ is the density fluctuation of the fluid relative to the static case, c_s is the speed of sound, and ν is the kinematic viscosity of the liquid. A full derivation is available in appendix D. The rectangular-symmetry of the AOF device allows to consider only a single spatial axis of propagation

$$\frac{\partial^2 \rho}{\partial t^2} - c_s^2 \frac{\partial^2}{\partial x^2} \left(\rho + \nu \frac{\partial \rho}{\partial t} \right) = 0 \quad (3.2)$$

This approximation neglects the angular spreading of the wave due to the finite size of the actuator but greatly simplifies the calculations while preserving the critical elements of the physical phenomenon. Indeed, the acoustic divergence angle is of the order of Λ/l . For typical ultrasound frequencies and cavity length of the order of centimeters, the divergence is small and can be neglected. The solution of equation 3.2 depends on the initial and boundary conditions. Assuming the fluid is at rest before the actuators start moving, we get the following initial conditions

$$\rho(x, t) \Big|_{t=0} = 0 \quad \frac{\partial \rho}{\partial t} \Big|_{t=0} = 0 \quad (3.3)$$

Assuming that the fluid has zero relative velocity with respect to the solid boundary [9], the movement of the piezoelectric plates determines the boundary conditions

$$v(x, t) \Big|_{x=x_0} = \pm v_a \cos(\Omega_d t) \quad (3.4)$$

where v is the fluid velocity, v_a is the amplitude of the plate speed, Ω_d is the driving angular frequency, and x_0 is the location of the boundary. This condition can hold for $x_0 = 0$, $x_0 = L$ or both, depending on which actuator is driven. The plate velocity can be assumed to be proportional to the applied voltage. In the next sections, we discuss the expression of the solution to the wave equation, found using numerical and analytical methods. The details of these calculations are available in appendix E.

3.2.1 Resonant solution

3.2.1.1 Transient behavior

When the piezoelectric plates are driven with a harmonic signal, two acoustic waves are launched propagating in opposite directions [10]. These waves overlap and interfere while traveling across the cavity length. If the driving frequency does not respect the resonant condition, the waves change their relative phase after a cavity round-trip. This situation is shown by the simulations of Figure 3.2a. As a consequence of the phase mismatch, the amplitude of the resulting mechanical oscillation varies in time every L/c_s . However, the interference is typically destructive. Viscous dumping produces a progressive decrease of the oscillation amplitude, which ends up being too low for the beam-shaping applications envisioned in this work.

Instead, the resonant condition is achieved by selecting a frequency such that the wave remains in phase with itself after each cavity round-trip. In terms of driving frequency and wave number this condition is written as

$$\Omega_m = \frac{\pi m c_s}{L} \quad K_m = \frac{\pi m}{L} \quad (3.5)$$

where m is the natural number that indexes the resonance order. In this condition, the two traveling waves always interfere constructively, thus forming a standing wave whose amplitude builds up every L/c_s . However, as shown in Figure 3.2b, cavity losses prevent the oscillation from growing indefinitely. In more detail, the amplitude increases in time as $1 - \exp(-K_m^2 \nu t/2)$, thus reaching steady-state after a characteristic time $\tau = \frac{2c_s^2}{\nu \Omega_d^2}$. Therefore, the lower is the kinematic viscosity of the medium, the longer is the time required to reach the steady-state, but the higher is the final amplitude.

3.2.1.2 Steady-state solution

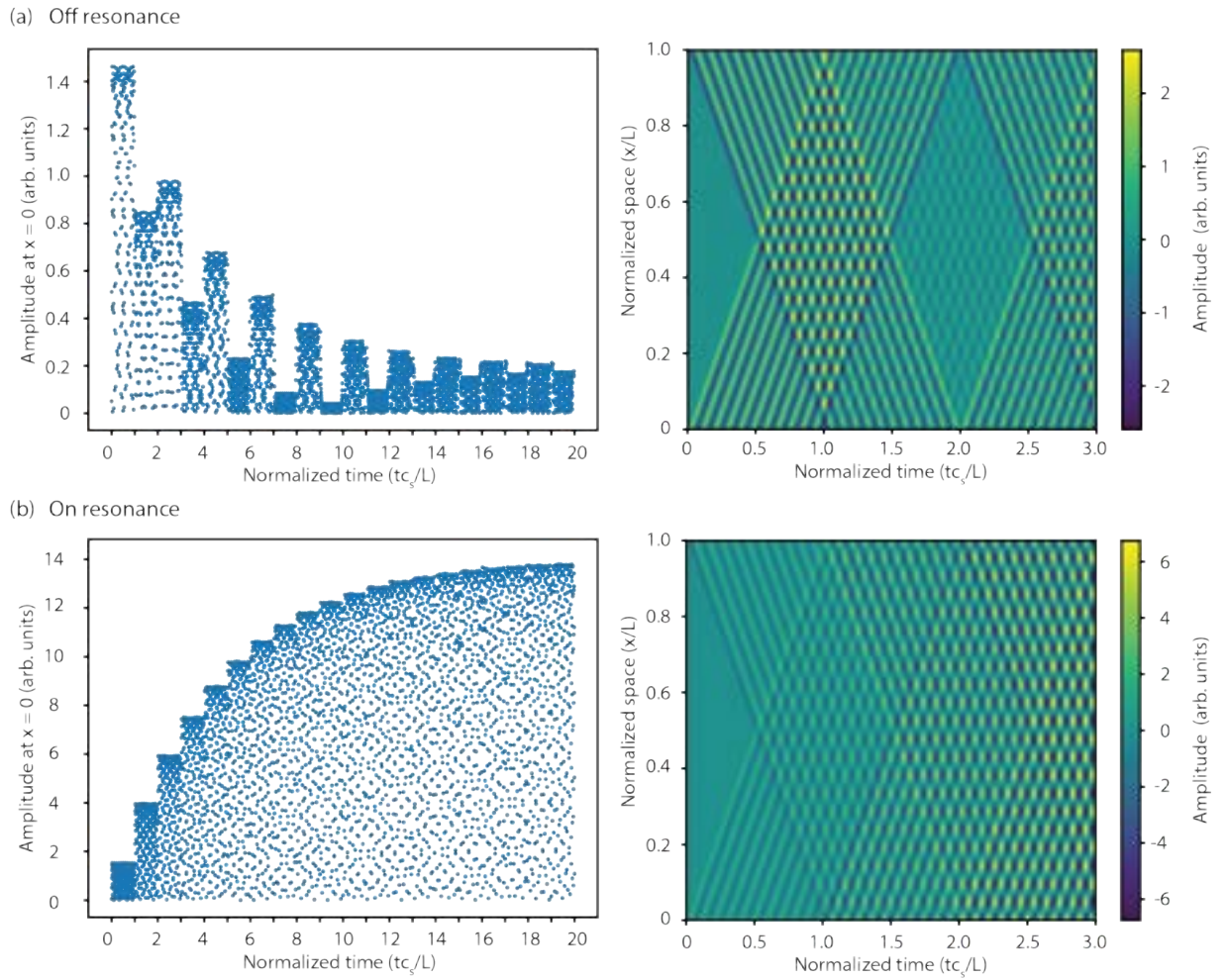


Figure 3.2: Simulation of the transient behaviour of the acoustic cavity under non-resonant and resonant driving conditions, obtained by numerically solving the damped wave equation. The normalized viscosity is set to $\nu/Lc_s = 10^{-4}$. On the left, Oscillation amplitude at border of the cavity. On the right, space-time propagation of the acoustic waves. The normalized frequency used is $\Omega L/c_s = 22\pi$ for the off resonance case and $\Omega L/c_s = 21\pi$ for the resonant case.

The resonant case is the most interesting one for practical applications, since it enables the highest acoustic amplitude, capable to induce a significant acousto-optic interaction. Indeed, all the experiments presented in chapter 4 are performed with a resonant AOF device. However, the damping induced by the viscosity of the medium limits the maximum amplitude of standing waves. In liquids, the damping is not uniquely related to the kinematic viscosity, but is also related to the acoustic frequency also plays a role. As shown in Figure 3.3a, the maximum value and the width of the resonant peaks decrease with increasing frequency, reducing the quality factor of the cavity. Thus, a low-viscosity medium is desirable to maximize the efficiency of the device. In more detail, the acoustic amplitude at the steady-state, with a driving frequency close to the

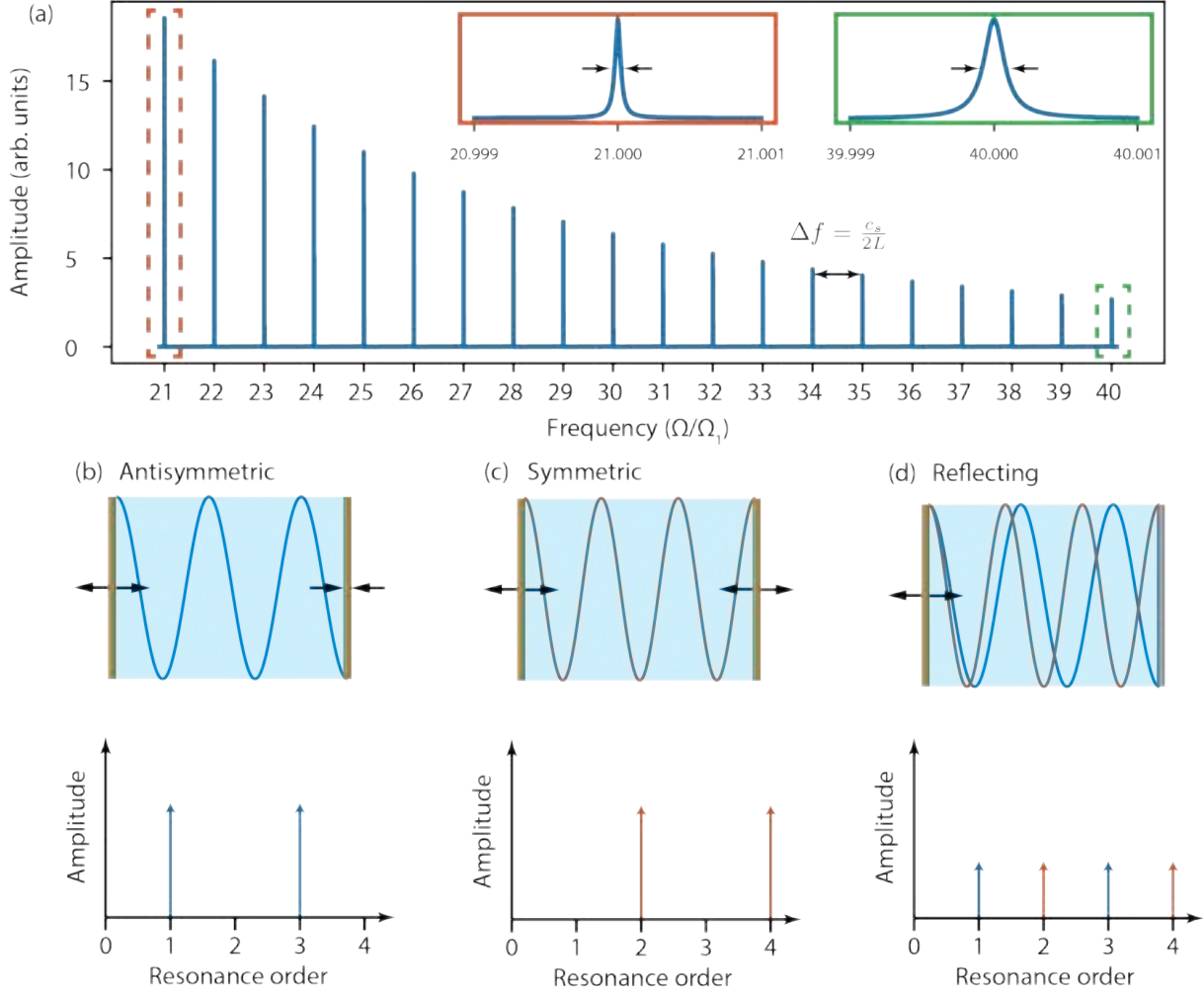


Figure 3.3: (a) Numerical simulation of the frequency response function of the acoustic cavity, showing the resonant peaks of the standing wave. The inset on the left is centered around the 21st resonance, the inset on the right is centered around the 40th resonance. The normalized viscosity is set to $\nu/Lc_s = 10^{-4}$. (b, c, d) Sketch of the possible solutions of the acoustic wave equation in the AOF device, depending on the boundary conditions.

n^{th} resonance is

$$\rho_m(\Omega_d) = \frac{2\rho_0}{L} \frac{c_s^2 \Omega_d^4 \nu v_a}{c_s^4 + \nu^2 \Omega_d^2} \frac{1}{(\Omega_m^2 - \Omega_d^2)^2 + \Omega_d^2 \nu^2 K_m^4} \quad (3.6)$$

where ρ_0 is the density of the fluid at rest. As expected, the amplitude is a decreasing function of viscosity and frequency. Applying the low-viscosity assumption ($\nu \ll c_s^2/\Omega_d$) and assuming a perfect resonant condition ($\Omega_d = \Omega_m$), we can finally write the explicit expression the standing

wave established in the cavity

$$\rho_m(x, t) = \xi_m \frac{2\rho_0 v_a c_s^2}{\nu L \omega_m^2} \cos(K_m x) \cos(\Omega_m t) \quad (3.7)$$

where ξ_m is the parameter that describes the driving condition of the actuators. The three most interesting cases are the following

$$\xi_m = \begin{cases} 1 + (-1)^{n+1} & \text{Anti-symmetric} \\ 1 + (-1)^n & \text{Symmetric} \\ 1 & \text{Reflecting} \end{cases} \quad (3.8)$$

These solutions, sketched in Figures 3.3b, 3.3c, and 3.3d, respect the symmetry imposed by the boundary conditions. Indeed, if the actuators are driven anti-symmetrically, the waves are generated in counter-phase and only odd resonance orders are allowed. Conversely, if the actuators are driven symmetrically, the waves are in phase and only even resonance orders are permitted. Indeed, the second sound source imposes an additional constraint to the resonance condition. In order for the interference to be constructive, each wave has to be in phase with itself after a round-trip and with the second wave after a single-trip. Despite these differences, the resonant amplitude is the same in these two cases. If only one piezoelectric plate is driven and we consider the second boundary a perfectly reflecting surface, both odd and even resonance orders become possible. As a side effect, the steady-state amplitude is one-half of that reached with both actuators turned on, making this condition less convenient for beam-shaping.

3.2.2 Traveling solution

A different solution is found by completely removing the second boundary from the cavity, which is practically achieved by substituting one actuator with an acoustic absorber. In this case, the actuator generates a single traveling wave whose expression is

$$\rho(x, t) = \frac{\rho_0 c_s v_a}{\sqrt{c_s^4 + \nu^2 \Omega^2}} \exp\left(-\frac{\Omega^2 \nu}{2c_s^3} x\right) \sin(Kx - \Omega t) \quad (3.9)$$

Since no resonances are involved, this solution fully describes the acoustic wave once it has traveled for the full length of the cavity. Namely, this solution is valid after $\tau = L/c_s$. The numerical simulations of Figure 3.4 depict the traveling wave solution, showing a viscous damping increasing with the driving frequency. Interestingly, in these working conditions, any driving frequency can be used. However, given a driving power, the oscillation amplitude is typically one or two orders of magnitude than that obtainable in resonant conditions. Thus, a much higher driving voltage is required to achieve a comparable result, making this case much less appealing from the practical point of view.

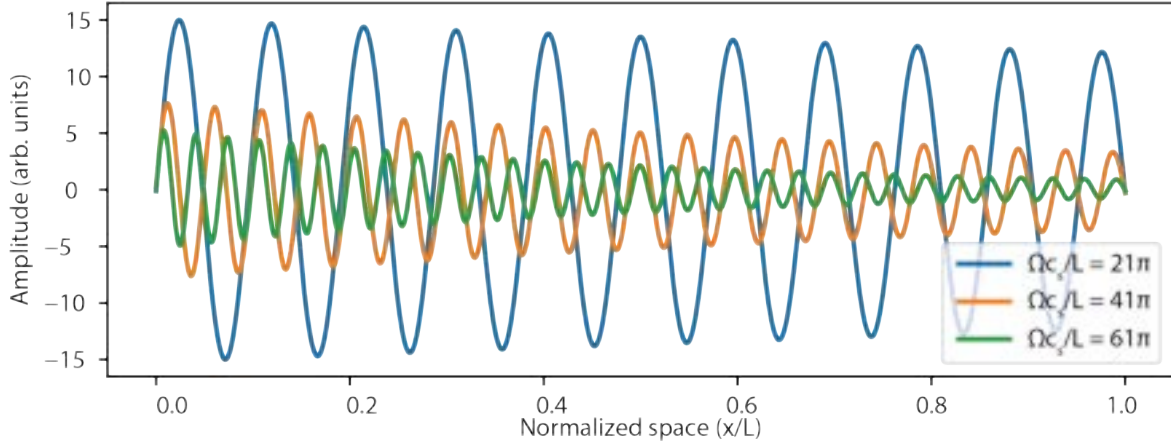


Figure 3.4: Simulations obtained by numerically solving the damped wave equation of a traveling wave at different driving frequencies. The normalized viscosity is set to $\nu/Lc_s = 10^{-4}$.

3.2.3 From density to refractive index

Local perturbations of the density of a material modify its optical properties. More in detail, we can relate mechanical waves to variations of the refractive index through a linearized Lorentz-Lorenz formula [11]

$$n(x, t) = n_0 + \Delta n(x, t) = n_0 + \frac{n_0^4 + n_0^2 - 2}{6n_0} \frac{\rho(x, t)}{\rho_0} \quad (3.10)$$

where n_0 is the refractive index of the medium at rest. Thanks to this simple model, we can regard all the results presented so far to be linearly related to the acoustically-induced optical properties of the AOF device. As seen in the previous section, the use of a resonant cavity with both actuators active enables the highest variation of density and – thus – of refractive index, maximizing the interaction with light. Thus, for the rest of the thesis, we consider the AOF device to be operating only in this modality.

3.3 Optical model

The mechanical model presented in the previous section enables to directly relate the driving conditions of the AOF device to a sinusoidal variation of refractive index, both in space and in time. The goal of the present section is to understand how the acousto-optic diffraction caused by a standing wave can generate structured light. The variation of the refractive index induced by the acoustic standing wave is

$$\Delta n(x, t) = \underbrace{\xi_m \frac{2v_a c_s^2}{\nu L \Omega_m^2} \frac{n_0^4 + n_0^2 - 2}{6n_0}}_{n_m} \cos(\Omega_m t) \cos(K_m x) \quad (3.11)$$

At typical working frequencies (such as those used in chapter 4) the acousto-optic interaction occurs the Raman-Nath regime, where the AOF device can be simply considered as thin optical element. In other words, the AOF device acts as a gradient-index optical element, with phase depth $\Phi = kl\Delta n$, where k is the wavenumber of light, and l is the depth of the acoustic cavity. Thus, the refractive index profile of equation 3.11 corresponds to a sinusoidal phase grating. The action of the device to an incident beam is to apply the following phase transformation

$$\begin{aligned} t_{\text{AOF}} &= \exp \left[kl n_m \cos(\Omega_m t) \sin \left(K_m x + \pi \frac{m+1}{2} \right) \right] = \\ &= \sum_{q=-\infty}^{+\infty} J_q [kl n_m \cos(\Omega_m t)] \exp(iqK_m x) \exp \left(iq\pi \frac{m+1}{2} \right) \end{aligned} \quad (3.12)$$

Here J_q is the Bessel function of the first kind of order q . for convenience, we centered the coordinate frame at the center of the AOF device and used the Bessel generating function to obtain the second identity. Indeed, this step is useful to calculate the analytical expression of the electric field emerging from the cavity. This latter is obtained simply by taking the product of the incident field and the above expression. In the following discussion, we present the expression of the near and far-field diffraction patterns calculated using Fourier optics. Further details are presented in appendix B and F.

3.3.1 Fresnel Diffraction

The goal of this section is to study the diffraction pattern emerging from the AOF device, focusing our attention at short distance. We begin considering a collimated Gaussian beam, being the typical output provided by a laser source. The corresponding field is

$$U(x, y) = U_0 \exp \left[-\frac{(x^2 + y^2)}{w^2} \right] \quad (3.13)$$

where w is the beam waist. The expression of the beam after interacting with the AOF device at $z = 0$ is given by the product of the above expression with the phase transformation of equation 3.12. The diffracted field at a distance z is calculated using the Fresnel propagation method. The result is

$$\begin{aligned} U(x, y, z) &= \frac{U_0 e^{ikz}}{1 + i \frac{\lambda z}{\pi w^2}} \sum_{q=-\infty}^{+\infty} \exp \left\{ -\frac{1}{w^2 + \frac{4z^2}{k^2 w^2}} \left[\left(x - q \frac{\lambda}{\Lambda_m} z \right)^2 + y^2 \right] \right\} \times \\ &\times J_q [n_m \cos(\Omega_m t)] \exp \left(-\frac{iq^2 K_m^2 z}{2k} \right) \exp \left[iq \left(K_m x + \pi \frac{m+1}{2} \right) \right] \end{aligned} \quad (3.14)$$

This expression might look complicated at first sight, but it has a quite simple physical interpretation visually described in Figure 3.5a. Indeed, it represents a set of diverging Gaussian beams

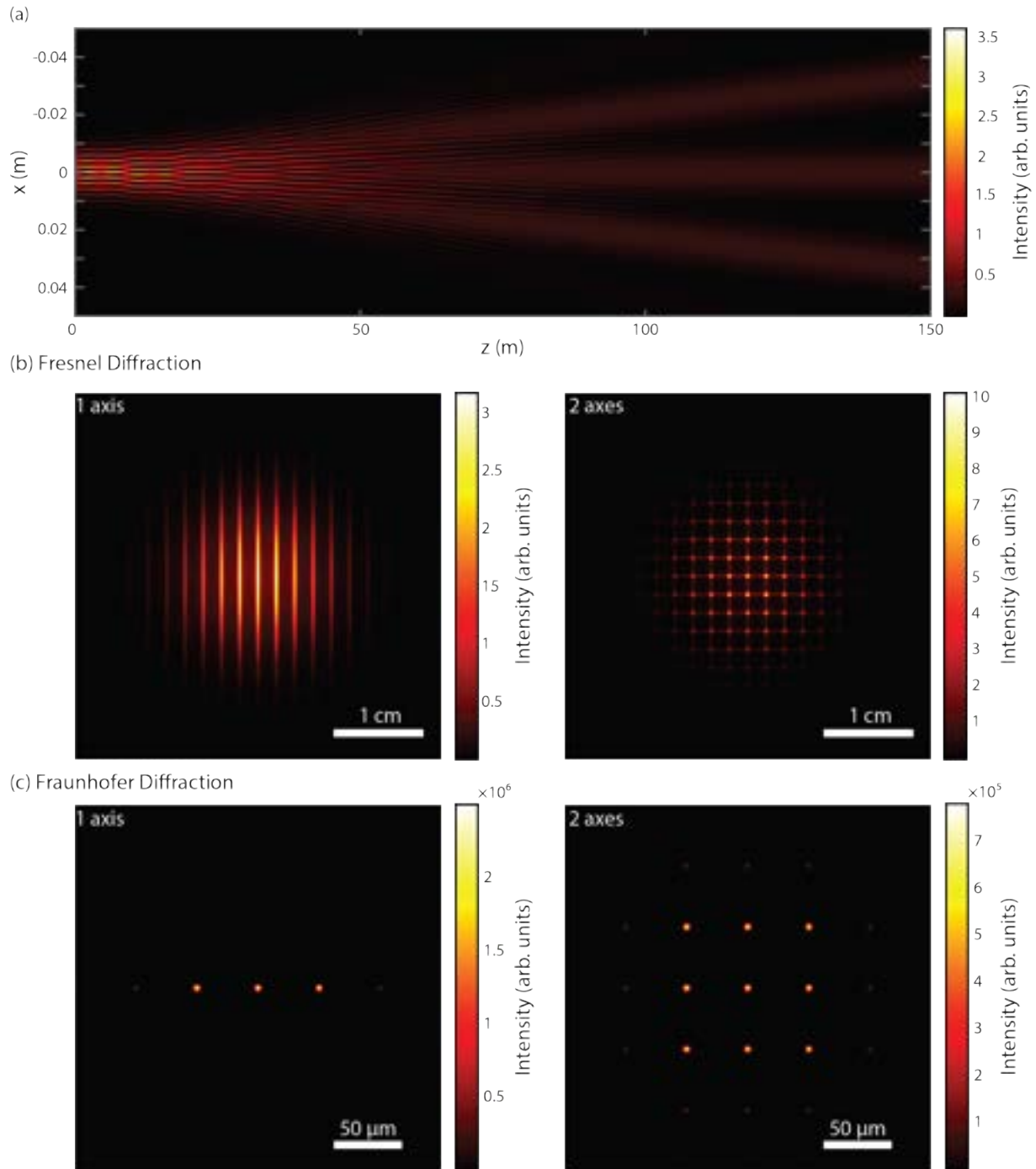


Figure 3.5: Simulation of light propagating after interacting with an AOF device active along the x -axis. The incident beam is Gaussian with size $w = 1$ cm at $\lambda = 444$ nm. The cavity length is $l = 2$ cm and the speed of sound is $c_s = 1489$ m/s, namely that of pure water at room temperature. The resonance order used is $m = 20$, corresponding to an acoustic frequency of $f = 744.5$ kHz. The variation of refractive index is $n_m = 5 \times 10^{-6}$ at time $t = 0$ s and the device depth is $L = 2$ cm. (a) Diffracted beams propagating along the optical axis z . (b) Diffraction pattern on the xy plane at $z = 1$ m for a single active axis (left) and for both active axes (right). (c) Far field diffraction pattern obtained with a lens of focal length 20 cm for a single active axis (left) and for both active axes (right).

deflected by an angle $\theta_q = q\lambda/\Lambda_m$ and amplitude modulated by the term $J_q[n_m \cos(\Omega_m t)]$. Importantly, even though the sum extends to infinity, the value of the Bessel functions approaches zero with increasing q . Therefore, in a realistic scenario, we can consider the number of diffracted beams to be finite. In more detail, the exact number of diffraction orders with non negligible energy depends on the driving parameters, especially the driving voltage (as described in greater detail in chapter 4). Given the limited size of each beam, they overlap and interfere as long as the propagation distance is smaller than the ratio between the deflection angle and the beam waist. For bigger distances, the beams propagate independently, eventually leading to the far-field diffraction pattern described in the next section. For small propagation distances ($\theta_q z \ll 2w$), we can approximate the field by neglecting the divergence. The result is

$$U(x, y, z) = U_0 \exp\left[-\frac{(x^2 + y^2)}{w^2}\right] \sum_{q=-\infty}^{+\infty} J_q[n_m \cos(\Omega_m t)] \times \exp\left(-\frac{iq^2 K_m^2 z}{2k}\right) \exp\left[iq\left(K_m x + \pi \frac{m+1}{2}\right)\right] \quad (3.15)$$

Notably, this expression contains two periodic functions: one oscillates along the optical axis (z), and the other oscillates along the axis parallel to the acoustic wave (x). The term oscillating along the z -axis is responsible for a 3D structure of the fringe, being periodic with period $z_T = \frac{2\Lambda^2}{\lambda}$. Indeed, the fringes on the xy plane suffer from a π phase shift every half a period, and if the distance from the AOF device matches an integer multiple of z_T , the periodic term has unit value, and the diffracted field is precisely an image of the input field. This phenomenon, widely known as *Talbot effect*, is a consequence of the periodicity of the acoustic phase grating [12]. Notably, the fringes' axial periodicity can also be modified by selecting the driving frequency.

The term oscillating along the x -axis generates fringes on the detector plane, due to the mutual interference of all the diffraction orders. The simulated intensity – calculated as the squared modulus of equation 3.15 – is shown in Figure 3.5b. If only a single axis is turned on, the interference fringes are oriented along the same axis. If both axes are active, fringes are formed in the two directions and overlap in a chessboard-like arrangement where the crossing points exhibit the highest intensity. Interestingly, the spatial frequency of the fringes is qK_m , namely an integer multiple of the frequency of the acoustic wave. This fact implies that for low q the pattern approaches a sinusoidal structure, while for high q the fringes are given by the superposition of multiple spatial frequencies and the complexity of the pattern increases. Therefore, we can easily tailor the diffraction pattern structure by changing the number of diffraction orders and the acoustic frequency.

3.3.2 Fraunhofer Diffraction

So far, we analyzed the near-field beam-shaping capabilities of the AOF device. Now, we focus our attention on the far-field description of the diffraction patterns, either at large distances from the AOF device or at the focal plane of a lens. In any of these conditions, the diffracted field is

the Fourier transform of the initial field

$$U(x, y, z) = \frac{\pi w^2 U_0}{i \lambda z} \sum_{q=-\infty}^{+\infty} J_q[k l n_m \cos(\Omega_m t)] \exp \left\{ -\frac{\pi^2 w^2}{\lambda^2 z^2} \left[\left(x - q z \frac{\lambda}{\Lambda_m} \right)^2 + y^2 \right] \right\} \quad (3.16)$$

where z is either the propagation distance or the focal length of the lens. Notably, if the diffraction orders do not overlap, any interference phenomenon can be neglected, and the intensity can be calculated simply by taking the square modulus of the terms of the series. This enables a simple interpretation of equation 3.16. It describes an array of Gaussian spots, laterally shifted by $qz\lambda/\Lambda_m$ and amplitude modulated by $J_q[kln_m \cos(\Omega_m t)]$. Therefore, we can select the number and positions of the spots on the plane with the driving parameters. If a single axis is active, the spots are aligned to the same axis. If both axes are active, the spots are distributed on a 2D grid as depicted in Figure 3.5c.

3.3.3 Parallelization of non-conventional beams

The parallelization acted by the AOF device in the far-field can be generalized for any input beam shape $B(x, y)$. Indeed, the acoustic wave splits the incoming light in multiple beamlets without distorting the shape of the individual orders. The resulting diffraction pattern in the far-field is

$$U(x, y, z) = \frac{1}{i \lambda z} \sum_{q=-\infty}^{+\infty} J_q[k l n_m \cos(\Omega_m t)] \hat{B} \left(\frac{x}{\lambda z} - \frac{q}{\Lambda_m}, \frac{y}{\lambda z} - \frac{q}{\Lambda_m} \right) \quad (3.17)$$

where \hat{B} is the Fourier transform of the input beam B . The above expression describes an array of beamlets, each being the amplitude-modulated and laterally-shifted Fourier transform of the incident beam. This result is valid for any beam whose shape is approximately constant across the depth of the AOF device. In Figure 3.6 we show the simulated diffraction pattern for two given shapes, namely an Annular beam and a Bessel beam. It is well known that the Fourier transform of one is the other and *vice versa* [13]. Thus, we see in Figure 3.6a that by feeding an annular beam to the AOF device, we obtain an array of Bessel beamlets in the far-field. Conversely, if we use a Bessel beam as the input, the result is an array of annular beamlets, as depicted in Figure 3.6b.

3.4 Conclusion

The mathematical model formulated in this chapter fully explains the working principle of the AOF device. The developed framework enables the engineering and optimization of new device implementations and opens the door for non-standard usage, such as diffracting the light with non-resonant waves or before reaching a steady state. The optical model relates the controlling parameters of the AOF device – such as the driving voltage, frequency, and phase – to the structure of the generated light patterns, enables reliable predictions of the capabilities of the device.

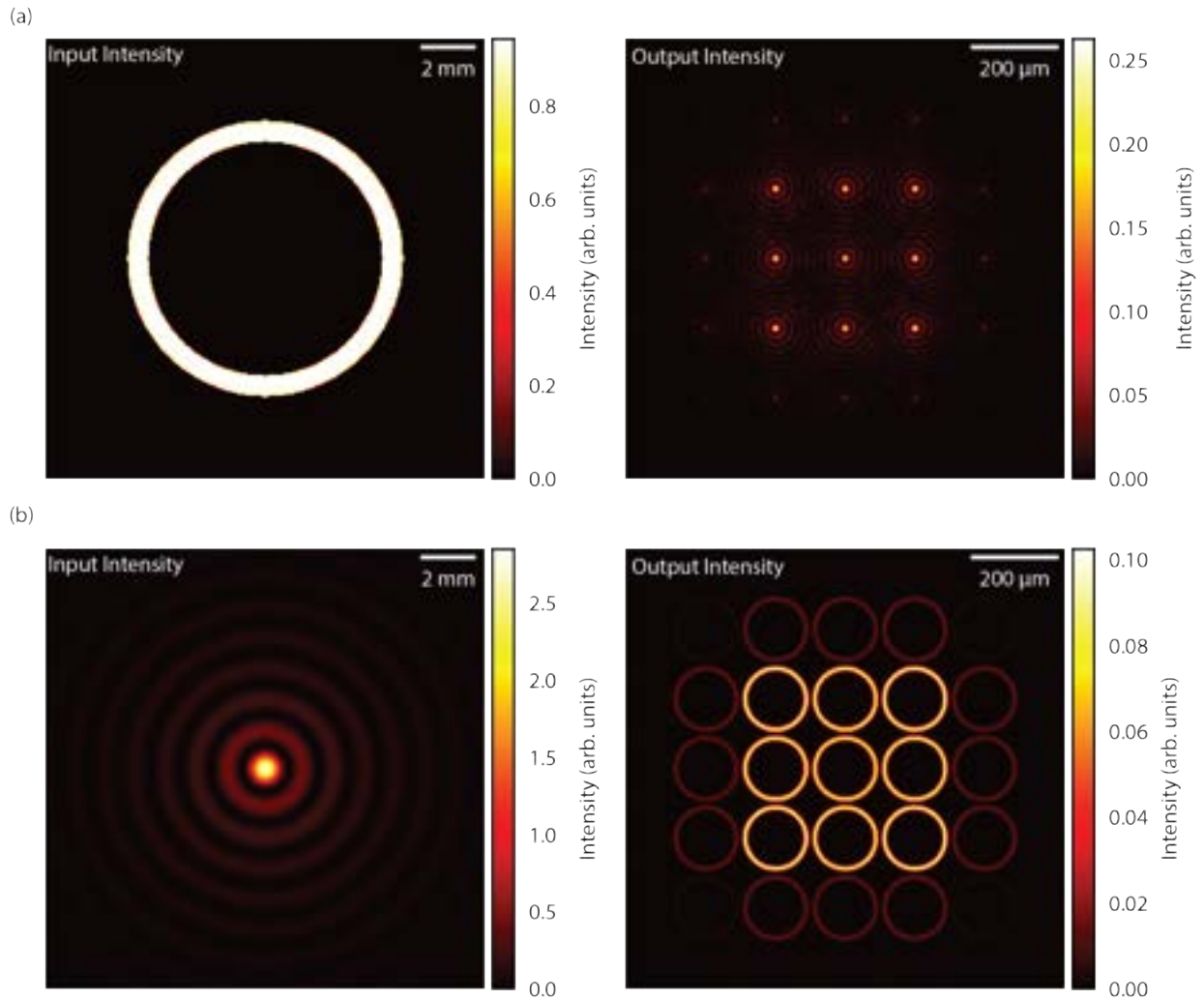


Figure 3.6: Simulation of diffraction pattern with both axes on at $f = 1.5$ MHz and $n_m = 0.6$. The AOF device depth is $l = 2$ cm and the optical wavelength is $\lambda = 520$ nm. The obtained patterns are instantaneous at $t = 0$ s. (a) The incident light (left) is an annular beam and the diffraction pattern (right) is a 2D array of Bessel beamlets. (b) The incident light (left) is a Bessel beam and the diffraction pattern (right) is a 2D array of annular beamlets.

The structure of the emerging light can be arbitrarily complex if the AOF device is combined with other beam-shaping tools, such as DOEs or SLMs. Notably, non-conventional beams typically extend for a large region in the Fourier plane of a lens, compared to a Gaussian beam. Thus, by selecting the proper driving conditions, it is possible to partially overlap the diffracted beamlets. Their mutual interference can be exploited to further increase the complexity of the patterns, paving the way to high-speed and high-flexibility beam shaping.

In the next chapter, we show how the extraordinary capabilities of the AOF device dramatically increase the throughput of a laser-writing system, enabling the processing of complex shapes on a wide range of materials.

References

- [1] Alberto Piqué, Raymond C.Y. Auyeung, Heungsoo Kim, Nicholas A. Charipar, and Scott A. Mathews. Laser 3D micro-manufacturing. *Journal of Physics D: Applied Physics*, 49(22), 2016.
- [2] James Jonkman and Claire M. Brown. Any way you slice it - A comparison of confocal microscopy techniques. *Journal of Biomolecular Techniques*, 26(2):54–65, 2015.
- [3] S. Surdo and M. Duocastella. Fast Acoustic Light Sculpting for On-demand Maskless Lithography. *Advanced Science*, 2019.
- [4] Alessandro Zunino, Salvatore Surdo, and Martí Duocastella. Dynamic Multifocus Laser Writing with Acousto-Optofluidics. *Advanced Materials Technologies*, 4(12):1–7, 2019.
- [5] W. R. Klein and Bill D. Cook. Unified Approach to Ultrasonic Light Diffraction. *IEEE Transactions on Sonics and Ultrasonics*, 14(3):123–134, 1967.
- [6] Alessandro Zunino, Salvatore Surdo, and Marti Duocastella. Design, implementation, and characterization of a fast acousto-optofluidic multi-focal laser system. In Ireneusz Grulkowski, Bogumił B. J. Linde, and Martí Duocastella, editors, *Fourteenth School on Acousto-Optics and Applications*, page 23. SPIE, nov 2019.
- [7] Salvatore Surdo, Alessandro Zunino, Alberto Diaspro, and Martí Duocastella. Acoustically shaped laser: A machining tool for Industry 4.0. *Acta IMEKO*, 9(4):60–66, 2020.
- [8] Michel Rieutord. *Fluid Dynamics*. Springer International Publishing, 2015.
- [9] Euan McLeod and Craig B. Arnold. Mechanics and refractive power optimization of tunable acoustic gradient lenses. *Journal of Applied Physics*, 102(3):1–9, 2007.
- [10] M Duocastella and C B Arnold. Transient response in ultra-high speed liquid lenses. *Journal of Physics D: Applied Physics*, 46:075102, 2013.

-
- [11] Max Born, Emil Wolf, A. B. Bhatia, P. C. Clemmow, D. Gabor, A. R. Stokes, A. M. Taylor, P. A. Wayman, and W. L. Wilcock. *Principles of Optics*. Cambridge University Press, oct 1999.
- [12] Layton A. Hall, Murat Yessenov, Sergey A. Ponomarenko, and Ayman F. Abouraddy. The space–time Talbot effect. *APL Photonics*, 6(5):056105, 2021.
- [13] John Goodman. *Introduction To Fourier Optics*. W.H. Freeman, 4th edition, 2017.

4

AOF Device: Characterization and Applications

Controlled delivery of light at targeted positions on a sample is key for precise, direct, and localized modification of materials using laser-based systems [1, 2]. Typically, laser writing is performed by focusing a beam into a single spot, which is successively scanned across a region of interest by either mirrors or translation stages [3, 4]. Even if sub-wavelength control of light can be achieved by tuning focusing-optics and scanning [5], the sequential nature of this approach seriously constrains processing throughput. A promising way to address this issue is irradiating the sample surface with the desired light intensity pattern. With this technique, there is no need to scan. Indeed, laser modification of an entire region can be performed with a single irradiation leading to an increased throughput. Light interference is one of the primary enablers maskless lithography, allowing the direct fabrication of periodic structures over large areas with no need of masks or molds, even at the sub-wavelength scale [6–10]. This technique is capable of either additive or subtractive nanofabrication with a larger throughput compared to the conventional direct-laser writing method. Typical implementations rely on splitting the light in multiple beams and recombining them with a defined angle, which dictates the spatial periodicity of the fringes. This is either achieved by fixed optical components – such as with diffractive optical elements [11], beam splitters [9, 12], Fresnel biprisms [13, 14], phase masks [15, 16], or mirrors [17, 18] – or with tunable devices – such as spatial light modulators [19, 20]. However, fixed elements lacks in tunability and active elements are typically limited in speed. This limit has been recently surpassed by the AOF device, which has been used to produce tailored interference patterns at high speed [21]. This approach demonstrated promising material processing capabilities. However, in some applications a point-by-point control of light is still desirable.

An entirely different approach enabling both high throughput and local control of light consists in splitting a beam into several beamlets, each focused at a different position on the sample. In this case, the throughput increases linearly with the number of beamlets, only limited by the available laser power. Successful implementations include the use of passive elements to gener-

ate fixed multi-focus distributions, such as diffractive optical elements [22], amplitude gratings [23] or beam splitters [24]. However, the lack of tunability in the selection of focus location or number heavily limits the flexibility of laser processing. Alternatively, active elements such as AODs [25, 26], SLMs [27, 28], or DMDs [29, 30] enable dynamic and customized light splitting, but can suffer from polarization dependence, low damage threshold and, more importantly, long response time. Thus, beam parallelization suffer from similar speed limitations of interference pattern generation. Simply put, a tool capable of generating multiple beams at high speed while preserving a high level of tunability is still not available.

In this chapter, we prove that the AOF device can fill this gap and create dynamic multi-focus distributions with unprecedented tunability and speed [31]. The first part of this chapter contains a detailed optical characterization of the system, in perfect agreement with the theoretical model of the previous chapter. In the second part, we demonstrate tailored micromachining of metals, ceramics, and polymers at ease and high throughput using either the multi-foci distribution or the interference patterns.

4.1 Dynamic generation of structured light

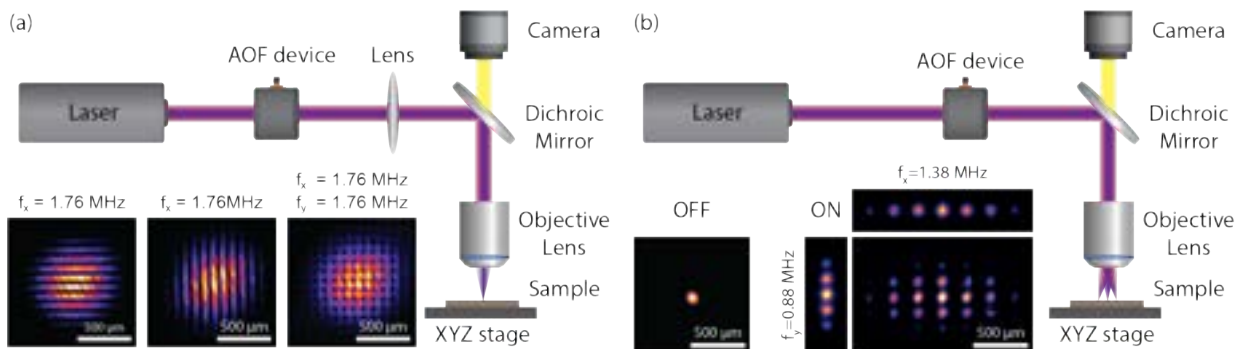


Figure 4.1: Schemes of the AOF-enabled laser direct-writing system. (a) The multi-focus distribution is realized by simply placing the AOF device before the objective lens. The insets show the measured intensity at the sample plane with the device off and on. (b) The interference patterns are conjugated to the sample plane with a 4f system composed of a lens and the objective lens. The insets show measured intensity at the sample plane with one or both axes on.

Our material processing setup consists of a conventional Laser Direct Writing (LDW) system modified to include the AOF device. When our system is used to generate the interference patterns, we conjugate the beams diffracted by the AOF device to the sample plane by means of a 4f system composed of a converging lens and the objective lens, as shown in Figure 4.1a. However, in the experiments shown in this chapter we used our system to parallelize the beam. In this case, the AOF device is placed before the focusing lens, as shown in Figure 4.1b.

As described in Chapter 3, driving the AOF device on resonance induces acoustic standing waves that oscillate in space and in time, modulating the refractive index of the medium and

enabling controlled diffraction of light. In detail, the periodic modulation of refractive index acts as a phase grating diffracting a laser beam into multiple beamlets with diffraction efficiency

$$\eta_q(t) = J_q^2[kln_m \cos(\Omega_m t)] \quad (4.1)$$

and a deflection angle

$$\theta_q = q \frac{\Omega_m \lambda}{2\pi c_s} \quad (4.2)$$

Equations 4.1 and 4.2 describe the fundamental operating principle of our generator of structured light — by adjusting driving frequency, amplitude voltage, or synchronized laser pulse arrival time, the number, intensity, or separation of the multiple diffraction orders can be tuned. Notably, the deflection angle governs the lateral separation of individual diffraction orders in the far-field. Instead, in the near-field, the angle determines the spatial periodicity of the interference fringes.

4.1.1 Acousto-Optofluidic device implementation

The prototype of the AOF device consists of a hollow metallic cylinder ($\varnothing = 2.54$ cm), a couple of optically transparent windows (Thorlabs, WG41010), and a plastic scaffold for properly holding four piezoelectric plates with sizes of 20 mm \times 9.5 mm \times 1.5 mm (APC international, PZT Navy type II). We employed a 3D-printer (CubePro, 3D Systems with a resolution of 100 μ m) to build the scaffold using poly-lactic acid (PLA). The piezoelectric plates were soldered on each face with metallic wires and subsequently assembled together with the scaffold to form a cavity with square symmetry – each plate corresponds to a face of a rectangular parallelepiped, and the distance between parallel plates is about 10 mm. Note that each pair of piezoelectric plates can be independently controlled. The cavity was positioned inside the metallic cylinder, enclosed with a pair of optically transparent windows, and sealed with an epoxy resin (Loctite, Hysol-9483). In experiments herein, the cavity was filled with Milli-Q water, and the AOF device was driven by an arbitrary waveform generator (Agilent 33521A). The choice of pure water as a medium is particularly convenient, being cheap, easily available, with low kinematic viscosity (less than 1.3×10^{-6} m²/s at room temperature) and a low absorption coefficient (between 0.06 m⁻¹ to 2 m⁻¹) for the wavelengths of our experiments, that is, 400 nm to 800 nm. Therefore, absorption, heating, or cavitation are negligible for a collimated beam that fills the size of the AOF system.

4.1.2 Stability and performance of the AOF device

The AOF device is essentially an acoustic resonant cavity immersed in a liquid, acting as the propagation medium for sound waves. In experiments herein, we used deionized water, but any weakly absorbing liquid could also be used. The choice of water is particularly convenient, being an isotropic and homogeneous medium. Thus, the AOF device is polarization-insensitive, in contrast to typical acousto-optic devices usually built with birefringent crystals [32]. However, many fluid parameters – such as the density, speed of sound, and viscosity – are sensitive to temperature variations. Consequently, the value of the resonant frequencies is not stable but fluctuates with

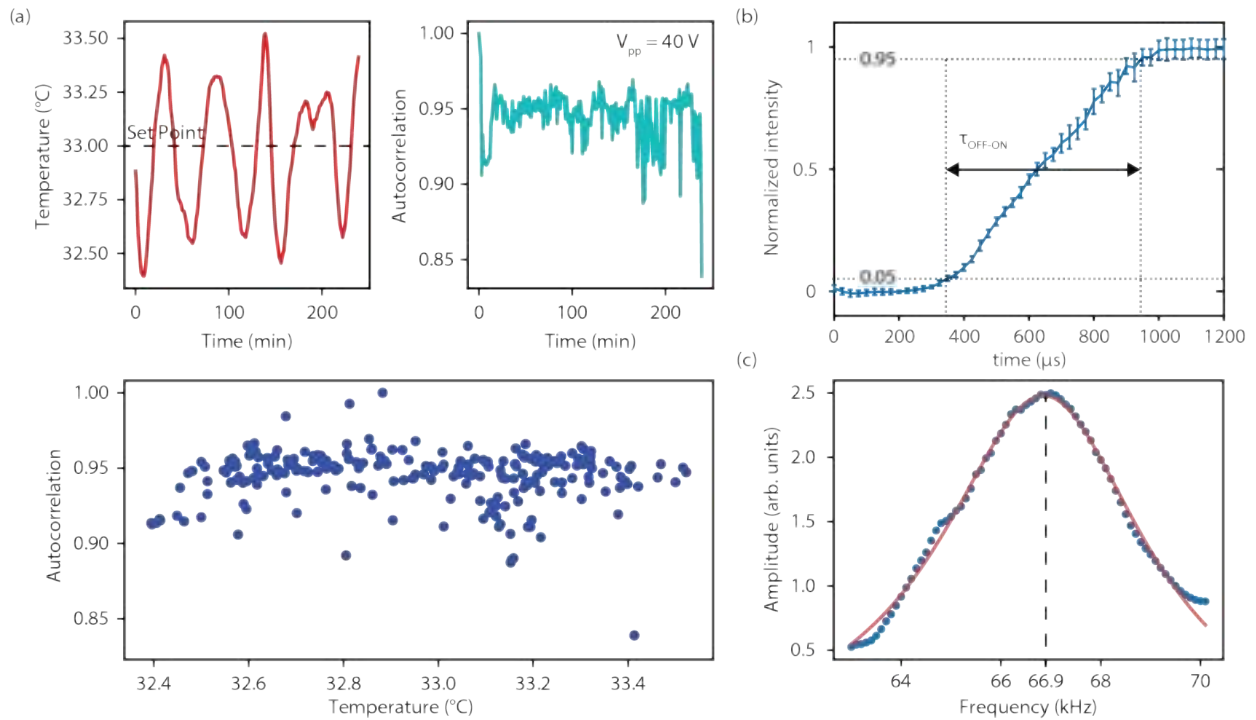


Figure 4.2: (a) Stability measurements of the temperature-controlled AOF device. (Top-left) Temperature oscillations over 240 minutes, measured with the temperature control system set at 33 °C. (Top-right) Correlation of the images of the diffraction patterns calculated over the same interval of time. (Bottom) Correlation values versus the measured temperature variations. This plot indicates reliable stability over the full temperature range. (b) Mean values (symbols) and standard deviation (bars) of the step response – from rest (OFF) to steady-state (ON) – of the AOF system. (c) First resonant peak of the acoustic cavity. The blue dots indicate the experimental points and the red line indicates the fit to the theoretical model.

changes in the temperature of the medium. This phenomenon can hinder the functionality of the AOF device when used for a prolonged time or when driven at high voltage. Thus, we implemented a closed-loop temperature control system. Specifically, we wrapped a flexible heating strip around the aluminum cylinder and integrated a thermocouple inside the cylinder close to the cavity. In this way, we can monitor and control the temperature of the liquid during the AOF operation. The result of our control system can be seen in Figure 4.2a. The temperature setpoint – in this case 33 °C – is set higher than the room temperature. As a result, the temperature inside the cavity fluctuates around the setpoint as a consequence of the continuous heat exchanges between the surrounding environment and the heating strip. In the meanwhile, the AOF device is driven at $V_{pp} = 40$ V and the diffraction pattern is continuously recorded with a CMOS camera. The images of the diffracted light are correlated in time with the pattern at the beginning of the operation. Noticeably, thanks to our feedback loop, the temperature variations are always small (no more than half a degree), enabling high optical stability of the AOF device. Indeed, within the 4 hours of operation, we did not measure any significant alteration of the diffraction pattern.

Another important parameter to describe the stability of the device is the step response time,

namely the amount of time required by the acoustic cavity to reach the steady-state after being switched on. We measured this quantity experimentally, as shown in Figure 4.2b. Notably, the step response time at $f = 1.5$ MHz is around $600 \mu\text{s}$, which is a value much smaller than that predicted by the theoretical model. This result indicates the presence of losses in the cavity other than the dissipation by the fluid viscosity. This hypothesis is corroborated by the result presented in Figure 4.2c, namely the experimental measure of the first resonant peak of the acoustic cavity. We performed this measurement by sweeping the driving frequency of an actuator and measuring the generated acoustic pressure using the second piezoelectric plate as a sensor. We fitted the peak to our theoretical model, finding an effective viscosity value of $\nu_{\text{eff}} = 2.5 \times 10^{-6} \text{ m}^2/\text{s}$, namely 2.5 times the viscosity value of water. The most likely cause for additional losses in the cavity is the non-ideality of the actuators, partially absorbing the acoustic energy of the reflected waves. Importantly, we have to highlight that, as long as the acoustic waves are strong enough, larger losses are useful for the functionality of the AOF device. Indeed, they grant shorter response time and broader resonant peaks, making the device faster and more robust against fabrication errors or noise sources.

4.1.3 Speed and tunability

The high-speed capabilities of the AOF system originate from the continuous operation at steady-state – the refractive index is continuously modulated at the same frequency of the acoustic wave. Thus, we only adjust the synchronization delay, which is solely limited by electronics, to achieve a sub-microsecond control of light. We investigated this remarkable property by recording the diffraction spots with a camera placed at the focal plane of a converging lens. Far-field characterization is convenient because it enables the study of each diffraction order isolated. More in detail, the optical characterization setup is shown in Figure 4.3a. We used a converging lens ($f_L = 400$ mm) to generate the far-field diffraction pattern that recorded at the lens focus with a CMOS camera (ThorLabs, DCC1545M). The light source was a 445 nm laser (Coherent CUBE 445-40C) that can be operated in either CW or pulsed mode. In the latter case, the laser was externally triggered, and a pulse delay generator (Stanford Research System, DG645) was used to control the delay time between laser pulses and the driving signal of the AOF device. The synchronized laser pulses have a duration (5 ns) much shorter than the AOF driving period. Thus, the acquired images are snapshots of the light interacting with the sound wave at a specific phase value. As shown in Figure 4.3b, changing the time delay Δt between pulses and the acoustic standing wave results in different distributions of Gaussian spots. Notably, the individual intensity of various diffraction orders – up to nine in this experiment — can be adjusted in a time scale of hundreds of nanoseconds. Such remarkable speed is well above the limits of most AODs, which use traveling acoustic waves and have a typical response time of microseconds, mainly limited by clear aperture and speed of sound [33, 34]. Notably, additional multi-focus distributions are accessible by tuning the frequency or amplitude of the driving signals. In this case, there is an inherent transition time until the acoustic standing wave reaches a new steady-state. The measured response time in water is about $600 \mu\text{s}$ (see Figure 4.2b), which corresponds to a frequency of approximately 1.7 kHz. This speed it is still significantly higher than most state-of-the-art active multi-beam generators. Notably, this is also the maximum

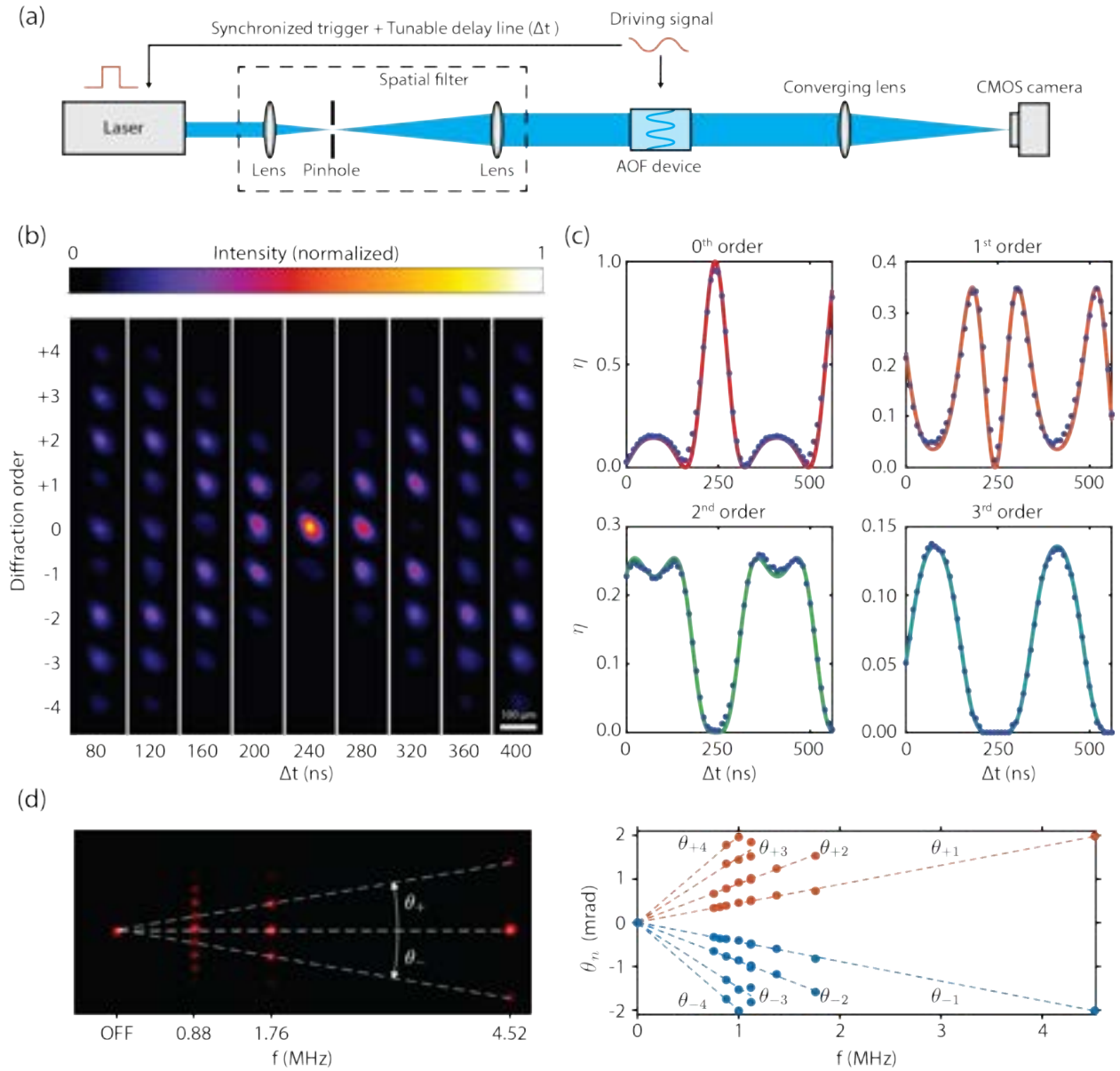


Figure 4.3: (a) Sketch of the time-resolved characterization setup. (b) Images of multi-focus distributions acquired with synchronized laser pulses at $V_{pp} = 20$ V and $f = 1.488$ MHz. The pulse duration was 5 ns while the delay between consecutive measurements was 10 ns. (c) Corresponding diffraction efficiency (blue dots) over time for the first four orders. Solid lines are fits to Equation 4.1. (d) Images of multi-focus distributions generated with a CW laser ($\lambda = 645$ nm) for various driving frequencies (left), and corresponding diffraction angles (right).

speed attainable with continuous-wave (CW) lasers or laser pulses longer than the AOF driving period. Indeed, the loss of any temporal dependency of the instantaneous refractive index – only an average acousto-optic interaction is detected in these instances – makes driving frequency or

voltage the only parameters available for modifying the diffraction pattern.

Generating diffraction patterns with the AOF device is not only fast but also predictable. Figure 4.3c displays the temporal evolution of the diffraction efficiency η_q for a single resonant frequency and four different values of q . Experimental results are in perfect agreement with the theoretical behavior described in the previous chapter. Similarly, adjusting the driving frequency produces multi-focus distributions at predictable spatial coordinates. As shown in Figure 4.3d, the angular spreading of the diffraction orders is symmetric and increases linearly with frequency. This behavior is in perfect agreement with Equation 4.2. Therefore, for a given focal length, the location of the diffraction orders can be precisely selected by tuning resonant frequency. In the focal plane of a lens with focal length f_L , the separation between two adjacent foci is

$$\Delta x = f_L \frac{\Omega_m \lambda}{2\pi c_s} \quad (4.3)$$

However, there is a frequency limit below which the separation between orders is too small to be resolved. This effect occurs if the lateral separation of diffraction orders is smaller than the beam width at the focal plane. Still, this scenario could be of interest for generating large spots with a customized intensity distribution.

The good agreement between experimental results and model allowed us to calculate the change in refractive index induced in the cavity. We fitted the data of figure 4.3c to equation 4.1, obtaining a value of $a = kl n_m$ of 3.49 ± 0.06 for $V_{pp} = 20$ V and $f = 1.488$ MHz. Knowing that $k = 1.412 \times 10^7 \text{ m}^{-1}$ (namely the wave number of the blue laser) and $l = (16 \pm 1)$ mm we obtained the maximum variation of refraction index of the liquid in the AOF cavity to be $n_m = \frac{a}{lk} = (1.5 \pm 0.1) \times 10^{-5}$. Using the Lorentz-Lorenz equation we can estimate that the variation of water density is $\rho_m \approx 0.04 \text{ kg/m}^3$, which can be converted into pressure variation making use of the equation of state $\Delta P = c_s^2 \Delta \rho$, thus obtaining $\Delta P \approx 90 \text{ kPa}$.

4.1.4 Role of the work parameters

A more in-depth experimental analysis of the different multi-focus distributions accessible when varying the main parameters, namely driving frequency, amplitude, and delay time is shown in Figure 4.4. As expected from theory, the separation between diffraction peaks increases with driving frequency (Figure 4.4a). Interestingly, the driving frequency also controls the diffraction efficiency of high order modes — the energy carried by higher modes decreases with this parameter. This effect can be explained considering the inverse relationship between the changes in refractive index induced in the liquid and the driving frequency, explained in detail in appendix F. Importantly, this effect can be compensated by increasing the amplitude V of the driving signal that results in a larger number of diffraction orders (Figure 4.4b). Note, though, that as more orders are present, conservation of energy causes the efficiency of every order to decrease. Such a trend can be broken by using synchronized pulsed illumination, as shown in Figure 4.4c. In this case, the time delay acts as an additional degree of freedom, and by adjusting this parameter, the efficiency of user-selected diffraction orders can be tuned.

The role of the different parameters can be properly described by using equation 4.1. Indeed, all the complex multi-focus distributions experimentally observed can be predicted with a single

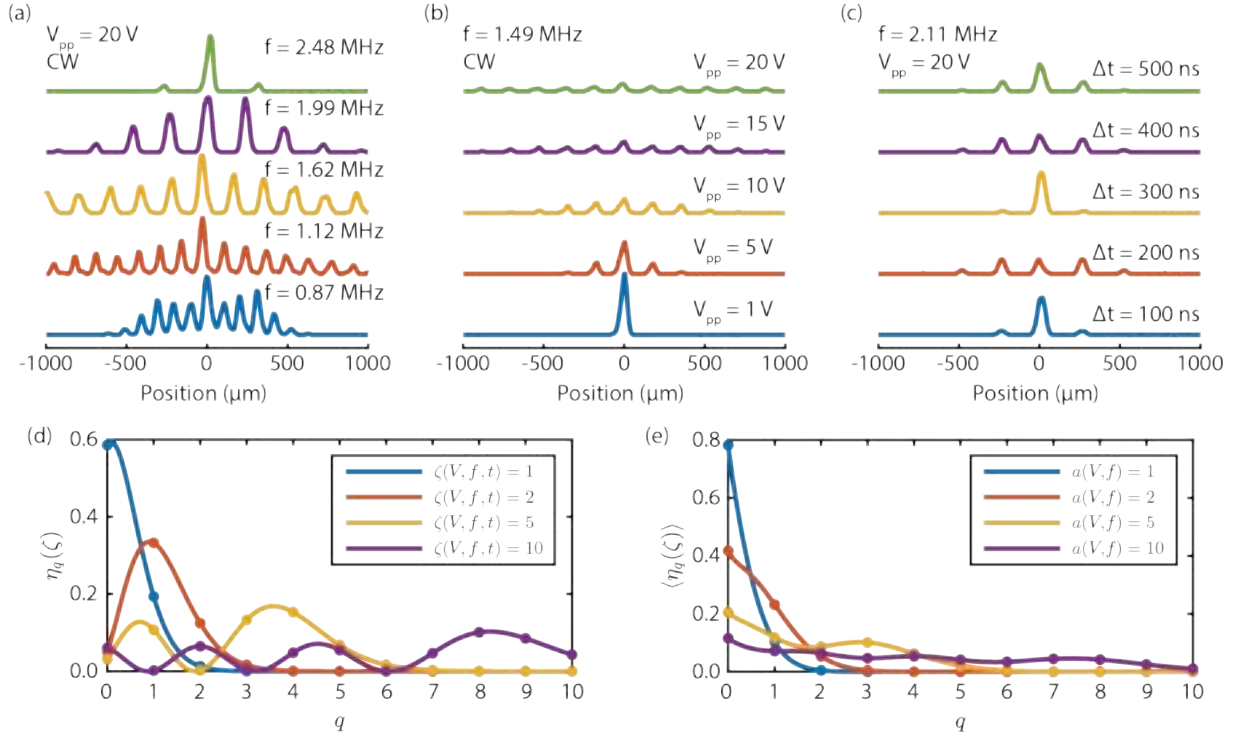


Figure 4.4: Experimental and computational study of the diffraction efficiency as a function of the main driving parameters: peak-to-peak Voltage V_{pp} , resonant frequency f and time delay Δt . (a) Intensity profiles at $V_{pp} = 20$ V across the peaks of multi-focus distributions obtained at different driving frequencies and using a CW laser as the illumination source. (b) Intensity profiles at $\nu = 1.49$ MHz, using a CW laser, and for different driving voltage amplitudes. (c) Intensities measured at $f = 2.11$ MHz, $V_{pp} = 20$ V, in synchronized mode, and at various time delays. All the experiments were performed using a blue laser ($\lambda = 445$ nm) as light source. (d) Simulated instantaneous diffraction efficiency for various arguments $\zeta = a \cos(\omega t)$ and diffraction orders q . (e) Simulated averaged diffraction efficiency with fixed $a = kLn_m$ (the integral mean of equation 4.1 over a period has been calculated numerically). In both plots the functions are presented as continuous just to guide the eye, but the physical relevant case is only when q is an integer.

variable, ζ , defined as the argument of the diffraction efficiency η_q

$$\zeta(V, f, t) = a(V, f) \cos(\Omega_m t) = kLn_m \cos(\Omega_m t). \quad (4.4)$$

Such functional dependency is graphically shown in Figures 4.4d and 4.4e. In all cases, only a finite number of diffraction orders possess a non-negligible amount of energy. The exact number depends on the driving voltage amplitude. For synchronized pulsed illumination, the efficiency of each order can be tailored, enabling higher diffraction orders to carry more energy than lower ones, even the zeroth. Instead, for CW illumination or when using laser pulses with a duration longer than the period of the driving oscillation, only an averaged efficiency can be attained. As a result, the diffraction efficiency decreases with the diffraction order. Interestingly, the spot distribution is also insensitive to the laser polarization that remains unaltered even after passing through the resonant cavity.

Indeed, the acoustic medium is pure water, which is well known to be homogeneous and isotropic. Therefore, no dependence on the polarization of the input beam is expected. To ensure this assumption, we performed two experiments. In the first one, we placed a half-wave plate on a rotatory mount before the AOF device to rotate the polarization angle of the incident laser. Figure 4.5a shows images of multi-spot distributions at a different angular position of the half-wave plate. As expected, shape, position, and the intensity of the diffraction pattern are not affected by the polarization of the incoming light. In the second experiment, we placed the AOF device between two crossed polarizers. When the AOF device is off, and because water does not alter the incoming polarization, only residual light is collected. We then switched on the AOF device and measured the new intensity collected after the polarizers. As shown in Figure 4.5b, the ratio of the measured intensity (AOF on versus AOF off) is constant for any angle θ of the polarizers. Therefore, the AOF device does not alter the polarization state of the incident light.

The two experiments confirm that the AOF device is a polarization-insensitive system. Given the important role that polarization plays in light-matter interactions [35–37], and with the advent of beam shapes exhibiting advanced polarization states [38] polarization insensitivity is a key feature of our AOF device.

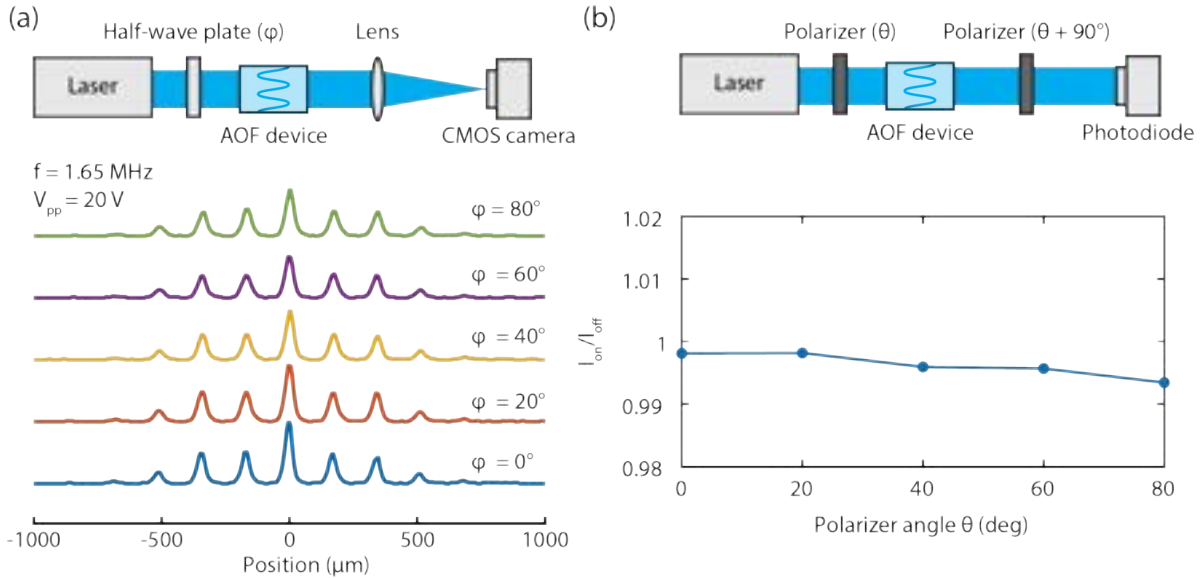


Figure 4.5: Experimental study of the polarization insensitivity of the AOF device. The diffraction patterns in (a) have been acquired with a different rotation angle φ of a half-wave plate placed before the AOF device. Note that the intensity distribution is not affected by the different polarization states of the incoming light. The setup shown in (b) consists of the AOF device placed between two crossed polarizers so that the detected intensity is at minimum. Any change in the polarization state of light induced by the AOF device would increase the measured intensity. However, the experimental results prove that the polarization state is unaltered when the device is turned on, confirming the polarization insensitivity of the AOF system.

4.2 Laser Direct Writing with the AOF device

4.2.1 Material processing setup

In order to demonstrate the potentialities of the AOF device, we integrated it into a laser direct-writing setup. It consists of a Ti:Sapphire amplifier (Coherent Legend, pulse duration = 70 fs, repetition rate = 1 kHz, $\lambda = 800$ nm), optical elements needed to guide the beam to objective lens (Mitutoyo M Plan Apo SL $50\times/0.75$ NA), and a fast XYZ stage (Prior Scientific, Inc.). The AOF device is placed at a conjugate plane of the back focal plane of the objective lens using a 4f system. We also integrated an upright bright-field microscope into the LDW system for direct inspection of the material modification. We controlled laser firing and stage motion by a computer using custom software written in LabView. To perform material processing in synchronized mode, we used the laser as the master and triggered the AOF device using the voltage generator in burst mode. In this way, the sound waves were generated after a controllable delay time, chosen greater than the time required for the cavity to reach the steady-state. Laser sources with longer pulses could be used in the described setup, but ultrashort pulses reduce heating effects on the samples and the acoustic cavity itself.

4.2.2 Multi-focus processing of materials

The simple integration of the AOF device in a laser direct-writing workstation enables modification of materials at high throughput. Figure 4.6a shows different ablated spots on a chromium thin film obtained by irradiation with the AOF-enabled system. The size, distance, or quantity of the ablated spots can be easily tuned by adjusting the driving conditions of the AOF device without the need for any mechanical motion of the sample. This represents a key advantage of our approach. The throughput of an LDW system can be increased by a factor that scales linearly with the number of diffracted foci.

Combining the tunability offered by acousto-optofluidics with sample translation enables writing complex structures. Notably, different processing modes can be distinguished based on the type of illumination or stage speed. With a pulsed laser and a scanning speed $v < Rw$ (where R is the laser repetition rate and w is the width of the ablated spot) and $v \ll fw$ (where f is the acoustic frequency), continuous lines can be generated (see Figure 4.6b). Because of the higher efficiency of the low diffraction orders, the lines become progressively thinner away from the center. Instead, operating with synchronized laser pulses enables generating structures in which the line width of each diffraction order can be tuned. The structures can be rendered continuous or discrete by simply adjusting the stage speed relative to the laser repetition rate. As a proof of concept, we used this patterning mode to locally modify the wetting properties of a target surface (see Figure 4.6c). We obtained a grid-like pattern on a glass sample by only selecting the first and second diffraction orders and scanning the multi-focus distribution along the x and y axis. As expected from Wenzel's model [39], the patterned surface exhibited an increase in roughness, and consequently, an enhancement of its wetting behavior—the patterned glass was transformed into a super-hydrophilic surface.

The capability of the AOF-enabled workstation for generating functionalized structures is

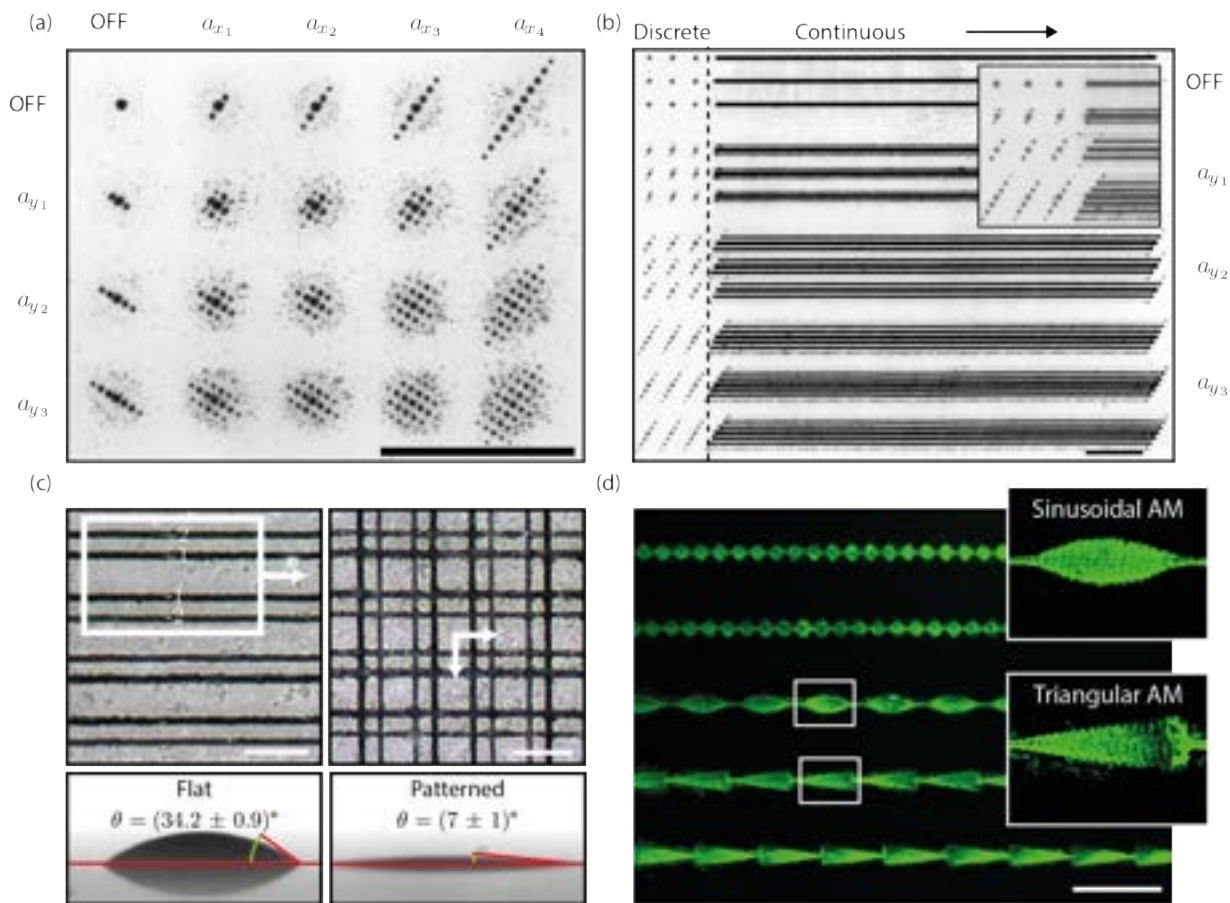


Figure 4.6: Materials processing with AOF-enabled LDW workstation. (a) Result of multi-focus laser ablation of chromium for different driving conditions. For each multi-focus distribution, 25 asynchronous laser pulses were fired. (b) Direct writing of lines on chromium with the AOF device on and the stage continuously moving. The stage speed was selected so that, at each position, multiple asynchronous laser pulses were shot. (c) Top-left: ablation of borosilicate glass using the AOF device with synchronized laser pulses. Note that the 0th order is missing, while the orders ± 1 and ± 2 generated lines of similar width. Top-right: scanning along the orthogonal direction resulted in a 2D grid. Bottom: contact angle measurements of water on a glass substrate before (left) and after laser patterning (right). (d) Wide-field fluorescence image of PDMS-coated glass after irradiation with the laser operated in brush-like mode and after wetting with an aqueous fluorescein solution. Only the irradiated parts are hydrophilic and fluorescent. White scale bars 10 μm . Black scale bars 50 μm .

shown in Figure 4.6d. In this case, we used a laser to locally remove a hydrophobic polymeric coating (polydimethylsiloxane or PDMS) from a glass substrate. As a result, only the laser-irradiated areas became hydrophilic. The different diffraction orders were merged by driving the AOF device with a low driving frequency and using a high laser fluence and asynchronous laser pulses. In other words, the laser beam acted as a brush, which thickness could be tuned by modulating the driving voltage amplitude. Therefore, laser beam scanning along one axis combined with sinusoidal or triangular modulation of the signal amplitude allows fabricating

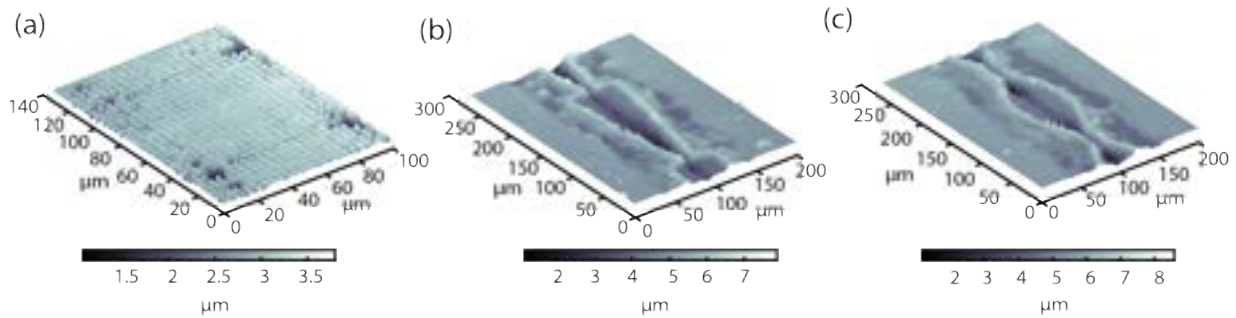


Figure 4.7: Morphological characterization of the ablated samples. Height maps of the glass (a) and PDMS substrates (b-c). The enhancement of surface roughness (a) justifies the increase in hydrophilicity of the glass, as predicted by Wenzel's model. The depth of the ablated patterns in (b-c) confirms that the thin PDMS layer is completely removed, leading to hydrophilic regions (glass) surrounded by hydrophobic surfaces.

significantly complex patterns at ease and at high-speed. Note that such a brush-like mode can lead to virtually any arbitrary pattern, with the only constraint to be symmetrical with respect to the scanning axis. After dropping a fluorescein-containing aqueous solution on the patterned surface and waiting for evaporation to occur, the domains exhibiting different wettability can be distinguished. As expected, only the laser-irradiated areas were fluorescent, proving the feasibility of AOF systems for writing complex and functional patterns.

To better quantify the quality of the fabricated patterns, we measured the ablation depth using an optical profiler. In this experiment, we coated the ablated samples with 15 nm of gold in order to increase the surface reflectivity and better investigate their morphology. Results of this study are shown in Figure 4.7. The surface modifications explain perfectly the change in the wettability discussed before.

4.2.3 Parallelized tailored writing

The efficiency of the AOF device is substantially insensitive to several properties of light such as polarization, wavelength, and incidence angle. This advantage makes the AOF inherently compatible with a large family of optical elements. In fact, the capabilities of the AOF device can be further expanded if used in combination with additional beam shaping tools. As a proof of principle, we used the far-field parallelization capabilities of our system to generate arrays of unconventional beams, such as Annular and Bessel beams. In Figure 4.8a we report the images of an asynchronous pattern of 9×11 Bessel beams, obtained entering the AOF device with an Annular beam which can be easily generated with an annular pinhole [2], an axicon [40], or a TAG lens [41]. Similarly, in Figure 4.8b we show the asynchronous image of a 9×13 Annular beams. We obtained this pattern entering the AOF with a Bessel beam, which can be generated with the same techniques named before. Interestingly, in the case of Annular beams, the individual rings partially overlap, enabling the generation of structures possessing a higher level of complexity than simple rings. In our experiments, we generated the Bessel and annular beams by illuminating an annular aperture (ThorLabs R1CA1000, external diameter 1 mm, internal diameter 0.85 mm)

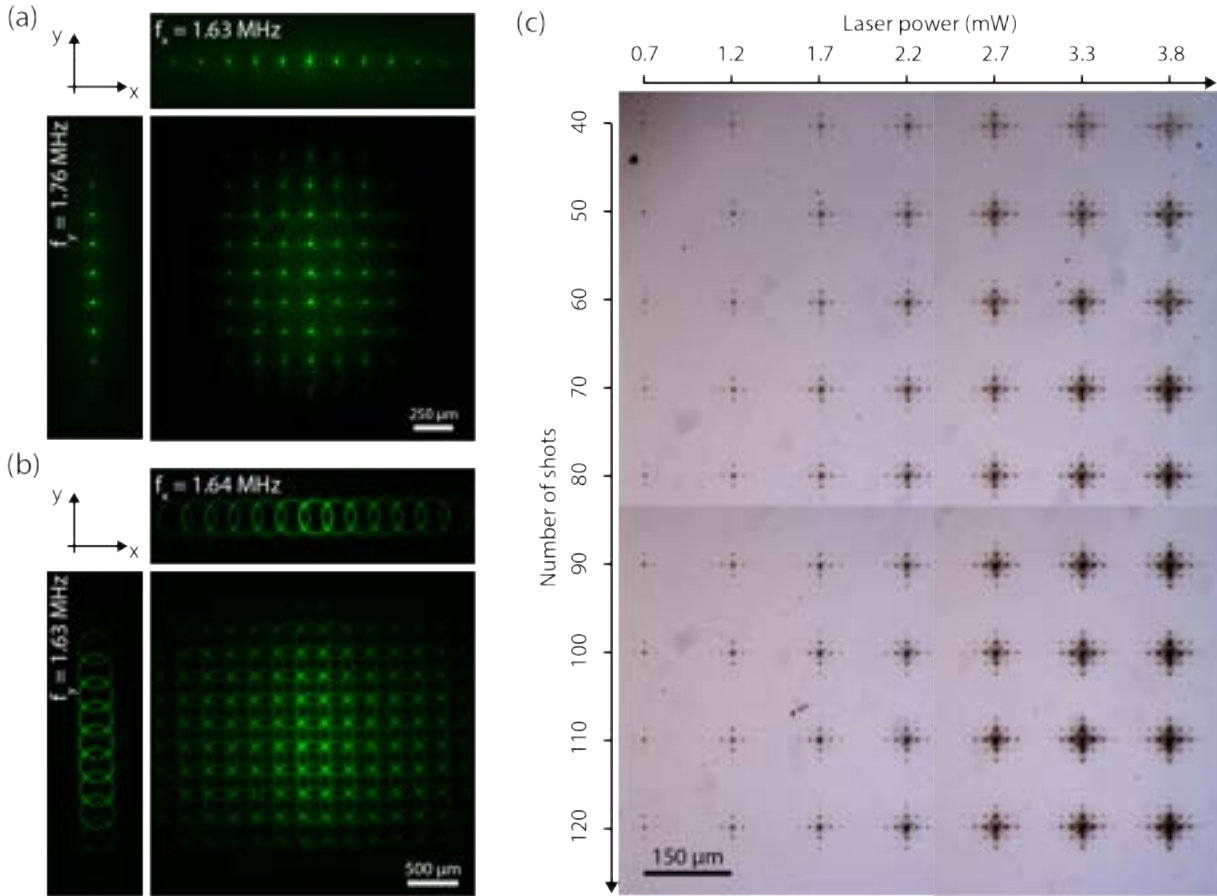


Figure 4.8: Parallelized beam shaping and application. 1D and 2D arrays of Bessel beams (a) and Annular beams (b) obtained in the far-field by entering the AOF device with an Annular beam and Bessel beam, respectively. (c) Ablation of Palladium using parallelized Bessel beams at different laser power and number of shots.

with a collimated Gaussian beam. We obtained the Bessel beams by optically conjugating the annular mask to the entrance of the AOF device with a 4f-system ($f_1 = 5$ cm and $f_2 = 20$ cm, $4\times$ magnification). Instead, we obtained the annular beams by entering the AOF device with the beam freely propagated (for 109 cm) after the annular aperture. In both cases, we recorded the far-field patterns at the focal plane of a converging lens ($f_L = 30$ cm) with a CMOS camera (ThorLabs, DCC1545M).

The combination of the speed and tunability of the AOF device with the capability to generate tailored light shapes enables writing complex shapes on virtually any substrate. This concept is demonstrated in Figure 4.8c, where we show the surface of a palladium substrate hosting complex patterns. Each of them was obtained without stage scanning, but simply structuring a femtosecond laser beam through a simple annular mask and the AOF device.

4.2.4 Sample preparation and characterization

We prepared metal surfaces by sputtering 200 nm of chromium on top of a glass substrate. We coated a glass surface with PDMS using the process known as dip coating. Specifically, we quickly rinsed a microscope slide into a solution of PDMS in heptane (5% v/v), creating a polymeric film with a thickness of approximately 500 nm. We measured the morphology of the ablated surfaces with a bright-field optical microscope (DM2500 M, Leica). In particular, we used a $10\times/0.25$ NA and a $50\times/0.75$ NA microscope objective lenses to acquire the images of the ablated patterns. We recorded the large field-of-view images of deposited fluorescein with a wide-field epifluorescence microscope (Nikon eclipse 80i) equipped with a $10\times/0.3$ NA objective lens (Plan Fluor, Nikon). The magnified images of the same sample were acquired with a $40\times/0.75$ NA microscope objective. We studied the wetting behavior of the laser-irradiated surfaces with an optical contact angle goniometer (Dataphysics OCA 15EC) by depositing $0.2\ \mu\text{L}$ of deionized water on top of the sample under test. In order to ensure good reliability, we repeated each measurement five times.

4.2.5 Considerations over the damage threshold

Possible damage or malfunctioning of the AOF system, due to the incident laser, ultimately depends on optical absorption, either linear or non-linear absorption. The former might cause heating of the filling fluid, whereas the latter might induce the generation of cavitation bubbles. Therefore, it is important to select filling fluids that weakly absorb the laser wavelength of interest. Water and silicon oil are good examples for operations with visible light. Heating effects are expected for laser pulses with a duration of ps and above (or fs pulses at MHz repetition rates). While a uniform temperature increase in the fluid will only cause a drift in the resonant frequency, something that can be corrected for with a feedback system, non-uniform heating will induce thermal gradients that can cause lensing effects. Therefore, when using high-power lasers, it is recommended to use lasers with a beam waist larger or comparable to the width of the AOF cavity. In these instances, the maximum laser power at which the device can correctly operate is limited by possible boiling of the liquid. The formation of cavitation bubbles poses a severe problem. Even if cavitation can occur with ps or ns pulses, this phenomenon is more likely to occur with ultra-short laser pulses. In these cases, the peak intensity at which the device can be operated depends on the conditions for cavitation bubble formation, which is about $100 \times 10^{11}\ \text{W}/\text{m}^2$ for 100 fs [42].

4.3 Conclusion

The variations in refractive index induced by ultrasound waves in a liquid-filled resonant cavity can be used to parallelize laser writing or generate tailored interference patterns for maskless lithography. Adjusting the sound parameters, namely frequency, amplitude, and phase, results in user-selectable patterns at high speeds, down to sub-microsecond time scales. This adds to the collection of degrees of control typically available in laser processing, thus providing, in a single

setup, an unrivaled combination of throughput, speed, and ease of use.

We anticipate that acousto-optofluidics will help to overcome the intrinsic trade-off between flexibility and throughput of laser-direct writing systems. As our results demonstrate, driving the cavity at moderate voltage amplitudes (below 20 V) complex patterns can be rapidly ablated on a surface. Further customization should also be possible by combining the AOF device with beam scanning systems, such as galvo mirrors, and driving it with multiple frequencies or off-resonance. The benefits of our innovation could be similarly extended to laser additive manufacturing, including laser induced forward transfer [43], laser sintering [44], or multi-photon polymerization [45]. Outside the manufacturing field, precise and fast light splitting can also have a key role in the realization of optical traps [46] or in beam multiplexing for fast microscopy [24]. Furthermore, by using higher driving amplitudes, novel acousto-optic interaction regimes could be explored, such as chaotic or subharmonic [47], paving the way to shaping the light with unprecedented spatiotemporal control.

References

- [1] Tow C. Chong, Minghui H. Hong, and Luping P. Shi. Laser precision engineering: From microfabrication to nanoprocessing. *Laser & Photonics Reviews*, 4(1):123–143, 2010.
- [2] Marti Duocastella and Craig B Arnold. Bessel and annular beams for materials processing. *Laser & Photonics Reviews*, 6(5):607–621, 2012.
- [3] R. Osellame, H. J.W.M. Hoekstra, G. Cerullo, and M. Pollnau. Femtosecond laser microstructuring: An enabling tool for optofluidic lab-on-chips. *Laser & Photonics Reviews*, 5(3):442–463, 2011.
- [4] Alberto Piqué, Raymond C.Y. Auyeung, Heungsoo Kim, Nicholas A. Charipar, and Scott A. Mathews. Laser 3D micro-manufacturing. *Journal of Physics D: Applied Physics*, 49(22), 2016.
- [5] R. Sahin, E. Simsek, and S. Akturk. Nanoscale patterning of graphene through femtosecond laser ablation. *Applied Physics Letters*, 104(5):053118, 2014.
- [6] Zhihong Nie and Eugenia Kumacheva. Patterning surfaces with functional polymers. *Nature Materials*, 7(4):277–290, apr 2008.
- [7] Trisha L. Andrew, Hsin-Yu Tsai, and Rajesh Menon. Confining Light to Deep Subwavelength Dimensions to Enable Optical Nanopatterning. *Science*, 324(5929):917–921, may 2009.
- [8] M. Campbell, D. N. Sharp, M. T. Harrison, R. G. Denning, and A. J. Turberfield. Fabrication of photonic crystals for the visible spectrum by holographic lithography. *Nature*, 404(6773):53–56, mar 2000.

- [9] Lars Müller-Meskamp, Yong Hyun Kim, Teja Roch, Simone Hofmann, Reinhard Scholz, Sebastian Eckardt, Karl Leo, and Andrés Fabián Lasagni. Efficiency Enhancement of Organic Solar Cells by Fabricating Periodic Surface Textures using Direct Laser Interference Patterning. *Advanced Materials*, 24(7):906–910, feb 2012.
- [10] Francesco Priolo, Tom Gregorkiewicz, Matteo Galli, and Thomas F. Krauss. Silicon nanostructures for photonics and photovoltaics. *Nature Nanotechnology*, 9(1):19–32, jan 2014.
- [11] Lóránd Kelemen, Sándor Valkai, and Pál Ormos. Parallel photopolymerisation with complex light patterns generated by diffractive optical elements. *Optics Express*, 15(22):14488, oct 2007.
- [12] Kanwar S. Nalwa, Joong-Mok Park, Kai-Ming Ho, and Sumit Chaudhary. On Realizing Higher Efficiency Polymer Solar Cells Using a Textured Substrate Platform. *Advanced Materials*, 23(1):112–116, jan 2011.
- [13] In-Yong Park, Sanghoon Ahn, Youngduk Kim, Han-Sung Bae, Hee-Shin Kang, Jason Yoo, and Jiwhan Noh. Serial number coding and decoding by laser interference direct patterning on the original product surface for anti-counterfeiting. *Optics Express*, 25(13):14644, jun 2017.
- [14] Lijun Wu, Yongchun Zhong, Che Ting Chan, Kam Sing Wong, and Guo Ping Wang. Fabrication of large area two- and three-dimensional polymer photonic crystals using single refracting prism holographic lithography. *Applied Physics Letters*, 86(24):241102, jun 2005.
- [15] Liang (Leon) Yuan and Peter R. Herman. Laser Scanning Holographic Lithography for Flexible 3D Fabrication of Multi-Scale Integrated Nano-structures and Optical Biosensors. *Scientific Reports*, 6(1):22294, apr 2016.
- [16] M. Vala and J. Homola. Multiple beam interference lithography: A tool for rapid fabrication of plasmonic arrays of arbitrary shaped nanomotifs. *Optics Express*, 24(14):15656, jul 2016.
- [17] Q. Xie, M.H. Hong, H.L. Tan, G.X. Chen, L.P. Shi, and T.C. Chong. Fabrication of nanostructures with laser interference lithography. *Journal of Alloys and Compounds*, 449(1-2):261–264, jan 2008.
- [18] Rajib Ahmed, Ali K Yetisen, Seok Hyun Yun, and Haider Butt. Color-selective holographic retroreflector array for sensing applications. *Light: Science & Applications*, 6(2):e16214–e16214, feb 2017.
- [19] Jolly Xavier, Martin Boguslawski, Patrick Rose, Joby Joseph, and Cornelia Denz. Reconfigurable Optically Induced Quasicrystallographic Three-Dimensional Complex Nonlinear Photonic Lattice Structures. *Advanced Materials*, 22(3):356–360, jan 2010.
- [20] Saraswati Behera, Manish Kumar, and Joby Joseph. Submicrometer photonic structure fabrication by phase spatial-light-modulator-based interference lithography. *Optics Letters*, 41(8):1893, apr 2016.

- [21] S. Surdo and M. Duocastella. Fast Acoustic Light Sculpting for On-demand Maskless Lithography. *Advanced Science*, 2019.
- [22] Yutaka Kuroiwa, Nobuhito Takeshima, Yoshihiro Narita, Shuhei Tanaka, and Kazuyuki Hirao. Arbitrary micropatterning method in femtosecond laser microprocessing using diffractive optical elements. *Optics Express*, 12(9):1908, 2004.
- [23] Y. Nakata, T. Okada, and M. Maeda. Lithographical laser ablation using femtosecond laser. *Applied Physics A: Materials Science and Processing*, 79(4-6):1481–1483, 2004.
- [24] Adrian Cheng, J. Tiago Gonçalves, Peyman Golshani, Katsushi Arisaka, and Carlos Portera-Cailliau. Simultaneous two-photon calcium imaging at different depths with spatiotemporal multiplexing. *Nature Methods*, 8(2):139–142, 2011.
- [25] M. A. Dugan, J. X. Tull, and W. S. Warren. High-resolution acousto-optic shaping of unamplified and amplified femtosecond laser pulses. *Journal of the Optical Society of America B*, 14(9):2348, 1997.
- [26] T. Häfner, J. Strauß, C. Roider, J. Heberle, and M. Schmidt. Tailored laser beam shaping for efficient and accurate microstructuring. *Applied Physics A*, 124(2):111, feb 2018.
- [27] Kotaro Obata, Jürgen Koch, Ulf Hinze, and Boris N. Chichkov. Multi-focus two-photon polymerization technique based on individually controlled phase modulation. *Optics Express*, 18(16):17193, 2010.
- [28] Bangshan Sun, Patrick S. Salter, Clemens Roider, Alexander Jesacher, Johannes Strauss, Johannes Heberle, Michael Schmidt, and Martin J. Booth. Four-dimensional light shaping: Manipulating ultrafast spatiotemporal foci in space and time. *Light: Science and Applications*, 7(1):17117, 2018.
- [29] Kunsik An, Sukjoon Hong, Seungyong Han, Hyungman Lee, Junyeob Yeo, and Seung Hwan Ko. Selective sintering of metal nanoparticle ink for maskless fabrication of an electrode micropattern using a spatially modulated laser beam by a digital micromirror device. *ACS Applied Materials and Interfaces*, 6(4):2786–2790, 2014.
- [30] Qiang Geng, Dien Wang, Pengfei Chen, and Shih Chi Chen. Ultrafast multi-focus 3-D nano-fabrication based on two-photon polymerization. *Nature Communications*, 10(1):1–7, 2019.
- [31] Alessandro Zunino, Salvatore Surdo, and Martí Duocastella. Dynamic Multifocus Laser Writing with Acousto-Optofluidics. *Advanced Materials Technologies*, 4(12):1–7, 2019.
- [32] Mariusz Lejman, Gwenaëlle Vaudel, Ingrid C. Infante, Ievgeniia Chaban, Thomas Pezeril, Mathieu Edely, Guillaume F. Nataf, Mael Guennou, Jens Kreisel, Vitalyi E. Gusev, Brahim Dkhil, and Pascal Ruello. Ultrafast acousto-optic mode conversion in optically birefringent ferroelectrics. *Nature Communications*, 7:1–10, 2016.

- [33] D. Maydan. Acoustooptical Pulse Modulators. *IEEE Journal of Quantum Electronics*, 6(2):15–24, jan 1970.
- [34] Richard V. Johnson. Temporal response of the acoustooptic modulator in the high scattering efficiency regime. *Applied Optics*, 18(6):903, mar 1979.
- [35] K. Venkatakrisnan, B. Tan, P. Stanley, and N. R. Sivakumar. The effect of polarization on ultrashort pulsed laser ablation of thin metal films. *Journal of Applied Physics*, 92(3):1604–1607, 2002.
- [36] S. Höhm, A. Rosenfeld, J. Krüger, and J. Bonse. Femtosecond laser-induced periodic surface structures on silica. *Journal of Applied Physics*, 112(1):014901, jul 2012.
- [37] Peter Gregorčič, Marko Sedlaček, Bojan Podgornik, and Jürgen Reif. Formation of laser-induced periodic surface structures (LIPSS) on tool steel by multiple picosecond laser pulses of different polarizations. *Applied Surface Science*, 387:698–706, 2016.
- [38] Halina Rubinsztein-Dunlop, Andrew Forbes, M V Berry, M R Dennis, David L Andrews, Masud Mansuripur, Cornelia Denz, Christina Alpmann, Peter Banzer, Thomas Bauer, Ebrahim Karimi, Lorenzo Marrucci, Miles Padgett, Monika Ritsch-Marte, Natalia M Litchinitser, Nicholas P Bigelow, C Rosales-Guzmán, A Belmonte, J P Torres, Tyler W Neely, Mark Baker, Reuven Gordon, Alexander B Stilgoe, Jacqueline Romero, Andrew G White, Robert Fickler, Alan E Willner, Guodong Xie, Benjamin McMorran, and Andrew M Weiner. Roadmap on structured light. *Journal of Optics*, 19(1):013001, jan 2017.
- [39] Robert N Wenzel. Resistance of solid surfaces to wetting by water. *Industrial & Engineering Chemistry*, 28(8):988–994, aug 1936.
- [40] Zhi Luo, Kai Yin, Xinran Dong, and Ji’an Duan. Optimal condition for employing an axicon-generated Bessel beam to fabricate cylindrical microlens arrays. *Journal of Physics D: Applied Physics*, 51(18):185104, may 2018.
- [41] Euan McLeod and Craig B Arnold. Optical analysis of time-averaged multiscale Bessel beams generated by a tunable acoustic gradient index of refraction lens. *Appl Opt*, 47(20):3609–3618, 2008.
- [42] A. Vogel, J. Noack, K. Nahen, D. Theisen, S. Busch, U. Parlitz, D. X. Hammer, G. D. Noojin, B. A. Rockwell, and R. Birngruber. Energy balance of optical breakdown in water at nanosecond to femtosecond time scales. *Applied Physics B: Lasers and Optics*, 68(2):271–280, 1999.
- [43] Salvatore Surdo, Alberto Diaspro, and Martí Duocastella. Microlens fabrication by replica molding of frozen laser-printed droplets. *Applied Surface Science*, 418:554–558, 2017.
- [44] Sukjoon Hong, Junyeob Yeo, Gunho Kim, Dongkyu Kim, Habeom Hyungman Habeom Lee, Jinhyeong Kwon, Habeom Hyungman Habeom Lee, Phillip Lee, and Seung Hwan Ko.

Nonvacuum , Maskless Fabrication of a Flexible Metal Grid Transparent Conductor by Low-Temperature Selective Laser Sintering of Nanoparticle Ink. *ACS Nano*, 7(6):5024–5031, 2013.

- [45] Joachim Fischer and Martin Wegener. Three-dimensional optical laser lithography beyond the diffraction limit. *Laser & Photonics Reviews*, 7(1):22–44, jan 2013.
- [46] Dimitris Trypogeorgos, Tiffany Harte, Alexis Bonnin, and Christopher Foot. Precise shaping of laser light by an acousto-optic deflector. *Optics Express*, 21(21):8619–8625, 2013.
- [47] John H. Cantrell, Laszlo Adler, and William T. Yost. Subharmonic generation, chaos, and subharmonic resurrection in an acoustically driven fluid-filled cavity. *Chaos*, 25(2):023115, 2015.

5

Multiplane Encoded Light-Sheet Microscopy

One of the main goals of optical microscopy is retrieving quantitative and volumetric information while minimizing sample photodamage. This requires three-dimensional (3D) imaging techniques with high spatio-temporal resolution and optical sectioning capabilities. Among the existing techniques, Light-sheet Fluorescence Microscopy (LSFM) has become the tool of choice for volumetric imaging of large samples [1], offering a unique combination of speed, Field-of-View (FoV), and spatial resolution [2]. In LSFM, the sample is illuminated with a light-sheet [3] – a thin (along the z-axis) and wide (in the x-y plane) beam of light – produced by a cylindrical lens or a rapidly scanning Gaussian, Bessel, or Airy beam [4–6]. An objective lens, mounted orthogonally to the illumination plane, collects the fluorescent light, and the corresponding image is recorded with a camera [7]. The combination of a wide-field acquisition scheme with shaped illumination allows fast optical sectioning over a large FoV, at diffraction-limited resolution while using low light doses. Unfortunately, traditional architectures are not optimized for fast 3D imaging. Typically, volumetric imaging in LSFM is performed by acquiring a sequence of 2D images from different focal planes of the sample, the so-called z-stack. Since the light-sheet and the focal plane of the detection lens must coincide to avoid blurring or image artifacts, collection of a z-stack is obtained either by sample translation or synchronized movement of light-sheet and objective lens. In both cases, a slow mechanical movement is needed, constraining the maximum acquisition rate. In order to overcome this limitation, various innovative LSFM architectures have been proposed. For instance, remote focusing detection enables axial scanning at high rates without introducing significant aberrations [8, 9]. While offering substantial speed advantages, its practical usage is hindered by the complexity of setup and alignment procedures. The combination of a light field camera – which exploits an array of micro-lenses to distinguish the axial origin of the light – with a thick light-sheet can be used to retrieve information of a whole volume from a single frame [10, 11]. However, the reconstruction algorithm needed for this solution is computationally demanding, and the resulting images typically have a heavily degraded lateral resolution. Another

possibility is to acquire fewer frames per stack and reconstruct the volume using a compressed sensing algorithm, thus reducing the total acquisition time [12]. Still, this strategy offers only a limited speed improvement and it is likely to generate artifacts when the sample is not sparse. Alternatively, it is possible to extend the Depth-of-Field (DoF) of the detection objective. With this approach, all the sample planes appear in focus, and the images can be acquired by only moving the light-sheet, with no need for mechanical synchronization. Notably, translation of the light-sheet can be performed in a few milliseconds, greatly increasing imaging speed. Several techniques exist for generating an Extended Depth-of-Field (EDoF), including the use of spherical aberrations [13], wavefront coding [14, 15], and varifocal lenses [16–18].

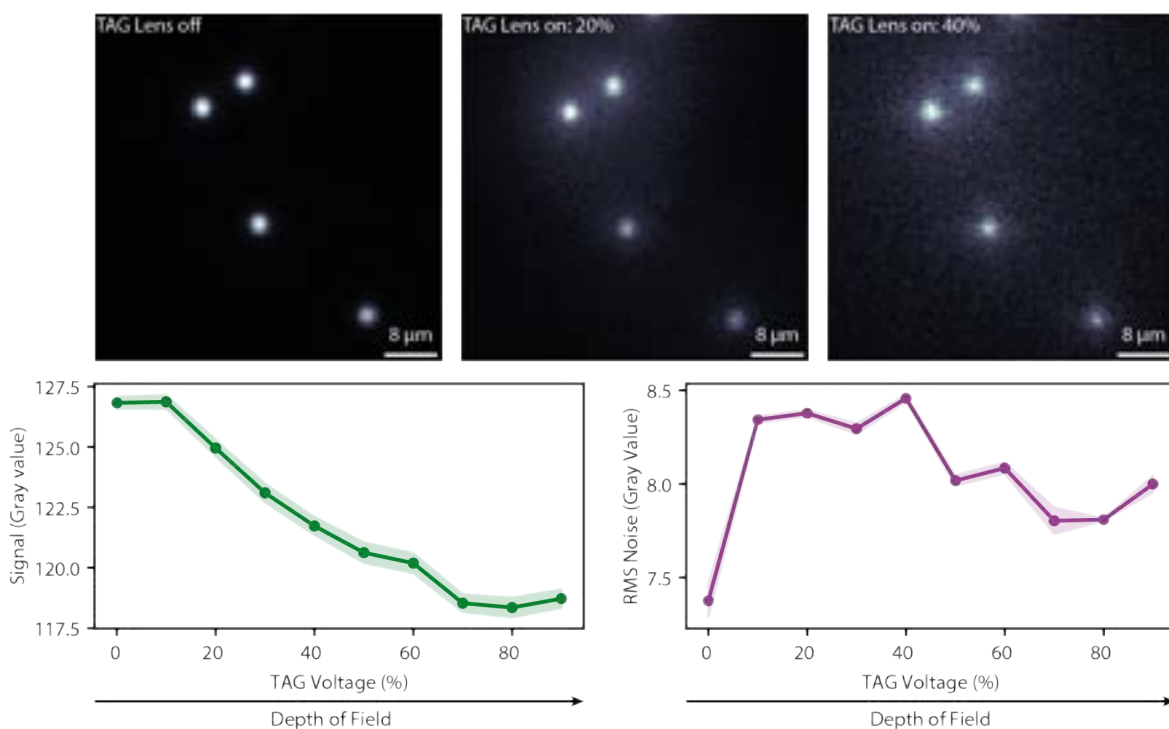


Figure 5.1: Images of 1 μm beads fluorescent beads acquired with a $10\times/0.3\text{NA}$ objective lens. From left to the right the driving voltage of the TAG lens is increasing with a corresponding increase of the DoF, but also a deterioration of the SNR of the images.

Unfortunately, EDoF techniques can produce a significant loss of photons per plane. We demonstrate this effect in Figure 5.1, where we increase the driving voltage of the TAG Lens, proportional to the DoF. As a result, the signal per plane is reduced and the noise level is increased. Thus, the acquired z-stack exhibits a degraded Signal-to-Noise Ratio (SNR). Other DoF extending techniques share the same issue [19].

A straightforward solution for this problem is to increase the excitation intensity. While the high power of current lasers enables this implementation in almost any EDoF light-sheet system, this approach faces two major drawbacks. First, the fluorophores response is non-linear and, above their saturation threshold, no additional fluorescence signal is gained from increasing illumination

levels [20], as depicted in Figure 5.2. Second, and more importantly, the higher the peak intensity, the greater the risk of photodamaging the sample – an enormous detriment for live microscopy. To prevent phototoxicity and gain SNR, increasing the exposure time of the images while keeping the illumination levels low is preferable [21, 22]. However, this irremediably comes at the cost of sacrificing acquisition speed.

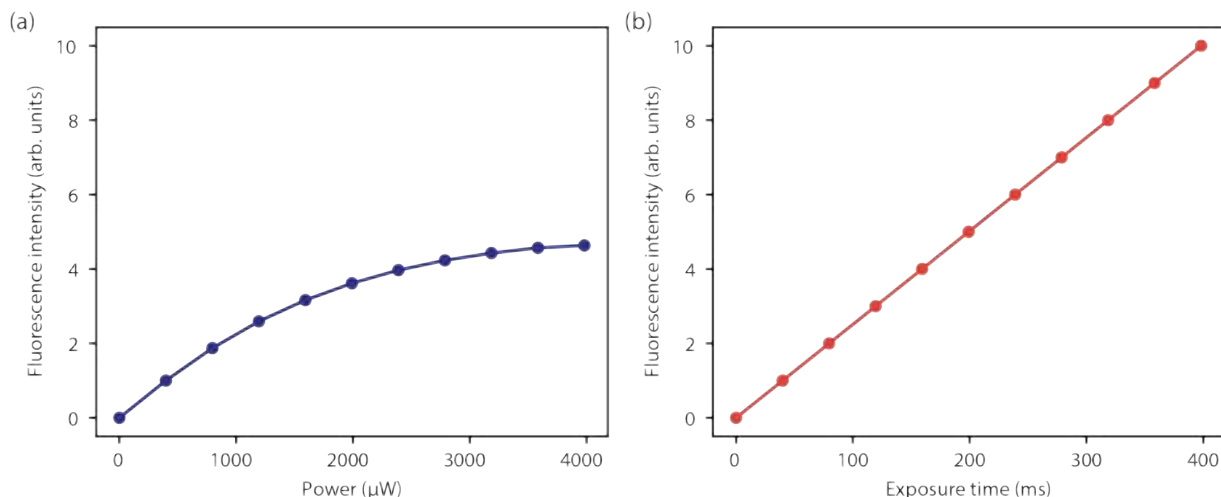


Figure 5.2: (a) Measured fluorescence intensity of fluorescein embedded in agar gel, seen as a function of the excitation power. Fluorescence tends to saturate at high excitation power. (b) Fluorescence intensity seen as a function of the exposure time. If the used laser power is low enough to prevent photobleaching, the trend is linear.

An alternative solution is parallelizing the illumination to increase the information captured per frame. In this case, several planes are simultaneously illuminated, thus the exposure time of individual planes can be increased without loss of acquisition speed. Although a common practice in laser scanning microscopy, such a multiplexing strategy remains difficult to implement in LSFM. Recent attempts include multibeam interference [23] and arrays of incoherent and frequency-modulated light-sheets [24], but they can be limited by the speed of spatial light modulators or require instrument-specific components not commercially available. So far, a light-sheet parallelization method that obviates mechanical moving parts and rapidly produces enhanced SNR volumetric images has not been reported. Here, we propose a novel and straightforward technique that fills this void and produces images with enhanced signal-to-noise/background ratio in EDoF Light-Sheet microscopes. It is named Multi-plane Encoded Light-sheet Microscopy (MELM) and is based on illuminating a sample with encoded sequences of simultaneous multiple light-sheets [25, 26]. As shown in Figure 5.3a, each sequence contains information from multiple planes. The sum of the corresponding images is collected in a single camera frame. By acquiring different frames – as many as sample sections desired to capture – images from individual planes can be decoded using a computationally inexpensive single-step reconstruction algorithm. Notably, the decoded images exhibit enhanced SNR depending on the illumination sequence used. Additionally, volumetric acquisition can occur at the same rate as in standard EDoF-LSFM, thus preserving the core advantages of this technique in terms of speed and ease of implementation.

In this manuscript, we provide a full theoretical framework to describe our method. Supported by numerical simulations, we demonstrate the feasibility of our instrument, and we quantify the gain in SNR with imaging experiments using fluorescent beads and biological samples.

5.1 Working principle of MELM

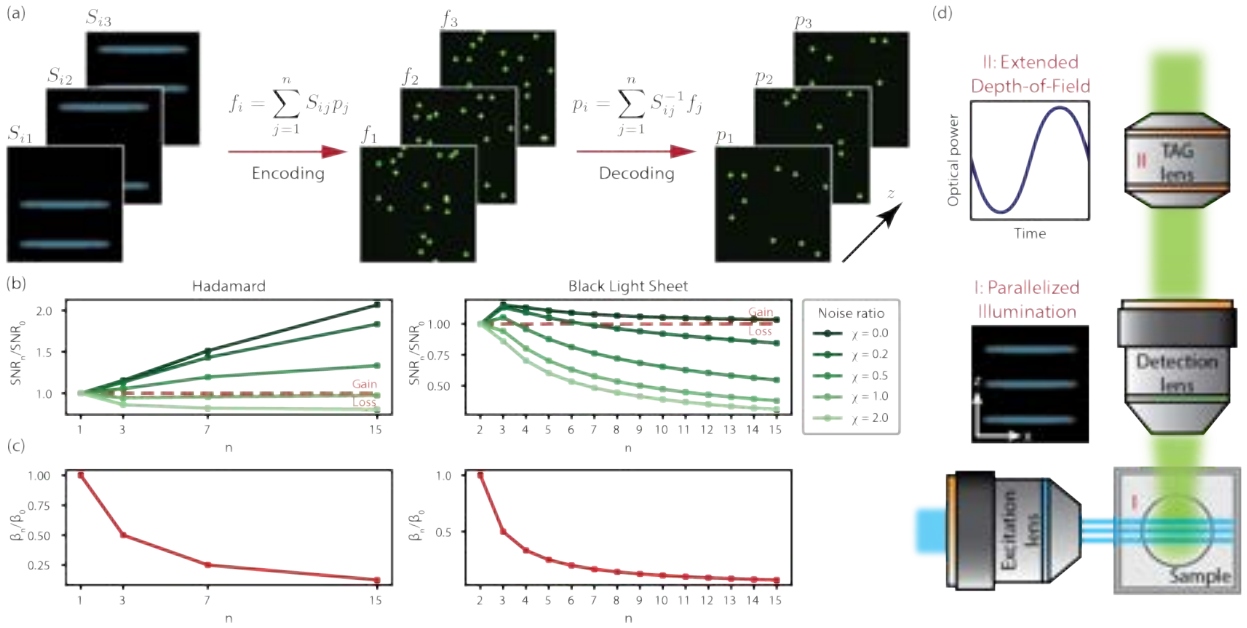


Figure 5.3: (a) Working principle of Multiplane Encoded Light-sheet Microscopy. A set S_{ij} of parallel light-sheets is shined on the sample, illuminating at the same time multiple planes P_j whose superposed images are collected as the frame F_i . In order to retrieve the individual images, it is simply needed to calculate the inverse of the encoding sequence S_{ij}^{-1} . (b) SNR of the decoded images acquired with the Hadamard encoding (left) and Black Light-sheet encoding (right), seen as functions of the number of acquired frames. Both plots are normalized by the SNR of a sequential scan. (c) Background of the decoded images acquired with the Hadamard encoding (left) and Black Light-sheet encoding (right), seen as functions of the number of acquired frames. Both plots are normalized by the background level of a sequential scan. (d) Scheme of the acquisition system. All the illuminated planes are acquired simultaneously thanks to a fast axial scan performed by a TAG lens.

The fundamental hypothesis of MELM is that parallelized illumination using tailored light sequences can enhance the SNR in EDoF-LSFM. Mathematically, we can describe such a process as follows. Let \mathbf{p} be the $1 \times n$ array of images composing the full z -stack, and \mathbf{f} be the $1 \times n$ array of acquired camera frames. Then, we can write the acquisition process as

$$f_i = \sum_{j=1}^n S_{ij} p_j + e_i \quad (5.1)$$

where S_{ij} is a coefficient whose value is 1 when the plane p_j is illuminated by a light-sheet and 0 when not, and e_i is the noise [27]. The above equation can also be represented using the following matrix form

$$\mathbf{f} = \mathbf{S}\mathbf{p} + \mathbf{e} \quad (5.2)$$

here, \mathbf{S} is a $n \times n$ matrix whose rows describe the encoding sequences of on/off light-sheets for each frame. If \mathbf{S} is invertible and well-conditioned, we can find an estimate of the images \mathbf{p} directly inverting the previous equation

$$\hat{\mathbf{p}} = \mathbf{S}^{-1}\mathbf{f} = \mathbf{p} + \mathbf{S}^{-1}\mathbf{e} \quad (5.3)$$

Notably, MELM enables decoding n planes p_j from n frames f_j , whose noise content is now $\mathbf{S}^{-1}\mathbf{e}$ instead of \mathbf{e} . To make this transformation advantageous, the signal-independent noise must be shared among multiple illuminated planes. Consequently, the larger the number of simultaneously acquired planes, the lesser the noise per plane. However, the decoding step needed to retrieve information from each plane can return some noise to the images. The amount of added noise depends on the encoding matrix. Therefore, the choice of \mathbf{S} is crucial in determining the SNR of the decoded images. To illustrate this effect, we used three different illumination patterns, each one represented by a unique matrix.

1. **Sequential scan.** This corresponds to the traditional implementation of LSFM, in which a single light-sheet illuminates a single plane, and it is moved to a different axial position at each frame. In this case, the encoding matrix is the identity \mathbf{I} . Consequently, $\mathbf{S}^{-1} = \mathbf{I} = \mathbf{S}$ and the noise content is unchanged. This non-parallelized acquisition scheme is used as a benchmark for the following multi-plane schemes.
2. **Black Light-sheet.** As its name indicates, it is based on using $n - 1$ parallel and identical light-sheets to simultaneously illuminate a volume divided into n sections. In other words, all planes within a volume are illuminated except for one. The axial position of the dark plane is changed after each frame. The corresponding matrix \mathbf{S} contains zeros on the main diagonal and ones everywhere else. The expected gain in SNR for an image in the z-stack is:

$$\frac{\text{SNR}_n}{\text{SNR}_0} = \sqrt{\frac{1 + \chi^2}{1 + (n - 1)\chi^2}} \frac{(n - 1)}{\sqrt{(n^2 - 3n + 3)}} \quad (5.4)$$

where χ is the ratio of the standard deviation of the photon noise to the standard deviation of the camera noise of each plane [28], and SNR_0 is the SNR of the image acquired using a sequential scheme with the same exposure time and peak intensity per light-sheet (the full derivation is available in appendix H). The parameter χ depends on several variables, such as detector type, brightness of the sample, and exposure time. In fast imaging experiments, the last variable is expected to be low, resulting in a small number of collected photons and, correspondingly, a low value of χ .

3. **Hadamard scan.** A volume, divided into n planes, is simultaneously illuminated by $(n + 1)/2$ identical light-sheets. At each frame, the axial positions of the light-sheets are changed accordingly to the rows of the Hadamard matrix \mathcal{S} [29]. In this case, the expected SNR gain is

$$\frac{\text{SNR}_n}{\text{SNR}_0} = \sqrt{\frac{1 + \chi^2}{1 + \frac{n+1}{2}\chi^2}} \frac{n+1}{2\sqrt{n}} \quad (5.5)$$

which also depends on the parameter χ . Note that Hadamard matrices are defined only for $n = 2^k - 1$, with $k > 1$ and integer, differently than Black Light-sheet matrices that can be defined for every natural number n (see appendix H).

Figures 5.3b and shows plots of the SNR enhancement for the Black Light-sheet and Hadamard encoding strategies as a function of the number of illuminated planes and photon noise. As expected, when the photon noise is negligible, both cases provide a gain in SNR over the traditional sequential scan. Such a gain increases with the number of planes for the Hadamard case – it scales as $\frac{\sqrt{n}}{2}$. Instead, when using the Black Light-sheet encoding, the SNR is maximized when 3 planes are illuminated and then asymptotically approaches the same value as the sequential scan. As the photon noise content increases, both cases exhibit a reduction of the SNR advantage. However, the two methods have a different tolerance to photon noise, with the Hadamard scan preserving its benefits for higher values of χ than the Black Light-sheet. These observations are valid assuming the detector is capable of collecting the additional light coming from all the illuminated planes. In other words, the dynamic range of the camera must be sufficient to gather all this information. Given that parallelization is useful to improve the SNR of images when the signal is low, this assumption is valid in the vast majority of practical situations in fluorescence bioimaging. Microscopy images are not only affected by noise, but they typically suffer from the presence of background. This latter is originated from various contributions such as out-of-focus fluorescence (signal-dependent background) or detector dark current and environmental light (signal-independent background). EDoF-LSFM inherently rejects the first type of background but can still suffer from the signal-independent contributions that we define as β . The parallelization of MELM also enables reducing this value, thus increasing the contrast of the reconstructed images. In particular, the expected background reduction with the Black Light-sheet encoding is

$$\frac{\beta_n}{\beta_0} = \frac{1}{n-1} \quad (5.6)$$

where β_0 is the background of the image acquired using the sequential scan. In the case of Hadamard scan, such a reduction can be written as

$$\frac{\beta_n}{\beta_0} = \frac{2}{n+1} \quad (5.7)$$

As shown in Figure 5.3c, both encoding methods enable reducing the background with respect to the sequential scan. In addition, such a reduction increases with the number of illuminated planes.

However, the Black Light-sheet approach has a better performance in background suppression. Therefore, while the Hadamard scan provides the best SNR gain of the strategies analyzed, the Black Light-sheet can be preferable when a strong background is present. Note that it is always possible to choose and tune the optimal encoding method that best suits the target application or sample.

5.2 MELM implementation

MELM can be implemented in any traditional or inverted light-sheet microscope, with two key modifications depicted in Figure 5.3d. First, incorporating a method for generating an array of parallel and identical light-sheets that can be individually switched on and off. Second, applying a technique to extend the DoF of the detection objective lens. In our microscope, presented in Figure 5.4a, we use a pair of AODs, optically conjugated in a 4f system, to generate multiple light-sheets. The first AOD – driven with a sinusoid which frequency is modulated by a triangular function – periodically deflects a Gaussian beam along the y-axis, thus generating a light-sheet when watched at the frame speed of the camera detector [30]. This approach, compared to the more traditional cylindrical lens, allows confining the illumination to a region of interest, thus optimizing the photon budget [31]. We use the second AOD to generate the encoded illumination sequences. To this end, we drive it with multiple sine waves V_i while collecting the superpositioned frames f_i :

$$V_i(t) \propto \sum_{j=1}^n S_{ij} \sin(\Omega_{ij}t) \quad (5.8)$$

The amplitudes S_{ij} are exactly the entries of the encoding matrix S and each acoustic frequency Ω_{ij} diffracts the light to a different axial position [32], thus obtaining a stack of parallel light-sheets illuminating the planes p_j only if $S_{ij} = 1$. As shown in Figure 5.4b, the illumination pattern produced with this technique shows good uniformity along the y-axis and the intensity of each beam is the same. Notably, the good uniformity of the frequency response of the AOD and the linearity of its control system granted the desired uniformity without the need of any additional correction. Other light-sheet parallelization techniques have already been proposed [33, 34], but acousto-optic light sculpting enables the fastest switch between an illumination pattern and the following one [35], which is key for preserving the speed of LSFM. In particular, in our current implementation, we can switch between two patterns within 5 ms. This value does not depend on the number of produced beams, thus in principle, it is possible to reach any amount of parallelization without sacrificing speed. Importantly, this value could be significantly decreased by implementing an optimized control system, and thus it does not represent an inherent limitation of the technique. Indeed, the generation of the light-sheets in principle is limited only by the access time of the deflectors [35].

MELM can be implemented with any DoF extending method. In our system, we conjugated the back focal plane of the detection objective lens with a varifocal lens [36]. Specifically, we used a TAG lens (described in detail in appendix G) that rapidly scans the object plane along the optical

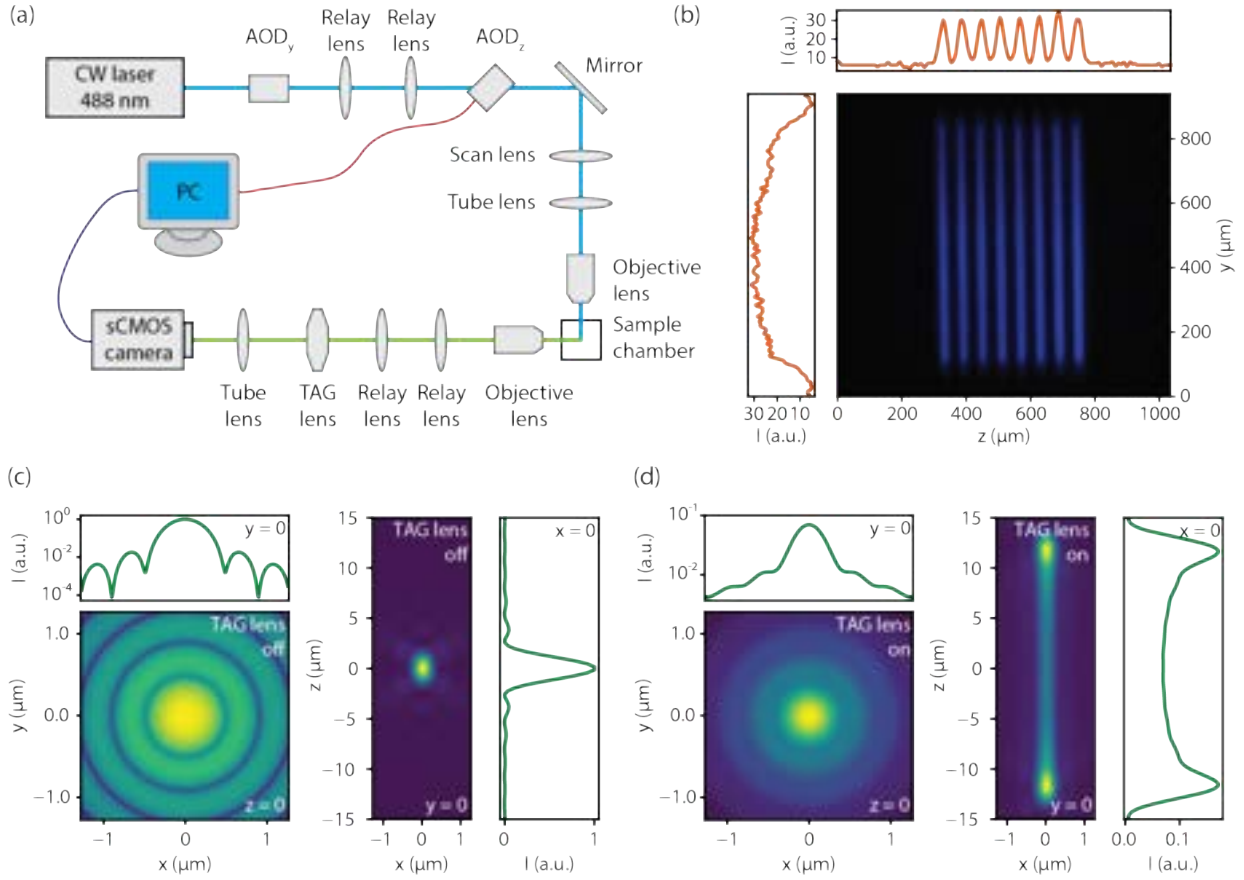


Figure 5.4: (a) Sketch of the experimental setup. The blue line defines the excitation arm, and the green line defines the detection arm. (b) Experimental image of light-sheets taken at the focal plane of the scan lens. On top, the intensity profile along the z -axis shows that the light-sheets have comparable intensity. On the left, the intensity profile along the y -axis shows a good longitudinal homogeneity. (c) Native PSF of the detection objective lens ($40\times/0.8\text{ NA}$) calculated with the Born & Wolf model. The image of the xy plane at $z = 0$ and the corresponding intensity profile are in a logarithmic scale. The DoF, defined as the FWHM along the z -axis, is $1.5\ \mu\text{m}$ (d) Extended PSF, obtained by scanning the native PSF along the z -axis with the TAG lens. In this example, the DoF extension is about $25\ \mu\text{m}$, but it can be tuned by applying a different voltage drive to the TAG lens. The intensity scale is the same as in (c). It can be seen that the lateral width is preserved, but the intensity per plane is reduced.

axis [37]. If the camera exposure time is greater than the period $T = 2\pi/\Omega$ of the axial scan (typically in the order of tens of microseconds), a dynamic and tunable EDoF is obtained. The resulting detection Point Spread Function (PSF) of the microscope is

$$h_e(x, y, z) = \frac{1}{T} \int_0^T h_o(x, y, z - \Delta z \cos(\Omega t)) dt \quad (5.9)$$

where h_o is the native detection PSF of the system, and Δz is half of the scanning range. Importantly, Δz can be tailored by changing the driving parameters of the TAG lens, namely the

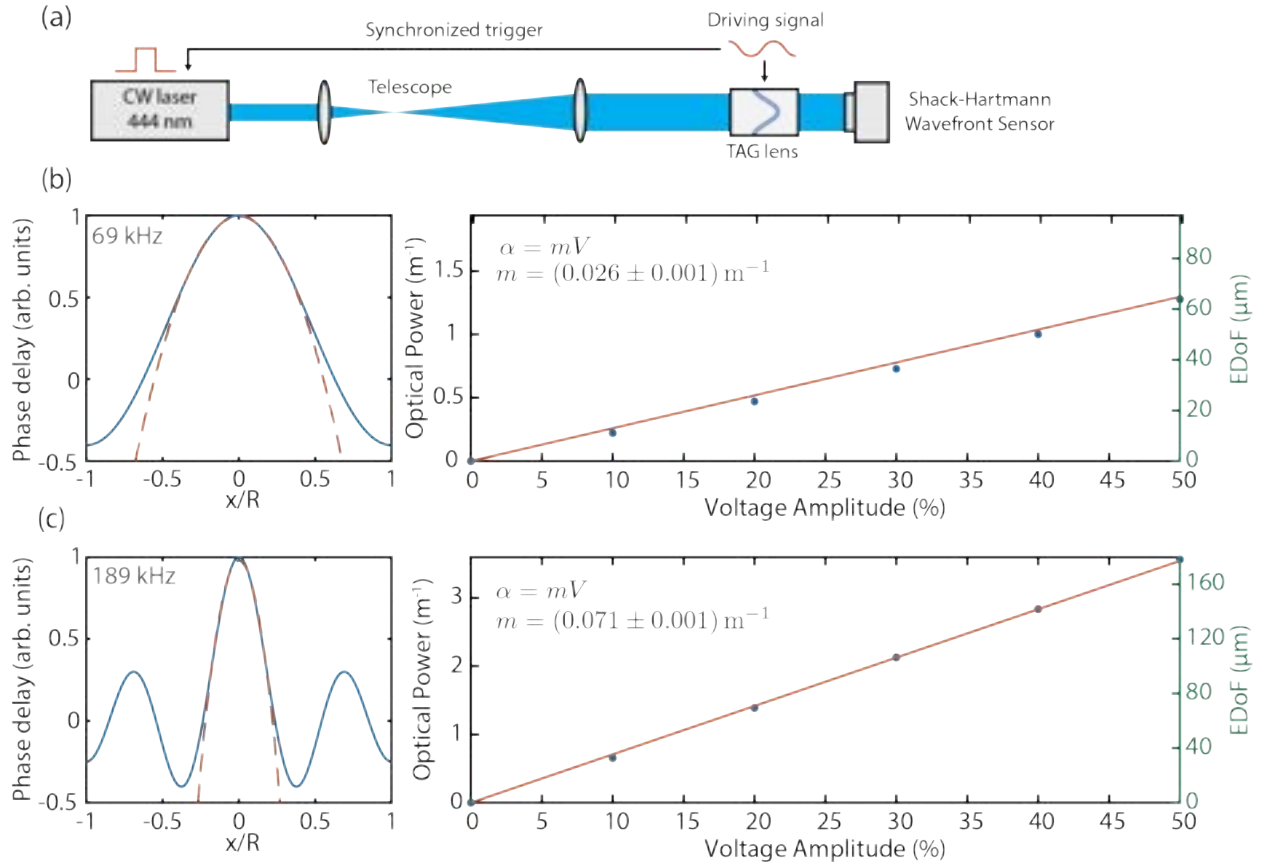


Figure 5.5: (a) Scheme of the TAG lens calibration setup. (b) Left: Spatial profile of the phase profile induced by the TAG lens at the resonant frequency of 69 kHz. The orange dashed line shows the parabolic approximation. The horizontal axis is normalized to the radius R of the lens. Right: calibration curve of the optical power versus the driving voltage amplitude. The horizontal axis is normalized to the maximum voltage the driving kit can provide. (c) Phase profile and calibration curve of the TAG lens at 189 kHz. The corresponding EDoF is calculated assuming the focal length of the detection objective lens to be 5 mm.

frequency and the voltage amplitude as shown in Figure 5.5. The resulting time-averaged PSF, shown in Figures 5.4c and 5.4d, is elongated along the optical axis while preserving its width in the xy plane. However, the out-of-focus contributions of the axially scanned PSF produce a lateral broadening of the tails of the extended PSF, resulting in additional fluorescent background. In order to restore the diffraction-limited images, a deconvolution step is needed, as it typically happens with all EDoF techniques. Since the lateral shape of extended PSF does not depend on the axial coordinate, it is possible to perform a simple 2D plane-by-plane deconvolution. This advantage significantly lowers the computational cost of the post-processing step compared to other DoF extending methods. Figure 5.4d also shows how the average intensity of the extended PSF is lower than the peak intensity of the native PSF. As discussed before, this is an inherent side effect of any DoF extending methods: the longer the EdoF, the lower the signal of each plane (see appendix G for a full derivation). With the two modifications in place, image acquisition in

MELM proceeds by shining the sample with a sequence of multiple light-sheets. The encoding method, the extension of the DoF, and the planes to be imaged are selected prior to launching the acquisition by selecting the driving frequencies of both AOD and TAG lens. Once the stack of encoded frames is collected, we reconstruct the images of the individual planes with a single-step decoding algorithm (see the materials and methods section and appendix I for further details).

5.2.1 Microscope setup

The light source is a CW laser at 488 nm (Coherent Sapphire), beam-expanded with a $5\times$ afocal telescope and then directed towards two AODs (IntraAction, ATD-7010CD2) at the Bragg angle. The deflectors are conjugated via a 4f system, thus generating a doubly diffracted beam which is then directed to the scan lens ($f = 200$ mm), while the secondary beams are blocked by an iris. The beam is then aligned towards the tube lens ($f = 200$ mm) and the excitation objective lens (Nikon $10\times/0.3$ NA, water dipping), finally reaching the sample inside a chamber. The latter is a cube with transparent windows, filled with pure water, glued to the water dipping detection objective (Leica $10\times/0.3$ NA or $40\times/0.8$ NA, both water dipping), mounted orthogonally to the excitation line. The back focal plane of the detection objective lens is conjugated through a 4f system to the TAG lens (TAG Optics Inc.). The TAG lens is typically driven at its first resonant frequency (70 kHz), while the voltage amplitude depends on the desired extension of the DoF and the properties of the objective lens. After the TAG Lens, light is directed towards the tube lens ($f = 200$ mm), which creates an image of the illuminated planes on the sensor of an sCMOS camera (ANDOR Neo 5.5). A notch filter (NF488-15, Thorlabs) rejects excitation light.

5.2.2 Acousto-optic light sculpting

The first AOD (IntraAction, ATD-7010CD2) is used to deflect a Gaussian beam along the y -axis, thus generating a light-sheet on average. It is driven by a voltage-controlled oscillator (IntraAction, DE-704M) at the central frequency of 70 MHz with a 20 kHz frequency modulation using a triangular wave. This waveform guarantees the optimal homogeneity of the light-sheet intensity along the y -axis. The second AOD (IntraAction, ATD-7010CD2) is driven by multiple frequencies in order to diffract the incident beam in multiple beamlets at different angles. The scan lens transforms the angles into unique axial positions, thus creating an array of parallel light-sheets. This AOD is controlled by a 14-bit arbitrary waveform generator (Signatec, PXDAC4800), whose output is amplified by a gain block (Mini-circuits, ZHL-1-2WX-S+). The camera acquisition and the generation of the driving signal for the AOD are synchronized through a digital I/O device (National Instruments, USB-6501). The complete system is controlled by a custom software programmed with LabView. In its present form, the light-sculpting system can switch between two illumination sequences in 5 ms.

5.2.3 TAG Lens calibration

In order to calibrate the DoF extension provided by the TAG Lens as a function of the voltage applied, we performed the following procedure. We filled the TAG Lens aperture with a Gaussian

Beam and measured the transmitted wavefront with a Shack-Hartmann sensor (see Figure 5.5a). We synchronized the emission of a laser pulse to a phase value of the oscillation of the TAG Lens, thus measuring the instantaneous wavefront. We fitted the measured wavefront ϕ to a parabolic model

$$\frac{\phi(x, y, t)}{\kappa} = \frac{\alpha(t)}{2} [(x - x_0)^2 + (y - y_0)^2] + \beta \quad (5.10)$$

Thus obtaining a measure of the instantaneous optical power $\alpha(t)$. By changing the delay t in the synchronization line, we measured the optical power at different times and fitted it to the following sinusoidal model

$$\alpha(t) = \alpha \cos(\omega t + \varphi) \quad (5.11)$$

The amplitude α is the optical power at fixed voltage V and frequency ω . Repeating this measurement for different values of driving voltage, we measured the calibration curve $\alpha(V)$ for two different resonant frequencies of the TAG lens. We fitted this latter to a linear model

$$\alpha(V) = mV \quad (5.12)$$

The optical power slope m is higher for higher resonant frequencies. However, the parabolic region is smaller, thus reducing the available physical aperture. The relationship between the DoF extension and the optical power is

$$\text{EDoF} = 2f_O^2\alpha \quad (5.13)$$

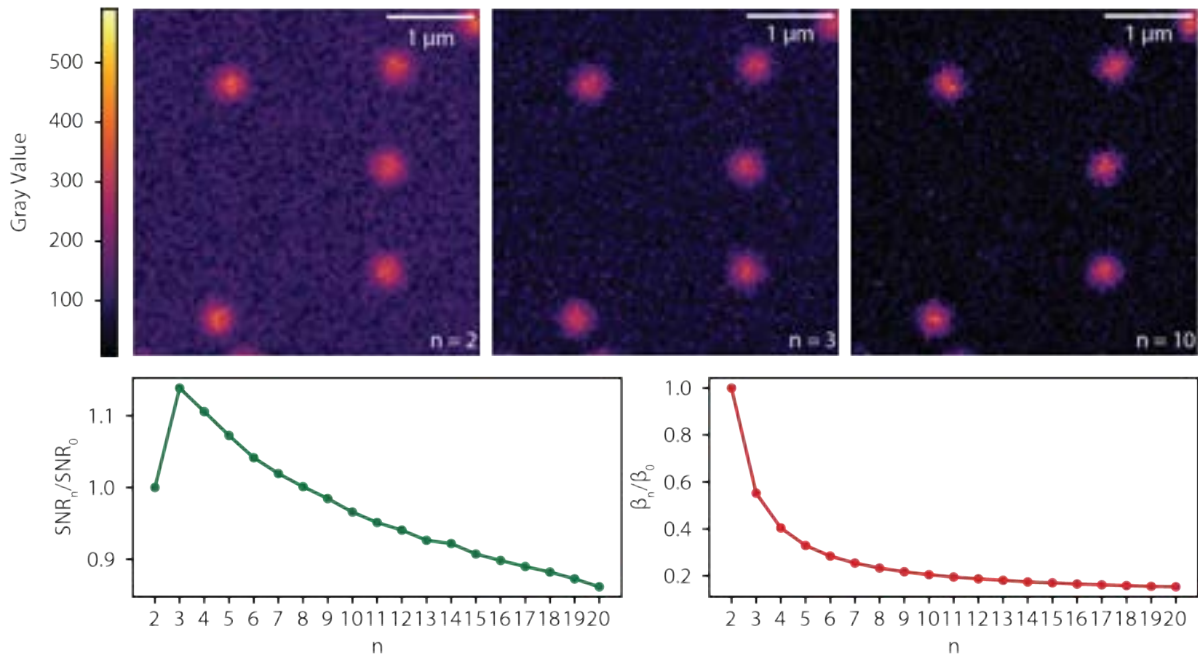
where f_O is the focal length of the objective lens.

5.3 Feasibility of MELM

5.3.1 Simulations

Initially, we validated our technique through numerical simulations. In Figure 5.6a, we show on the left a synthetic image of sub-diffraction beads in presence of a signal-independent background, readout (Gaussian) noise, and photon (Poisson) noise. The image is extracted from a z -stack decoded with an increasing number of frames encoded and subsequently decoded using the Black Light Sheet algorithm. The same image, decoded at $n = 3$ and $n = 7$, is shown on the right. In Figure 5.6b we show the result of a similar simulation, but performed using the Hadamard method. On the bottom of both simulations, we plot the quantitative analysis of the SNR gain and background reduction. Strikingly, the result of the simulations perfectly agrees with the predictions of the theoretical model presented before. Indeed, the quantitative analysis of the decoded images confirms that the both methods greatly suppress the background, while the Hadamard method is more successful in reducing the random noise, especially at high n values and also in presence of photon noise.

(a) Black Light Sheet



(b) Hadamard

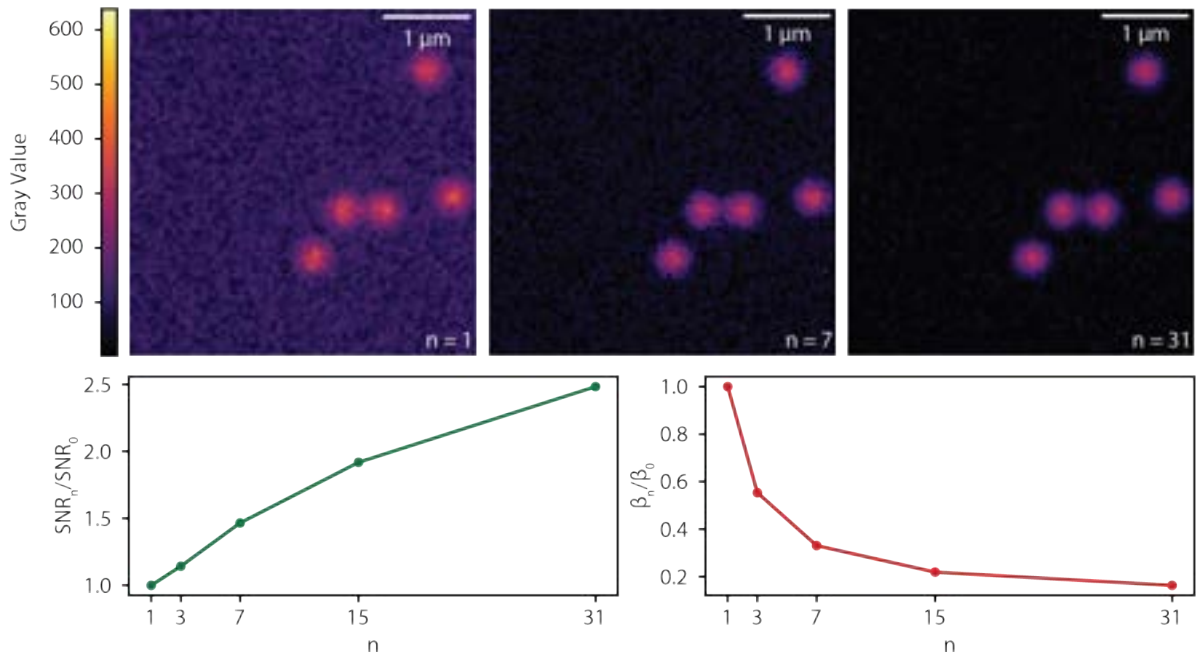


Figure 5.6: On top, Simulated images of sub-diffraction fluorescent beads in presence of photon noise, readout noise and signal-independent background. In (a) the images are encoded using the Black Light Sheet sequence at $n = 2, 3, 10$. In (b) the images are encoded using the Hadamard sequence at $n = 1, 7, 31$. On bottom, quantitative analysis of the SNR enhancement and background suppression of the corresponding set of images. Both quantities are plotted against the number n of acquired frames.

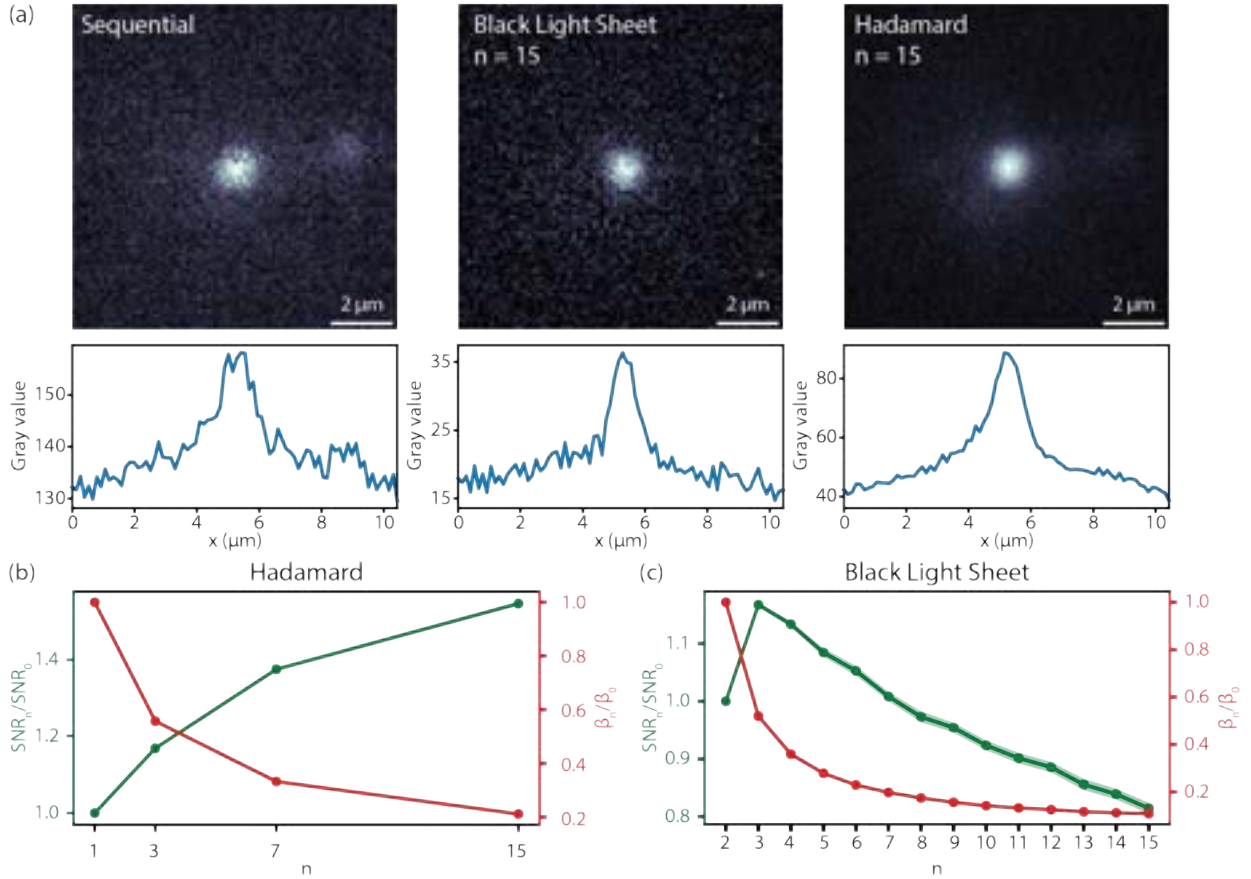


Figure 5.7: (a) Top: the same image of a single $1\ \mu\text{m}$ fluorescent bead taken with three different encoding methods (Sequential, Black Light-sheet, and Hadamard scan). Bottom: Intensity profile, averaged over the columns, of the corresponding images. (b) Quantitative analysis of the normalized SNR gain (green) and background suppression (red) obtained with the Hadamard encoding. (c) Quantitative analysis of the normalized SNR gain (green) and background suppression (red) obtained with the Black Light-sheet encoding. The error bar is shown as a shaded area, when bigger than the line width. The images have been acquired with a $40\times/0.8\ \text{NA}$ objective lens, whose DoF has been extended from $1\ \mu\text{m}$ to $60\ \mu\text{m}$ with the TAG lens.

5.3.2 Experimental results

In order to experimentally validate our technique, we performed the imaging of fluorescent beads embedded in agar gel. Figure 5.7a shows the image of the same bead acquired with the sequential, Black Light-sheet, and Hadamard scan. For a fair comparison, all three cases were obtained using the same energy per light-sheet and the same camera exposure time. These parameters grant a comparable level of phototoxicity and the same acquisition speed. The exposure time has been set to 2 ms, which added to the 5 ms required to switch between two encoding patterns, resulting in an acquisition rate of about 150 frames/second. As expected from such short exposure, the image acquired with the sequential scan is noisy and background-dominated. Instead, the Black Light-sheet scan shows a great suppression of the background, clearly noticeable in the intensity

profile. However, there is no perceptible improvement in the noise level. With the Hadamard scan, the background level is not as low as with the previous encoding, but the noise suppression is significantly greater. Exact noise and background quantification has been performed using a Fourier-based algorithm, described in detail in the materials and methods section. The results are shown in Figures 5.7b and 5.7c, where we plot the SNR and contrast gain of both encoding methods as a function of the number of frames. The Hadamard scan provides an SNR gain monotonically increasing with n , reaching an improvement of about 50% at $n = 15$. Instead, the Black Light-sheet scan provides the maximum gain at $n = 3$, which then decreases. Eventually, for high values of n , it loses its SNR advantage but maintains the background suppression. Both trends are in perfect agreement with the theoretical models discussed before.

5.3.2.1 SPED measurements

A central benefit of MELM is its compatibility with any DoF extending method. To verify this aspect of the technique, we imaged a pollen grain with an EDoF generated by introducing spherical aberrations to our system [13]. A widely used strategy given its simplicity, SPHERICAL-aberration-assisted Extended Depth-of-field (SPED) results in an elongated PSF – however, it comes at the cost of losing uniformity. Indeed, the shape of the aberrated PSF strongly depends on the axial coordinate, thus requiring a more computationally expensive 3D deconvolution for image restoration [13, 38]. In this experiment, we increased spherical aberration by placing a slab of glass between a $40\times/0.8\text{NA}$ objective lens and the sample, resulting in an EDoF of about $30\ \mu\text{m}$. Note that, in contrast to varifocal lenses for EDoF, this technique is not tunable in real-time. Figure 5.8 shows images of a pollen grain obtained with the sequential, Black Light-sheet and Hadamard scans for up to $n = 7$ frames. The results are in line with those obtained with the TAG lens and in agreement with theory. Thus, the SNR gain is about 20% and the contrast gain about 300% using the Hadamard scan at $n = 7$, and the Black Light-sheet offers the best background reduction of the three encoding strategies. These results confirm that MELM is a general and versatile technique, which is not constrained to a specific DoF extending method.

5.3.2.2 Imaging of biological samples

As a proof of concept, we imaged a fluorescently labeled spheroid of human embryonic kidney cells. Given the superior SNR enhancement capabilities of Hadamard scan in the presence of shot noise, we selected this encoding sequence. Figure 5.9a shows the maximum intensity projections of a reconstructed volume of $278.5\ \mu\text{m} \times 278.5\ \mu\text{m} \times 83.7\ \mu\text{m}$, with a voxel size of $0.5\ \mu\text{m} \times 0.5\ \mu\text{m} \times 5.6\ \mu\text{m}$ ($n = 15$). The camera exposure time was 100 ms and the volumetric imaging time was 1.5 s. Under these conditions, and considering the dense labeling of spheroids, the photon noise is not negligible. Consequently, the enhancement in SNR is lower than that reported using fluorescent beads. A more in-depth analysis of the noise and background reduction is presented in Figure 5.9b. At the described experimental conditions the SNR is still increasing with n , but for $n = 3$ and $n = 7$ it is lower than that of the sequential scan. However, for $n = 15$, we reached an SNR gain of about 20% and a contrast gain of about 100%. Significantly, such a gain comes with no cost in terms of 3D imaging speed. Raising the number of frames n could

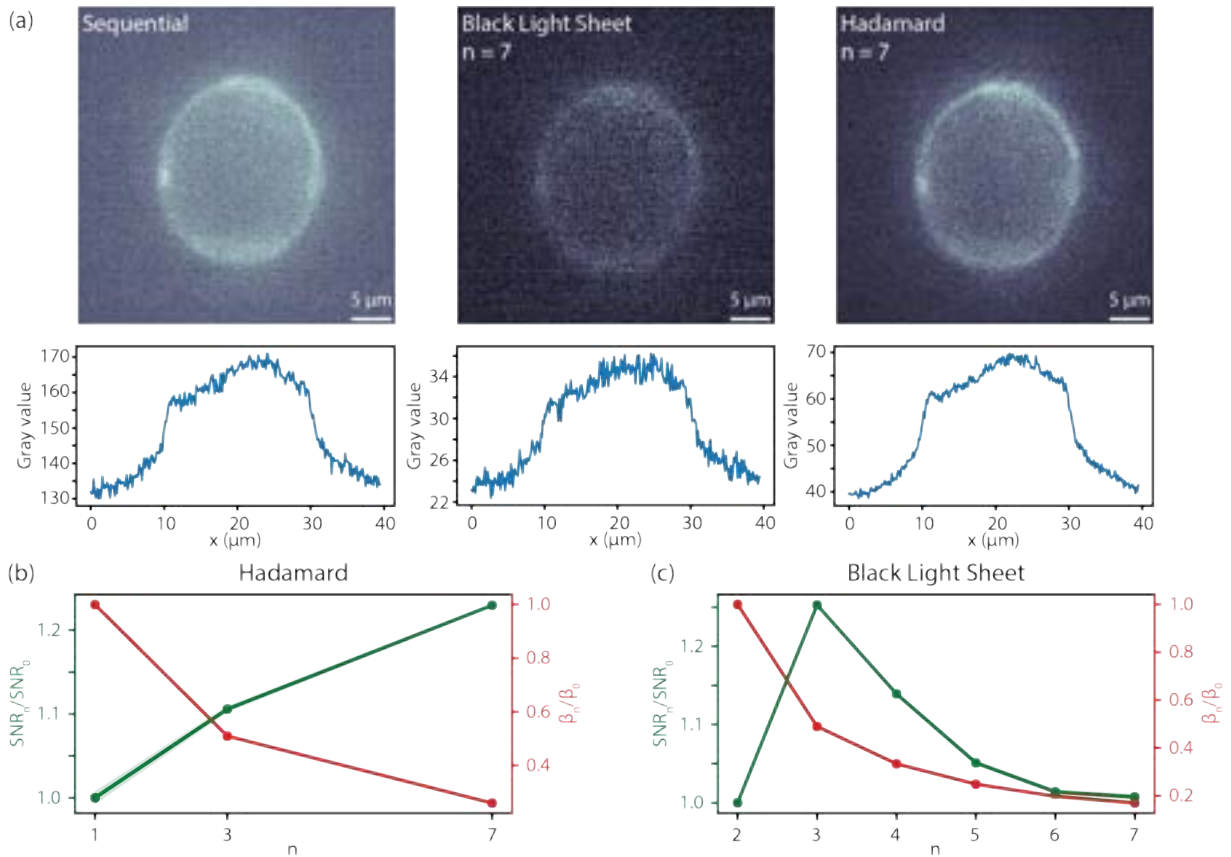


Figure 5.8: (a) Top: the same image of a single pollen grain bead taken with three different encoding methods and depth-of-field extended through spherical aberration. Bottom: Intensity profile, averaged over the columns, of the corresponding images. (b) Quantitative analysis of the normalized SNR gain (left) and background suppression (right) obtained with the Hadamard encoding. (c) Quantitative analysis of the normalized SNR gain (left) and background suppression (right) obtained with the Black Light Sheet encoding.

further increase the SNR gain, which is expected to approximately scale with the square root of the number of frames. However, practical limitations such as the resolution and the angular range of the deflector, or the power of the laser source, mitigate the feasibility of this strategy. Also, some care must be taken when using our parallelization method. When the beams are generated, one should carefully avoid cross-talks. If beams are overlapping, a region of the sample will be illuminated by more than a light-sheet, failing the hypothesis of independent planes needed for the reconstruction. In this case, reconstruction is still possible, but it is likely to generate artifacts. On a positive note, MELM is an extremely efficient technique when it comes to illumination. Indeed, all available power of the light source can be used – the higher the power, the higher the number of planes that can be illuminated. Thus, we can maximize the photon budget and speed of EDoF-LSM, and still preserve the very low photodamage of LSM. In addition, even when the maximum number of illuminated planes is reached, it is still possible to acquire a volume of any arbitrary depth by performing a hybrid parallelized-sequential scan. It suffices to divide the

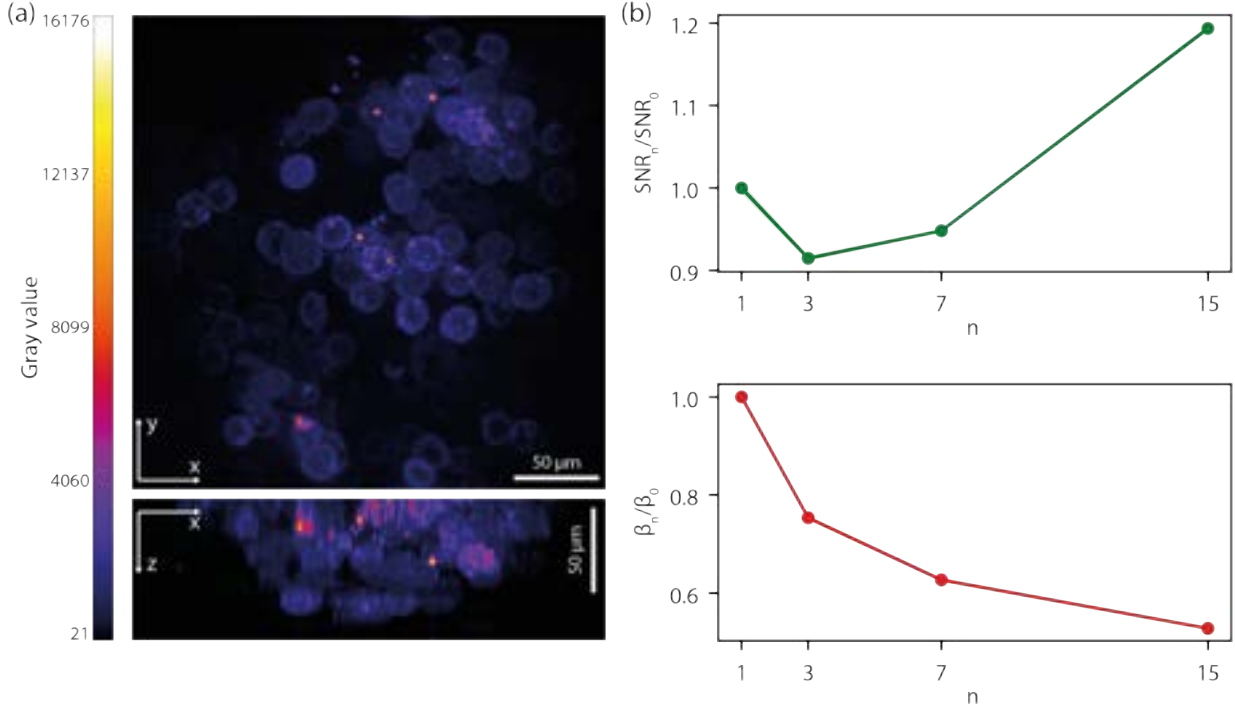


Figure 5.9: (a) Maximum intensity projection of a volumetric image of a spheroid acquired using the Hadamard encoding. The images have been deconvoluted with the Wiener filter algorithm, using a PSF simulated with equation 5.9. (b) SNR gain and background suppression versus the number of acquired frames. The images have been acquired with a $10\times/0.3$ NA objective lens, whose DoF has been extended from $7\ \mu\text{m}$ to $215\ \mu\text{m}$ with the TAG lens. The 3D image is composed of two interdigitated stacks of 15 frames

imaged volume in m stacks, each one composed of n planes acquired in parallel. The resulting volume will be composed of $m \times n$ images with an improved SNR of about $\sqrt{n}/2$.

5.3.3 Sample preparation

We prepared the beads samples using solutions of yellow-green beads (FluoSpheres, Invitrogen) with a diameter of $1\ \mu\text{m}$, diluted in 2% agarose gel at a concentration of 1:500. We prepared spheroids samples using human embryonic kidney cells (HEK 293), stably transfected with the plasmid encoding for EGFP- Δ 50 lamin-A (Addgene plasmid 17653). Starting from a dish of confluent cells, we diluted them to form a suspension of 10000 cells/mL and we seeded them into a 96-wells microplate (Corning Spheroid Microplate). After three days of growth, we fixed the spheroids with 4% paraformaldehyde for 30 minutes at room temperature and cleared with Rapiclear 1.47 for 10 minutes (Sun Jin Lab Co.). Once prepared, we embedded the individual spheroids in a 2% agarose gel cylinder for imaging.

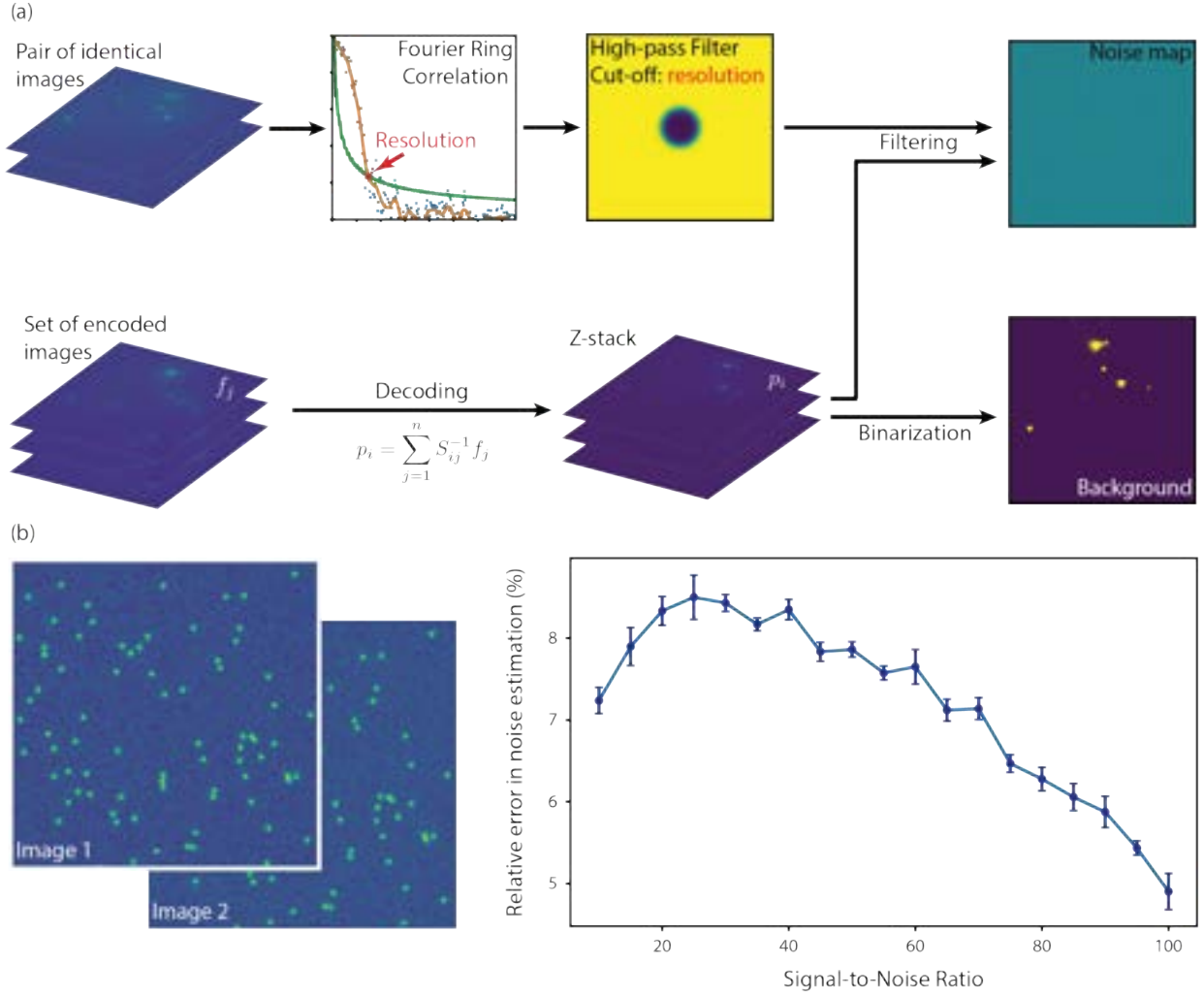


Figure 5.10: (a) Scheme of the data analysis pipeline used for the quantification of the noise and background in the images. (b) Accuracy of the FRC-based algorithm in the estimation of the noise level of the images.

5.4 Image analysis

For each experiment, we acquired a set \mathbf{f} of encoded frames. These are decoded, using the following single-step calculation

$$\mathbf{p} = \mathbf{S}^{-1} \mathbf{f} \quad (5.14)$$

where \mathbf{S}^{-1} is the inverse of the encoding matrix. Thus, we obtained the z-stack \mathbf{p} of decoded images. Additionally, we acquired two identical images used to identify the effective resolution of the images using the Fourier Ring Correlation (FRC) algorithm [39–41]. We used the inverse of

the resolution as the cut-off spatial frequency q_t for the following high-pass filter

$$S(q) = \frac{1}{1 + \exp[-(q - q_t)/s]} \quad (5.15)$$

where q is the radial spatial frequency and s is the parameter that defines the steepness of the sigmoid function. In our work, we set $s = 0.02$. Applying the high-pass filter to the z-stack of decoded images we obtained the corresponding noise maps. Since white noise power is frequency-independent, by calculating the standard deviation of the noise maps we got a quantification of the noise content of the images [42]. Finally, the SNR gain is calculated as the ratio of the standard deviation of the noise of the sequential image to the standard deviation of the noise of the decoded image. In order to validate this method, we run the simulations shown in figure 5.5. We generated pair of images at different SNRs and calculated the relative error in the estimation of the noise level. As shown, the discrepancy is always below 10% and decreases at higher SNR, proving the good reliability of this algorithm.

To identify the background content of the analyzed images, we applied a binarization algorithm to the acquired z-stack, classifying the content of the images in signal or background. We quantified the amount of background in the images by calculating the mean value of the background pixels.

Lastly, we deconvolved the z-stack using a simulated PSF. The deconvolution procedure we used is known as *Wiener Filter*. We used the Born & Wolf model to estimate the PSF, modified with equation 5.9 in order to calculate the extended PSF. Thanks to the homogeneity of the PSF along the z -axis it has been possible to deconvolve the full z-stack simply by a 2D-deconvolution of each frame. Typical values of the regularization parameter were 0.01.

5.5 Conclusion

The combination of EDoF detection with parallelized illumination enables overcoming the tradeoff between speed and SNR in LSFM when low photon noise is present. Such a condition is typically encountered in fast volumetric imaging, where the exposure time is kept low. As our results demonstrate, illuminating the sample with sequences of multiple light-sheets produces images with enhanced SNR and contrast. Because no moving optics are being used, the intrinsic high speed of EDoF-LSFM is preserved. The encoding sequence can be selected to address the imaging needs of a particular sample or application. Furthermore, the increased SNR also enables smaller laser peak intensities, further decreasing the risk of photodamage. Thanks to the simplicity and versatility of MELM, it can be used with any DoF extending technique, making it suitable for any LSFM system. We expect MELM to become an invaluable tool to investigate dynamic biological processes at high spatiotemporal resolution in thick objects.

References

- [1] Ernst H.K. Stelzer. Light-sheet fluorescence microscopy for quantitative biology. *Nature Methods*, 12(1):23–26, 2014.

- [2] Francesca Cella Zancchi, Zeno Lavagnino, Michela Perrone Donnorso, Alessio Del Bue, Laura Furia, Mario Faretta, and Alberto Diaspro. Live-cell 3D super-resolution imaging in thick biological samples. *Nature Methods*, 8(12):1047–1050, 2011.
- [3] J. M. Girkin and M. T. Carvalho. The light-sheet microscopy revolution. *Journal of Optics (United Kingdom)*, 20(5), 2018.
- [4] Florian O. Fahrbach and Alexander Rohrbach. Propagation stability of self-reconstructing Bessel beams enables contrast-enhanced imaging in thick media. *Nature Communications*, 3, 2012.
- [5] Tom Vettenburg, Heather I.C. Dalgarno, Jonathan Nylk, Clara Coll-Lladó, David E.K. Ferrier, Tomáš Čížmár, Frank J. Gunn-Moore, and Kishan Dholakia. Light-sheet microscopy using an Airy beam. *Nature Methods*, 11(5):541–544, 2014.
- [6] Hao Jia, Xianghua Yu, Yanlong Yang, Xing Zhou, Shaohui Yan, Chao Liu, Ming Lei, and Baoli Yao. Axial resolution enhancement of light-sheet microscopy by double scanning of Bessel beam and its complementary beam. *Journal of Biophotonics*, 12(1):1–10, 2019.
- [7] Jan Huisken, Jim Swoger, Filippo Del Bene, Joachim Wittbrodt, and Ernst H K Stelzer. Optical Sectioning Deep Inside Live Embryos by Selective Plane Illumination Microscopy. *Science*, 305(5686):1007–1009, aug 2004.
- [8] Venkatakaushik Voleti, Kripa B. Patel, Wenze Li, Citlali Perez Campos, Srinidhi Bharadwaj, Hang Yu, Caitlin Ford, Malte J. Casper, Richard Wenwei Yan, Wenxuan Liang, Chentao Wen, Koutarou D. Kimura, Kimara L. Targoff, and Elizabeth M. C. Hillman. Real-time volumetric microscopy of in vivo dynamics and large-scale samples with SCAPE 2.0. *Nature Methods*, 16(10):1054–1062, oct 2019.
- [9] Tonmoy Chakraborty, Bingying Chen, Stephan Daetwyler, Bo-Jui Chang, Oliver Vanderpoorten, Etai Sapoznik, Clemens F. Kaminski, Tuomas P. J. Knowles, Kevin M. Dean, and Reto Fiolka. Converting lateral scanning into axial focusing to speed up three-dimensional microscopy. *Light: Science & Applications*, 9(1):165, dec 2020.
- [10] Thai V. Truong, Daniel B. Holland, Sara Madaan, Andrey Andreev, Kevin Keomanee-Dizon, Josh V. Troll, Daniel E.S. Koo, Margaret J. McFall-Ngai, and Scott E. Fraser. High-contrast, synchronous volumetric imaging with selective volume illumination microscopy. *Communications Biology*, 3(1):1–8, 2020.
- [11] Nils Wagner, Nils Norlin, Jakob Gierten, Gustavo de Medeiros, Bálint Balázs, Joachim Wittbrodt, Lars Hufnagel, and Robert Prevedel. Instantaneous isotropic volumetric imaging of fast biological processes. *Nature Methods*, 16(6):497–500, 2019.
- [12] Maxime Woringier, Xavier Darzacq, Christophe Zimmer, and Mustafa Mir. Faster and less phototoxic 3D fluorescence microscopy using a versatile compressed sensing scheme. *Optics Express*, 25(12):13668, jun 2017.

- [13] Raju Tomer, Matthew Lovett-Barron, Isaac Kauvar, Aaron Andalman, Vanessa M. Burns, Sethuraman Sankaran, Logan Grosenick, Michael Broxton, Samuel Yang, and Karl Deisseroth. SPED Light Sheet Microscopy: Fast Mapping of Biological System Structure and Function. *Cell*, 163(7):1796–1806, dec 2015.
- [14] Omar E. Olarte, Jordi Andilla, David Artigas, and Pablo Loza-Alvarez. Decoupled illumination detection in light sheet microscopy for fast volumetric imaging. *Optica*, 2(8):702, 2015.
- [15] Sean Quirin, Darcy S. Peterka, and Rafael Yuste. Instantaneous three-dimensional sensing using spatial light modulator illumination with extended depth of field imaging. *Optics Express*, 21(13):16007, 2013.
- [16] Florian O. Fahrbach, Fabian F. Voigt, Benjamin Schmid, Fritjof Helmchen, and Jan Huisken. Rapid 3D light-sheet microscopy with a tunable lens. *Optics Express*, 21(September):21010–21026, 2013.
- [17] Martí Duocastella, Giuseppe Sancataldo, Peter Saggau, Paola Ramoino, Paolo Bianchini, and Alberto Diaspro. Fast Inertia-Free Volumetric Light-Sheet Microscope. *ACS Photonics*, 4(7):1797–1804, 2017.
- [18] SeungYeon Kang, Martí Duocastella, and Craig B. Arnold. Variable optical elements for fast focus control. *Nature Photonics*, 14(9):533–542, sep 2020.
- [19] Yijian Wu, Yuejin Zhao, Xiaohu Guo, Liquan Dong, Wei Jia, Ming Liu, Ji Zhao, and Yun Liu. Research on signal-to-noise ratio characteristics and image restoration for wavefront coding. In Abdul A. S. Awwal, Khan M. Iftekharruddin, Mohammad A. Matin, Mireya García Vázquez, and Andrés Márquez, editors, *Optics and Photonics for Information Processing IX*, volume 9598, page 959800, sep 2015.
- [20] William Chaze, Ophélie Caballina, Guillaume Castanet, and Fabrice Lemoine. The saturation of the fluorescence and its consequences for laser-induced fluorescence thermometry in liquid flows. *Experiments in Fluids*, 57(4):1–18, 2016.
- [21] Jean Yves Tinevez, Joe Dragavon, Lamya Baba-Aissa, Pascal Roux, Emmanuelle Perret, Astrid Canivet, Vincent Galy, and Spencer Shorte. *A quantitative method for measuring phototoxicity of a live cell imaging microscope*, volume 506. Elsevier Inc., 1 edition, 2012.
- [22] Jaroslav Icha, Michael Weber, Jennifer C. Waters, and Caren Norden. Phototoxicity in live fluorescence microscopy, and how to avoid it. *BioEssays*, 39(8):1–15, 2017.
- [23] Benjamin Judkewitz and Changhui Yang. Axial standing-wave illumination frequency-domain imaging (SWIF). *Optics Express*, 22(9):11001, 2014.
- [24] Yu-xuan Xuan Ren, Jianglai Wu, Queenie T.K. K Lai, Hei Ming Lai, Dickson M.D. D Siu, Wutian Wu, Kenneth K.Y. Y Wong, and Kevin K. Tsia. Parallelized volumetric fluorescence

- microscopy with a reconfigurable coded incoherent light-sheet array. *Light: Science and Applications*, 9(1), 2020.
- [25] Alberto Diaspro. Taking three-dimensional two-photon excitation microscopy further: Encoding the light for decoding the brain. *Microscopy Research and Technique*, 76(10):985–987, oct 2013.
- [26] Mathieu Ducros, Yannick Goulam Houssen, Jonathan Bradley, V. de Sars, and Serge Charpak. Encoded multisite two-photon microscopy. *Proceedings of the National Academy of Sciences*, 110(32):13138–13143, aug 2013.
- [27] Andreas Wuttig. Optimal transformations for optical multiplex measurements in the presence of photon noise. *Applied Optics*, 44(14):2710, may 2005.
- [28] Guenter Nitzsche and Rainer Riesenberger. Noise, fluctuation, and HADAMARD-transform spectrometry. In Derek Abbott, Jeffrey H. Shapiro, and Yoshihisa Yamamoto, editors, *Fluctuations and Noise in Photonics and Quantum Optics*, volume 5111, page 273, may 2003.
- [29] Martin Harwit, Neil J A Sloane, I Sloane, and Neil James. *Hadamard Transform Optics*. Elsevier, 1979.
- [30] Vladislav Gavryusev, Giuseppe Sancataldo, Pietro Ricci, Alberto Montalbano, Chiara Fernetto, Lapo Turrini, Annunziatina Laurino, Luca Pesce, Giuseppe de Vito, Natascia Tiso, Francesco Vanzi, Ludovico Silvestri, and Francesco S. Pavone. Dual-beam confocal light-sheet microscopy via flexible acousto-optic deflector. *Journal of Biomedical Optics*, 24(10):1, oct 2019.
- [31] Philipp J. Keller, Annette D. Schmidt, Joachim Wittbrodt, and Ernst H.K. Stelzer. Reconstruction of zebrafish early embryonic development by scanned light sheet microscopy. *Science*, 322(5904):1065–1069, 2008.
- [32] Dimitris Trypogeorgos, Tiffany Harte, Alexis Bonnin, and Christopher Foot. Precise shaping of laser light by an acousto-optic deflector. *Optics Express*, 21(21):8619–8625, 2013.
- [33] Kavya Mohan, Subhajit B. Purnapatra, and Partha Pratim Mondal. Three dimensional fluorescence imaging using multiple light-sheet microscopy. *PLoS ONE*, 9(6):1–8, 2014.
- [34] Kevin M. Dean, Philippe Roudot, Erik S. Welf, Theresa Pohlkamp, Gerard Garrelts, Joachim Herz, and Reto Fiolka. Imaging subcellular dynamics with fast and light-efficient volumetrically parallelized microscopy. *Optica*, 4(2):263, 2017.
- [35] Martí Duocastella, Salvatore Surdo, Alessandro Zunino, Alberto Diaspro, and Peter Saggau. Acousto-optic systems for advanced microscopy. *Journal of Physics: Photonics*, 3(1):012004, nov 2020.

- [36] Manuel Martinez-Corral, Po-Yuan Yuan Hsieh, Ana Doblas, Emilio Sanchez-Ortiga, Genaro Saavedra, and Yi-Pai Pai Huang. Fast Axial-Scanning Widefield Microscopy with Constant Magnification and Resolution. *IEEE/OSA Journal of Display Technology*, 11(11):913–920, nov 2015.
- [37] Euan McLeod and Craig B. Arnold. Mechanics and refractive power optimization of tunable acoustic gradient lenses. *Journal of Applied Physics*, 102(3):1–9, 2007.
- [38] W. Wallace, L. H. Schaefer, and J. R. Swedlow. A workingperson’s guide to deconvolution in light microscopy. *BioTechniques*, 31(5):1076–1097, 2001.
- [39] Marin Van Heel and Michael Schatz. Fourier shell correlation threshold criteria. *Journal of Structural Biology*, 151(3):250–262, 2005.
- [40] Sami Koho, Giorgio Tortarolo, Marco Castello, Takahiro Deguchi, Alberto Diaspro, and Giuseppe Vicidomini. Fourier Ring Correlation Simplifies Image Restoration in. *Nature Communications*, 10(2):1–45, 2019.
- [41] Giorgio Tortarolo, Marco Castello, Alberto Diaspro, Sami Koho, and Giuseppe Vicidomini. Evaluating image resolution in stimulated emission depletion microscopy. *Optica*, 5(1):32, 2018.
- [42] Sheng Liu, Michael J Mlodzianoski, Zhenhua Hu, Yuan Ren, Kristi McElmurry, Daniel M Suter, and Fang Huang. sCMOS noise-correction algorithm for microscopy images. *Nature Methods*, 14(8):760–761, aug 2017.

6

Conclusion

Light is one of the most important tools used in scientific fields as important as laser material processing and optical imaging. The capability of controlling the spatio-temporal properties of an optical beam is invaluable, being the enabling technology for high-speed and highly customizable processes. So far, state-of-the-art devices used to generate structured light offered groundbreaking opportunities, such as microscopy with spatial resolution beyond the diffraction limit or laser writing of complex patterns in a single-shot. However, existing devices typically lack of tunability or speed, leaving real-time customization of the properties of light still an unbeaten challenge.

In this Ph.D. thesis we explored the capabilities of acousto-optics to overcome this trade-off. As described in chapter 2, the acousto-optic effect exploits ultrasonic waves propagating in a medium to diffract the light. Ultrasounds are relatively easy to produce and to control – a piezoelectric actuator and a waveform generator suffice – and the properties of the acoustically-diffracted beam are directly related to those of sound waves, both in space and in time. Additionally, ultrasonic frequencies are typically in the order of MHz or GHz, enabling high-speed generation of tailored light. These premises led us to design and build the AOF device, presented in chapter 3. This novel tool contains two orthogonal acoustic resonant cavities immersed in a fluid (pure water, in the experiments described in this thesis). When driven on resonance, it generates standing waves which diffract light and generate multiple beamlets. Interestingly, the diffracted beamlets can be used to build complex intensity patterns in two drastically different ways. In the far-field, the diffraction orders are typically separated and the device acts as a beam-parallelizer. In the near-field, the beams overlap and give rise to interference fringes. Notably, the shape and structure of the diffraction patterns can be tuned by changing the driving parameters at a timescale as small as the period of the sound wave – typically, below one microsecond. In chapter 3 we presented a detailed theoretical analysis of the mechanics of sound formation within the AOF device, paving the way for further optimization. Additionally, we provided a reliable predictive model of the generation of diffraction patterns, enabling light-shape engineering. In chapter 4, we

performed a complete optical characterization of the prototype of an AOF device that we designed and built. The results show a perfect agreement with the mathematical model, demonstrating the predictability of its high-speed capabilities even for prolonged usage. The reliability of the device, when implemented in our custom laser-direct-writing station, enabled high-throughput material processing. Importantly, our novel device opens the door to a change in the paradigm of laser processing by obviating the need for slow point-by-point scanning of the sample surface. Indeed, our approach enables region-by-region processing, allowing the generation of complex shapes in a single exposure. The consequent drastic reduction of the processing time paves the way for the large-scale and precise modification of surfaces. In addition, the efficiency of the AOF device is essentially insensitive to many properties of light – such as wavelength, polarization, and incidence angle – making it compatible with virtually any optical element. This powerful feature allows to combine beam-shaping with fast and tunable parallelization, as demonstrated by the generation of tens of Bessel and annular beams shown in this thesis. This further extends the capabilities of the AOF device and its range of application. Lastly, in this research work we demonstrated how acousto-optics can provide breakthroughs also in the field of fluorescence imaging. In chapter 5, we presented the design and implementation of an all-acousto-optic light-sheet microscope that lacks any mechanical moving parts and is capable of fast imaging with enhanced SNR. This novel technique is enabled by a TAG lens, namely a cylindrical acoustic resonant cavity, and a couple of orthogonal AODs. The TAG lens performs a fast axial scan at tens of kHz, extending the effective depth-of-field of the microscope. The two AODs generate a tailored array of light sheets. The first AOD – driven with a frequency modulated sine wave – scans a Gaussian beam vertically. The second one – driven with a superposition of sine waves – parallelizes the scanned beam and generates an array of parallel light-sheets. Exciting the fluorescence of multiple planes simultaneously allows the collection of all the illuminated planes on a single camera frame. With this parallelization strategy, it is possible to obtain information from multiple axial positions at once. By using a simple inversion algorithm, the images of the individual planes can be retrieved. As demonstrated by our results, the z-stack of decoded images has an enhanced SNR compared to traditional single-plane methods. Thus, our technique enables high-speed imaging of large volumes, paving the way for a gentle investigation of fast dynamics in biological samples.

In conclusion, we believe that the research work presented in this thesis laid another brick towards the design of strategies for the generation of highly-customizable light shapes at high-speed. We showed how acousto-optics can be effectively used for that purpose, with important benefits for the fields of material processing, imaging. We envision that further discoveries could extend the advantages of acousto-optic light structuring to an even wider range of applications.



Elements of Geometrical Optics

A.1 Rays and ray transfer matrices

In geometrical optics, the light is described by rays. These latter are 2-dimensional vectors

$$\mathbf{r} = \begin{pmatrix} x \\ \theta \end{pmatrix} \quad (\text{A.1})$$

whose first element is the distance from the optical axis, and the second is the angle between the ray and the optical axis. The propagation of light through an optical element is calculated with ray transfer matrices (see table [A.1](#))

$$\mathbf{M} = \begin{pmatrix} A & B \\ C & D \end{pmatrix} \quad (\text{A.2})$$

The new ray vector is calculated as the product between the matrix and the input vector

$$\mathbf{r}_1 = \mathbf{M} \cdot \mathbf{r}_0 = \begin{pmatrix} Ax + B\theta \\ Cx + D\theta \end{pmatrix} \quad (\text{A.3})$$

The ray transfer matrix of a compound system is calculated as the product of the matrices of each component

$$\mathbf{M}_{\text{tot}} = \mathbf{M}_n \dots \mathbf{M}_2 \cdot \mathbf{M}_1 \quad (\text{A.4})$$

Free space	Thin lens	Flat interface
$\begin{pmatrix} 1 & d \\ 0 & 1 \end{pmatrix}$	$\begin{pmatrix} 1 & 0 \\ -\frac{1}{f} & 1 \end{pmatrix}$	$\begin{pmatrix} 1 & 0 \\ 0 & \frac{n_1}{n_2} \end{pmatrix}$

Table A.1: Ray transfer matrices of three common optical elements.

A.2 Scanning lens

A lens can be used to convert the angular displacement of a ray into a lateral displacement. Indeed, consider a ray originating from the optical axis with an angle θ . If its origin is distant f from a lens with focal length f , we find the following result

$$\begin{pmatrix} 1 & 0 \\ -\frac{1}{f} & 1 \end{pmatrix} \begin{pmatrix} 1 & f \\ 0 & 1 \end{pmatrix} \begin{pmatrix} 0 \\ \theta \end{pmatrix} = \begin{pmatrix} f\theta \\ 0 \end{pmatrix} \quad (\text{A.5})$$

The exiting ray is laterally displaced by a quantity $f\theta$ and propagates with no angle.

A.3 Image formation

With one or more lenses it is possible to generate an image, namely to generate a rescaled copy of rays of light. In this section, we discuss imaging systems in terms of ray transfer matrices.

A.3.1 Single lens system

Consider a system composed by a single lens. Taking also into account the space before and after the lens, we find the following matrix

$$\begin{pmatrix} 1 & z_2 \\ 0 & 1 \end{pmatrix} \begin{pmatrix} 1 & 0 \\ -\frac{1}{f} & 1 \end{pmatrix} \begin{pmatrix} 1 & z_1 \\ 0 & 1 \end{pmatrix} = \begin{pmatrix} 1 - \frac{z_2}{f} & z_1 + z_2 - \frac{z_1 z_2}{f} \\ -\frac{1}{f} & 1 - \frac{z_1}{f} \end{pmatrix} \quad (\text{A.6})$$

In order to have the formation of an image, the B element of the matrix has to be zero. Thus, the following condition has to be verified

$$\frac{1}{z_1} + \frac{1}{z_2} = \frac{1}{f} \quad (\text{A.7})$$

Consequently, the A element equals $-\frac{z_2}{z_1}$ and can be interpreted as the magnification factor.

A.3.2 Two lenses system

Consider a system composed by two lenses separated by a distance d . The corresponding matrix is

$$\begin{aligned}
& \begin{pmatrix} 1 & z_2 \\ 0 & 1 \end{pmatrix} \begin{pmatrix} 1 & 0 \\ -\frac{1}{f_2} & 1 \end{pmatrix} \begin{pmatrix} 1 & d \\ 0 & 1 \end{pmatrix} \begin{pmatrix} 1 & 0 \\ -\frac{1}{f_1} & 1 \end{pmatrix} \begin{pmatrix} 1 & z_1 \\ 0 & 1 \end{pmatrix} = \\
& = \frac{1}{f_1 f_2} \begin{pmatrix} f_1 f_2 + dz_2 - f_2 d - f_2 z_2 - f_1 z_2 & f_1 f_2 d + f_1 f_2 z_1 + f_1 f_2 z_2 - f_2 z_1 z_2 - f_1 z_1 z_2 + dz_1 z_2 - f_2 dz_1 - f_1 dz_2 \\ -f_1 - f_2 + d & f_2 f_1 + dz_1 - f_1 d - f_1 z_1 - f_2 z_1 \end{pmatrix} \quad (\text{A.8})
\end{aligned}$$

It is easy to verify that the B element is zero if $z_1 = f_1$ and $z_2 = f_2$. Moreover, if $d = f_1 + f_2$ the C element is also zero, meaning that the system is afocal. In this case, the lateral magnification is $A = -f_2/f_1$ and the angular magnification is $D = -f_1/f_2$.

B

Elements of Fourier Optics

As seen in chapter 1, light propagation is described by six wave equations for all the components of the electric and magnetic field. If the light is propagating through an homogeneous medium, the wave equations are identical. Therefore, it is sufficient to solve only one scalar equation. In this case, the electromagnetic wave is effectively described by a scalar field that we identify with the symbol U . In the real world, no medium is perfectly homogeneous. Thus, a scalar description of light can be considered a good approximation only under certain conditions. The main assumption behind that theory is that the coupling between the differential equations is small, which is valid as long as the spatial inhomogeneities have a characteristic size much larger than the optical wavelength λ . Notably, different polarization components of light can still be described by the scalar theory as long as they can be treated independently.

B.1 Diffraction

Diffraction of scalar fields is described by the Huygens-Fresnel integral

$$U_z(\mathbf{x}) = \frac{z}{i\lambda} \int_{\mathbb{R}^2} U_0(\mathbf{x}_0) \frac{\exp(ik\varrho)}{\varrho^2} d\mathbf{x}_0 \quad (\text{B.1})$$

where the position vector is $\mathbf{x} = (x, y)$ – the location on a plane orthogonal to the optical axis z – and ϱ is the distance between two planes, assumed to be much greater than λ , defined as

$$\varrho = \sqrt{(x - x_0)^2 + (y - y_0)^2 + z^2} = z \sqrt{1 + \left(\frac{x - x_0}{z}\right)^2 + \left(\frac{y - y_0}{z}\right)^2} \quad (\text{B.2})$$

The diffraction integral can be simplified using the proper approximation. The choice for this latter depends on the value of

$$F = \frac{D^2}{z\lambda} \quad (\text{B.3})$$

called the *Fresnel number*. In this definition, D is the linear size of field at the starting plane.

If $F \gtrsim 1$ the diffraction takes place in the *near-field* region and the propagation is better described by the Fresnel approximation. If $F \ll 1$ the diffraction takes place in the *far-field* region. In this case the Fresnel approximation still holds, but it can be further simplified with the Fraunhofer approximation.

B.1.1 Fresnel diffraction

Under the *paraxial approximation*, namely the assumption that diffraction angles are small with respect to the optical axis, we can expand ϱ in series

$$\varrho \sim z \left[1 + \frac{1}{2} \left(\frac{x - x_0}{z} \right)^2 + \frac{1}{2} \left(\frac{y - y_0}{z} \right)^2 \right] \quad (\text{B.4})$$

and replace it in equation B.1. Keeping only the linear term for the denominator and up to the quadratic term for the argument of the exponential, we obtain

$$U_z(\mathbf{x}) = \frac{e^{ikz}}{i\lambda z} \int_{\mathbb{R}^2} U_0(\mathbf{x}_0) \exp \left[\frac{ik}{2z} (\mathbf{x} - \mathbf{x}_0)^2 \right] d\mathbf{x}_0 \quad (\text{B.5})$$

This equation is known as the *Fresnel diffraction integral*, which can be seen as the convolution

$$U_z(\mathbf{x}) = [U_0(\mathbf{x}_0) * F_z(\mathbf{x}_0)](\mathbf{x}) \quad (\text{B.6})$$

where F_z the Fresnel convolution kernel

$$F_z(x, y) = \frac{e^{ikz}}{i\lambda z} \exp \left[\frac{ik}{2z} (x^2 + y^2) \right] \quad (\text{B.7})$$

Interestingly, this kernel has a simple Fourier transform which greatly simplifies the analytical and numerical calculations of the propagation of light in free space

$$\hat{F}_z(\nu_x, \nu_y) = e^{ikz} \exp \left[-i\pi\lambda z (\nu_x^2 + \nu_y^2) \right] \quad (\text{B.8})$$

where $\boldsymbol{\nu} = (\nu_x, \nu_y)$ are the spatial frequencies.

B.1.2 Fraunhofer diffraction

At very large distances, the diffraction formula can be further simplified. Indeed, if we can neglect the quadratic terms of the argument of the exponential of equation B.5, we obtain

$$U_z(\mathbf{x}) = \frac{e^{ikz} e^{\frac{ik}{2z}(x^2+y^2)}}{i\lambda z} \int_{\mathbb{R}^2} U_0(\mathbf{x}_0) \exp\left(i\frac{2\pi}{\lambda z} \mathbf{x} \cdot \mathbf{x}_0\right) d\mathbf{x}_0 \quad (\text{B.9})$$

This result is known as the *Fraunhofer diffraction integral*. Aside from negligible multiplicative factors, this integral is the Fourier transform of the field U_0 evaluated at spatial frequencies $\boldsymbol{\nu} = \left(\frac{x}{\lambda z}, \frac{y}{\lambda z}\right)$

$$U_z(\mathbf{x}) \propto \mathcal{F}\{U_0(\mathbf{x}_0)\}\left(\frac{\mathbf{x}}{\lambda z}\right) \quad (\text{B.10})$$

B.2 Fourier transforming property of the lenses

The phase transformation applied by a lens to a field is

$$t_l(\mathbf{x}) = \exp\left(-\frac{ik}{2f} \mathbf{x}^2\right) \quad (\text{B.11})$$

Notably, this transmission function has the expression of the Fresnel propagation kernel evaluated at $z = -f$, except for multiplicative constants

$$t_l(\mathbf{x}) \propto F_{-f}(\mathbf{x}) \quad (\text{B.12})$$

Now, we calculate what is the effect of a lens with focal length f and a free-space propagation of the same length on a field U_0 originating from a distance z behind the lens. The result U_1 is calculated as follows

$$U_1 = [(U_0 * F_z) \cdot F_{-f}] * F_f \quad (\text{B.13})$$

The above equation can be rewritten in frequency space exploiting the convolution property of the Fourier transform

$$\begin{aligned} \hat{U}_1(\boldsymbol{\nu}') &= \left(\left[\hat{U}_0(\boldsymbol{\nu}) \cdot \hat{F}_z(\boldsymbol{\nu}) \right] * \hat{F}_{-f}(\boldsymbol{\nu}) \right)(\boldsymbol{\nu}') \cdot \hat{F}_f(\boldsymbol{\nu}') = \\ &= \int_{\mathbb{R}^2} \hat{U}_0(\boldsymbol{\nu}) \exp[-i\pi\lambda(z-f)\boldsymbol{\nu}^2] \exp[-i2\pi\lambda f \boldsymbol{\nu} \cdot \boldsymbol{\nu}'] d\boldsymbol{\nu} \end{aligned} \quad (\text{B.14})$$

Transforming back into real space, we obtain

$$\begin{aligned}
U_1(\mathbf{x}) &= \int_{\mathbb{R}^2} \hat{U}_0(\boldsymbol{\nu}) \exp[-i\pi\lambda(z-f)\nu^2] \underbrace{\int_{\mathbb{R}^2} \exp[-i2\pi\lambda f\boldsymbol{\nu} \cdot \boldsymbol{\nu}'] \exp[i2\pi\mathbf{x} \cdot \boldsymbol{\nu}'] d\boldsymbol{\nu}'}_{\delta(\mathbf{x}-\boldsymbol{\nu}\lambda f)} d\boldsymbol{\nu} = \\
&= \hat{U}_0\left(\frac{\mathbf{x}}{\lambda f}\right) \exp\left[\frac{ik}{2f}\left(1-\frac{z}{f}\right)\mathbf{x}^2\right]
\end{aligned} \tag{B.15}$$

Interestingly, the field at the focal plane of the lens is the Fourier transform of the input field evaluated at spatial frequencies $\boldsymbol{\nu} = (\frac{x}{\lambda f}, \frac{y}{\lambda f})$, aside from a phase factor. when the distance between the input and the lens is matching the focal length, i.e. $z = f$, the phase factor equals to 1 and the result is exactly the Fourier transform. In other words, the field at the focal plane can be calculated as as Fraunhofer diffraction evaluated at $z = f$.

B.3 Image Formation

We now consider a system composed by two lenses – with focal length f_1 and f_2 – separated by a distance d . We consider the starting field at a distance z_1 from the first lens and the output field at a distance z_2 from the second lens. The propagation is calculated as follows

$$U_1 = (((U_0 * F_{z_1}) \cdot F_{-f_1}) * F_d) \cdot F_{-f_2}) * F_{z_2} \tag{B.16}$$

The Fourier transform of the above equation is

$$\hat{U}_1 = \left(\left(\left(\hat{U}_0 \cdot \hat{F}_{z_1}\right) * \hat{F}_{-f_1}\right) \cdot \hat{F}_d\right) * \hat{F}_{-f_2}) \cdot \hat{F}_{z_2} \tag{B.17}$$

Explicitly, it is written as

$$\hat{U}_1(\boldsymbol{\nu}'') = \int_{\mathbb{R}^4} \hat{U}_0(\boldsymbol{\nu}) \exp\left[-i\pi\lambda\left(z_1\nu^2 - f_1(\boldsymbol{\nu}' - \boldsymbol{\nu})^2 + d\nu'^2 - f_2(\boldsymbol{\nu}'' - \boldsymbol{\nu}')^2 + z_2\nu''^2\right)\right] d\boldsymbol{\nu} d\boldsymbol{\nu}' \tag{B.18}$$

Assuming $z_1 = f_1$ and $z_2 = f_2$, we have

$$\hat{U}_1(\boldsymbol{\nu}'') = \int_{\mathbb{R}^4} \hat{U}_0(\boldsymbol{\nu}) e^{-i\pi\lambda(d-f_1-f_2)\nu^2} e^{-i2\pi\lambda f_1\nu\nu'} e^{-i2\pi\lambda f_2\nu'\nu''} d\boldsymbol{\nu} d\boldsymbol{\nu}' \tag{B.19}$$

Transforming back to the real space, we obtain

$$\begin{aligned}
U_1(\mathbf{x}) &= \int_{\mathbb{R}^4} \hat{U}_0(\boldsymbol{\nu}) e^{-i\pi\lambda(d-f_1-f_2)\nu'^2} e^{-i2\pi\lambda f_1 \boldsymbol{\nu} \cdot \boldsymbol{\nu}'} \underbrace{\int_{\mathbb{R}^2} e^{-i2\pi\lambda f_2 \boldsymbol{\nu}' \cdot \boldsymbol{\nu}''} e^{i2\pi \mathbf{x} \cdot \boldsymbol{\nu}''} d\boldsymbol{\nu}''}_{\delta(\mathbf{x} - \boldsymbol{\nu}' \lambda f_2)} d\boldsymbol{\nu} d\boldsymbol{\nu}' = \\
&= e^{-i\pi\lambda(d-f_1-f_2)\frac{r^2}{\lambda^2 f_2^2}} \int_{\mathbb{R}^2} \hat{U}_0(\boldsymbol{\nu}) e^{-i2\pi \boldsymbol{\nu} \cdot \mathbf{x} f_1 / f_2} d\boldsymbol{\nu} = \\
&= U_0\left(-\frac{f_1}{f_2} \mathbf{x}\right) e^{-i\pi\lambda(d-f_1-f_2)\frac{r^2}{\lambda^2 f_2^2}} \tag{B.20}
\end{aligned}$$

This result shows that under imaging conditions (i.e. $z_1 = f_1$ and $z_2 = f_2$) the amplitude of the output field U_1 is a copy of the amplitude of the initial field U_0 , but inverted and rescaled by the magnification factor $M = \frac{f_2}{f_1}$. This implies that the light intensity at the two planes is identical, thus at z_2 there is an *image* of the plane at z_1 . If the distance between the two lenses is equal to $d = f_1 + f_2$, then the two fields are identical both in amplitude and in phase. In this case the two planes are said to be *optically conjugated*.

B.4 Impulse response of an imaging system

We now consider the effect of the finite size of the lenses. The pupil function describes the limited aperture of a lens and it is defined as follows

$$P(r) = \begin{cases} 1 & \text{if } r \leq R \\ 0 & \text{if } r > R \end{cases} \tag{B.21}$$

where $r = \sqrt{x^2 + y^2}$ and R is the radius of the lens. We now calculate the propagation of a point-like source $U_0(\mathbf{x}) = \delta(\mathbf{x})$ through a two-lenses imaging system. As shown before, the value of d has no effect on the intensity at the image plane. Therefore, we choose $d = 0$ for the sake of simplicity. The output field is

$$H = ((\delta * F_{z_1}) \cdot P \cdot F_{-f_1} \cdot F_{-f_2}) * F_{z_2} \tag{B.22}$$

Explicitly

$$H(\mathbf{x}) = \int_{\mathbb{R}^2} P(\mathbf{x}') \exp\left[\frac{ik}{2}\left(\frac{1}{nz_1} - \frac{1}{f_1} - \frac{1}{f_2} + \frac{1}{z_2}\right)r'^2\right] \exp\left[-\frac{ik}{z_2} \mathbf{x} \cdot \mathbf{x}'\right] d\mathbf{x}' \tag{B.23}$$

Where we neglected pure multiplicative phase factors. The imaging condition implies

$$\frac{1}{nz_1} + \frac{1}{z_2} - \frac{1}{f_1} - \frac{1}{f_2} = 0 \tag{B.24}$$

Therefore, we impose $z_2 = f_2$ and $z_1 = f_1/n + z$. Using a McLaurin expansion, we get $\frac{1}{nz_1} \sim \frac{1}{f_1}\left(1 - n\frac{z}{f_1}\right)$. By substituting these values, we get

$$H(\mathbf{x}) = \int_{\mathbb{R}^2} P(r') \exp\left[-\frac{ik}{2}\frac{nzr'^2}{f_1^2}\right] \exp\left[-\frac{ik}{f_2} \mathbf{x} \cdot \mathbf{x}'\right] d\mathbf{x}' \tag{B.25}$$

That is the Fourier transform of a circularly symmetric function. Therefore, we can rewrite the integral as a zero-order Hankel transform

$$H(r) = \int_0^R \exp\left(-\frac{ik}{2} \frac{nzr'^2}{f_1^2}\right) J_0\left(\frac{k}{f_2} rr'\right) r' dr' \quad (\text{B.26})$$

Changing the variable r' with $\rho = r'/R$ and defining the numerical aperture of the first lens as $\text{NA} = nR/f_1$ we finally obtain

$$H(r, z) = \int_0^1 \exp\left(-\frac{ik}{2} \frac{\text{NA}^2}{n} \rho^2 z\right) J_0\left(\frac{k\text{NA}}{M} \rho r\right) \rho d\rho \quad (\text{B.27})$$

where we neglected pure multiplicative factors and used the definition of the magnification as $M = nf_2/f_1$.

B.5 Coherence of light

The finite temporal coherence of light can be described by random phase shifts of the electromagnetic wave

$$E_1(t) = \sum_{n=-\infty}^{+\infty} \exp(i\omega t + i\phi_n) \Pi\left(\frac{t}{T} - \frac{n}{2}\right) \quad (\text{B.28})$$

Now consider the same electric field, time-shifted by τ

$$E_2(t - \tau) = \sum_{m=-\infty}^{+\infty} \exp(i\omega t - i\omega\tau + i\phi_m) \Pi\left(\frac{t - \tau}{T} - \frac{m}{2}\right) \quad (\text{B.29})$$

The total intensity of the sum of the two fields is calculated as

$$|E_1 + E_2|^2 = |E_1|^2 + |E_2|^2 + E_1^* E_2 + E_1 E_2^* \quad (\text{B.30})$$

The first two terms are proportional to the intensity of each field, the last two terms describe the interference between the two fields.

$$E_1^* E_2 = \exp(-i\omega\tau) \sum_{m,n} \exp(i\phi_n - i\phi_m) \Pi\left(\frac{t}{T} - \frac{n}{2}\right) \Pi\left(\frac{t - \tau}{T} - \frac{m}{2}\right) \quad (\text{B.31})$$

given a fixed τ , the product of the two rectangular functions is either 0 or 1, depending on the value of $n - m$. We now consider only the couple (n, m) such as this product is equal to 1. Therefore,

$$\sum_{m,n} \exp(i\phi_n - i\phi_m) \approx \delta_{m,n} \quad (\text{B.32})$$

Therefore the interference term is not zero only if $m = n$ and

$$\Pi\left(\frac{t}{T}\right)\Pi\left(\frac{t-\tau}{T}\right) > 0 \quad (\text{B.33})$$

which implies $|\tau| < T$. Indeed, T is the coherence time and defines the maximum delay beyond which the interference term can be neglected.

The value τ defines the visibility of the interference. Indeed, the total signal collected in an ideally infinite amount of time from the interference terms is

$$\begin{aligned} \int_{\mathbb{R}} [E_1^*(t)E_2(t-\tau) + E_1(t)E_2^*(t-\tau)] dt &= 2 \cos(\omega\tau) \int_{\mathbb{R}} \Pi\left(\frac{t}{T}\right)\Pi\left(\frac{t-\tau}{T}\right) dt = \\ &= (T - |\tau|)2 \cos(\omega\tau) \end{aligned} \quad (\text{B.34})$$

Thus, the visibility of the interference $\cos(\omega\tau)$ decreases linearly with $|\tau|$. This linear behaviour is a consequence of this simplified model which uses rectangular coherence windows. A more realistic model would still predict a visibility monotonically decreasing with τ , but with a non-linear trend. For perfectly incoherent light $T \rightarrow 0$ and the interference signal can be seen as $\delta(\tau)$.

The same reasoning which led to the results of this section can be applied to space to describe spatial coherence.

B.6 Incoherent imaging

$$\begin{aligned} i(\mathbf{x}) &= \int_0^T |[O(\mathbf{x}', t - \tau(\mathbf{x}')) * H(\mathbf{x}')](\mathbf{x})|^2 dt = \\ &= \int_0^T \int_{\mathbb{R}^6} O(\mathbf{x}', t - \tau(\mathbf{x}')) O^*(\mathbf{x}'', t - \tau(\mathbf{x}'')) H(\mathbf{x} - \mathbf{x}') H^*(\mathbf{x} - \mathbf{x}'') d\mathbf{x}' d\mathbf{x}'' dt \end{aligned} \quad (\text{B.35})$$

where $\tau(\mathbf{x})$ is the time the light needs to reach the detector starting from the coordinate \mathbf{x} of the object plane. Since H is a sharply peaked function, the product $H(\mathbf{x} - \mathbf{x}')H^*(\mathbf{x} - \mathbf{x}'')$ is non zero only for $\mathbf{x}' \approx \mathbf{x}''$. Therefore, we can approximate $\tau(\mathbf{x}') \approx \tau(\mathbf{x}'')$ and neglect both time delays. Thus, the time integral is just the correlation function at zero delay. For perfectly incoherent light it becomes

$$\int_0^T O(\mathbf{x}', t) O^*(\mathbf{x}'', t) dt = T |O(\mathbf{x}')|^2 \delta(\mathbf{x}' - \mathbf{x}'') \quad (\text{B.36})$$

Therefore, the image formed with incoherent light is

$$i(\mathbf{x}) = T \int_{\mathbb{R}^3} |O(\mathbf{x}')|^2 |H(\mathbf{x} - \mathbf{x}')|^2 d\mathbf{x}' \propto [o * h](\mathbf{x}) \quad (\text{B.37})$$

where

$$h(\mathbf{x}) = |H(\mathbf{x})|^2 \quad (\text{B.38})$$

is the intensity Point Spread Function (PSF) and

$$o(\mathbf{x}) = |O(\mathbf{x})|^2 \quad (\text{B.39})$$

is the distribution of light-emitters in the object plane.

B.7 Lateral and axial resolution

Using equation B.27 with object plane coordinates, the intensity PSF is

$$h(r, z) = \left| \int_0^1 \exp\left(-\frac{ik}{2} \frac{\text{NA}^2}{n} \rho^2 z\right) J_0(k\text{NA}\rho r) \rho \, d\rho \right|^2 \quad (\text{B.40})$$

In perfect focus condition ($z = 0$), this equation becomes

$$h(r, 0) = \left| \int_0^1 J_0(k\text{NA}r\rho) \rho \, d\rho \right|^2 = \left| \int_0^{k\text{NA}r} \frac{J_0(x)x}{(k\text{NA}r)^2} dx \right|^2 = \left| \frac{J_1(k\text{NA}r)}{k\text{NA}r} \right|^2 \quad (\text{B.41})$$

where we used the property of Bessel functions $\frac{d}{dx}[J_\nu(x)x^\nu] = J_{\nu-1}(x)x^\nu$. The first zero of $J_1(x)$ is at $x_0 \approx 3.8317$. Solving the equation $k\text{NA}r = x_0$ for r , we obtain the distance between the peak of the PSF and its first minimum

$$r_{\min} = 0.61 \frac{\lambda}{\text{NA}} \quad (\text{B.42})$$

This is the minimum lateral distance resolvable by a standard imaging system, according to the Rayleigh's criterion.

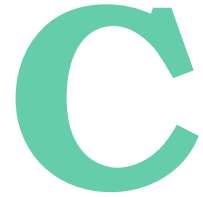
Along the optical axis ($r = 0$) the intensity profile is

$$\begin{aligned} h(0, z) &= \left| \int_0^1 \exp\left(-\frac{ik}{2} \frac{\text{NA}^2}{n} \rho^2 z\right) \rho \, d\rho \right|^2 = \left| \frac{n}{\text{NA}^2 k z} \left[\exp\left(-\frac{ik}{2} \frac{\text{NA}^2}{n} z\right) - 1 \right] \right|^2 = \\ &= \left(\frac{2n}{kz\text{NA}^2} \right)^2 \sin^2\left(\frac{kz\text{NA}^2}{4n}\right) \end{aligned} \quad (\text{B.43})$$

The first zero of the cardinal sine function $\frac{\sin(x)}{x}$ is at $x_0 = \pi$. Solving the equation $\frac{kz\text{NA}^2}{4n} = x_0$ for z , we obtain the distance between the peak of the axial PSF and its first minimum

$$z_{\min} = \frac{2\lambda n}{\text{NA}^2} \quad (\text{B.44})$$

This is the minimum axial distance resolvable by a standard imaging system, according to the Rayleigh's criterion.



Principles of Acousto-Optics

In this appendix we use Maxwell equations to derive the wave equation in presence of a sinusoidally varying refractive index. We calculate the solution of this equation in two cases, namely Raman-Nath and Bragg regimes. The derivation is done for both traveling and standing waves.

C.1 Electromagnetic wave equation in a sound field

Consider the macroscopic Maxwell equations

$$\nabla \cdot \mathbf{D} = \rho \quad (\text{C.1})$$

$$\nabla \cdot \mathbf{B} = 0 \quad (\text{C.2})$$

$$\nabla \times \mathbf{E} = -\frac{\partial \mathbf{B}}{\partial t} \quad (\text{C.3})$$

$$\nabla \times \mathbf{H} = \frac{\partial \mathbf{D}}{\partial t} + \mathbf{J} \quad (\text{C.4})$$

where \mathbf{E} is the electric field, \mathbf{B} is the magnetic field, $\mathbf{D} = \varepsilon \mathbf{E}$ is the displacement field, $\mathbf{H} = \mathbf{B}/\mu$ is the magnetizing field, ρ is the volumetric density of free charges and \mathbf{J} is current density of free charges. ε is the dielectric permittivity, and μ is the magnetic permeability of the medium. Assuming that this latter is not conductive, we can set $\rho = 0$ and $\mathbf{J} = 0$.

A sound wave can locally and instantaneously compress and expand the medium, therefore the dielectric permittivity varies in space and time. In a linear approximation, we have $\varepsilon(\mathbf{x}, t) = \varepsilon_0 \varepsilon_r + \Delta\varepsilon(\mathbf{x}, t)$ where $\Delta\varepsilon \ll \varepsilon_0 \varepsilon_r$ and $\Delta\varepsilon$ is a periodic function with circular frequency $\Omega = c_s K$.

K and c_s are, respectively, the wavenumber and the speed of sound. Equation C.4 becomes

$$\nabla \times \mathbf{B} = \mu \frac{\partial \varepsilon}{\partial t} \mathbf{E} + \mu \varepsilon \frac{\partial \mathbf{E}}{\partial t} \quad (\text{C.5})$$

assuming $\mathbf{E} \propto e^{ikx-i\omega t}$ and $\varepsilon \propto e^{iKx-i\Omega t}$, we have that

$$\left| \frac{\partial \varepsilon}{\partial t} \mathbf{E} \right| = |\Omega \varepsilon \mathbf{E}| \ll |\omega \varepsilon \mathbf{E}| = \left| \mu \varepsilon \frac{\partial \mathbf{E}}{\partial t} \right| \quad (\text{C.6})$$

if $\Omega \ll \omega$, that is typically true for sound and light waves¹. Therefore, we can neglect the first term of the right side of equation C.5. Taking the curl of equation C.3 and using equation C.5, we get

$$\nabla(\nabla \cdot \mathbf{E}) - \nabla^2 \mathbf{E} = -\frac{\partial}{\partial t} \left(\mu \varepsilon \frac{\partial \mathbf{E}}{\partial t} \right) \quad (\text{C.7})$$

Now, consider equation C.1

$$\nabla \cdot \mathbf{D} = \nabla \varepsilon \cdot \mathbf{E} + \varepsilon \nabla \cdot \mathbf{E} = 0 \quad (\text{C.8})$$

once again, we have

$$|\nabla \varepsilon \cdot \mathbf{E}| = |\varepsilon \mathbf{K} \cdot \mathbf{E}| \ll |\varepsilon \mathbf{k} \cdot \mathbf{E}| = |\varepsilon \nabla \cdot \mathbf{E}| \quad (\text{C.9})$$

therefore, we can consider $\nabla \cdot \mathbf{E} = 0$. Neglecting again the time derivative of ε , equation C.7 becomes

$$\nabla^2 \mathbf{E} = \mu \varepsilon \frac{\partial^2 \mathbf{E}}{\partial t^2} \quad (\text{C.10})$$

This is the familiar electromagnetic wave equation, except that the refractive index is a function of space and time. Indeed, $\mu \varepsilon = n^2/c^2$ where n is the refractive index and c is the speed of light. Therefore the refractive index is

$$n = c\sqrt{\mu \varepsilon} = \sqrt{\frac{\mu \varepsilon_0 \varepsilon_r + \mu \Delta \varepsilon}{\mu_0 \varepsilon_0}} = \sqrt{\mu_r \varepsilon_r} \sqrt{1 + \frac{\Delta \varepsilon}{\varepsilon_0 \varepsilon_r}} \sim n_0 + \frac{1}{2} \frac{\Delta \varepsilon}{\varepsilon_0 \varepsilon_r} \quad (\text{C.11})$$

where n_0 is the static refractive index of the medium. Therefore, the refractive index is a function of time and space with the same periodicity of the sound wave. In formula

$$n(x + \Lambda, t) = n(x, t) \quad (\text{C.12})$$

$$n(x, t + T) = n(x, t) \quad (\text{C.13})$$

¹for visible light $\omega \approx 10^{15}$ Hz, for ultrasounds $\Omega \approx 10^7$ Hz.

where $T = 2\pi/\Omega$ and we have assumed x to be the propagation axis of the sound wave. Lastly, we notice the equation C.10 is identical for each component of the electric field. Therefore, we can consider only one component, obtaining the scalar wave equation

$$\boxed{\nabla^2 E(z, x, t) = \left[\frac{n(x, t)}{c} \right]^2 \frac{\partial^2 E(z, x, t)}{\partial t^2}} \quad (\text{C.14})$$

where we have neglected the y axis for simplicity and assumed z to be the optical axis.

C.2 Raman-Nath equations and their solutions

Now we rewrite equation C.14 for $x \mapsto x + \Lambda$ and $t \mapsto t + T$

$$\nabla^2 E(z, x + \Lambda, t + T) = \left[\frac{n(x, t)}{c} \right]^2 \frac{\partial^2 E(z, x + \Lambda, t + T)}{\partial t^2} \quad (\text{C.15})$$

this implies that

$$E(z, x + \Lambda, t + T) = C(\Lambda, T) \cdot E(z, x, t) \quad (\text{C.16})$$

and we can impose

$$C(\Lambda, T) = \exp(\beta\Lambda + \gamma T) \quad (\text{C.17})$$

where $a, b \in \mathbb{C}$. We now define

$$F(z, x, t) = E(z, x, t) \exp(-\alpha z - \beta x - \gamma t) \quad (\text{C.18})$$

therefore

$$\begin{aligned} F(z, x + \Lambda, t + T) &= E(z, x + \Lambda, t + T) \exp[-\alpha z - \beta(x + \Lambda) - \gamma(t + T)] = \\ &= E(z, x, t) \exp(\beta\Lambda + \gamma T) \exp[-\alpha z - \beta(x + \Lambda) - \gamma(t + T)] = \\ &= E(z, x, t) \exp(-\alpha z - \beta x - \gamma t) = F(z, x, t) \end{aligned} \quad (\text{C.19})$$

so, $F(z, x, t)$ is a periodic function in space and time. Using equation C.18 we can write the electric field as

$$E(z, x, t) = F(z, x, t) \exp(\alpha z + \beta x + \gamma t) \quad (\text{C.20})$$

namely, the solution of equation C.14 is a plane wave times a periodic function, with the same periodicity of the sound wave.

We now assume that the electric field travels in a vacuum before entering the vibrating medium. Therefore, we can write it as the standard plane-wave $E(z, x, t) = E_0 \exp(i\mathbf{k} \cdot \mathbf{x} - i\omega t)$. To be consistent with this assumption, we write the solution as

$$\begin{aligned}
E(z, x, t) &= F(z, x, t) \exp(in_0 \mathbf{k} \cdot \mathbf{x} - i\omega t) = \\
&= F(z, x, t) \exp[in_0 k(z \cos \theta + x \sin \theta) - i\omega t]
\end{aligned} \tag{C.21}$$

where θ is the angle of incidence of the light on the vibrating medium.

C.2.1 Traveling wave

Being $F(z, x, t)$ periodic, we can write it as a double Fourier series

$$F(z, x, t) = \sum_{j=-\infty}^{+\infty} \sum_{m=-\infty}^{+\infty} \varphi_{jm}(z) e^{ij\Omega t} e^{imKx} \tag{C.22}$$

In the case of a traveling wave, we have the additional property that

$$F(z, x + s\Lambda, t) = F(z, x, t - sT) \quad \forall s \in \mathbb{Z} \tag{C.23}$$

Expanding both sides of the above equation in Fourier series

$$F(z, x + s\Lambda, t) = \sum_{j=-\infty}^{+\infty} \sum_{m=-\infty}^{+\infty} \varphi_{jm}(z) e^{ij\Omega t} e^{imK(x+s\Lambda)} = \tag{C.24}$$

$$= \sum_{j=-\infty}^{+\infty} \sum_{m=-\infty}^{+\infty} \varphi_{jm}(z) e^{ij\Omega(t-sT)} e^{imKx} = F(z, x, t - sT) \tag{C.25}$$

comparing the two Fourier series, we get the condition $m = -j$. Therefore, we can rewrite the electric field in the simpler form

$$E(z, x, t) = e^{in_0 k(z \cos \theta + x \sin \theta) - i\omega t} \sum_{m=-\infty}^{+\infty} \varphi_m(z) e^{imKx} e^{-im\Omega t} \tag{C.26}$$

where we assume that the amplitude of the plane wave is $E_0 = 1$ in the proper units. It is useful to simplify the next calculations factorizing the terms of the summation from the above equation

$$E(z, x, t) = \sum_{m=-\infty}^{+\infty} \varphi_m(z) e^{in_0 k \cos \theta z} e^{i(n_0 k \sin \theta + mK)x} e^{-i(\omega + m\Omega)t} \tag{C.27}$$

Now, we can calculate the partial derivatives of the scalar field

$$\begin{aligned}
\frac{\partial^2 E}{\partial z^2} &= \sum_{m=-\infty}^{+\infty} e^{in_0 k \cos \theta z} e^{i(n_0 k \sin \theta + mK)x} e^{-i(\omega + m\Omega)t} \left(-n_0^2 k^2 \cos^2 \theta \varphi_m + 2ikn_0 \cos \theta \frac{\partial \varphi_m}{\partial z} + \frac{\partial^2 \varphi_m}{\partial z^2} \right) \\
\frac{\partial^2 E}{\partial x^2} &= \sum_{m=-\infty}^{+\infty} \varphi_m(z) e^{in_0 k \cos \theta z} e^{i(n_0 k \sin \theta + mK)x} e^{-i(\omega + m\Omega)t} (-n_0^2 k^2 \sin^2 \theta - m^2 K^2 - 2mn_0 k K \sin \theta) \\
\frac{\partial^2 E}{\partial t^2} &= \sum_{m=-\infty}^{+\infty} \varphi_m(z) e^{in_0 k \cos \theta z} e^{i(n_0 k \sin \theta + mK)x} e^{-i(\omega + m\Omega)t} (-\omega^2 - m^2 \Omega^2 - 2m\omega\Omega) \quad (C.28)
\end{aligned}$$

we now assume that the behavior of the refractive index is harmonic

$$n(x, t) = n_0 + \Delta n \sin(Kx - \Omega t) \quad (C.29)$$

where Δn is the maximum refractive index variation relative to the static value n_0 . Therefore

$$\begin{aligned}
\left[\frac{n(x, t)}{c} \right]^2 &= \frac{n_0^2 + 2n_0 \Delta n \sin(Kx - \Omega t) + (\Delta n)^2 \sin^2(Kx - \Omega t)}{c^2} \sim \\
&\sim \frac{n_0^2}{c^2} - \frac{in_0 \Delta n}{c^2} (e^{i(Kx - \Omega t)} - e^{-i(Kx - \Omega t)}) \quad (C.30)
\end{aligned}$$

where we have neglected the second-order term in Δn , because $\Delta n \ll n_0$. We can now rewrite equation C.14 as

$$\begin{aligned}
&\varphi_m \left(\frac{n_0^2}{c^2} m^2 \Omega^2 + \frac{n_0^2}{c^2} 2m\omega\Omega - m^2 K^2 - 2mn_0 k K \sin \theta \right) + \frac{\partial \varphi_m}{\partial z} (2ikn_0 \cos \theta) + \frac{\partial^2 \varphi_m}{\partial z^2} = \\
&= \frac{in_0 \Delta n}{c^2} [(\omega^2 + (m-1)^2 \Omega^2 + 2(m-1)\omega\Omega)\varphi_{m-1} - (\omega^2 + (m+1)^2 \Omega^2 + 2(m+1)\omega\Omega)\varphi_{m+1}] \quad (C.31)
\end{aligned}$$

where we have equated only the Fourier components at the same frequency². We now make the further assumption that the amplitude $\varphi(z)$ is slowly varying, namely

$$\left| \frac{\partial \varphi_m}{\partial z} \right| \ll k |\varphi_m(z)| \quad (C.32)$$

Therefore, we can neglect the second derivative of $\varphi_m(z)$. Furthermore, if we use the typical values of the parameters³, we see that the terms $\omega\Omega/c^2$ and Ω^2/c^2 are much smaller with respect

²This is possible by multiplying both sides of the equation with the function $\exp[is(Kx - \omega t)]$, where $s \in \mathbb{Z}$, and then integrating over a period. The orthogonality property of these functions leaves only the components at the same frequency.

³For visible light and ultrasounds the typical values are: $\omega \approx 10^{15}$ Hz, $\Omega \approx 10^7$ Hz, $c \approx 3 \times 10^8$ m/s, $c_s \approx 10^3$ m/s, $\theta \approx \lambda/\Lambda \approx 10^{-2}$ rad.

to the others and they can be neglected and we can approximate $\cos \theta \sim 1$ and $\sin \theta \sim \theta$. Rearranging the differential equation, we finally obtain

$$\boxed{\frac{\partial \varphi_m}{\partial z} + i \frac{mQ}{2L} (m - 2\alpha) \varphi_m = \frac{\nu}{2L} (\varphi_{m-1} - \varphi_{m+1})} \quad (\text{C.33})$$

where we have defined the dimensionless parameters

$$Q = \frac{K^2 L}{kn_0} \quad (\text{C.34})$$

$$\alpha = -\frac{n_0 k}{K} \theta \quad (\text{C.35})$$

$$\nu = \Delta n k L \quad (\text{C.36})$$

where L is the length of the vibrating medium along the optical axis. Equation C.33 describes a countable set of coupled differential equations and it is known as *Raman-Nath equation*. The boundary conditions for equation C.33 are

$$\begin{cases} \varphi_m(0) = 1 & \text{if } m = 0 \\ \varphi_m(0) = 0 & \text{if } m \neq 0 \end{cases} \quad (\text{C.37})$$

C.2.1.1 Solutions of the Raman-Nath equation

To understand the role of the parameters Q , α , and ν , we solve the differential equations adding the additional assumption that only two orders ($m = 0$ and $m = 1$) are present. The set of differential equations become

$$\frac{\partial \varphi_0}{\partial z} = -\frac{\nu}{2L} \varphi_1 \quad (\text{C.38})$$

$$\frac{\partial \varphi_1}{\partial z} = -i \frac{Q}{2L} (1 - 2\alpha) \varphi_1 + \frac{\nu}{2L} \varphi_0 \quad (\text{C.39})$$

To simplify the next calculations, we define $\beta = \frac{\nu}{2L}$ and $\gamma = \frac{Q}{2L} (1 - 2\alpha)$. Additionally, we rewrite the above set of ODE in matrixial form

$$\frac{\partial}{\partial z} \begin{pmatrix} \varphi_0 \\ \varphi_1 \end{pmatrix} = \begin{pmatrix} 0 & -\beta \\ \beta & -i\gamma \end{pmatrix} \begin{pmatrix} \varphi_0 \\ \varphi_1 \end{pmatrix} \quad (\text{C.40})$$

we refer to the coupling matrix as M . In order to decouple the ODEs, we need to diagonalize M . Its characteristic polynomial is

$$\det(M - \lambda I) = \lambda^2 + i\gamma\lambda + \beta^2 \quad (\text{C.41})$$

whose roots, and therefore the eigenvalues of M , are

$$\lambda_{1,2} = \frac{i}{2} \left(-\gamma \pm \sqrt{\gamma^2 + 4\beta^2} \right) \quad (\text{C.42})$$

The corresponding eigenvectors – given by the relation $M\mathbf{v}_{1,2} = \lambda_{1,2}\mathbf{v}_{1,2}$ – are

$$\mathbf{v}_{1,2} = \begin{pmatrix} \frac{i}{2\beta} \left(\gamma \pm \sqrt{\gamma^2 + 4\beta^2} \right) \\ 1 \end{pmatrix} \quad (\text{C.43})$$

therefore, the change of basis matrix is

$$O = \begin{pmatrix} \frac{i}{2\beta} \left(\gamma + \sqrt{\gamma^2 + 4\beta^2} \right) & \frac{i}{2\beta} \left(\gamma - \sqrt{\gamma^2 + 4\beta^2} \right) \\ 1 & 1 \end{pmatrix} \quad (\text{C.44})$$

therefore, the diagonalized matrix is

$$O^{-1}MO = J = \begin{pmatrix} \frac{i}{2} \left(-\gamma + \sqrt{\gamma^2 + 4\beta^2} \right) & 0 \\ 0 & -\frac{i}{2} \left(\gamma + \sqrt{\gamma^2 + 4\beta^2} \right) \end{pmatrix} \quad (\text{C.45})$$

Using the new basis, we can rewrite the differential equation C.40 as

$$\frac{\partial}{\partial z} \underbrace{O^{-1}\varphi}_{\psi} = \underbrace{O^{-1}MO}_J \underbrace{O^{-1}\varphi}_{\psi} \quad (\text{C.46})$$

where we have used the fact that $OO^{-1} = I$. Therefore, we obtain the uncoupled ODEs

$$\frac{\partial \psi_0}{\partial z} = \frac{i}{2} \left(-\gamma + \sqrt{\gamma^2 + 4\beta^2} \right) \psi_0 \quad (\text{C.47})$$

$$\frac{\partial \psi_1}{\partial z} = -\frac{i}{2} \left(\gamma + \sqrt{\gamma^2 + 4\beta^2} \right) \psi_1 \quad (\text{C.48})$$

whose solutions are

$$\psi_0(z) = A \exp \left[\frac{i}{2} \left(-\gamma + \sqrt{\gamma^2 + 4\beta^2} \right) z \right] \quad (\text{C.49})$$

$$\psi_1(z) = B \exp \left[-\frac{i}{2} \left(\gamma + \sqrt{\gamma^2 + 4\beta^2} \right) z \right] \quad (\text{C.50})$$

where $A, B \in \mathbb{C}$. Using the relation $\varphi = O\psi$, we finally obtain

$$\varphi_0(z) = \frac{iA}{2\beta} \left(\gamma + \sqrt{\gamma^2 + 4\beta^2} \right) e^{\frac{i}{2} \left(-\gamma + \sqrt{\gamma^2 + 4\beta^2} \right) z} + \frac{iB}{2\beta} \left(\gamma - \sqrt{\gamma^2 + 4\beta^2} \right) e^{-\frac{i}{2} \left(\gamma + \sqrt{\gamma^2 + 4\beta^2} \right) z} \quad (\text{C.51})$$

$$\varphi_1(z) = A e^{\frac{i}{2} \left(-\gamma + \sqrt{\gamma^2 + 4\beta^2} \right) z} + B e^{-\frac{i}{2} \left(\gamma + \sqrt{\gamma^2 + 4\beta^2} \right) z} \quad (\text{C.52})$$

using the boundary conditions from equation C.37, we get

$$B = -A \quad (\text{C.53})$$

$$A = \frac{1}{2i} \frac{2\beta}{\sqrt{\gamma^2 + 4\beta^2}} \quad (\text{C.54})$$

by substituting A and B in the solutions, we get

$$\varphi_0(z) = \frac{e^{-i\gamma z/2}}{\sqrt{\gamma^2 + 4\beta^2}} \left[i\gamma \sin\left(\sqrt{\gamma^2 + 4\beta^2} z/2\right) + \sqrt{\gamma^2 + 4\beta^2} \cos\left(\sqrt{\gamma^2 + 4\beta^2} z/2\right) \right] \quad (\text{C.55})$$

$$\varphi_1(z) = e^{-i\gamma z/2} 2\beta \frac{\sin\left(\sqrt{\gamma^2 + 4\beta^2} z/2\right)}{\sqrt{\gamma^2 + 4\beta^2}} \quad (\text{C.56})$$

We can easily see that for $\gamma \rightarrow \infty$, $|\varphi_0| \rightarrow 1$ and $|\varphi_1| \rightarrow 0$. On the contrary, $|\varphi_1|$ is maximum when $\gamma \rightarrow 0$. This fact implies that we can have non-zero diffraction order only when γ_m is small. This can happen only in two situations: either $Q = 0$ or $\alpha = m/2$. In the first case all the diffraction orders can be excited, in the second case only the m^{th} one.

C.2.1.2 Bragg regime

We consider now the case in which $Q \gg 1$, but $\alpha = m/2$. Since only adjacent diffraction orders are coupled and only the 0th order contains energy at the beginning of the process, we are constrained to choose $m = \pm 1$, therefore $\alpha = \pm 1/2$. Using the definition of α (equation C.35) and solving with respect to θ we find

$$\theta_B = \mp \frac{\lambda}{2n_0\Lambda} \quad (\text{C.57})$$

which is exactly the *Bragg angle*.

In this scenario, our previous assumption of only two diffraction orders ($m = 0$ and $m = \pm 1$) is justified, therefore we can calculate the diffraction amplitudes is just given by equations C.55 and C.56 in the limit $\gamma \rightarrow 0$.

$$\varphi_0(z) = \cos(\nu z/2L) \quad (\text{C.58})$$

$$\varphi_{\pm 1}(z) = \sin(\nu z/2L) \quad (\text{C.59})$$

Therefore, the diffraction efficiency is given by the normalized intensity of the orders, evaluated at $z = L$

$$\eta_0 = |\varphi_0(L)|^2 = \cos^2(\nu/2) = \cos^2(\Delta nkL/2) \quad (\text{C.60})$$

$$\eta_{\pm 1} = |\varphi_{\pm 1}(L)|^2 = \sin^2(\nu/2) = \sin^2(\Delta nkL/2) \quad (\text{C.61})$$

Using equation C.26 we can rewrite the complete electric field coming out from the vibrating medium as

$$E(z, x, t) = \cos(\nu/2) \exp [in_0k(z \cos \theta + x \sin \theta) - i\omega t] + \sin(\nu/2) \exp [in_0k \cos \theta z + (n_0k \sin \theta \pm K)x - i(\omega \pm \Omega)t] \quad (\text{C.62})$$

We can see that the first term is just the undiffracted plane wave with a lower amplitude. However, the second term describes a second plane wave whose x -component of the wave-vector has been down or up-shifted by K and frequency-shifted by Ω . Consequently, the 1st diffracted order has a slightly different wavelength and propagates with a new angle θ_1 given by

$$n_0k_1 \sin \theta_1 = n_0k \sin \theta \pm K \quad (\text{C.63})$$

where $k_1 = \frac{\omega \pm \Omega}{c}$. Since $\omega \gg \Omega$, we can approximate $k_1 \approx k$. Furthermore $\sin \theta \sim \theta_B = \mp \frac{K}{2n_0k}$. Solving with respect to θ_1 we finally get

$$\sin \theta_1 \sim \theta_1 = \pm \frac{K}{2n_0k} \quad (\text{C.64})$$

namely, the diffraction angle is double the Bragg angle.

C.2.1.3 Raman-Nath regime

In case $Q \ll 1$, we can neglect the γ parameter for every diffraction order m . As such, the two-order assumption is no longer valid: every diffraction order can be excited, and we need to solve the following set of differential equations

$$\frac{\partial \varphi_m}{\partial z} = \frac{\nu}{2L} (\varphi_{m-1} - \varphi_{m+1}) \quad (\text{C.65})$$

We can notice that now, having set $\gamma = 0$, the function φ_m satisfies the same differentiation rule of the Bessel functions of the first kind

$$\frac{\partial J_m(z)}{\partial z} = \frac{1}{2} (J_{m-1}(z) - J_{m+1}(z)) \quad (\text{C.66})$$

Therefore, we find out immediately that the solution of C.65 is

$$\varphi_m(z) = J_m(\nu z/L) \quad (\text{C.67})$$

We notice that Bessel functions automatically satisfy boundary conditions C.37. The diffraction efficiencies are

$$\eta_m = |\varphi_m(L)|^2 = J_m^2(\nu) = J_m^2(\Delta n k L) \quad (\text{C.68})$$

Using equation C.27 we can rewrite the total electric field as

$$E(z, x, t) = e^{in_0k \cos \theta z} \sum_{m=-\infty}^{+\infty} J_m(\nu) e^{i(n_0k \sin \theta + mK)x} e^{-i(\omega + m\Omega)t} \quad (\text{C.69})$$

Assuming an incidence close to normal ($\theta \approx 0$), we have that each diffraction order propagates with an angle $\theta_m \sim \tan \theta_m = \frac{mK}{n_0k}$ and is frequency shifted by $m\Omega$.

Using the Bessel generating function, we can rewrite

$$\sum_{m=-\infty}^{+\infty} J_m(\nu) e^{im(Kx - \Omega t)} = \exp [i\nu \sin(Kx - \Omega t)] \quad (\text{C.70})$$

Therefore, the acoustic wave behaves as a thin phase grating, whose transmittance function is described by the above equation. Namely, the incoming plane wave is phase-shifted by $\phi(x, t) = \nu \sin(Kx - \Omega t)$.

C.2.1.4 About the meaning of the parameter Q

We have just seen that we can describe the vibrating medium as a thin grating in the Raman-Nath regime. In other words, it can be considered an optical element completely localized in a definite z -position. In this case, the incoming wave is phase-shifted by

$$\phi(x, t) = k \int_0^L n(x, t) dz = kLn(x, t) = kL\Delta n \sin(Kx - \Omega t) \quad (\text{C.71})$$

For this description to be legit, a ray of light needs to interact with the acoustic wave at a fixed phase for the whole optical path. This assumption is justified only when the medium is thin enough to neglect the divergence of the incoming beam and refraction inside the material. These observations bring us to the most important interpretation of the Klein-Cook parameter: when $Q \ll 1$ the sound wave acts as a thin phase grating, while when $Q \gg 1$ it acts as a thick phase grating. Therefore, the parameter Q quantifies the effective thickness of the vibrating medium.

C.2.2 Standing wave

In the case of a standing wave, we expand in Fourier series the periodic function $F(z, x, t)$ only with respect to the x coordinate

$$F(z, x, t) = \sum_{m=-\infty}^{+\infty} \varphi_m(z, t) e^{imKx} \quad (\text{C.72})$$

Therefore, we can rewrite the electric field as

$$E(z, x, t) = \sum_{m=-\infty}^{+\infty} \varphi_m(z, t) e^{-i\omega t} e^{in_0k \cos \theta z} e^{i(n_0k \sin \theta + mK)x} \quad (\text{C.73})$$

The partial derivatives of the above field are

$$\begin{aligned}
\frac{\partial^2 E}{\partial z^2} &= \sum_{m=-\infty}^{+\infty} e^{in_0 k \cos \theta z} e^{i(n_0 k \sin \theta + mK)x} e^{-i\omega t} \left(-n_0^2 k^2 \cos^2 \theta \varphi_m + 2ikn_0 \cos \theta \frac{\partial \varphi_m}{\partial z} + \frac{\partial^2 \varphi_m}{\partial z^2} \right) \\
\frac{\partial^2 E}{\partial x^2} &= \sum_{m=-\infty}^{+\infty} \varphi_m e^{in_0 k \cos \theta z} e^{i(n_0 k \sin \theta + mK)x} e^{-i\omega t} \left(-n_0^2 k^2 \sin^2 \theta - m^2 K^2 - 2mn_0 k K \sin \theta \right) \\
\frac{\partial^2 E}{\partial t^2} &= \sum_{m=-\infty}^{+\infty} e^{in_0 k \cos \theta z} e^{i(n_0 k \sin \theta + mK)x} e^{-i\omega t} \left(-\omega^2 \varphi_m - 2i\omega \frac{\partial \varphi_m}{\partial t} + \frac{\partial^2 \varphi_m}{\partial t^2} \right) \quad (C.74)
\end{aligned}$$

Now, we assume that the refractive index is a harmonic standing wave

$$n(x, t) = n_0 + \Delta n \sin(Kx) \sin(\Omega t) \quad (C.75)$$

where Δn is the maximum variation of refractive index with respect to the static value n_0 . Therefore

$$\begin{aligned}
\left[\frac{n(x, t)}{c} \right]^2 &= \frac{n_0^2 + 2n_0 \Delta n \sin(Kx) \sin(\Omega t) + (\Delta n)^2 \sin^2(Kx) \sin^2(\Omega t)}{c^2} \sim \\
&\sim \frac{n_0^2}{c^2} - \frac{in_0 \Delta n \sin(\Omega t)}{c^2} (e^{iKx} - e^{-iKx}) \quad (C.76)
\end{aligned}$$

where we have neglected the second-order term in Δn , because $\Delta n \ll n_0$. We can now rewrite equation C.14 as

$$\begin{aligned}
&\frac{n_0^2}{c^2} 2i\omega \frac{\partial \varphi_m}{\partial t} - \frac{n_0^2}{c^2} \frac{\partial^2 \varphi_m}{\partial t^2} - \varphi_m (m^2 K^2 + 2mn_0 k K \sin \theta) + \frac{\partial \varphi_m}{\partial z} (2ikn_0 \cos \theta) + \frac{\partial^2 \varphi_m}{\partial z^2} = \\
&= \frac{in_0 \Delta n \sin(\Omega t)}{c^2} \left[\left(\omega^2 \varphi_{m-1} + 2i\omega \frac{\partial \varphi_{m-1}}{\partial t} - \frac{\partial^2 \varphi_{m-1}}{\partial t^2} \right) - \left(\omega^2 \varphi_{m+1} + 2i\omega \frac{\partial \varphi_{m+1}}{\partial t} - \frac{\partial^2 \varphi_{m+1}}{\partial t^2} \right) \right] \quad (C.77)
\end{aligned}$$

where we have equated only the Fourier components at the same frequency. We now assume that the amplitude $\varphi(z, t)$ is slowly varying

$$\left| \frac{\partial \varphi_m}{\partial z} \right| \ll k |\varphi_m(z, t)| \quad \left| \frac{\partial \varphi_m}{\partial t} \right| \ll \omega |\varphi_m(z, t)| \quad (C.78)$$

Therefore, we can neglect the time derivatives and the second space derivative of $\varphi_m(z, t)$. We can approximate again $\cos \theta \sim 1$ and $\sin \theta \sim \theta$. Rearranging the differential equation, we obtain

$$\boxed{\frac{\partial \varphi_m}{\partial z} + i \frac{mQ}{2L} (m - 2\alpha) \varphi_m = \frac{\nu \sin(\Omega t)}{2L} (\varphi_{m-1} - \varphi_{m+1})} \quad (C.79)$$

Where Q , α and ν are defined as in equations C.34, C.35 and C.36. Interestingly, this is the same equation as C.33, just with the parameter ν replaced with $\nu \sin(\Omega t)$.

C.2.2.1 Bragg Regime

Using the results already obtained in the case of the traveling wave, we have that if $Q \gg 1$ and $\theta = \mp \frac{\lambda}{2n_0\Lambda}$ there are only two diffraction orders with a non-zero solution. The corresponding amplitudes are

$$\varphi_0(z, t) = \cos\left(\frac{\nu \sin(\Omega t)z}{2L}\right) \quad (\text{C.80})$$

$$\varphi_{\pm 1}(z, t) = \sin\left(\frac{\nu \sin(\Omega t)z}{2L}\right) \quad (\text{C.81})$$

Therefore, the diffraction efficiencies are

$$\eta_0(t) = |\varphi_0(L, t)|^2 = \cos^2\left(\frac{\nu \sin(\Omega t)}{2}\right) \quad (\text{C.82})$$

$$\eta_{\pm 1}(t) = |\varphi_{\pm 1}(L, t)|^2 = \sin^2\left(\frac{\nu \sin(\Omega t)}{2}\right) \quad (\text{C.83})$$

Using the Jacobi–Anger identity, we can expand the amplitudes into Fourier series

$$\varphi_0(L, t) = \sum_{m=-\infty}^{+\infty} J_{2m}(\nu/2) e^{i2m\Omega t} \quad (\text{C.84})$$

$$\varphi_{\pm 1}(L, t) = \sum_{m=-\infty}^{+\infty} J_{2m+1}(\nu/2) e^{i(2m+1)\Omega t} \quad (\text{C.85})$$

Therefore, both diffraction orders have a broad-band spectrum. More in detail, the 0th and 1st order are frequency-shifted by all even and odd integer multiples of Ω , respectively.

C.2.2.2 Raman-Nath Regime

The solutions of equation C.79 in case $Q \ll 1$ is

$$\varphi_m(z, t) = J_m\left(\frac{\nu \sin(\Omega t)z}{L}\right) \quad (\text{C.86})$$

The corresponding diffraction efficiencies are

$$\eta_m(t) = |\varphi_m(L, t)|^2 = J_m^2[\nu \sin(\Omega t)] \quad (\text{C.87})$$

Using Graf's addition theorem, we can expand the amplitudes into Fourier series

$$\varphi_{2m}(L, t) = \sum_{l=0}^{+\infty} (-1)^l J_{m-l}(\nu/2) J_{m+l}(\nu/2) (e^{i2l\Omega t} - e^{-i2l\Omega t}) \quad (\text{C.88})$$

$$\varphi_{2m+1}(L, t) = -i \sum_{l=0}^{+\infty} (-1)^l J_{m-l}(\nu/2) J_{m+l+1}(\nu/2) (e^{i(2l+1)\Omega t} - e^{-i(2l+1)\Omega t}) \quad (\text{C.89})$$

Therefore, even diffraction orders are frequency-shifted by even multiples of Ω , and odd diffraction orders are frequency-shifted by odd multiples of Ω .

D

Wave Equation in Liquids

It is well-known that sound propagates as a wave. In this appendix, we prove this fact, deriving the wave equation in fluids as an approximation of the Navier-Stokes equations. More in detail, we study the case of Newtonian liquids.

D.1 Conservation of mass

Let $\rho = \frac{dm}{dV}$ be the mass density of a liquid. The corresponding flow current is $\rho\mathbf{v}$, where \mathbf{v} is the fluid velocity. Given a volume V , the rate of mass variation inside this volume is

$$\frac{dm}{dt} = \frac{d}{dt} \int_{V(t)} \rho dV \quad (\text{D.1})$$

Using the Reynolds transport theorem, we can rewrite the right-hand side of the above equation as

$$\frac{d}{dt} \int_{V(t)} \rho dV = \int_{V(t)} \frac{\partial \rho}{\partial t} dV + \int_{\partial V(t)} \rho \mathbf{v} \cdot d\mathbf{S} \quad (\text{D.2})$$

Using the divergence theorem, we get

$$\int_{\partial V(t)} \rho \mathbf{v} \cdot d\mathbf{S} = \int_{V(t)} \nabla \cdot (\rho \mathbf{v}) dV \quad (\text{D.3})$$

The conservation of mass requires equation D.1 to be equal to zero. Therefore, we get

$$\int_{V(t)} \frac{\partial \rho}{\partial t} dV + \int_{V(t)} \nabla \cdot (\rho \mathbf{v}) dV = 0 \quad (\text{D.4})$$

Since the volume $V(t)$ is arbitrary, the integrands must be the same. In this way, we get the continuity equation in differential form.

$$\boxed{\frac{\partial \rho}{\partial t} + \nabla \cdot (\rho \mathbf{v}) = 0} \quad (\text{D.5})$$

D.2 Conservation of momentum

The second Newton's law is

$$\frac{d\mathbf{p}}{dt} = \mathbf{F} \quad (\text{D.6})$$

where \mathbf{F} is the sum of all the external (both body and surface) forces. We can rewrite the above equation in integral form

$$\frac{d}{dt} \int_{V(t)} \rho \mathbf{v} dV = \int_{V(t)} \mathbf{f} dV + \int_{\partial V(t)} \boldsymbol{\sigma} \cdot d\mathbf{S} \quad (\text{D.7})$$

where \mathbf{f} accounts for body forces and $\boldsymbol{\sigma}$ accounts for surface forces.

Using the Reynolds transport theorem, we can rewrite the left-hand side of the above equation as

$$\frac{d}{dt} \int_{V(t)} \rho \mathbf{v} dV = \int_{V(t)} \frac{\partial(\rho \mathbf{v})}{\partial t} dV + \int_{\partial V(t)} (\rho \mathbf{v}) \otimes \mathbf{v} \cdot d\mathbf{S} \quad (\text{D.8})$$

Using the divergence theorem and the vector identity $\nabla \cdot (\rho \mathbf{v} \otimes \mathbf{v}) = (\mathbf{v} \cdot \nabla)(\rho \mathbf{v}) + (\rho \mathbf{v}) \nabla \cdot \mathbf{v}$, we can rewrite the above equation as

$$\begin{aligned} \frac{d}{dt} \int_{V(t)} \rho \mathbf{v} dV &= \int_{V(t)} \left(\rho \frac{\partial \mathbf{v}}{\partial t} + \mathbf{v} \frac{\partial \rho}{\partial t} + \rho(\mathbf{v} \cdot \nabla \mathbf{v}) + \underbrace{\mathbf{v}(\mathbf{v} \cdot \nabla \rho) + \rho \mathbf{v} \nabla \cdot \mathbf{v}}_{=\mathbf{v}(\nabla \cdot \rho \mathbf{v})} \right) dV = \\ &= \int_{V(t)} \left(\rho \frac{\partial \mathbf{v}}{\partial t} + \rho(\mathbf{v} \cdot \nabla \mathbf{v}) + \mathbf{v} \underbrace{\left(\frac{\partial \rho}{\partial t} + \nabla \cdot \rho \mathbf{v} \right)}_{=0} \right) dV = \\ &= \int_{V(t)} \left(\rho \frac{\partial \mathbf{v}}{\partial t} + \rho(\mathbf{v} \cdot \nabla \mathbf{v}) \right) dV \end{aligned} \quad (\text{D.9})$$

where we have used the continuity equation. Using the divergence theorem, we can also rewrite the right-hand term of equation D.7.

$$\int_{V(t)} \mathbf{f} dV + \int_{\partial V(t)} \boldsymbol{\sigma} \cdot d\mathbf{S} = \int_{V(t)} (\mathbf{f} + \nabla \cdot \boldsymbol{\sigma}) dV \quad (\text{D.10})$$

Since the volume $V(t)$ is arbitrary, we can rewrite equation D.7 as

$$\rho \frac{\partial \mathbf{v}}{\partial t} + \rho(\mathbf{v} \cdot \nabla \mathbf{v}) = \mathbf{f} + \nabla \cdot \boldsymbol{\sigma} \quad (\text{D.11})$$

The force density $\boldsymbol{\sigma}$ is known as *Cauchy stress tensor*, and its explicit form is

$$\boldsymbol{\sigma} = \begin{pmatrix} \sigma_{xx} & \tau_{xy} & \tau_{xz} \\ \tau_{yx} & \sigma_{yy} & \tau_{yz} \\ \tau_{zx} & \tau_{zy} & \sigma_{zz} \end{pmatrix} \quad (\text{D.12})$$

where σ_{ii} are the normal stresses and τ_{ij} are the shear stresses. We can define the mechanical pressure as $P = -\frac{1}{3} \sum_{i=1}^3 \sigma_{ii}$ and rewrite the Cauchy stress tensor as

$$\boldsymbol{\sigma} = - \begin{pmatrix} P & 0 & 0 \\ 0 & P & 0 \\ 0 & 0 & P \end{pmatrix} + \begin{pmatrix} \sigma_{xx} + P & \tau_{xy} & \tau_{xz} \\ \tau_{yx} & \sigma_{yy} + P & \tau_{yz} \\ \tau_{zx} & \tau_{zy} & \sigma_{zz} + P \end{pmatrix} = -P\mathbf{I} + \boldsymbol{\tau} \quad (\text{D.13})$$

where \mathbf{I} is the identity matrix and $\boldsymbol{\tau}$ is the deviatoric stress tensor.

Using the above identity we can rewrite equation D.11 as

$$\boxed{\rho \frac{\partial \mathbf{v}}{\partial t} + \rho(\mathbf{v} \cdot \nabla \mathbf{v}) = -\nabla P + \nabla \cdot \boldsymbol{\tau} + \mathbf{f}} \quad (\text{D.14})$$

We must now select a particular family of fluids to write the explicit form of $\boldsymbol{\tau}$, namely compressible Newtonian fluids. Indeed, most liquids and gases belong to this family in ordinary conditions. Therefore, we assume that

- (a) $\nabla \cdot \boldsymbol{\tau} = 0$ when the fluid is at rest
- (b) $\boldsymbol{\tau}$ is a linear function of $\nabla \mathbf{v}$
- (c) The fluid is isotropic, and the viscosity coefficient is a scalar

Furthermore, from the conservation of momentum it is possible to prove that the Cauchy stress tensor is symmetric ($\sigma_{ij} = \sigma_{ji}$). As a consequence, also $\boldsymbol{\tau}$ is symmetric ($\tau_{ij} = \tau_{ji}$). Therefore, we can define $\boldsymbol{\tau}$ as $\tau_{ij} = \mu \left(\frac{\partial v_i}{\partial x_j} + \frac{\partial v_j}{\partial x_i} \right)$, where μ is a scalar. From the definition of mechanical pressure and equation D.13 we know that

$$P = -\frac{1}{3} \sum_{i=1}^3 \sigma_{ii} = P - \frac{1}{3} \sum_{i=1}^3 \tau_{ii} = P - \frac{2}{3} \mu \nabla \cdot \mathbf{v} \quad (\text{D.15})$$

the above equation implies that $\nabla \cdot \mathbf{v} = 0$, but this relation holds only for incompressible fluids. Therefore, we have to add a term (the compressible term) to the deviatoric stress tensor for compressible fluids. As a result, we can write

$$\tau_{ij} = \mu \left(\frac{\partial v_i}{\partial x_j} + \frac{\partial v_j}{\partial x_i} \right) + \delta_{ij} \lambda \sum_{k=1}^3 \frac{\partial v_k}{\partial x_k} \quad (\text{D.16})$$

where μ and λ are, respectively, the first and second coefficients of viscosity. For compressible fluids $\lambda = -\frac{2}{3}\mu$ (this is known as *Stokes' hypothesis*).

Therefore, the conservation of momentum equation becomes

$$\rho \frac{\partial \mathbf{v}}{\partial t} + \rho(\mathbf{v} \cdot \nabla \mathbf{v}) = -\nabla P + \nabla \cdot [\mu \nabla \mathbf{v} + \mu(\nabla \mathbf{v})^T] - \frac{2}{3} \nabla \cdot [\mu(\nabla \cdot \mathbf{v})\mathbf{I}] + \mathbf{f} \quad (\text{D.17})$$

D.3 Equation of state

In the following discussion, we assume the mechanical and thermodynamical pressure to be identical. The ideal gas law is

$$PV = nK_B T \quad (\text{D.18})$$

where n is the number of particles that compose the gas, k_B is the Boltzmann constant, and T is the temperature. Experimental evidence shows that for typical acoustic frequencies and amplitudes, the temperature gradients and the thermal conductivity of the fluid are small enough that no significant thermal flux occurs. Therefore, we can approximate the acoustic processes to be adiabatic. In this case, we can rewrite the equation of state as

$$\frac{P}{P_0} = \left(\frac{\rho}{\rho_0} \right)^\gamma \quad (\text{D.19})$$

where P_0 and ρ_0 are, respectively, the rest values of the pressure and the gas density, and γ is the adiabatic coefficient.

D.4 Linearization of variables

We now assume that the fluctuations in density and fluid velocity in the acoustic processes are small compared to the unperturbed values.

$$\rho(\mathbf{x}, t) = \rho_0 + \rho_1(\mathbf{x}, t), \text{ where } \rho_1/\rho_0 \sim 0 \quad (\text{D.20})$$

$$\mathbf{v}(\mathbf{x}, t) = \mathbf{0} + \mathbf{v}_1(\mathbf{x}, t), \text{ where } \mathbf{v}_1 \sim \mathbf{0} \quad (\text{D.21})$$

We can linearize the equation D.19 with a Taylor expansion:

$$P = P_0 + \left. \frac{\partial P}{\partial \rho} \right|_{\rho_0} (\rho - \rho_0) + o(\rho - \rho_0) \quad (\text{D.22})$$

The adiabatic bulk modulus is $B = \rho_0 \left. \frac{\partial P}{\partial \rho} \right|_{\rho_0}$. The speed of sound is defined as $c_s = \sqrt{\frac{B}{\rho_0}}$. Therefore, we obtain the relationship

$$\boxed{P - P_0 = c_s^2(\rho - \rho_0) \quad \text{Equation of state}} \quad (\text{D.23})$$

Using the assumptions of equations D.20–D.21 and neglecting the second-order terms, we can rewrite the continuity equation. The result is

$$\boxed{\frac{\partial \rho_1}{\partial t} + \rho_0 \nabla \cdot (\mathbf{v}_1) = 0 \quad \text{Conservation of mass}} \quad (\text{D.24})$$

Following the same procedure and using equation D.23, we can rewrite the equation of the conservation of momentum as

$$\rho_0 \frac{\partial \mathbf{v}_1}{\partial t} + c_s^2 \nabla \rho_1 - \nabla \cdot \boldsymbol{\tau}_1 = \mathbf{0} \quad (\text{D.25})$$

where we have neglected all body forces \mathbf{f} (such as gravity) and $\boldsymbol{\tau}_1$ is

$$\begin{aligned} \tau_{1ij} &= \mu \left(\frac{\partial v_{1i}}{\partial x_j} + \frac{\partial v_{1j}}{\partial x_i} \right) - \delta_{ij} \frac{2\mu}{3} \sum_{k=1}^3 \frac{\partial v_{1k}}{\partial x_k} = \\ &= \mu \left(\frac{\partial v_{1i}}{\partial x_j} + \frac{\partial v_{1j}}{\partial x_i} \right) + \delta_{ij} \frac{2\mu}{3\rho_0} \frac{\partial \rho_1}{\partial t} \end{aligned} \quad (\text{D.26})$$

where we used equation D.24. The divergence of $\boldsymbol{\tau}_1$ is

$$\begin{aligned} \sum_{i=1}^3 \frac{\partial \tau_{1ij}}{\partial x_i} &= \mu \sum_{i=1}^3 \left(\frac{\partial^2 v_{1i}}{\partial x_i \partial x_j} + \frac{\partial^2 v_{1j}}{\partial x_i \partial x_i} \right) + \frac{2\mu}{3\rho_0} \frac{\partial^2 \rho_1}{\partial x_j \partial t} = \\ &= 2\mu \frac{\partial}{\partial x_j} \sum_{i=1}^3 \frac{\partial v_{1i}}{\partial x_i} + \frac{2\mu}{3\rho_0} \frac{\partial^2 \rho_1}{\partial x_j \partial t} = -\frac{4\mu}{3\rho_0} \frac{\partial^2 \rho_1}{\partial x_j \partial t} \end{aligned} \quad (\text{D.27})$$

where we used equation D.24 and the fact¹ that $\sum_{i=1}^3 \frac{\partial^2 v_{1j}}{\partial x_i \partial x_i} = \sum_{i=1}^3 \frac{\partial^2 v_{1i}}{\partial x_i \partial x_j}$. Therefore, the equation for the conservation of momentum becomes

$$\boxed{\rho_0 \frac{\partial \mathbf{v}_1}{\partial t} + c_s^2 \nabla \rho_1 + \nu \nabla \frac{\partial \rho_1}{\partial t} = \mathbf{0} \quad \text{Conservation of momentum}} \quad (\text{D.28})$$

where we have defined the kinematic viscosity $\nu = \frac{4\mu}{3\rho_0}$.

¹It follows from $\nabla \times (\nabla \times \mathbf{v}) = \mathbf{0}$.

D.5 The damped wave equation

If we calculate the divergence of equation D.28, we get

$$\rho_0 \frac{\partial}{\partial t} \nabla \cdot \mathbf{v}_1 + c_s^2 \nabla^2 \rho_1 + \nu \nabla^2 \frac{\partial \rho_1}{\partial t} = 0 \quad (\text{D.29})$$

where we used the fact that $\nabla \cdot \nabla = \nabla^2$. Using, once again, equation D.24, we obtain the acoustic damped wave equation

$$\boxed{\frac{\partial^2 \rho_1}{\partial t^2} - c_s^2 \nabla^2 \rho_1 - \nu \nabla^2 \frac{\partial \rho_1}{\partial t} = 0} \quad (\text{D.30})$$



Solution of the Acoustic Wave Equation

In this appendix, we solve the following one-dimensional damped wave equation

$$\frac{\partial^2 \rho}{\partial t^2} - \frac{\partial^2}{\partial x^2} \left(c_s^2 \rho + \nu \frac{\partial \rho}{\partial t} \right) = 0 \quad (\text{E.1})$$

where ρ is the oscillation density relative to the unperturbed case. In addition, we assume the following initial conditions

$$\rho(x, t) \Big|_{t=0} = 0 \quad (\text{E.2})$$

$$\frac{\partial \rho}{\partial t} \Big|_{t=0} = 0 \quad (\text{E.3})$$

that represent an initial state at rest.

E.1 Actuators in phase

E.1.1 Boundary conditions

$$v(x, t) \Big|_{x=0} = v_a \cos(\Omega_d t) \quad (\text{E.4})$$

$$v(x, t) \Big|_{x=L} = v_a \cos(\Omega_d t) \quad (\text{E.5})$$

If we assume that $v(x, t) = f(x)g(t)$, we can specialize the conservation of momentum law in $x = 0$ and $x = L$, defining $\psi(t) = \left. \frac{\partial p}{\partial x} \right|_{x=0,L}$

$$\underbrace{\rho_0 \frac{\partial v}{\partial t} \Big|_{x=0,L}}_{=-\Omega_d \rho_0 v_a \sin(\Omega_d t)} + c_s^2 \psi + \nu \frac{\partial \psi}{\partial t} = 0 \quad (\text{E.6})$$

therefore, we get a non-homogeneous first-order ordinary differential equation

$$\nu \frac{\partial \psi}{\partial t} + c_s^2 \psi = \Omega_d \rho_0 v_a \sin(\Omega_d t) \quad (\text{E.7})$$

the solution of this ODE is the sum of the solution of the homogeneous equation and a particular solution. The characteristic equation associated with the homogeneous ODE is

$$\nu \alpha + c_s^2 = 0 \implies \alpha = -\frac{c_s^2}{\nu} \quad (\text{E.8})$$

therefore, the homogeneous solution is

$$\psi_o(t) = C \exp\left(-\frac{c_s^2 t}{\nu}\right) \xrightarrow{t \rightarrow +\infty} 0 \quad (\text{E.9})$$

To calculate the particular solution, we can use the Fourier transform method. The Fourier transform of E.7 is

$$\begin{aligned} i\nu\Omega\tilde{\psi}(\Omega) + c_s^2\tilde{\psi}(\Omega) &= \rho_0\Omega_d v_a \frac{1}{2i} \left[\frac{\delta(\Omega - \Omega_d) - \delta(\Omega + \Omega_d)}{2\pi} \right] \\ \tilde{\psi}(\Omega) &= \frac{\rho_0\Omega_d v_a}{4\pi i} \left[\frac{\delta(\Omega - \Omega_d) - \delta(\Omega + \Omega_d)}{i\nu\Omega + c_s^2} \right] \end{aligned} \quad (\text{E.10})$$

the inverse Fourier transform of $\tilde{\psi}(\Omega)$ is

$$\begin{aligned} \psi(t) &= \frac{\rho_0\Omega_d v_a}{2i} \left[\frac{e^{i\Omega_d t}}{c_s^2 + i\nu\Omega_d} - \frac{e^{-i\Omega_d t}}{c_s^2 - i\nu\Omega_d} \right] = \\ &= \frac{\rho_0\Omega_d v_a}{c_s^4 + \nu^2\Omega_d^2} \frac{c_s^2(e^{i\Omega_d t} - e^{-i\Omega_d t}) - i\nu\Omega_d(e^{i\Omega_d t} + e^{-i\Omega_d t})}{2i} \end{aligned} \quad (\text{E.11})$$

finally, the particular solution is

$$\psi_p(t) = \frac{\rho_0\Omega_d v_a}{c_s^4 + \nu^2\Omega_d^2} [c_s^2 \sin(\Omega_d t) - \nu\Omega_d \cos(\Omega_d t)] \quad (\text{E.12})$$

If we consider only the steady-state solution, we can neglect the exponential decaying part. Therefore, we can now write the boundary condition in the Neumann form

$$\left. \frac{\partial \rho}{\partial x} \right|_{x=0,L} = \underbrace{\frac{\rho_0 \Omega_d v_a}{c_s^4 + \nu^2 \Omega_d^2} [c_s^2 \sin(\Omega_d t) - \nu \Omega_d \cos(\Omega_d t)]}_{=f(t)} \quad (\text{E.13})$$

To make these boundary conditions homogeneous, we define a new function $u(t)$ so that

$$\rho(x, t) = u(x, t) + \int_0^x f(t) dx = u(x, t) + x f(t) \quad (\text{E.14})$$

using this substitution in equation E.7 we have

$$\left. \frac{\partial \rho}{\partial x} \right|_{x=0,L} = \left. \frac{\partial u}{\partial x} \right|_{x=0,L} + f(t) = f(t) \implies \boxed{\left. \frac{\partial u}{\partial x} \right|_{x=0,L} = 0} \quad (\text{E.15})$$

Using the substitution of equation E.14 in equation E.1, we get

$$\boxed{\frac{\partial^2 u}{\partial t^2} - \frac{\partial^2}{\partial x^2} \left(c_s^2 u + \nu \frac{\partial u}{\partial t} \right) = S(x, t)} \quad (\text{E.16})$$

where the source term $S(x, t)$ is

$$S(x, t) = -x \frac{\partial^2 f}{\partial t^2} = x \frac{\rho_0 \Omega_d^3 v_a}{c_s^4 + \nu^2 \Omega_d^2} [c_s^2 \sin(\Omega_d t) - \nu \Omega_d \cos(\Omega_d t)] \quad (\text{E.17})$$

E.1.1.1 Homogeneous solution

Assume that the solution can be factorized as $u(x, t) = X(x)T(t)$. The homogeneous equation associated to E.16 becomes

$$X \frac{\partial^2 T}{\partial t^2} - c_s^2 T \frac{\partial^2 X}{\partial x^2} - \nu \frac{\partial^2 X}{\partial x^2} \frac{\partial T}{\partial t} = 0 \quad (\text{E.18})$$

this equation can be rewritten as

$$\frac{\frac{\partial^2 X}{\partial x^2}}{X} = \frac{\frac{\partial^2 T}{\partial t^2}}{c_s^2 T + \nu \frac{\partial T}{\partial t}} \quad (\text{E.19})$$

since the above identity must be valid for every possible value of both x and t , both terms have to be equal to the same constant r . Therefore, we obtain two ordinary differential equations

$$\frac{\partial^2 X}{\partial x^2} = r X \quad (\text{E.20})$$

$$\frac{\partial^2 T}{\partial t^2} = r \left(c_s^2 T + \nu \frac{\partial T}{\partial t} \right) \quad (\text{E.21})$$

the characteristic equation associated to E.20 is

$$\beta^2 = r \implies \beta = \pm\sqrt{r} \quad (\text{E.22})$$

therefore, the solution is

$$X(x) = ae^{\sqrt{r}x} + be^{-\sqrt{r}x} \quad (\text{E.23})$$

we now apply the boundary conditions

$$\left. \frac{\partial u}{\partial x} \right|_{x=0,L} = 0 \implies T(t) \left. \frac{\partial X}{\partial x} \right|_{x=0,L} = 0 \quad \forall t \implies \left. \frac{\partial X}{\partial x} \right|_{x=0,L} = 0 \quad (\text{E.24})$$

this implies the following system of equations

$$\begin{cases} a = b & \text{when } x = 0 \\ ae^{\sqrt{r}L} - be^{-\sqrt{r}L} = 0 & \text{when } x = L \end{cases} \quad (\text{E.25})$$

substituting the first equation into the second one, we get

$$e^{\sqrt{r}L}(1 - e^{-2\sqrt{r}L}) = 0 \implies 2\sqrt{r}L = i2\pi n, \text{ with } n \in \mathbb{Z} \quad (\text{E.26})$$

therefore, we can redefine r such as

$$\sqrt{r} = iK_n = i\frac{\pi n}{L} \quad (\text{E.27})$$

therefore, the solution becomes

$$\boxed{X(x) = C \cos(K_n x)} \quad (\text{E.28})$$

Using this result, we can now solve the differential equation E.21

$$\frac{\partial^2 T}{\partial t^2} + K_n^2 \nu \frac{\partial T}{\partial t} + K_n^2 c_s^2 T = 0 \quad (\text{E.29})$$

that is the equation of a damped harmonic oscillator with angular frequency $\Omega_n = K_n c_s$. The characteristic equation associated is

$$\gamma^2 + K_n^2 \nu \gamma + K_n^2 c_s^2 = 0 \quad (\text{E.30})$$

whose solution are

$$\gamma = -\frac{K_n^2 \nu}{2} \pm \frac{\sqrt{K_n^4 \nu^2 - 4K_n^2 c_s^2}}{2} \underset{\nu \rightarrow 0}{\sim} -\frac{K_n^2 \nu}{2} \pm i \underbrace{\frac{\sqrt{4K_n^2 c_s^2 - K_n^4 \nu^2}}{2}}_{=\Omega'_n} \quad (\text{E.31})$$

where we have assumed that the coefficient is small enough to have $\nu < \frac{2c_s}{K_n}$. Therefore the solution is

$$T(t) = \exp\left(-\frac{K_n^2 \nu t}{2}\right) [A \sin(\Omega'_n t) + B \cos(\Omega'_n t)] \quad (\text{E.32})$$

E.1.1.2 Complete solution

We decompose the functions $u(x, t)$ and $S(x, t)$ over the eigenfunctions E.28 of the homogeneous differential equation

$$u(x, t) = \sum_{n=1}^{+\infty} u_n(t) X_n(x) = \sum_{n=1}^{+\infty} u_n(t) \cos(K_n x) \quad (\text{E.33})$$

$$S(x, t) = \sum_{n=1}^{+\infty} s_n(t) X_n(x) = \sum_{n=1}^{+\infty} s_n(t) \cos(K_n x) \quad (\text{E.34})$$

where $s_n(t)$ is

$$\begin{aligned} s_n(t) &= \frac{2}{L} \int_0^L S(x, t) \cos(K_n x) dx = \\ &= \frac{2}{L} \frac{\rho_0 \Omega_d^3 v_a}{c_s^4 + \nu^2 \Omega_d^2} [c_s^2 \sin(\Omega_d t) - \nu \Omega_d \cos(\Omega_d t)] \int_0^L x \cos(K_n x) dx = \\ &= \frac{2}{L} \frac{\rho_0 \Omega_d^3 v_a}{c_s^4 + \nu^2 \Omega_d^2} [c_s^2 \sin(\Omega_d t) - \nu \Omega_d \cos(\Omega_d t)] \frac{1}{K_n^2} [\cos(\pi n) - 1] = \\ &= \frac{2}{L} \frac{\rho_0 \Omega_d^3 v_a}{c_s^4 + \nu^2 \Omega_d^2} [c_s^2 \sin(\Omega_d t) - \nu \Omega_d \cos(\Omega_d t)] \frac{1}{K_n^2} [(-1)^n - 1] \end{aligned} \quad (\text{E.35})$$

where we have used the fact that $K_n = \frac{\pi n}{L}$. We can now rewrite equation E.17 as

$$\sum_{n=1}^{+\infty} \ddot{u}_n(t) \cos(K_n x) - \sum_{n=1}^{+\infty} K_n^2 \nu \dot{u}_n(t) \cos(K_n x) - \sum_{n=1}^{+\infty} K_n^2 c_s^2 u_n(t) \cos(K_n x) = \sum_{n=1}^{+\infty} s_n(t) \cos(K_n x) \quad (\text{E.36})$$

where we have identified the dot symbol as the time derivative. We can now exploit the orthogonality of the trigonometric functions. If we multiply both the left and right-hand terms of the above equation with $\cos(K_n x)$ and integrate them with respect to x on a period, we get

$$\ddot{u}_n(t) + K_n^2 \nu \dot{u}_n(t) + K_n^2 c_s^2 u_n(t) = s_n(t) \quad (\text{E.37})$$

this is the differential equation of a driven harmonic oscillator. We already solved the associated homogeneous equation, whose solution is

$$u_{on}(t) = \exp\left(-\frac{K_n^2 \nu t}{2}\right) [A_0 \sin(\Omega'_n t) + B_0 \cos(\Omega'_n t)] \quad (\text{E.38})$$

where the constants A_0 and B_0 can be calculated using the initial conditions E.2 and E.3. To obtain the particular solution, we calculate the Fourier transform of equation E.37, that is

$$-\Omega^2 \tilde{u}_n(\Omega) + i\Omega K_n^2 \nu \tilde{u}_n(\Omega) + K_n^2 c_s^2 u_n(\Omega) = \tilde{s}_n(\Omega) \quad (\text{E.39})$$

solving with respect to \tilde{u}_n , we have

$$\begin{aligned} \tilde{u}_n(\Omega) &= \frac{\tilde{s}_n(\Omega)}{\Omega_n^2 - \Omega^2 + i\Omega\nu K_n^2} = \\ &= \underbrace{\frac{(-1)^n - 1}{2\pi K_n^2 L} \frac{2\rho_0 \Omega_d^3 \nu_a}{c_s^4 + \nu^2 \Omega_d^2}}_{=A_n/2\pi} \left[\frac{c_s^2 \delta(\Omega - \Omega_d) - \delta(\Omega + \Omega_d)}{2i \frac{\Omega_n^2 - \Omega^2 + i\Omega\nu K_n^2}{\Omega_n^2 - \Omega^2 + i\Omega\nu K_n^2}} - \frac{\nu\Omega_d \delta(\Omega - \Omega_d) + \delta(\Omega + \Omega_d)}{2 \frac{\Omega_n^2 - \Omega^2 + i\Omega\nu K_n^2}{\Omega_n^2 - \Omega^2 + i\Omega\nu K_n^2}} \right] \end{aligned} \quad (\text{E.40})$$

calculating the inverse Fourier transform of $\tilde{u}_n(\Omega)$ we obtain

$$\begin{aligned} u_{pn}(t) &= A_n \left[\left(\frac{c_s^2}{2i} - \frac{\nu\Omega_d}{2} \right) \frac{e^{i\Omega_d t}}{\Omega_n^2 - \Omega_d^2 + i\Omega_d \nu K_n^2} - \left(\frac{c_s^2}{2i} + \frac{\nu\Omega_d}{2} \right) \frac{e^{-i\Omega_d t}}{\Omega_n^2 - \Omega_d^2 - i\Omega_d \nu K_n^2} \right] = \\ &= A_n \left[\left(\frac{c_s^2}{2i} - \frac{\nu\Omega_d}{2} \right) \frac{e^{i\Omega_d t} (\Omega_n^2 - \Omega_d^2 - i\Omega_d \nu K_n^2)}{(\Omega_n^2 - \Omega_d^2)^2 + \Omega_d^2 \nu^2 K_n^4} - \left(\frac{c_s^2}{2i} + \frac{\nu\Omega_d}{2} \right) \frac{e^{-i\Omega_d t} (\Omega_n^2 - \Omega_d^2 + i\Omega_d \nu K_n^2)}{(\Omega_n^2 - \Omega_d^2)^2 + \Omega_d^2 \nu^2 K_n^4} \right] = \\ &= A_n c_s^2 \underbrace{\frac{\Omega_n^2 - \Omega_d^2}{(\Omega_n^2 - \Omega_d^2)^2 + \Omega_d^2 \nu^2 K_n^4}}_{=B_n} \frac{e^{i\Omega_d t} - e^{-i\Omega_d t}}{2i} + \\ &\quad - A_n c_s^2 \underbrace{\frac{\Omega_d \nu K_n^2}{(\Omega_n^2 - \Omega_d^2)^2 + \Omega_d^2 \nu^2 K_n^4}}_{=C_n} \frac{e^{i\Omega_d t} + e^{-i\Omega_d t}}{2} + \\ &\quad - A_n \nu \Omega_d \underbrace{\frac{\Omega_n^2 - \Omega_d^2}{(\Omega_n^2 - \Omega_d^2)^2 + \Omega_d^2 \nu^2 K_n^4}}_{=D_n} \frac{e^{i\Omega_d t} + e^{-i\Omega_d t}}{2} + \\ &\quad - A_n \nu \Omega_d \underbrace{\frac{\Omega_d \nu K_n^2}{(\Omega_n^2 - \Omega_d^2)^2 + \Omega_d^2 \nu^2 K_n^4}}_{=E_n} \frac{e^{i\Omega_d t} - e^{-i\Omega_d t}}{2i} = \\ &= A_n [\sin(\Omega_d t)(B_n - E_n) - \cos(\Omega_d t)(C_n + D_n)] \end{aligned} \quad (\text{E.41})$$

Therefore, the complete solution is

$$\rho(x, t) = x f(t) + \sum_{n=0}^{+\infty} [u_{on}(t) + u_{pn}(t)] \cos(K_n x) \quad (\text{E.42})$$

We focus our attention on the resonant ($\Omega_d \rightarrow \Omega_n$) and low viscosity ($\nu \rightarrow 0$) case. In this situation, we have

$$A_n \sim \frac{2\rho_0\Omega_n^3 v_a}{K_n^2 L c_s^4} [(-1)^n - 1] \quad (\text{E.43})$$

$$B_n \sim 0 \quad (\text{E.44})$$

$$C_n \sim \frac{c_s^2}{\Omega_n \nu K_n^2} \rightarrow +\infty \quad (\text{E.45})$$

$$D_n \sim 0 \quad (\text{E.46})$$

$$E_n \sim \frac{1}{\Omega_n K_n^4} \quad (\text{E.47})$$

we see that the coefficient term C_n is dominant. In this case, we can approximate the solution to $\rho_n(t) \sim -A_n C_n \cos(K_n x) \cos(\Omega_n t)$. Explicitly

$$\rho_n(x, t) = [1 - (-1)^n] \frac{2\rho_0 v_a c_s^2}{\nu L \Omega_n^2} \cos(K_n x) \cos(\Omega_n t) \quad (\text{E.48})$$

where we remind that $K_n = \frac{\pi n}{L}$ and $\Omega_n = c_s K_n$.

E.2 Actuators in phase opposition

E.2.1 Boundary conditions

$$v(x, t) \Big|_{x=0} = v_a \cos(\Omega_d t) \quad (\text{E.49})$$

$$v(x, t) \Big|_{x=L} = -v_a \cos(\Omega_d t) \quad (\text{E.50})$$

following the same procedure of the previous case, we obtain the following boundary conditions

$$\frac{\partial \rho}{\partial x} \Big|_{x=0} = f(t) \quad (\text{E.51})$$

$$\frac{\partial \rho}{\partial x} \Big|_{x=L} = -f(t) \quad (\text{E.52})$$

where $f(t)$ is the same as before. We define a new function $u(t)$ so that

$$\rho(x, t) = u(x, t) + x f(t) - \frac{x^2}{L} f(t) \quad (\text{E.53})$$

so

$$\left. \frac{\partial \rho}{\partial x} \right|_{x=0} = \left. \frac{\partial u}{\partial x} \right|_{x=0} + f(t) = f(t) \implies \left. \frac{\partial u}{\partial x} \right|_{x=0} = 0 \quad (\text{E.54})$$

$$\left. \frac{\partial \rho}{\partial x} \right|_{x=L} = \left. \frac{\partial u}{\partial x} \right|_{x=L} + f(t) - \frac{2L}{L} f(t) = -f(t) \implies \left. \frac{\partial u}{\partial x} \right|_{x=L} = 0 \quad (\text{E.55})$$

Using the substitution of equation E.53 in equation E.1, we get again

$$\frac{\partial^2 u}{\partial t^2} - \frac{\partial^2}{\partial x^2} \left(c_s^2 u + \nu \frac{\partial u}{\partial t} \right) = S(x, t) \quad (\text{E.56})$$

where in this case the source term $S(x, t)$ is

$$\begin{aligned} S(x, t) &= - \left[\left(x - \frac{x^2}{L} \right) \frac{\partial^2 f}{\partial t^2} + \frac{2\nu}{L} \frac{\partial f}{\partial t} + \frac{2c_s^2}{L} f(t) \right] = \\ &= - \frac{\rho_0 \Omega_d \nu a}{c_s^4 + \nu^2 \Omega_d^2} \left[\left(x - \frac{x^2}{L} \right) \left(-\Omega_d^2 c_s^2 \sin(\Omega_d t) + \nu \Omega_d^3 \cos(\Omega_d t) \right) + \right. \\ &\quad \left. + \frac{2\nu}{L} \left(\Omega_d c_s^2 \cos(\Omega_d t) + \nu \Omega_d^2 \sin(\Omega_d t) \right) + \right. \\ &\quad \left. + \frac{2c_s^2}{L} \left(c_s^2 \sin(\Omega_d t) - \nu \Omega_d \cos(\Omega_d t) \right) \right] \end{aligned} \quad (\text{E.57})$$

that can be rewritten as

$$S(x, t) = a(t) + b(t)x + c(t)x^2 \quad (\text{E.58})$$

with the appropriate choice of the functions $a(t)$, $b(t)$, and $c(t)$.

E.2.2 Complete solution

We have already solved the homogeneous wave equation, and we know the eigenfunctions $X(x) = \cos(K_n x)$. Therefore, we can calculate the coefficients $s_n(t)$ of the eigenfunction expansion of the source term

$$\begin{aligned} s_n(t) &= \frac{2}{L} \int_0^L S(x, t) \cos(K_n x) dx = \\ &= \frac{2}{L} a(t) \underbrace{\int_0^L \cos(K_n x) dx}_{=0} + \frac{2}{L} b(t) \underbrace{\int_0^L x \cos(K_n x) dx}_{=\frac{1}{K_n^2} [(-1)^n - 1]} + \frac{2}{L} c(t) \int_0^L x^2 \cos(K_n x) dx \end{aligned} \quad (\text{E.59})$$

where we have used the results of the previous section. The last integral that we have to calculate is

$$\begin{aligned}
 \int_0^L x^2 \cos(K_n x) dx &= \frac{1}{K_n} [\sin(K_n x) x^2]_0^L - \frac{1}{K_n} \int_0^L 2x \cos(K_n x) dx = \\
 &= \frac{1}{K_n^2} [\cos(K_n x) 2x]_0^L - \frac{1}{K_n^2} \int_0^L 2 \cos(K_n x) dx = \\
 &= \frac{2L}{K_n^2} \cos(K_n L) = \frac{2L}{K_n^2} (-1)^n
 \end{aligned} \tag{E.60}$$

since $c(t) = -\frac{b(t)}{L}$, we have that

$$s_n(t) = \frac{2}{L} b(t) \frac{1}{K_n^2} [(-1)^n - 1 - 2(-1)^n] = \frac{2b(t)}{LK_n^2} [(-1)^{n+1} - 1] \tag{E.61}$$

as a result, we get

$$s_n(t) = [(-1)^{n+1} - 1] \frac{2}{LK_n^2} \frac{\rho_0 \Omega_d^3 v_a}{c_s^4 + \nu^2 \Omega_d^2} (c_s^2 \sin(\Omega_d t) - \nu \Omega_d \cos(\Omega_d t)) \tag{E.62}$$

Therefore, the approximate solution is obtained just substituting $[1 - (-1)^n] \mapsto [1 - (-1)^{n+1}]$ in the solution of the previous case

$$\boxed{\rho_n(x, t) = [1 - (-1)^{n+1}] \frac{2\rho_0 v_a c_s^2}{\nu L \Omega_n^2} \cos(K_n x) \cos(\Omega_n t)} \tag{E.63}$$

E.3 Reflecting plate

E.3.1 Boundary conditions

$$v(x, t) \Big|_{x=0} = v_a \cos(\Omega_d t) \tag{E.64}$$

$$\frac{\partial \rho}{\partial x} \Big|_{x=L} = 0 \tag{E.65}$$

following the same procedure of the first case, we obtain the following boundary conditions

$$\frac{\partial \rho}{\partial x} \Big|_{x=0} = f(t) \tag{E.66}$$

$$\frac{\partial \rho}{\partial x} \Big|_{x=L} = 0 \tag{E.67}$$

where $f(t)$ is the same as before. We define a new function $u(t)$ so that

$$\rho(x, t) = u(x, t) + xf(t) - \frac{x^2}{2L}f(t) \quad (\text{E.68})$$

so the source term $S(x, t)$ is

$$\begin{aligned} S(x, t) &= - \left[\left(x - \frac{x^2}{2L} \right) \frac{\partial^2 f}{\partial t^2} + \frac{2\nu}{L} \frac{\partial f}{\partial t} + \frac{2c_s^2}{L} f(t) \right] = \\ &= - \frac{\rho_0 \Omega_d v_a}{c_s^4 + \nu^2 \Omega_d^2} \left[\left(x - \frac{x^2}{2L} \right) \left(-\Omega_d^2 c_s^2 \sin(\Omega_d t) + \nu \Omega_d^3 \cos(\Omega_d t) \right) + \right. \\ &\quad \left. + \frac{2\nu}{L} \left(\Omega_d c_s^2 \cos(\Omega_d t) + \nu \Omega_d^2 \sin(\Omega_d t) \right) + \right. \\ &\quad \left. + \frac{2c_s^2}{L} \left(c_s^2 \sin(\Omega_d t) - \nu \Omega_d \cos(\Omega_d t) \right) \right] \end{aligned} \quad (\text{E.69})$$

that, similarly as before, can be rewritten as

$$S(x, t) = a(t) + b(t)x + c(t)x^2 \quad (\text{E.70})$$

with the appropriate choice of the functions $a(t)$, $b(t)$, and $c(t)$.

E.3.2 Complete solution

This case is analogous to the previous one, with the difference that now $c(t) = -\frac{b(t)}{2L}$. Therefore, we have that

$$s_n(t) = \frac{2}{L} b(t) \frac{1}{K_n^2} [(-1)^n - 1 - (-1)^n] = -\frac{2b(t)}{LK_n^2} \quad (\text{E.71})$$

therefore, now

$$s_n(t) = \frac{2}{LK_n^2} \frac{\rho_0 \Omega_d v_a}{c_s^4 + \nu^2 \Omega_d^2} \left(\nu \Omega_d^3 \cos(\Omega_d t) - \Omega_d^2 c_s^2 \sin(\Omega_d t) \right) \quad (\text{E.72})$$

Therefore, the approximate solution is obtained just substituting $[1 - (-1)^n] \mapsto 1$ in the solution of the first case

$$\boxed{\rho_n(x, t) = \frac{2\rho_0 v_a c_s^2}{\nu L \Omega_n^2} \cos(K_n x) \cos(\Omega_n t)} \quad (\text{E.73})$$

E.4 Traveling wave

E.4.1 Boundary conditions

In this case, we apply a condition only on a single boundary

$$v(x, t) \Big|_{x=0} = v_a \cos(\Omega_d t) \quad (\text{E.74})$$

which translates to the following boundary condition

$$\frac{\partial \rho}{\partial x} \Big|_{x=0} = f(t) \quad (\text{E.75})$$

where $f(t)$ is the same as before.

E.4.2 Complete solution

In order to find the solution, we use the following *ansatz*:

$$\rho(x, t) = A \exp(ikx - i\Omega t) \quad (\text{E.76})$$

substituting this expression into the wave equation, we obtain

$$-\Omega^2 + c_s^2 k^2 - ik^2 \Omega \nu = 0 \quad (\text{E.77})$$

which leads to the following dispersion relation

$$k^2 = \Omega^2 \frac{c_s^2 + i\Omega \nu}{c_s^4 + \Omega^2 \nu^2} \quad (\text{E.78})$$

We now write the wave number explicitly as the sum of the real and imaginary part $k = k_R + ik_I$, thus obtaining the following system of equations

$$\begin{cases} k_R k_I = \frac{\Omega^3 \nu}{2(c_s^4 + \Omega^2 \nu^2)} \\ k_R^2 - k_I^2 = \frac{\Omega^2 c_s^2}{c_s^4 + \Omega^2 \nu^2} \end{cases} \quad (\text{E.79})$$

whose solution is

$$\begin{cases} k_I = \sqrt{\frac{\Omega^2 c_s^2}{2(c_s^4 + \Omega^2 \nu^2)} \left(\sqrt{1 + \left(\frac{\Omega \nu}{c_s}\right)^2} - 1 \right)} \\ \sqrt{\frac{\Omega^2 c_s^2}{2(c_s^4 + \Omega^2 \nu^2)} \left(\sqrt{1 + \left(\frac{\Omega \nu}{c_s}\right)^2} - 1 \right)} \end{cases} \quad (\text{E.80})$$

for small viscosities ($\nu \ll c_s^2/\Omega$), we can simplify the solution can as follows

$$\begin{cases} k_I = \frac{\Omega^2 \nu}{2c^3} \\ k_R = \frac{\Omega}{c_s} \end{cases} \quad (\text{E.81})$$

The generic solution can be found by taking the real part of the ansatz

$$\rho(x, t) = \exp(-k_I x) [a \cos(k_R x - \Omega t) + b \sin(k_R x - \Omega t)] \quad (\text{E.82})$$

The amplitude of the wave can be found using the boundary conditions. The final result is

$$\rho(x, t) = \frac{\rho_0 c_s v_a}{\sqrt{c_s^4 + \nu^2 \Omega^2}} \exp(-k_I x) \sin(k_R x - \Omega t) \quad (\text{E.83})$$

where we neglected a phase shift unimportant for the description of the steady state.



Derivation of the Diffraction Patterns

In this appendix, we use the scalar diffraction theory to model the interaction of light with an acoustic wave. More in detail, we define the transmittance function of the acoustic cavity, and we find the diffraction patterns both in the near and in the far-field.

F.1 Acousto-optic interaction regime

To determine the type of diffraction that occurs when the light passes through the acoustic cavity, we can use the Klein-Cook parameter defined as

$$Q = \frac{2\pi\lambda l}{n_0\Lambda^2} \quad (\text{F.1})$$

being n_0 the static refractive index of the medium, λ the wavelength of the laser beam, l the length of the actuator (≈ 2 cm), and Λ the wavelength of the acoustic wave. Considering visible light and a typical driving frequency of 1 MHz (with a corresponding wavelength of the acoustic wave of about 1.5 mm), we get $Q \approx 0.03$. At this condition ($Q \ll 1$), the acoustic wave acts as an optically thin grating, legitimizing the use of the scalar diffraction theory.

F.2 Transmittance function

The m^{th} resonant solution of the acoustic wave equation is

$$\Delta\rho_m(x, t) = \rho_m \cos(K_m x) \cos(\Omega_m t) \quad (\text{F.2})$$

where the oscillation amplitude is

$$\rho_m = [1 - (-1)^m] \frac{2\rho_0 d_{33} V c_s^2}{\nu L \Omega_m}, \quad \rho_m = [1 - (-1)^{m+1}] \frac{2\rho_0 d_{33} V c_s^2}{\nu L \Omega_m}, \quad \rho_m = \frac{2\rho_0 d_{33} V c_s^2}{\nu L \Omega_m} \quad (\text{F.3})$$

depending on the boundary conditions. In the above equations, we assumed that $v_a = \Omega_m d_{33} V$, where V is the voltage amplitude applied to the piezoelectric plates and $d_{\alpha\beta}$ is the piezoelectric charge tensor.

To relate density and refractive index, we use the Lorentz-Lorenz equation

$$\frac{n^2 - 1}{n^2 + 2} = \frac{4\pi}{3} N \langle \alpha \rangle = A\rho \quad (\text{F.4})$$

where we have indicated with N the number of molecules per unit volume and with $\langle \alpha \rangle$ the mean polarizability. A is the molar refractivity, that we assume to be independent from the density. We can rewrite the above equation as

$$n(\rho) = \sqrt{\frac{1 + 2A\rho}{1 - A\rho}} \quad (\text{F.5})$$

Acoustic perturbations are small. Thus, we can linearize this equation performing a Taylor expansion. The first derivative of the refractive index is

$$\left. \frac{dn}{d\rho} \right|_{\rho_0} = \frac{3A}{2n_0} \frac{1}{(1 - A\rho_0)^2} \quad (\text{F.6})$$

where $n_0 = n(\rho_0)$ and ρ_0 are, respectively, the static refractive index and density of water. We now use equation F.4 evaluated at ρ_0 to substitute for A . The final result is

$$n(\rho_0 + \Delta\rho_m) \sim n_0 + \left. \frac{dn}{d\rho} \right|_{\rho_0} \Delta\rho_m = n_0 + \frac{n_0^4 + n_0^2 - 2}{6n_0} \frac{\Delta\rho_m}{\rho_0} \quad (\text{F.7})$$

Combining equations F.2 and F.7 it is possible to obtain an analytic expression for the instantaneous refractive index in the cavity:

$$n(x, t) = n_0 + \underbrace{\frac{\rho_m}{\rho_0} \frac{n_0^4 + n_0^2 - 2}{6n_0}}_{\Delta n(x, t)} \cos(K_m x) \cos(\Omega_m t) \quad (\text{F.8})$$

The optical path length traveled by a light beam after passing through an acoustic cavity (with the beam propagation direction being orthogonal to the sound waves) is $\delta(x, t) = ln_0 + l\Delta n(x, t)$. However, the ln_0 term generates a constant phase factor, which we can neglect to calculate the intensity. Therefore, we can describe the optical cavity with the following complex transmittance function

$$t_A = \exp [ikl\Delta n(x, y, t)] \quad (\text{F.9})$$

In order to simplify the following calculations, it is helpful to rewrite the transmittance function t_A for a reference frame centered in the middle of the device. The result is

$$t_A = \exp \left[i k l n_m \cos(\Omega_m t) \sin \left(K_m x + \frac{m+1}{2} \pi \right) \right]. \quad (\text{F.10})$$

It is advantageous to rewrite this exponential function using the Bessel generating function

$$\exp [(\chi/2)(\tau - 1/\tau)] = \sum_{q=-\infty}^{+\infty} J_q(\chi) \tau^q. \quad (\text{F.11})$$

Using the following identifications

$$\chi = k l n_m \cos(\Omega_m t) \quad (\text{F.12a})$$

$$\tau = \exp \left(i K_m x + i \pi \frac{m+1}{2} \right) \quad (\text{F.12b})$$

we obtain

$$t_A(x) = \sum_{q=-\infty}^{+\infty} J_q [k l n_m \cos(\Omega_m t)] \exp \left(i q \pi \frac{m+1}{2} \right) \exp(i K_m q x) \quad (\text{F.13})$$

In case both axes are driven, the induced density variations are the solutions of two independent wave equations (one for each axis). Therefore, we can write the total density as the superposition of the two solutions

$$\rho(x, y, t) = \rho_0 + \rho_m \cos(K_m x) \cos(\Omega_m t) + \rho_j \cos(k_j x) \cos(\omega_j t) \quad (\text{F.14})$$

Repeating the previous calculations with the above expression for the density, we obtain the following transmittance function

$$\begin{aligned} t_A(x, y) &= \sum_{q=-\infty}^{+\infty} J_q [k l n_m \cos(\Omega_m t)] \exp \left(i q \pi \frac{m+1}{2} \right) \exp(i K_m q x) \times \\ &\times \sum_{p=-\infty}^{+\infty} J_p [k l n_j \cos(\omega_j t)] \exp \left(i p \pi \frac{j+1}{2} \right) \exp(i k_j p x) \end{aligned} \quad (\text{F.15})$$

F.3 Gaussian beam

In the following sections, we consider the diffraction of a single Gaussian beam traveling along the z -axis and hitting the center of the acoustic cavity. The complete expression is

$$U(r, z) = U_0 \frac{w_0}{w(z)} \exp \left[\frac{-r^2}{w^2(z)} \right] \exp \left[-i \left(k z + k \frac{r^2}{2R(z)} - \psi(z) \right) \right] \quad (\text{F.16})$$

where w_0 is the beam waist, w the beam width, k is the wavenumber, R is the radius of curvature, and ψ is the Guoy phase. However, in the subsequent discussion, we consider the case of a collimated beam. Thus, we can neglect the phase contributions from the radius of curvature and the Guoy phase. The expression of the collimated beam can be approximated to

$$U(r, 0) = U_0 \exp\left(-\frac{r^2}{w^2}\right) \quad (\text{F.17})$$

where we neglected phase factors that do not depend on r and grouped together constant amplitude terms.

F.4 Fraunhofer diffraction

The scalar field emerging from the acoustic cavity is the product of equations F.17 and F.13. The full expression is

$$U(x, y, 0) = U_0 \sum_{q=-\infty}^{+\infty} J_q[n_m \cos(\Omega_m t)] \exp\left(iq\pi \frac{m+1}{2}\right) \times \quad (\text{F.18})$$

$$\times \exp(iK_m q x) \exp\left[-\frac{(x^2 + y^2)}{w^2}\right]$$

The Fraunhofer diffraction pattern is obtained either in the far-field or in the focal plane of a converging lens. In the following discussion, we consider the case of a lens with focal length f . The diffracted field is calculated as the Fourier transform of the initial field ((see appendix B). Thus, we obtain

$$U_f(u, v) = \frac{1}{i\lambda f} \mathcal{F}\{U(x, y, 0)\} \left(\frac{u}{\lambda f}, \frac{v}{\lambda f}\right) \quad (\text{F.19})$$

where u and v are, respectively, the horizontal and vertical coordinates of the focal plane. The terms of the sum in equation F.18 can be written as the product of two functions, whose Fourier transforms are

$$\mathcal{F}\{\exp(iK_m q x)\} = \delta\left(\nu_x - \frac{qK_m}{2\pi}\right) \delta(\nu_y) \quad (\text{F.20a})$$

$$\mathcal{F}\left\{\exp\left[-\frac{(x^2 + y^2)}{w^2}\right]\right\} = \pi w^2 \exp\left[-\pi^2 w^2 (\nu_x^2 + \nu_y^2)\right] \quad (\text{F.20b})$$

where ν_x and ν_y correspond to the horizontal and vertical spatial frequencies. Therefore, the total Fourier transform is given by the convolution of the two above equations. Performing the

calculation we get

$$U_f(\nu_x, \nu_y) = \frac{\pi w^2 U_0}{i \lambda f} \sum_{q=-\infty}^{+\infty} J_q[kl n_m \cos(\Omega_m t)] \exp\left(iq\pi \frac{m+1}{2}\right) \times \exp\left\{-\pi^2 w^2 \left[\left(\nu_x - \frac{qK_m}{2\pi}\right)^2 + \nu_y^2\right]\right\} \quad (\text{F.21})$$

Identifying (ν_x, ν_y) as $\frac{1}{\lambda f}(u, v)$, where u and v are the spatial coordinates of the focal plane of the lens, we finally obtain

$$U_f(u, v) = \frac{\pi w^2 U_0}{i \lambda f} \sum_{q=-\infty}^{+\infty} J_q[kl n_m \cos(\Omega_m t)] \exp\left(iq\pi \frac{m+1}{2}\right) \times \exp\left\{-\frac{\pi^2 w^2}{\lambda^2 f^2} \left[\left(u - qf \frac{\lambda}{\Lambda_m}\right)^2 + v^2\right]\right\} \quad (\text{F.22})$$

The above equation corresponds to a weighted sum of Gaussian functions. The corresponding intensity is calculated as the square modulus of the above equation. Suppose that Ω_m is big enough to prevent the overlap of neighboring Gaussian spots. Under this hypothesis, we can neglect the cross-product of the terms of the sum and write the intensity function as

$$I(u, v) = I_0 \sum_{q=-\infty}^{+\infty} J_q^2[kl n_m \cos(\Omega_m t)] \exp\left\{-\frac{2\pi^2 w^2}{\lambda^2 f^2} \left[\left(u - qf \frac{\lambda}{\Lambda_m}\right)^2 + v^2\right]\right\} \quad (\text{F.23})$$

where I_0 is the square modulus of all the constant prefactors divided by the impedance of free space. The spatial separation between peaks is

$$\Delta x = \frac{\lambda}{\Lambda_m} f = \frac{\Omega_m}{2\pi c_s} \lambda f \quad (\text{F.24})$$

and the diffraction efficiency, defined as the peak intensity divided by I_0 , is

$$\eta_q(t) = J_q^2[kl n_m \cos(\Omega_m t)] \quad (\text{F.25})$$

A similar procedure can be repeated with the transmittance function [F.15](#) to obtain the following two-dimensional diffraction intensity

$$I(u, v) = I_0 \sum_{q=-\infty}^{+\infty} J_q^2[kl n_m \cos(\Omega_m t)] \exp\left[-\frac{2\pi^2 w^2}{\lambda^2 f^2} \left(u - \frac{\lambda}{\Lambda_m} f\right)^2\right] \times \sum_{p=-\infty}^{+\infty} J_p^2[kl n_m \cos(\omega_j t)] \exp\left[-\frac{2\pi^2 w^2}{\lambda^2 f^2} \left(u - \frac{\lambda}{\Lambda_j} f\right)^2\right] \quad (\text{F.26})$$

In case the Gaussian beam is not collimated, it is enough to substitute w^2 with $\left(\frac{1}{w^2} - \frac{ik}{2R}\right)^{-1}$ in equation F.22. This implies that each argument of the exponentials of equations F.23 and F.26 has to be divided by $1 + \frac{k\pi^2 w^4}{R}$.

F.5 Fresnel diffraction

The scalar field propagated to a distance z from the acoustic cavity is calculated as follows

$$U(x, y, z) = [U(x', y', 0) * F_z(x', y')] (x, y) \quad (\text{F.27})$$

where $U(x', y', 0)$ is given by F.18 and $F_z(x', y')$ is the Fresnel propagation kernel (see appendix B). To calculate the convolution product, we consider only the terms depending on the variables x and y . By completing the square, we can rewrite the last two terms of equation F.18 as

$$\begin{aligned} & \exp(iK_m q x') \exp\left[-\frac{(x'^2 + y'^2)}{w^2}\right] = \\ & = \exp\left[-\frac{q^2 K_m^2 w^2}{4}\right] \exp\left[-\frac{(x' - iqK_m w^2/2)^2}{w^2}\right] \exp\left[-\frac{y'^2}{w^2}\right] \end{aligned} \quad (\text{F.28})$$

This is the product of a constant with two Gaussian functions. Therefore, we can factorize the convolution product as follows:

$$\begin{aligned} & U(x', y', 0) * F_z(x', y') = \\ & = \left(\exp\left[-\frac{q^2 K_m^2 w^2}{4}\right] \exp\left[-\frac{(x' - iqK_m w^2/2)^2}{w^2}\right] * \exp\left[\frac{ik}{2z} x'^2\right] \right) \times \\ & \times \left(\exp\left[-\frac{y'^2}{w^2}\right] * \exp\left[\frac{ik}{2z} y'^2\right] \right) \end{aligned} \quad (\text{F.29})$$

where the first convolution is calculated only with respect to the variable x and the second one only with respect to the variable y . Both terms of both convolution products can be seen as Gaussian functions. Therefore, we can easily calculate the result using the fact that the convolution product of two normalized Gaussian functions is still a normalized Gaussian function having as mean the sum of the means ($\mu = \mu_1 + \mu_2$) and as variance the sum of the variances ($\sigma^2 = \sigma_1^2 + \sigma_2^2$). For the first convolution, we perform the following identifications

$$\mu_1 = iqK_m w^2/2 \quad \sigma_1^2 = \frac{w^2}{2} \quad (\text{F.30a})$$

$$\mu_2 = 0 \quad \sigma_2^2 = -\frac{z}{ik} \quad (\text{F.30b})$$

Therefore, we can write the result of the first convolution as

$$\frac{\sqrt{2\pi}}{\sqrt{\frac{2}{w^2} - \frac{ik}{z}}} \exp \left[\underbrace{-\frac{q^2 K_m^2 w^2}{4} - ik \frac{(x - iqK_m w^2/2)^2}{ikw^2 - 2z}}_{\Phi} \right] \quad (\text{F.31})$$

where the argument of the above exponential is more conveniently rewritten as

$$\Phi = \frac{-4k^2 w^2 x^2 + 8qw^2 k K_m z x - 4q^2 w^2 K_m^2 z^2 + i(8kzx^2 + 4qK_m k - 2q^2 k K_m^2 w^4 z)}{4k^2 w^4 + 16z^2} \quad (\text{F.32})$$

Instead, for the second convolution, we have

$$\mu_1 = 0 \quad \sigma_1^2 = \frac{w^2}{2} \quad (\text{F.33a})$$

$$\mu_2 = 0 \quad \sigma_2^2 = -\frac{z}{ik} \quad (\text{F.33b})$$

Therefore, the result is

$$\frac{\sqrt{2\pi}}{\sqrt{\frac{2}{w^2} - \frac{ik}{z}}} \exp \left[\frac{-4k^2 w^2 y^2 + i8kzy^2}{4k^2 w^4 + 16z^2} \right] \quad (\text{F.34})$$

Therefore, equation F.29 can be rewritten as the product of F.31 with F.34. Finally we have

$$U(x, y, z) = \frac{U_0}{1 + i\frac{\lambda z}{\pi w^2}} \exp \left[-\frac{(x^2 + y^2)}{w^2 + \frac{4z^2}{k^2 w^2}} \right] \sum_{q=-\infty}^{+\infty} \exp \left[\frac{8qw^2 k K_m z x - 4q^2 w^2 K_m^2 z^2}{4k^2 w^4 + 16z^2} \right] \times \\ \times J_q [n_m \cos(\Omega_m t)] \exp \left(-\frac{iq^2 K_m^2 z}{2k} \right) \exp \left[iq \left(K_m x + \pi \frac{m+1}{2} \right) \right] \quad (\text{F.35})$$

Where we have neglected the phase factors $\exp\left(\frac{i8kzx^2}{4k^2 w^4 + 16z^2}\right)$, $\exp\left(\frac{i8kzy^2}{4k^2 w^4 + 16z^2}\right)$, and $\exp(ikz)$ because they are global (they do not depend on the index q) and do not contribute in the calculation of the square modulus of the field. After some algebra, we finally have

$$U(x, y, z) = \frac{U_0}{1 + i\frac{\lambda z}{\pi w^2}} \sum_{q=-\infty}^{+\infty} \exp \left\{ -\frac{1}{w^2 + \frac{4z^2}{k^2 w^2}} \left[\left(x - q \frac{\lambda}{\Lambda_m} z \right)^2 + y^2 \right] \right\} \times \\ \times J_q [n_m \cos(\Omega_m t)] \exp \left(-\frac{iq^2 K_m^2 z}{2k} \right) \exp \left[iq \left(K_m x + \pi \frac{m+1}{2} \right) \right] \quad (\text{F.36})$$

The above equation represents many Gaussian beams initially (at $z = 0$ m) in the same position, but diverging with an angle $\theta = \lambda/\Lambda_m$ and each with a different amplitude and phase shift. The finite size of each beam implies that for short distances, those beams overlap and interfere, but for longer distances, the beams get separated. We define z_0 as the distance after which the beams no longer overlap. To find its analytical expression, we require the separation along the x -axis to be equal to the diameter of the beams

$$\frac{\lambda}{\Lambda_m} z_0 = 2\sqrt{w^2 + \frac{4z_0^2}{kw^2}} \Rightarrow z_0 = \sqrt{\frac{4\pi^2\Lambda_m^2 w^4}{\pi^2 w^2 \lambda^2 - 4\lambda^2 \Lambda_m^2}} \quad (\text{F.37})$$

Now we do some numerical considerations. For a realistic case we have that $w \approx 10^{-2}$ m, $k \approx 10^7$ m⁻¹, $K_m \approx 10^3$ m⁻¹, and $q \approx 1$ (because the diffraction efficiency is not negligible only for the first diffraction orders). For $z \ll z_0 \approx 10^2$ m, we can consider $z \approx 1$ m. Therefore, we can make the following approximations

$$w^2 + \frac{4z^2}{k^2 w^2} \approx w^2 \quad (\text{F.38a})$$

$$qz \frac{\lambda}{\Lambda_m} \approx 0 \quad (\text{F.38b})$$

$$\frac{1}{1 + i \frac{\lambda z}{\pi w^2}} \approx 1 \quad (\text{F.38c})$$

Therefore, the field propagated for a distance $z \ll z_0$ is

$$U(x, y, z) = U_0 \exp\left[-\frac{(x^2 + y^2)}{w^2}\right] \sum_{q=-\infty}^{+\infty} J_q[n_m \cos(\Omega_m t)] \times \exp\left(-\frac{iq^2 K_m^2 z}{2k}\right) \exp\left[iq\left(K_m x + \pi \frac{m+1}{2}\right)\right] \quad (\text{F.39})$$

The intensity is given by the square modulus of the above equation, divided by the impedance of free space. Notably, every time the distance along the optical axis is

$$z = p \frac{4\pi k}{k_m^2} = p \frac{2\Lambda^2}{\lambda} \quad (\text{F.40})$$

where $p \in \mathbb{Z}$ and $\Lambda = \frac{2\pi}{K_m}$, we have that

$$\exp\left(-\frac{iq^2 K_m^2 z}{2k}\right) = 1 \quad (\text{F.41})$$

Therefore, the propagated field is equal to those at the exit of the acoustic cavity. In other words, $U(x, y, 0) = U(x, y, p \frac{2\Lambda^2}{\lambda})$ as long as $z \ll z_0$. This phenomenon is known as the *Talbot effect*, and it is a consequence of the periodicity of the acoustically-induced phase grating.

It is also interesting to notice that in the result of equation F.39, the argument of the sum is the same that we would have got doing the calculation of the Fresnel diffraction with a plane

wave instead of a Gaussian beam. In this case, the Gaussian function acts only as an envelope on the xy plane.

Repeating the above calculations with the two-dimensional transmittance function F.15, we obtain

$$\begin{aligned}
 U(x, y, z) &= U_0 \exp \left[-\frac{(x^2 + y^2)}{w^2} \right] \times \\
 &\times \sum_{q=-\infty}^{+\infty} J_q [n_m \cos(\Omega_m t)] \exp \left(-\frac{iq^2 K_m^2 z}{2k} \right) \exp \left[iq \left(K_m x + \pi \frac{m+1}{2} \right) \right] \times \\
 &\times \sum_{p=-\infty}^{+\infty} J_p [n_j \cos(\omega_j t)] \exp \left(-\frac{ip^2 k_j^2 z}{2k} \right) \exp \left[ip \left(k_j x + \pi \frac{j+1}{2} \right) \right]
 \end{aligned} \quad (\text{F.42})$$

We now consider the limit $z \gg z_0$. In this case, we can make the following approximations

$$w^2 + \frac{4z^2}{k^2 w^2} \approx \frac{\lambda^2 z^2}{\pi^2 w^2} \quad (\text{F.43a})$$

$$\frac{1}{1 + i \frac{\lambda z}{\pi w^2}} \approx \frac{\pi w^2}{i \lambda z} \quad (\text{F.43b})$$

that lead to the following field

$$U(x, y, z) = \frac{\pi w^2 U_0}{i \lambda z} \sum_{q=-\infty}^{+\infty} J_q [k l n_m \cos(\Omega_m t)] \exp \left\{ -\frac{\pi^2 w^2}{\lambda^2 z^2} \left[\left(x - qz \frac{\lambda}{\Lambda_m} \right)^2 + y^2 \right] \right\} \quad (\text{F.44})$$

where we also dropped the phase factor $\exp[iq(K_m x + \pi \frac{m+1}{2})]$ because it is useless in the calculation of the square modulus of the field if the beams are separated. As expected, this result is equivalent to the Fraunhofer diffraction.



The Tunable Acoustic Gradient Lens

G.1 Cylindrical acoustic wave equation

The TAG lens is a cylindrical acoustic resonant cavity, composed by a piezoelectric hollow tube filled in low-viscosity silicon oil. The differential equation governing the wave propagation inside the cylinder is the following damped wave equation

$$\frac{\partial^2 \rho}{\partial t^2} - c_s^2 \nabla^2 \rho - \nu \nabla^2 \frac{\partial \rho}{\partial t} = 0 \quad (\text{G.1})$$

We exploit the circular symmetry of the device to rewrite the above equation in polar coordinates

$$\frac{\partial^2 \rho}{\partial t^2} - \frac{1}{r} \frac{\partial}{\partial r} \left[r \frac{\partial}{\partial r} \left(c_s^2 \rho - \nu \frac{\partial \rho}{\partial t} \right) \right] = 0 \quad (\text{G.2})$$

where we assumed that the solution does not depend on the angle. We couple this differential equation with the following boundary condition

$$v(r, t) \Big|_{r=R} = v_a \cos(\Omega_d t) \quad (\text{G.3})$$

where v is the velocity of the fluid, v_a is the amplitude of the velocity oscillation, R is the radius of the piezoelectric tube, and Ω_d is the angular frequency of the driving signal. Additionally, we use the following initial conditions

$$\rho(r, t) \Big|_{t=0} = 0 \quad \frac{\partial \rho}{\partial t} \Big|_{t=0} = 0 \quad (\text{G.4})$$

that represent an initial state at rest. Using the law of the conservation of momentum, the boundary condition can be rewritten as

$$\left. \frac{\partial \rho}{\partial r} \right|_{r=R} = \underbrace{\frac{\rho_0 v_A \Omega_d c_s^2}{\nu^2 \Omega_d^2 + c_s^4} \sin(\Omega_d t) - \frac{\rho_0 v_A \Omega_d^2 \nu}{\nu^2 \Omega_d^2 + c_s^4} \cos(\Omega_d t)}_{f(t)} \quad (\text{G.5})$$

Thus, we can rewrite a new inhomogeneous differential equation for the function $u(r, t) = \rho(r, t) - r f(t)$, obtaining

$$\frac{\partial^2 u}{\partial t^2} - \frac{1}{r} \frac{\partial}{\partial r} \left[r \frac{\partial}{\partial r} \left(c_s^2 u - \nu \frac{\partial u}{\partial t} \right) \right] = S(r, t) \quad (\text{G.6})$$

where the source term is defined as

$$S(r, t) = c_s^2 \frac{f(t)}{r} - \frac{\nu}{r} \frac{\partial f}{\partial t} - r \frac{\partial^2 f}{\partial t^2} \quad (\text{G.7})$$

and the new boundary condition is

$$\left. \frac{\partial u}{\partial r} \right|_{r=R} = 0 \quad (\text{G.8})$$

Following a similar procedure to that shown in detail in appendix E, we find the solution of the homogeneous equation by separating the variables. Plugging $u(r, t) = X(r)T(t)$ in the homogeneous version of equation G.6, we obtain

$$X \frac{\partial^2 T}{\partial t^2} - \left(\frac{\partial^2 X}{\partial r^2} + \frac{1}{r} \frac{\partial X}{\partial r} \right) \left(c_s^2 T - \nu \frac{\partial T}{\partial t} \right) = 0 \quad (\text{G.9})$$

which leads to the following two independent differential equations

$$r^2 \frac{\partial^2 X}{\partial r^2} + r \frac{\partial X}{\partial r} + X(Kr)^2 = 0 \quad (\text{G.10})$$

$$\frac{\partial^2 T}{\partial t^2} + K^2 \left(c_s^2 T + \nu \frac{\partial T}{\partial t} \right) = 0 \quad (\text{G.11})$$

where K is a constant. We recognize the temporal equation as the differential equation of a damped harmonic oscillator. Instead, the spatial equation is the Bessel equation of order 0. Thus, the spatial solution is

$$X(r) = AJ_0(Kr) + BY_0(Kr) \quad (\text{G.12})$$

where J_0 and Y_0 are, respectively, the Bessel functions of first and second kind of order 0. However, Bessel functions of second kind are singular at the origin leading to a non-physical behaviour. Therefore, we have to assume $B = 0$. Now, we apply the boundary condition, using the following property of Bessel functions

$$\frac{d}{dx} [x^q J_q(x)] = x^q J_{q-1}(x) \quad (\text{G.13})$$

evaluated at $q = 0$. Thus, the boundary condition is

$$\left. \frac{\partial u}{\partial r} \right|_{r=R} = AJ_{-1}(KR) = -AJ_1(KR) = 0 \quad (\text{G.14})$$

which leads to a quantization rule. Indeed, the only allowable values of K are those such $K_m = x_m/R$ and x_m is the m^{th} root of $J_1(x)$. Thus, the eigenfunctions of the differential equation are

$$X_m(r) = J_0(K_m r) \quad (\text{G.15})$$

This result enables following a procedure similar to the one shown in detail in appendix E, decomposing the solution of the full wave equation on the basis of the eigenfunctions. This approach leads to a solution which, in the low-viscosity and resonant case, can be written as

$$\rho(r, t) = \rho_m J_0(K_m r) \cos(\Omega_m t) \quad (\text{G.16})$$

where $\Omega_m = c_s K_m$ is the angular frequency and ρ_m is the oscillation amplitude which is proportional to the driving power applied to the piezoelectric tube.

G.2 TAG lens focal length

The Lorentz-Lorenz equation enables to convert the acoustic wave into the following profile of refractive index

$$n(r, t) = n_0 + \Delta n J_0(Kr) \cos(\Omega t) \quad (\text{G.17})$$

where n_0 is the static refractive index of the liquid and Δn is the maximum variation of refractive index. If a beam of light hits only the central part of the TAG lens, we can simplify the above expression with a McLaurin expansion

$$n(r, t) \underset{r \rightarrow 0}{\sim} -\frac{K^2 \Delta n}{2} \cos(\Omega t) \frac{x^2 + y^2}{2} \quad (\text{G.18})$$

approximating the central lobe of the Bessel function as a parabola. The transmission function of the TAG lens is

$$t_A(r, t) = \exp[kln(r, t)] = \exp\left[-\frac{\kappa r^2}{2} \frac{lK^2 \Delta n}{2} \cos(\Omega t)\right] \quad (\text{G.19})$$

where κ is the optical wave number and l is the depth of the TAG lens. By comparison with the transmission function of a lens, we find out that the optical power (i.e. the inverse of the focal length) of the TAG lens is

$$\frac{1}{f_T} = \underbrace{\frac{lK^2 \Delta n}{2}}_{:=\alpha} \cos(\Omega t) \quad (\text{G.20})$$

G.2.1 Working distance of the detection system

The complete ray transfer matrix of the detection system, using the thin lens approximation, is

$$M = \begin{pmatrix} 1 & f_L \\ 0 & 1 \end{pmatrix} \begin{pmatrix} 1 & 0 \\ -\frac{1}{f_L} & 1 \end{pmatrix} \begin{pmatrix} 1 & d \\ 0 & 1 \end{pmatrix} \underbrace{\begin{pmatrix} 1 & 0 \\ -\frac{1}{f_T} & 1 \end{pmatrix} \begin{pmatrix} 1 & f_O \\ 0 & 1 \end{pmatrix} \begin{pmatrix} 1 & 0 \\ -\frac{1}{f_O} & 1 \end{pmatrix}}_{\text{EDoF lens}} \begin{pmatrix} 1 & s \\ 0 & 1 \end{pmatrix} \quad (\text{G.21})$$

where s is the working distance, d is an arbitrary distance, and f_O , f_T , and f_L are respectively the focal length of the objective, TAG, and tube lens. After some algebra, we find that the ray transfer matrix is

$$M = \begin{pmatrix} -\frac{f_T}{f_O} & -\frac{f_O^2 f_T - f_O f_T f_L + f_T f_L s}{f_O f_T} \\ \frac{f_T - f_L}{f_O f_L} & -\frac{f_O^2 f_L + f_O f_T^2 - f_O f_T f_L - f_T^2 s + f_T f_L s}{f_O f_T f_L} \end{pmatrix} \quad (\text{G.22})$$

Notably, having placed the TAG lens in the back focal plane of the objective lens, the effective focal length of the EDoF lens is equal to f_O , even if f_L is a function of time. Therefore, the lateral magnification of the system (given by the A element of the ABCD matrix) is constant.

In order to have the formation of an image, we have to impose that the B element is zero. Therefore, the working distance has to be

$$s(t) = f_O - \frac{f_O^2}{f_L(t)} = f_O - f_O^2 \alpha \cos(\Omega t) \quad (\text{G.23})$$

The instantaneous position of the imaged plane with respect to the focal plane of the objective lens is

$$\zeta(t) = f_O - s(t) = \Delta z \cos(\Omega t) \quad (\text{G.24})$$

Therefore, the axial position of the plane in focus varies sinusoidally, with an amplitude $\Delta z = f_O^2 \alpha$ which is half of the scanning range along the z -axis.

G.3 Time-averaged Point Spread Function

Given a native PSF $h_o(x, y, z)$ of the imaging system, the instantaneous PSF of the objective lens conjugated with the TAG lens is simply

$$h_o(x, y, z, t) = h_o(x, y, z - \zeta(t)) \quad (\text{G.25})$$

Therefore, the effective PSF seen by a detector whose acquisition time is significantly larger than the oscillation period $T = 2\pi/\Omega$ is

$$h_e(x, y, z) = \frac{1}{T} \int_{-T/2}^{+T/2} h_o(x, y, z - \zeta(t)) dt \quad (\text{G.26})$$

that is the incoherent superposition of instantaneous PSFs at axial position $z - \zeta(t)$, weighted by the ratio of time spent dt over the total time T . Equivalently, it can also be rewritten as

$$h_e(x, y, z) = \frac{1}{\pi} \int_{-\Delta z}^{+\Delta z} \frac{h_o(x, y, z - \zeta)}{\sqrt{\Delta z^2 - \zeta^2}} d\zeta \quad (\text{G.27})$$

If $h(x, y, z)$ is quickly vanishing along the z -axis – as typically happens for a PSF of a standard microscope – and $|z| \ll \Delta z$, then the integrand gives contribution to the complete integral only for small values of ζ . Thus, we can approximate $\zeta \ll \Delta z$ and have as a result

$$h_e(x, y, z) \sim \frac{1}{\pi \Delta z} \int_{\mathbb{R}} h_o(x, y, \zeta) d\zeta \quad \text{if } |z| \ll \Delta z \quad (\text{G.28})$$

Namely, we approximate the central part of the extended PSF as constant along the z -axis. As expected, the intensity of the extended PSF scales roughly as $1/\Delta z$.

G.3.1 Effect on the MTF

The Optical Transfer Function (OTF) of a microscope is given by the Fourier transform of its PSF. Its amplitude, called Modulation Transfer Function (MTF), defines the contrast of a feature in an image as a function of the corresponding spatial frequency. In a diffraction-limited microscope, the support of the MTF is finite. This implies the existence of a cut-off spatial frequency that defines the smallest resolvable detail in an image. The inverse of the cut-off frequency is the optical resolution.

From the discussion of the previous section, it follows that the OTF \mathcal{H}_e of a microscope with DoF extended by a TAG lens is

$$\mathcal{H}_e(k_x, k_y, z) = \frac{1}{T} \int_{-T/2}^{+T/2} \mathcal{H}_o(k_x, k_y, z - \zeta(t)) dt \quad (\text{G.29})$$

where \mathcal{H}_o is the native OTF of the microscope and k_x, k_y are, respectively, the horizontal and vertical spatial frequency. Therefore, the MTF is

$$|\mathcal{H}_e(k_x, k_y, z)| = \frac{1}{T} \left(\int_{-T/2}^{+T/2} \int_{-T/2}^{+T/2} \mathcal{H}_o(k_x, k_y, z - \zeta(t)) \mathcal{H}_o^*(k_x, k_y, z - \zeta(t')) dt dt' \right)^{1/2} \quad (\text{G.30})$$

The native PSF – and the corresponding OTF – has a finite support on the z -axis because of the limited DoF. Thus, the integrand in the above equation is vanishing except for $t \approx t'$. Using this approximation, we can rewrite the MTF as

$$|\mathcal{H}_e(k_x, k_y, z)| \approx \frac{1}{T} \left(\int_{-T/2}^{+T/2} |\mathcal{H}_o(k_x, k_y, z - \zeta(t))|^2 dt \right)^{1/2} \quad (\text{G.31})$$

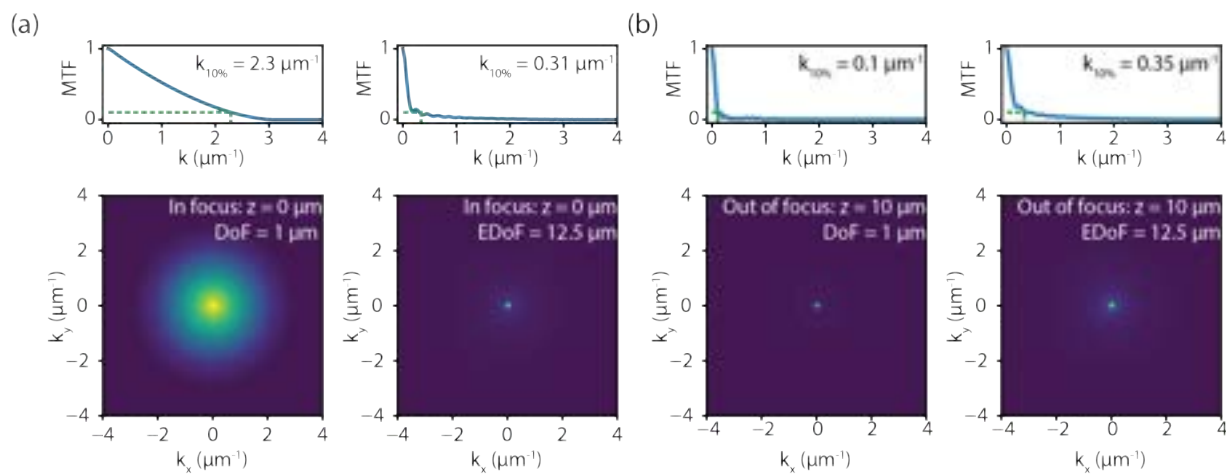


Figure G.1: Modulation transfer functions simulations. (a) MTF in focus of a standard unaberrated microscope, simulated using the Born & Wolf model (left). MTF of a microscope with DoF extended by means of the TAG lens, in focus (right). (b) Unaberrated MTF out of focus (left). MTF of the system with extended DoF out of focus. On top, the radial profile of the MTFs is reported, accompanied with the value of the spatial frequency at which the MTF value drops below the 10% of the maximum.

Noticeably, the EDoF-MTF is a weighted root mean square of the native MTFs at all z -position of the axial scan performed by the TAG lens. Consequently, depending on the magnitude of the DoF extension, out of focus contributions might play an important role and decrease the values of the MTF at high frequencies, reducing the effective resolution of the system. In general, the higher is the DoF extension and the lower is the resolution. However, within the region of the extended DoF the resolution is approximately constant. This phenomenon is shown in detail by the numerical simulations reported in Figure G.1. Indeed, Figure G.1a shows the native MTF and the EDoF-MTF when the emitter is in focus. As expected, the MTF support in the frequency space is reduced. In Figure G.1b we show the same MTFs but out of focus of 10 times the native DoF. The native MTF is narrower, but the EDoF-MTF remains about the same size of when in focus and is larger than the defocused native MTF. In other words, an imaging system implementing a TAG lens has a reduced resolution – compared to the diffraction limit – but it is maintained constant for a longer axial range.



Noise Reduction Through Parallelization

Let f_i be a measurement, performed sampling up to n points p_j together. The sequence of measured points detected in the same measurement can be encoded in the weights $w_{ij} \in \{0, 1\}$. Therefore

$$f_i = \sum_{j=1}^n w_{ij} p_j \quad (\text{H.1})$$

Define \mathbf{W} as a square $n \times n$ matrix, whose entries are the weights $w_{ij} \in \{0, 1\}$. Therefore, the whole array of n encoded measurements can be written in matrix form as

$$\mathbf{f} = \mathbf{W}\mathbf{p} \quad (\text{H.2})$$

The individual points can be decoded simply by inverting the above equation

$$\mathbf{p} = \mathbf{W}^{-1}\mathbf{f} \quad (\text{H.3})$$

H.1 Noise types

H.1.1 Random noise

Suppose now the presence of random noise \mathbf{e} , that we assume to be independent of the signal

$$\mathbf{f} = \mathbf{W}\mathbf{p} + \mathbf{e} \quad (\text{H.4})$$

Furthermore, we make the following assumptions

- The expected value of the noise is zero

$$\mathbb{E}[e_i] = 0 \quad (\text{H.5})$$

- The noise is uncorrelated and has variance σ^2

$$\mathbb{E}[e_i e_j] = \sigma^2 \delta_{ij} \quad (\text{H.6})$$

The reconstruction is done with the inverse matrix $\mathbf{M} = \mathbf{W}^{-1}$

$$\hat{\mathbf{p}} = \mathbf{M} \mathbf{f} = \mathbf{p} + \mathbf{M} \mathbf{e} \quad (\text{H.7})$$

From the previous equation, it is clear that

$$\mathbb{E}[\hat{\mathbf{p}}] = \mathbf{p} \quad (\text{H.8})$$

and that the noise in the reconstructed signal is $\mathbf{M} \mathbf{e}$. Therefore, the mean square error (i.e. the variance of $\hat{\mathbf{p}}$) in presence of random noise is

$$\begin{aligned} \epsilon_i &= \mathbb{E}[(\hat{p}_i - p_i)^2] = \mathbb{E} \left[\left(\sum_{j=1}^n m_{ij} e_j \right)^2 \right] = \\ &= \sum_{j=1}^n \sum_{k=1}^n m_{ij} m_{ik} \mathbb{E}[e_j e_k] = \sigma^2 \sum_{j=1}^n m_{ij}^2 \end{aligned} \quad (\text{H.9})$$

H.1.2 Photon Noise

Suppose now that the measurements $\mathbf{f} = \mathbf{W} \mathbf{p}$ are random variables following the Poisson distribution. This implies that

$$\mathbb{E}[f_j] = \mathbb{E}[(\mathbb{E}[f_j] - f_j)^2] = \text{Var}[f_j] \quad (\text{H.10})$$

Consequently

$$\begin{aligned} \text{Var}[p_i] &= \mathbb{E} \left[\left(\mathbb{E} \left[\sum_{j=1}^n m_{ij} f_j \right] - \sum_{j=1}^n m_{ij} f_j \right)^2 \right] = \\ &= \sum_{j=1}^n m_{ij}^2 \mathbb{E}[(\mathbb{E}[f_j] - f_j)^2] = \sum_{j=1}^n m_{ij}^2 \mathbb{E}[f_j] = \\ &= \sum_{j=1}^n m_{ij}^2 \sum_{k=1}^n w_{jk} \mathbb{E}[p_k] \end{aligned} \quad (\text{H.11})$$

where we used the fact that different measures are independent and uncorrelated (i.e. $\mathbb{E}[f_j f_k] = \mathbb{E}[f_j] \mathbb{E}[f_k]$ for any $j \neq k$).

Define $\nu = \sum_{k=1}^n w_{jk}$, namely the number of entries in the j -th column of W whose value is equal to one (for a cyclic matrix this number does not depend on the index j). Assume now, for simplicity, that the signal p_k is almost flat, namely $\mathbb{E}[p_k] \approx \rho^2$ for every k . This approximation allows us to write the mean square error due to photon noise as

$$\epsilon_i = \nu \rho^2 \sum_{j=1}^n m_{ij}^2 \quad (\text{H.12})$$

Interestingly, this is the same result we would have got adding a noise $\boldsymbol{\eta}$ to the measurements, with the following properties

$$\mathbb{E}[\eta_i] = 0 \quad \mathbb{E}[\eta_i \eta_j] = f_j \delta_{ij} \quad (\text{H.13})$$

Finally, the mean square error due to the presence of both random and photon noise is

$$\epsilon_i = (\sigma^2 + \nu \rho^2) \sum_{j=1}^n m_{ij}^2 \quad (\text{H.14})$$

H.1.3 Background

Suppose now the presence of a uniform background $\boldsymbol{\beta}$, such that $\beta_i = \beta_j = \beta \quad \forall i, j$, independent from the signal.

$$\boldsymbol{f} = \boldsymbol{W} \boldsymbol{p} + \boldsymbol{\beta} \quad (\text{H.15})$$

Therefore, the resulting background after the decoding is

$$\boldsymbol{\beta}' = \boldsymbol{M} \boldsymbol{\beta} \quad (\text{H.16})$$

Explicitly

$$\beta'_i = \sum_{j=1}^n m_{ij} \beta_j = \beta \sum_{j=1}^n m_{ij} \quad (\text{H.17})$$

On the other hand, if a background $\boldsymbol{\gamma}$ that depends on the signal is present

$$\boldsymbol{f} = \boldsymbol{W} (\boldsymbol{p} + \boldsymbol{\gamma}) \quad (\text{H.18})$$

the expected value of $\boldsymbol{\gamma}$ is unaltered after the decoding. However, it contributes as a source of photonic noise, worsening the signal-to-noise ratio.

H.2 Encoding matrices

H.2.1 Sequential Scan

The encoding matrix is the identity, i.e. $w_{ij} = \delta_{ij}$. The inverse matrix is still the identity, i.e. $m_{ij} = \delta_{ij}$, and $\nu = 1$. This implies that the mean square error is

$$\epsilon_i = (\sigma^2 + \rho^2) \quad (\text{H.19})$$

This quantity does not depend on the index i , thus we name it ϵ_0 and we define the SNR of the point p_i acquired with a sequential scan as

$$\text{SNR}_0 = \frac{p_i}{\sqrt{\epsilon_0}} = \frac{p_i}{\sqrt{\sigma^2 + \rho^2}} \quad (\text{H.20})$$

H.2.2 Black Light Sheet

The encoding matrix is $w_{ij} = 1 - \delta_{ij}$, that is a matrix whose entries are all ones, except on the main diagonal where the entries are zeros. Defining \mathbf{J} as the $n \times n$ matrix whose entries are all ones and \mathbf{I} as the $n \times n$ identity matrix, we can rewrite \mathbf{W} as $\mathbf{W} = \mathbf{J} - \mathbf{I}$. By construction $\mathbf{W} = \mathbf{W}^T$. Therefore

$$\mathbf{W}\mathbf{W}^T = (n - 2)\mathbf{J} + \mathbf{I} \quad (\text{H.21})$$

It follows that the inverse matrix is

$$\mathbf{W}^{-1} = \frac{\mathbf{J}}{(n - 1)} - \mathbf{I} \quad (\text{H.22})$$

Therefore

$$m_{ij} = \frac{1}{n - 1} - \delta_{ij} \quad (\text{H.23})$$

and the corresponding mean square error is

$$\begin{aligned} \epsilon_i(n) &= (\sigma^2 + \nu\rho^2) \sum_{j=1}^n \left(\frac{1 - (n-1)\delta_{ij}}{n-1} \right)^2 = \frac{\sigma^2 + \nu\rho^2}{(n-1)^2} (n-1 + (2-n)^2) = \\ &= (\sigma^2 + \nu\rho^2) \frac{(n^2 - 3n + 3)}{(n-1)^2} \end{aligned} \quad (\text{H.24})$$

In this case, $\nu = n - 1$. Therefore, the total mean square error is

$$\begin{aligned}\epsilon_i &= [\sigma^2 + (n-1)\rho^2] \frac{(n^2 - 3n + 3)}{(n-1)^2} = \\ &= \sigma^2 \frac{(n^2 - 3n + 3)}{(n-1)^2} + \rho^2 \frac{(n^2 - 3n + 3)}{(n-1)} \sim\end{aligned}\quad (\text{H.25})$$

$$\sim \sigma^2 + n\rho^2 \quad (\text{if } n \rightarrow \infty) \quad (\text{H.26})$$

Therefore, the SNR of the i^{th} point is $p_i/\sqrt{\epsilon_i}$. If the points are acquired at the same experimental conditions of a sequential scan, the signal p_i is unchanged and the SNR gain is

$$\frac{\text{SNR}_n}{\text{SNR}_0} = \sqrt{\frac{\epsilon_0}{\epsilon_n}} = \sqrt{\frac{1 + \chi^2}{1 + (n-1)\chi^2} \frac{n-1}{\sqrt{n^2 - 3n + 3}}} \quad (\text{H.27})$$

Where $\chi^2 = \sigma^2/\rho^2$ is the ratio of the mean square random noise over the mean square photon noise. Instead, the background becomes

$$\beta'_i = \beta \sum_{j=1}^n \frac{1 - (n-1)\delta_{ij}}{n-1} = \frac{\beta}{n-1} \quad (\text{H.28})$$

H.2.3 Hadamard Encoding

A Hadamard matrix \mathbf{H}_n of order n is a square matrix whose entries are either +1 or -1 and whose rows are mutually orthogonal. From this definition, it follows that

$$\mathbf{H}_n \mathbf{H}_n^T = n\mathbf{I} \quad (\text{H.29})$$

Explicitly, the first two Hadamard matrices are

$$\mathbf{H}_1 = (1) \quad \mathbf{H}_2 = \begin{pmatrix} 1 & 1 \\ 1 & -1 \end{pmatrix} \quad (\text{H.30})$$

Following Sylvester's construction, higher-order Hadamard matrices can be built as

$$\mathbf{H}_{2^k} = \mathbf{H}_2 \otimes \mathbf{H}_{2^{k-1}} = \begin{pmatrix} \mathbf{H}_{2^{k-1}} & \mathbf{H}_{2^{k-1}} \\ \mathbf{H}_{2^{k-1}} & -\mathbf{H}_{2^{k-1}} \end{pmatrix} \quad (\text{H.31})$$

where \otimes is the Kronecker product and $k \geq 2$. The encoding matrix is built from a Hadamard matrix of order $n+1$ through the following steps

- Remove the first row and the first column from \mathbf{H}_{n+1} . The new $n \times n$ matrix is called G .

$$\mathbf{H}_{n+1} = \begin{pmatrix} 1 & \mathbf{1}^T \\ \mathbf{1} & G_n \end{pmatrix} \quad (\text{H.32})$$

By construction, any row or column of the matrix \mathbf{G}_n contains exactly $(n+1)/2$ entries with value -1 and $(n-1)/2$ entries with value 1 . As a consequence

$$\mathbf{G}_n \mathbf{J}_n = \mathbf{J}_n \mathbf{G}_n = -\mathbf{J}_n \quad (\text{H.33})$$

From equations H.29 and H.32, it follows that

$$\mathbf{G}_n \mathbf{G}_n^T = (n+1)\mathbf{I}_n - \mathbf{J}_n \quad (\text{H.34})$$

Using also equation H.33, we have

$$\mathbf{G}_n^{-1} = \frac{1}{n+1}(\mathbf{G}_n^T - \mathbf{J}_n) \quad (\text{H.35})$$

- Replace all the 1 with 0 and all the -1 with 1 from \mathbf{G} . The new $n \times n$ matrix is called \mathbf{S} .

$$\mathbf{S}_n = (\mathbf{J}_n - \mathbf{G}_n)/2 \quad (\text{H.36})$$

By construction, any row or column of the matrix \mathbf{S}_n contains exactly $(n+1)/2$ entries with value 1 and $(n-1)/2$ entries with value 0 . From equation H.36 it follows that

$$\mathbf{S}_n \mathbf{S}_n^T = \frac{n+1}{4}(\mathbf{I}_n + \mathbf{J}_n) \quad (\text{H.37})$$

Therefore, the inverse of the matrix \mathbf{S} is

$$\mathbf{S}_n^{-1} = \frac{2}{n+1}(2\mathbf{S}_n^T - \mathbf{J}_n) \quad (\text{H.38})$$

By defining $\mathbf{M} = \mathbf{S}^{-1}$ we have

$$m_{ij} = \frac{2}{n+1}(2s_{ji} - 1) \quad (\text{H.39})$$

The corresponding mean square error is

$$\epsilon_i = (\sigma^2 + \nu\rho^2) \frac{4}{(n+1)^2} \sum_{j=1}^n (2s_{ji} - 1)^2 = (\sigma^2 + \nu\rho^2) \frac{4n}{(n+1)^2} \quad (\text{H.40})$$

where we used the fact that $(2s_{ji} - 1)$ can only be equal to ± 1 . In this case, $\nu = (n+1)/2$. Therefore, the total mean square error is

$$\begin{aligned}\epsilon_i &= \left[\sigma^2 + \frac{(n+1)}{2} \rho^2 \right] \frac{4n}{(n+1)^2} \\ &= \sigma^2 \frac{4n}{(n+1)^2} + \rho^2 \frac{2n}{(n+1)} \sim\end{aligned}\tag{H.41}$$

$$\sim \frac{4\sigma^2}{n} + 2\rho^2 \quad (\text{if } n \rightarrow \infty)\tag{H.42}$$

Therefore, the SNR gain is

$$\frac{\text{SNR}_n}{\text{SNR}_0} = \sqrt{\frac{\epsilon_0}{\epsilon_n}} = \sqrt{\frac{1 + \chi^2}{1 + \frac{n+1}{2}\chi^2} \frac{n+1}{2\sqrt{n}}}\tag{H.43}$$

Instead, the background becomes

$$\beta'_i = \beta \sum_{j=1}^n \frac{2}{n+1} (2s_{ji} - 1) = \frac{2\beta}{n+1}\tag{H.44}$$



Image Analysis

I.1 Fourier Ring Correlation

The Fourier Ring Correlation (FRC) analysis calculates the Discrete Fourier Transform (DFT) of two images i_1 and i_2 , identical but acquired in two separate moments. Thus, under the hypothesis of uncorrelated noise, only the signal contents of the two images correlate. Therefore, a correlation function in frequency space drops to zero above a certain spatial frequency. The inverse of this latter is the resolution of the imaging setup at the experimental conditions used to acquire the images.

In order to reduce the inherent spectral leakage, we apply to the images a 2D Hann window defined as follows

$$W(n_x, n_y) = \frac{1}{4} \left[1 - \cos \left(\frac{2\pi n_x}{N_x - 1} \right) \right] \left[1 - \cos \left(\frac{2\pi n_y}{N_y - 1} \right) \right] \quad (1.1)$$

where $n_{x,y}$ and $N_{x,y}$ are, respectively, the pixel index and the pixel size of the image. The FRC is defined as the normalized cross-correlation function between $I_1 = \text{DFT}(i_1)$ and $I_2 = \text{DFT}(i_2)$. It is calculated as

$$\text{FRC}(q) = \frac{\sum_{k_x, k_y \in q} I_1(k_x, k_y) I_2^*(k_x, k_y)}{\sqrt{\sum_{k_x, k_y \in q} |I_1(k_x, k_y)|^2 \sum_{k_x, k_y \in q} |I_2(k_x, k_y)|^2}} \quad (1.2)$$

where k_x and k_y are, respectively, the horizontal and vertical spatial frequencies, and $q = \sqrt{k_x^2 + k_y^2}$ is the radial spatial frequency. The resulting curves are denoised using a Locally Weighted Scatterplot Smoothing (LOWESS) algorithm. Importantly, if the SNR of the images

is low, correlations from the camera detector may appear at high frequencies. Therefore, we subtract from the FRC curves an offset calculated as the mean of FRC samples at frequencies above Abbe's resolution limit.

In order to measure the effective resolution of the microscope, we calculate the following variable-threshold function

$$T(q) = \frac{\sigma}{\sqrt{N_q/2}} \quad (1.3)$$

where N_q is the number of pixels contained in the ring of radius q . In this work, we used the so-called 3- σ threshold criterion by setting $\sigma = 3$. The intersection between the threshold and FRC curves identifies the spatial frequency q_t . Below this latter, correlations between the two images emerge from the random noise correlations. Thus, we can interpret q_t as the highest spatial periodicity with enough contrast to be distinguishable from noise fluctuations. The optical resolution of the images is $1/q_t$.

1.2 Image deconvolution

The Bayes theorem states

$$P(o | i) = \frac{P(i | o)P(o)}{P(i)} \quad (1.4)$$

where

- $P(o)$ is the *prior* probability, i.e. the probability of the hypothesis i before the data o are observed.
- $P(i)$ is the *marginal likelihood*, i.e. the probability model for the data i .
- $P(i | o)$ is the *likelihood*, i.e. the conditional probability of measuring i , having fixed an hypothesis o .
- $P(o | i)$ is the *posterior* probability, i.e. the conditional probability of the probability o , having measured i .

It is possible to estimate \hat{o} as the mode of the *posterior* probability by maximizing it. If there is no knowledge on the prior distribution, it is possible to assume it as uniform. In that case, maximizing the *posterior* is the same as maximizing the *likelihood*

$$\hat{o} = \arg \max_o P(i | o) \quad (1.5)$$

In imaging problems, i is the image and o is the object. Those quantities are related by the law

$$i = o * h + \epsilon \quad (1.6)$$

where h is the point spread function of the imaging device and ϵ is the noise.

I.2.1 Wiener Filter

Under the assumption of Gaussian noise, the likelihood – seen as a function of the object o – is

$$P(i | o) = \prod_x \frac{1}{\sqrt{2\pi}\sigma} e^{-\frac{|i-(o*h)|^2}{2\sigma^2}} \quad (1.7)$$

finding its maximum is equivalent to finding the minimum of the log-likelihood, which is defined as

$$\mathcal{L}(o) = -\ln [P(i | o)] = \int \ln(\sqrt{2\pi}\sigma) dx + \frac{1}{2\sigma^2} \int |i - (o * h)|^2 dx \quad (1.8)$$

This problem is equivalent to minimizing the following loss function

$$\ell(o) = \underbrace{\int |i - o * h|^2 dx}_{\ell_1} + \lambda \underbrace{\int |o|^2 dx}_{\ell_2} \quad (1.9)$$

where we added a regularization term.

Since we want to minimize $\ell(o)$, we need to impose its functional derivative to be equal to zero. This latter, is defined from the following relation:

$$\lim_{\rho \rightarrow 0} \frac{\ell(o + \rho s) - \ell(o)}{\rho} = \left\langle \frac{\partial \ell}{\partial o}, s \right\rangle \quad (1.10)$$

where ρ is a constant, s is an arbitrary function, and $\langle \cdot, \cdot \rangle$ is the L^2 inner product.

We start calculating the derivative of $\ell_1(o)$. We have that

$$\begin{aligned} \ell_1(o + \rho s) &= \int |i - o * h - \rho s * h|^2 dx \sim \\ &\sim \int |i - o * h|^2 dx + 2\rho \int (s * h)(o * h - i) dx \end{aligned} \quad (1.11)$$

Therefore, the difference quotient is

$$\begin{aligned} \lim_{\rho \rightarrow 0} \frac{\ell_1(o + \rho s) - \ell_1(o)}{\rho} &= 2 \int (s * h)(o * h - i) dx = \\ &= 2\langle o * h, s * h \rangle - 2\langle i, s * h \rangle = 2\langle h^* * (o * h), s \rangle - 2\langle h^* * i, s \rangle = \\ &= \langle 2h^* * [(o * h) - i], s \rangle = \left\langle \frac{\partial \ell_1}{\partial o}, s \right\rangle \end{aligned} \quad (1.12)$$

where h^* is the adjoint function of h , defined as $h^*(x) = h(-x)$. By comparison, we find that the derivative of ℓ_1 is

$$\frac{\partial \ell_1}{\partial o} = 2h^* * [(o * h) - i] \quad (1.13)$$

Repeating the same calculations for the regularization term, we find

$$\ell_2(o + \rho s) = \int |o + \rho s|^2 dx \sim \int |o|^2 dx + 2 \int os dx \quad (1.14)$$

$$\lim_{\rho \rightarrow 0} \frac{\ell_2(o + \rho s) - \ell_2(o)}{\rho} = 2 \int os dx = \left\langle \frac{\partial \ell_2}{\partial o}, s \right\rangle \quad (1.15)$$

Therefore, the derivative of ℓ_2 is

$$\frac{\partial \ell_2}{\partial o} = 2o \quad (1.16)$$

In order to find the minimum, we now want to impose the complete derivative to be equal to zero

$$\frac{\partial \ell}{\partial o} = \frac{\partial \ell_1}{\partial o} + \lambda \frac{\partial \ell_2}{\partial o} = 0 \quad (1.17)$$

Therefore

$$h^* * [(o * h) - i] + \lambda o = 0 \quad (1.18)$$

Calculating the Fourier Transform of the above equation, we have

$$H^* O H + \lambda O = H^* I \quad (1.19)$$

where the capital letters represent the Fourier transformed functions and H^* is the complex transpose of H . In Fourier space this equation has a simple solution, which in real space is

$$\hat{o} = \mathcal{F}^{-1} \left\{ \frac{H^* I}{|H|^2 + \lambda} \right\} \quad (1.20)$$

1.2.2 Richardson-Lucy

Under the assumption of Poissonian noise, the likelihood is

$$P(i | o) = \prod_x \frac{(h * o)^i e^{-(h * o)}}{i!} \quad (1.21)$$

The corresponding log-likelihood is

$$\mathcal{L}(o) = -\ln [P(i | o)] = \int [(h * o) - i \cdot \ln(h * o) + \ln(i!)] dx \quad (1.22)$$

and the functional to be minimized is

$$\ell(o) = \int [h * o - i \cdot \ln(h * o)] dx + \lambda \int |o|^2 dx \quad (1.23)$$

where we added a regularization term.

In order to find the derivative, we calculate

$$\ell_1(o + \rho s) = \int \left(h * o + \rho s * h - i \cdot \ln \left[(h * o) \left(1 + \frac{\rho s * h}{o * h} \right) \right] \right) dx \sim \quad (1.24)$$

$$\sim \int \left[h * o - i \cdot \ln(h * o) + (\rho s * h) \left(1 - \frac{i}{o * h} \right) \right] dx \quad (1.25)$$

Therefore,

$$\lim_{\rho \rightarrow 0} \frac{\ell_1(o + \rho s) - \ell_2(o)}{\rho} = \int (s * h) \left(1 - \frac{i}{o * h} \right) dx = \langle s * h, 1 \rangle - \left\langle s * h, \frac{i}{o * h} \right\rangle = \quad (1.26)$$

$$= \langle s, h^* * 1 \rangle - \left\langle s, h^* * \frac{i}{o * h} \right\rangle = \left\langle h^* * \left(1 - \frac{i}{o * h} \right), s \right\rangle = \quad (1.27)$$

$$= \left\langle \frac{\partial \ell_1}{\partial o}, s \right\rangle \quad (1.28)$$

So, the derivative is

$$\frac{\partial \ell_1}{\partial o} = h^* * \left(1 - \frac{i}{o * h} \right) \quad (1.29)$$

Therefore,

$$\frac{\partial \ell}{\partial o} = h^* * \left(1 - \frac{i}{o * h} \right) + 2\lambda o = 0 \quad (1.30)$$

If h is normalized, we have that $h^* * 1 = \int h dx = 1$. Therefore, the above equation is satisfied when

$$\left[h^* * \left(\frac{i}{o * h} \right) \right] \frac{1}{1 + 2\lambda o} = 1 \quad (1.31)$$

This equation implies an iterative algorithm. Assuming that at convergence $\frac{o_{k+1}}{o_k} \rightarrow 1$, we can build the following multiplicative gradient-descent iteration rule:

$$o_{k+1} = \left[h^* * \left(\frac{i}{o_k * h} \right) \right] \frac{o_k}{1 + 2\lambda o_k} \quad (1.32)$$

List of Scientific Contributions

Peer-reviewed papers

1. Purnima N. Manghnani, Valentina Di Francesco, Carlo Panella La Capria, Michele Schlich, Marco Elvino Miali, Thomas Lee Moore, **Alessandro Zunino**, Marti Duocastella, and Paolo Decuzzi. Preparation of anisotropic multiscale micro-hydrogels via two-photon continuous flow lithography. *Journal of Colloid and Interface Science*, 608:622–633, feb 2022
2. **Alessandro Zunino**, Francesco Garzella, Alberta Trianni, Peter Saggau, Paolo Bianchini, Alberto Diaspro, and Marti Duocastella. Multiplane Encoded Light-Sheet Microscopy for Enhanced 3D Imaging. *ACS Photonics*, 8(11):3385–3393, nov 2021
3. Fabio Callegari, Aymeric Le Gratiet, **Alessandro Zunino**, Ali Mohebi, Paolo Bianchini, and Alberto Diaspro. Polarization Label-Free Microscopy Imaging of Biological Samples by Exploiting the Zeeman Laser Emission. *Frontiers in Physics*, 9, oct 2021
4. Salvatore Surdo, **Alessandro Zunino**, Alberto Diaspro, and Marti Duocastella. Acoustically-shaped laser: a machining tool for Industry 4.0. *ACTA IMEKO*, 9(4):60, dec 2020
5. Marti Duocastella, Salvatore Surdo, **Alessandro Zunino**, Alberto Diaspro, and Peter Saggau. Acousto-optic systems for advanced microscopy. *Journal of Physics: Photonics*, 3(1):012004, nov 2020
6. **Alessandro Zunino**, Salvatore Surdo, and Marti Duocastella. Dynamic Multifocus Laser Writing with Acousto-Optofluidics. *Advanced Materials Technologies*, 4(12):1–7, 2019

Conference proceedings

1. **Alessandro Zunino**, Salvatore Surdo, and Marti Duocastella. Design, implementation, and characterization of a fast acousto-optofluidic multi-focal laser system. In Ireneusz Grulkowski, Bogumił B. J. Linde, and Marti Duocastella, editors, *Fourteenth School on Acousto-Optics and Applications*, page 23. SPIE, nov 2019

Conference talks

1. **Alessandro Zunino**, Francesco Garzella, Alberta Trianni, Peter Saggau, Paolo Bianchini, Alberto Diaspro, and Marti Duocastella. Parallelized Light-sheet Microscopy with Flexible and Encoded Illumination. In *2021 Conference on Lasers and Electro-Optics Europe & European Quantum Electronics Conference (CLEO/Europe-EQEC)*, pages 1–1. IEEE, jun 2021
2. Marti Duocastella, **Alessandro Zunino**, and Salvatore Surdo. On-The-Fly Laser Beam Shaping With Acousto-Optofluidics. In *2021 Conference on Lasers and Electro-Optics Europe & European Quantum Electronics Conference (CLEO/Europe-EQEC)*, pages 1–1. IEEE, jun 2021
3. **Alessandro Zunino**, Francesco Garzella, Alberta Trianni, Peter Saggau, Paolo Bianchini, Alberto Diaspro, and Martí Duocastella. Multi-plane encoded light-sheet microscopy with acousto-optics. In Keisuke Goda and Kevin K. Tsia, editors, *Photonics West – High-Speed Biomedical Imaging and Spectroscopy VI*, page 29. SPIE, mar 2021
4. **Alessandro Zunino**, Francesco Garzella, Alberta Trianni, Peter Saggau, Paolo Bianchini, Alberto Diaspro, and Martí Duocastella. Multi-plane Encoded Light-sheet Microscopy for Fast Volumetric Imaging. In *Conference on Lasers and Electro-Optics*, page AM3C.3, Washington, D.C., 2021. OSA
5. Salvatore Surdo, **Alessandro Zunino**, Alberto Diaspro, and Martí Duocastella. Rapid parallelization of tailored laser beams with acousto-optofluidics. In *2020 International Conference Laser Optics (ICLO)*, pages 1–1. IEEE, nov 2020
6. **Alessandro Zunino**, Salvatore Surdo, and Marti Duocastella. Parallelized Laser Writing with Acousto-Optofluidics. In *International Congress on Applications of Lasers and Electro-Optics (ICALEO)*. LIA, oct 2019
7. **Alessandro Zunino**, Salvatore Surdo, and Marti Duocastella. Acousto-Optofluidic Multi-spot Generation for High-throughput Laser Material Processing. In *Fourteenth School on Acousto-Optics and Applications*. SPIE, jun 2019

Acknowledgments

My gratitude goes first to my supervisors, Alberto and Martí, whose guidance has been invaluable in those years. If this Ph.D. experience has been a chance to grow both as a professional and human being, it is their merit. The help and support received from Giuseppe and Salvatore are in no way secondary, and I am deeply grateful to them. Another round of thanks goes to all the people at the *Nanoscopy* and *Molecular Microscopy and Spectroscopy* groups and at *Genoa Instruments* for the friendship, support, and all the experiences we shared during these three years. Some special thanks go to a few individuals who made my time in IIT unique. Thank you, Fabio, for all the scattering. Always beware of the phase. Thank you, Giorgio, for all the help – either on the skis or in the lab. Thank you, Agnes, for the pollen and much else. Thank you, Eli, for all the amazing discussions we had. Thank you, Francesco, for all the beads and the time we shared in the lab. I am truly grateful for all the time spent with everyone and looking forward to building even more with all the amazing people I have met, and I still have to meet. This is only the beginning. My gratitude also goes to my family. I would not be who I am now without them. Lastly, I want to thank my biggest supporter. No achievement is as great as having you at my side, Martina.